Origin of the spin Seebeck effect

Dissertation

zur Erlangung des Grades
"**Doktor der Naturwissenschaften**"
am Fachbereich Physik, Mathematik und Informatik
der Johannes Gutenberg-Universität
in Mainz

Andreas Kehlberger

geb. in Mainz
Mainz, 2015

Andreas Kehlberger
Origin of the spin Seebeck effect
Dissertation, Date of the oral defense: October 30, 2015
Reviewers: Removed due to data privacy
Supervisor: Removed due to data privacy
MAINZ supervisors: Removed due to data privacy

D77, Dissertation of the Johannes Gutenberg-Universität Mainz

Johannes Gutenberg Universität Mainz
AG Kläui
Institute of Physics
Staudinger Weg 7
55118 and Mainz

Abstract

The spin Seebeck effect presents a novel spin caloric effect which possesses promising properties for spintronic and thermoelectric applications. Currently the effect leaves open questions about its origin and dependences.

In this thesis, we present a comprehensive study of the spin Seebeck effect in insulating magnetic garnets providing answers to its controversially discussed origin. To fulfill this task we probed the dependence of the spin Seebeck effect on the thickness of the ferromagnetic material, the temperature, the magnetic strength field, the interface and the detection material as well as combinations of the afore mentioned parameters. In order to be able to exclude influences of the insufficient sample material quality, we optimized the growth of investigated magnetic garnets and performed a comprehensive analysis of the crystalline and magnetic material parameters. Furthermore the magnetoresistance of the detection layer, previously claimed to be the origin of the effect, has been determined and a systematic study of the self-designed and constructed setups is presented to rule out parasitic signal contributions. Thus our experimental results are of high quality and show a characteristic saturation of the spin Seebeck effect with increasing thickness of the used ferromagnetic material. The observed saturation additionally depends on the temperature as the length scale increases with decreasing temperature. Further temperature dependent studies reveal the occurrences of a thickness, temperature, and magnetic field dependent peaking of the spin Seebeck effect signals, which also can be shifted to different temperatures by the detector material. For measurements performed at high magnetic fields we find a suppression of the spin Seebeck signals. Our observed signal features are in agreement with the results of numerical simulations of a magnon based spin Seebeck effect, highlighting that the spin Seebeck effect is based on magnonic spin currents emitted by the bulk of the ferromagnetic material. In the last part of this thesis we present measurements in a so far not investigated ferrimagnetic material, revealing two sign changes of the spin Seebeck effect as a function of temperature. These novel signal features highlight that the spin Seebeck effect originates from a complex interplay of the magnonic modes of the material, strongly depending on the detection material.

Thereby our results and findings are able to a provide valuable answers to the origin of the spin Seebeck effect and reveal novel, so far unknown effects, opening up a new interesting chapter for the field of spin caloritronics.

Zusammenfassung

Der Spin Seebeck Effekt repräsentiert einen neuartigen Spin kalorischen Effekt mit vorteilhaften und aussichtsreichen Eigenschaften für Anwendungen in den Gebieten der Spintronik und Thermoelektrik.

In dieser Arbeit präsentieren wir eine umfangreiche Untersuchung des Spin Seebeck Effekts in isolierenden, magnetischen Granaten und geben Antworten zum kontrovers diskutierten Ursprung des Effekts. Um dieses Ziel zu erreichen, haben wir die Abhängigkeit des Spin Seebeck Effekts von der Dicke des Ferromagneten, der Temperatur, der Stärke des magnetisches Feldes, der Grenzflächen und des Detektormaterials, sowie Kombinationen dieser Parameter gemessen. Im Zuge dessen haben wir das Wachstum der untersuchten magnetischen Granate optimiert und eine umfassende Analyse der strukturellen und magnetischen Parameter durchgeführt, um Einflüsse der Probenqualität auszuschließen. Des Weiteren zeigte eine Untersuchung des magnetoresistiven Effekts, welcher als mögliche Ursache des Effekts galt, in Kombination mit einer Studie des Messaufbaus, dass parasitäre Einflüsse auf das Messergebnis ausgeschlossen werden können. Unsere Ergebnisse zeigen, dass der Spin Seebeck Effekt mit zunehmender Dicke des Ferromagneten eine Sättigung des Signals aufweist. Diese hängt zudem von der Temperatur ab, da mit abnehmender Temperatur die Sättigung erst bei dickeren Filmen auftritt. Außerdem fanden unsere Messungen ein Maximum des Spin Seebeck Effekts für Temperaturen unterhalb der Raumtemperatur, welcher sowohl von der Dicke des Materials als auch der Magnetfeldstärke und dem Detektormaterial beeinflusst wird. In Messungen bei hohen magnetischen Feldstärken beobachteten wir eine Unterdrückung des Messsignals, dessen Ursache mithilfe von Simulationen auf den magnonischen Ursprung des Spin Seebeck Effekts zurückgeführt werden kann. Dies unterstreicht, dass der Effekt auf vom Ferromagneten emittierten Magnonen basiert. Im letzten Abschnitt dieser Arbeit präsentieren wir Messungen in einem bislang nicht untersuchten ferrimagnetischen Material, welche zwei Vorzeichenwechsel des Spin Seebeck Effekts als Funktion der Temperatur aufzeigen. Dieses bisher unbekannte Signalverhalten betont, dass der Effekt aus einem komplexen Zusammenspiel der magnonischen Moden resultiert und zusätzlich vom Detektormaterial abhängt.

Somit tragen unsere Ergebnisse und Beobachtungen im hohen Maße zur Beantwortung der Frage nach dem Ursprungs des Spin Seebeck Effekts bei und zeigen neuartige bisher nicht beobachtete Effekte, welche ein neues Kapitel für das Gebiet der Spin Kaloritronik eröffnen.

Contents

Introduction

1

Thermoelectric effects are the result of an interaction between the heat and the charge carrier transport in conductors. The first experimental reports of thermoelectric effects range back to the beginnings of the 19th century, where in 1821 [1] T. Seebeck reported the occurrence of a magnetic polarization of metal circuits induced by a temperature difference. In his original concept Seebeck assumed that the heat flow creates magnetic moments in the metal, which would characterize the effect as thermomagnetic. Later it could be shown that the appearance of magnetization resulted from a magnetic field by a thermoelectrical current in the metallic circuit loop, which is known as the Seebeck effect. The comprehension that the effect allows to convert the heat flow of a system into an electric potential difference, has led to the development of several applications, such as the usage as thermocouples or as thermoelectric generators. More than ever the effect is of high relevance for current technologies, as the demand for more efficient technologies and concepts led to an increasing request for waste heat recovery [2]. Thus current aim of research is to maximize its efficiency by a reduction of the heat transport while maintaining the conduction properties [3]. Furthermore the understanding of the involved physical processes allowed to identify the Peltier effect [4] as the reciprocal process [5] describing the control of the heat flow by the electrical currents. Thus the thermometric description of a conducting system enables one to link charge carrier flow with the heat transport, while the expansion of the conventional electronics by the spin degree of freedom represents the field of Spintronics. The field was boosted by the discovery of the giant magnetoresistance (GMR) which led to the development of modern data storage technology. The state of the art industrial applications are based on the tunnel magnetoresistance (TMR) which is also employed in the magnetic random access memory (MRAM). The recent aim of Spintronics is to develop a replacement technology of current charge based electronics by exploiting pure spin currents. In contrast to architectures for charge carriers Spintronics utilizes the spin as carrier of the information. This concept makes use of the fact that pure spin currents can evade some of the problems limiting further miniaturization of conventional electronics. e.g. the need for high current densities for movement of magnetic domain walls. However the challenge of this concept relies on an efficient interaction between the spin current and the magnetization as well as on the requirement to generate a pure spin current by a low amount of energy. Research in this direction has led to the discovery of new phenomena like spin pumping and the spin Hall effect. Spin pumping describes the transfer of angular moment of a microwaves excited, precessing ferromagnet into an adjacent non magnetic metal. On the other hand the spin Hall effect is identified as a transport phenomenon, which causes a spin dependent charge carrier separation by a conventional current in conductors. It has been shown that the combination of both effects allows to convert a charge current into an angular moment and vice versa [6]. Now the effects that provide the possibility for the generation of spin currents by thermal excitations are gathered in the novel research field of spin caloritronics. The effects involve an interplay between the electrons, their spins, the magnetic and the crystal lattice as illustrated in Fig. 1.1.

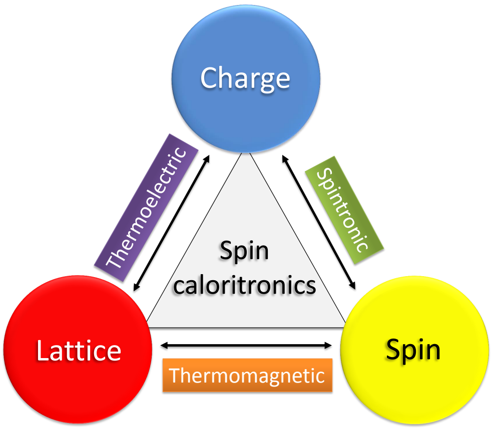

Fig. 1.1: Schematic of involved processes per research field.

A milestone for the spin caloritronics meant the discovery of the spin Seebeck effect in 2008 by Uchida *et al.* [7], who reported the possibility to create a pure spin current by temperature gradient in magnetic metals. The first theoretical concept of the effect described it as the spin current equivalent of the classical Seebeck effect, leading to the naming of the effect. Like for the Seebeck effect, later experiments could show that the initial explanation cannot provide a sufficient explanation for the experimentally observed results. Furthermore the the original experiments could not be reproduced, which triggered the discussion about the origin of the spin Seebeck effect. While the discussion is still ongoing, the search for the origin led to the discovery of the spin dependent expansions of the classic thermoelectric effects. Especially the discovery of the spin dependent Seebeck effect could show that the effect named as spin Seebeck effect must originate from other mechanisms than initially assumed as it had been also detected in magnetic semiconductors and even insulators. Despite the unknown origin various applications have been suggested such as the spin thermoeletric coating [8], which makes use of the fact that the thermoelectrically produced power scales with area of the material. This allows one to simply coat the material in order to increase the output in contrast to the elaborate scaling of conventional thermoelectric power generators, which scale with number of used modules. Furthermore the output of the effect can be enhanced by a thermopile [9] geometry on macroscopic scale or be used as a nanosized power generator [10]. Its combination of heat, magnetization and area scaling enables the application as heat position [11] or magnetic sensor. For the emerging amount of applications the current contradicting explanations of the effect limit further progress. Several possible mechanisms have been put forward to explain the effect either by the temperature difference between the ferromagnet and detection layer [12], the magnons emitted from the bulk of the ferromagnet [13] or even parasitic Nernst effects [14, 15].

The aim of the thesis is to determine the origin of the spin Seebeck effect and thus to push the prospering development of spin caloritronics. To gain further insight we present a comprehensive study of the spin Seebeck effect and its dependences on temperature, interface quality, detection material and magnetic field strength. The development of deposition techniques to grow high quality thin film materials enables us to probe the correlation between the spin Seebeck effect and the thickness of the ferromagnetic materials. We show that our experimental results can be explained by a theoretical approach based on atomistic simulations of the thermally driven magnetodynamic processes in the material itself. This allows us to conclude that the effect must originate from the thermally excited ferromagnet, consisting of magnetic spin waves which propagate within the magnetic lattice. Our final results of the spin Seebeck effect in more complex materials provide an outlook for further research.

The thesis is structured as following:
Chapter 2 presents an overview and brief introduction to the relevant theoretical background for the understanding of the results presented in this thesis. The chapter is subdivided into four parts in which we discuss thermoeletric transport 2.1, the magnetostatic and magnetodynamic concepts of magnetism 2.2 as well as an overview of effects within the field of spintronics 2.3. The last part 2.4 focuses on a more detailed introduction to the spin Seebeck effect and spin caloritronics. We furthermore present the simulation model, which has been used to derive the later discussed theoretical results of the thermally excited magnons. The method and model have been developed by our collaborating group of Prof. Ulrich Nowak from the University of Konstanz.
The first section 3.1 of **Chapter 3** gives a summary and technical details of the most important experimental methods applied to determine the materials properties. The second section 3.2 introduces the materials class of magnetic garnets, which have been used for the investigation of the spin Seebeck effect in magnetic insulators. We explain in detail the optimal deposition conditions for three different types of magnetic garnets, which have been developed in collaboration with the group of Prof. Caroline Ross at the Massachusetts Institute of Technology (MIT) in Boston. Our results of the optimization of the growth of Yttrium Iron Garnet are published in Ref. [p2], while the discussion about Cerium substituted Yttrium Iron Garnet and Gadolinium Iron Garnet is work in progress of the publications [p3] and [p8]. The magneto-optic Kerr effect loops have been measured at the University of Bielefeld in the group of Prof. Günter Reiss.
Chapter 4 discusses the spin Seebeck effect in Yttrium Iron Garnet out as a central theme and is separated into two parts. The first part 4.1 explains the measurement principles and basic dependences of the effect using the magnonic interpretation of the effect. After this we show that the spin Seebeck effect can be used as a novel method to investigate the magnetic anisotropy of insulating ferromagnets and present an approach developed to determine the absolute signal amplitude. The concept and results of using the spin Seebeck effect as a tool for the detection of the magnetic anisotropy are part of the publication [p4].
The second part of **Chapter 4**, section 4.2 focuses on the origin of the spin Seebeck effect. We present our findings obtained by probing the thickness dependence of the spin Seebeck effect at room temperature and $50\,\mathrm{K}$. Our combined experimental and theoretical approach

unambiguously reveals that the spin Seebeck can only be explained by magnonic spin currents emitted by the bulk of the ferromagnetic material. The work presents collaboration between the University of Konstanz, the MIT and the University of Mainz and is part of publication [p5]. Phrases of the publication have been taken over, while small modifications of language and adaptations to the current context have been performed to improve the readability without further notice. The following section 4.3 focuses on the combined temperature and thickness dependence of the spin Seebeck effect. Our results reveal the occurrence of a peak of the spin Seebeck signals at lower temperatures, which depends on the ferromagnetic film thickness and the detection layer. We show that the thickness dependence can be well explained by our concept of thermally excited magnons. The thermal conductivity results presented in this section are taken from the publication [p9], while the experimental SSE data are part of publication [p10]. The last section 4.4 of this chapter addresses the magnetic field suppression of the spin Seebeck effect. In collaboration with the University of Konstanz, we can show that the observed behavior agrees with expectations from the thermal magnon propagation and strengthens our theory of magnonic spin Seebeck effect. The results of the numerical simulations and room temperature measurements are part of the publication [p6]. **Chapter 5** presents our temperature and thickness dependent results of the spin Seebeck effect in Gadolinium Iron Garnet. We observe two sign changes of the effect, one close to magnetic compensation point and one at lower temperatures. In our international collaboration between Walther-Meißner-Institut (WMI), the Tohoku University and University of Mainz, we are able to show that the found sign changes originate from a complex interplay of the magnetic sub-lattices of the material. Results presented in this chapter have been taken from publication [p7] as well as from publication [p8], which present work in progress.

The first author publications [p3], [p4] and [p5] have been written by A. Kehlberger with comments and suggestions from all authors. The investigated YIG and Ce:YIG grown PLD have been produced at the MIT in the group of Prof. C. A. Ross by M.C. Onbasli, D.H. Kim and A. Kehlberger. The presented sample characterization by XRD, XRR, SQUID and VNA-FMR as well as the Pt deposition, the SSE and the MR measurements of the PLD grown YIG and Ce:YIG films have been done in Mainz by A. Kehlberger and G. Jakob. The SSE and VNA-FMR measurements setups have been designed and partially constructed by A. Kehlberger. The numerical simulations and the magnonic model have been performed and developed by the group of Prof. U. Nowak at University of Konstanz. The MOKE measurements have been carried out by G. Götz and T. Kuschel at the University Bielefeld. The MOKE microscopy images have been taken in Mainz by K. Richter and A. Kehlberger. The thermal conductivity measurements have been performed by C. Euler. The SSE measurements on the LPE samples have been done by E.J. Guo and A. Kehlberger. The GIG samples have been produced by E.J. Guo, C. Mix and A. Kehlberger. The GIG sample characterization and SSE measurements have been done by E.J. Guo, A. Kehlberger and T. Schulz.

1.1 List of abbreviations

Effects

(SSE) Spin Seebeck effect

(TSSE) Transverse spin Seebeck effect

(LSSE) Longitudinal spin Seebeck effect

(SHE) Spin Hall effect

(ISHE) Inverse spin Hall effect

(ANE) Anomalous Nernst effect

(PNE) Planar Nernst effect

(MR) Magnetoresistance

(SMR) Spin Hall magnetoresistance

(LLG) Landau-Lifshitz-Gilbert

(FMR) Ferromagnetic resonance

Materials

(YIG) Yttrium Iron Garnet ($Y_3Fe_5O_12$)

(Ce:YIG) Cerium substituted Yttrium Iron Garnet ($CeY_2Fe_5O_12$)

(GIG) Gadolinium Iron Garnet ($Gd_3Fe_5O_12$)

(GGG) Gadolinium Gallium Garnet ($Gd_3Ga_5O_12$)

Techniques

(PLD) Pulsed laser deposition

(XRD) X-ray diffraction

(XRR) X-ray reflectivity

(RSM)	Reciprocal space map
(SQUID)	Superconducting quantum interference device
(VNA)	Vector network analyzer
(MOKE)	Magneto-optic Kerr effect

2

Theoretical description of magnetism, spin dynamics and spintronics

The spin Seebeck effect (SSE) involves a complex interplay between the magnetic and crystal lattice and relies on concepts from classic thermoelectric as well as on novel effects like the spin Hall effect (SHE). In the following theory chapter we will provide a mostly phenomenological overview of the relevant mechanisms, that is necessary to understand the later discussed properties of the SSE. An appropriate theoretical description of presented effects exceeds the scope of this experimental thesis, therefore we point the interested reader to the cited literature in each section.

The theory chapter is divided into four thematic sections, where the first three sections provide the basic knowledge and the last chapter presents a more detailed overview of the emerging research field of spin caloritronic.

The first section introduces the classical thermoelectric effects and thermal transport in crystals, illustrating the correlation between charge carriers and heat flow in a system. Furthermore the section includes a description of the Nernst effect, which presents an important thermoelectric effect for the correct interpretation of the SSE signals.

The second section gives a basic introduction to concepts of magnetism and the underlying magnetic interactions. On the basis of the interactions we will introduce the Landau Lifshitz Gilbert equation and use it to explain the ferromagnetic resonance. We illustrate that the excitation of the magnetic lattice leads to spin waves in the magnetic lattice, which are fundamental for the later understanding of the SSE.

The third section focuses on the spintronics concepts related to magnetodynamics, such as spin pumping, which is used in most theories of the SSE. After this we explain the spin Hall and inverse spin Hall effect (ISHE), which is used as the detection mechanism for spin currents. Furthermore we present the concept of the spin Hall magnetoresistance (SMR) effect.

In the last section we introduce the novel research field of spin caloritronics and the so far discovered spin equivalents of the conventional thermoelectric effects. To provide a better understanding of the difficulties and challenges of the research of the SSE, a detailed introduction explains the inconsistencies between theory and experiments encountered for the SSE. As a last point a brief introduction to the numerical model used for the simulation of thermally excited magnons is given.

2.1 Thermoelectric transport

The thermoelectric effects have been studied since the mid of the 19th century and are of high relevance for current technologies due to the demand of waste heat recovery. In the following section we will show that it is possible to correlate the heat flow and charge carrier transport in conductors, which allows to explain all experimentally observed thermoelectric effects by the Onsager reciprocal relations. For a further reading we recommend the standard textbooks [16–18].

2.1.1 Seebeck effect

The Seebeck effect describes the concurrence of an electrical field in presence of a temperature gradient in conducting materials. To understand the effect we have to take a look on the charge carrier density distribution at the Fermi energy E_F. Fig. 2.1 illustrates the occupation number at the hot and cold end of a conducting material in case of an applied temperature gradient, resembling the Drude–Sommerfeld model [18].

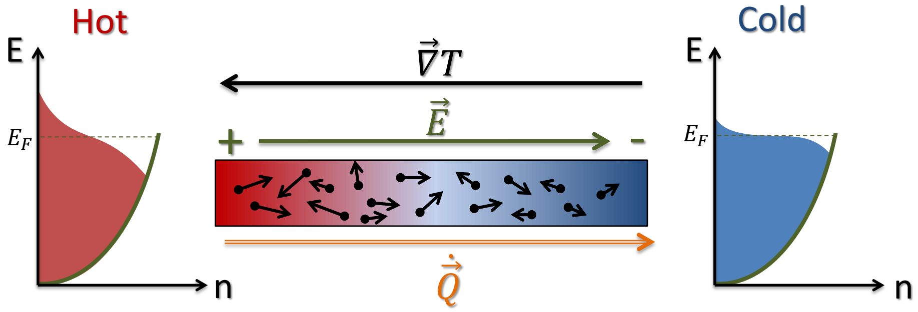

Fig. 2.1: Illustration of theoretical concept of the classical Seebeck effect. The graphics for the hot and cold end show the occupation number $n = \int D(E)f(E,T)dE$ of energy states, where D(E) describes the density of states and f(E,T) the Fermi-Dirac distribution.

At the hot end the distribution shows a larger spread to high and low energy states around the Fermi edge E_F compared to the cold end, causing an equilibration of the energy by diffusion. This heat current $\dot{Q}$ carried by the charge carriers represents the electronic contribution to the thermal conductivity. In the case of equal conductivity for all Fermi levels, the charge currents from both sides cancel one another.

Only in the case of energy dependent conductance the thermal imbalance leads additionally to a net flow of electrons. Fig. 2.1 illustrates this situation for higher conductance for states above the Fermi level, causing a net electron flow from the hot to the cold side [19].

Depending on the majority carrier mechanism the Seebeck effect builds up a positive voltage difference for holes and negative one for electrons. In applications it is convenient to make use of this and to enhance the effect by using two different materials with different charge

carriers. This allows for measuring the temperature difference between the joined part of both materials using a voltmeter only and thus using the effect as a thermometer.
The generated electric field and hence the voltage follows the linear dependence of $V = S\,\Delta T$, where S marks the so called Seebeck coefficient. The coefficient defines the generated voltage per Kelvin of temperature difference and thus marks the efficiency of the effect. For joint materials, S is defined as the difference between the Seebeck coefficient of both. Generally Pt is used as a reference system, which itself has a coefficient of $\sim 5\,\mu\mathrm{V/K}$ [20, 21]. Since beside Pt, additionally Copper, Gold and Constantan (a Nickel Copper alloy) wires are used in later described experimental setups, it should be pointed out that these materials possess non negligible coefficients of several μV/K [21].

2.1.2 Thomson effect and Peltier effect

From description of the thermally driven charge carrier flow, we have already seen that it is accompanied by the heat flow $\dot{Q}$. The Thompson and Peltier effect, discovered in 1848 [22] and 1834 [4], describe the reciprocal phenomena between an electrical current I and the heat current $\dot{Q}$. Using the model of Fig. 2.1, it easy to understand that current between the hot and cold end of the material will cause conduction charge carrier flow, which additionally transports thermal energy from one side to the other. This effect of a thermal transport by the electric current within one material is called Thomson effect. Usually the Thomson effect by itself only causes a small thermal drag and can be neglected. The Peltier effect also makes use of this drag of thermal energy by the electric current but in the combination of two different materials. By joining to two different materials at one interface as shown in Fig. 2.2, it is possible to make use of the differences within the dragged heat currents. If $\dot{Q}_B > \dot{Q}_A$ the sum of the heat currents leads to a heat flow away from the interface, the cooling is proportional to the applied current.

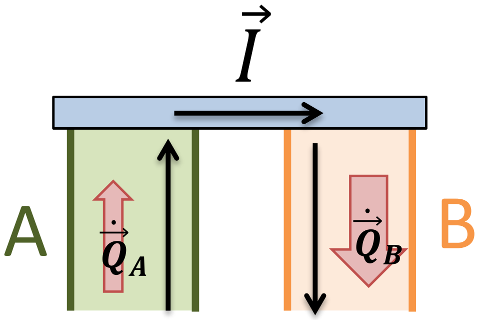

Fig. 2.2: Illustration of concept of the classical Peltier effect. Two materials A and B are electrically and thermally connected at one joined interface. The applied electrical current I causes a net heat current, which carries energy away from the interface.

Like the Seebeck effect, the Peltier effect can be described by a linear relation $\dot{\vec{Q}} = \Pi\,\vec{I}$, where Π denotes the Peltier coefficient. Since the Peltier effect scales only linearly with the applied

current, it can easily be surpassed by the Joule heating, which is proportional to I^2.
The Onsager reciprocity [5, 23] allows to connect heat and charge flow in conductors, using the intrinsic properties of electrical σ and thermal κ conductivity. A consequence of the Onsager reciprocity is the connection between the Seebeck and Peltier coefficient via the Kelvin-Onsager relation $\Pi = ST$ [24]. The investigation of spin based thermoelectric phenomena, such as the spin dependent Peltier effect [25], have shown that the Onsager reciprocity can be expanded to include the spin of electron, and derives the same reciprocity for the spin dependent effects [26] (see Sec. 2.4.1).

2.1.3 Thermal conductivity

From the description of the heat transport in the last section it could be seen that the thermal conductivity is related to flow of electrons within the system and thus influences the thermoelectric effects in the system. To understand the temperature dependence of the thermoelectric effects it is therefore important to understand the different mechanisms, which influence the thermal conductivity of the system. For conductors the thermal conductivity can be divided into a contribution by the charge carrier and the lattice of the solid. The electronic contribution can be sufficiently described by the Drude-Sommerfeld model, which derives the Wiedemann-Franz law as relation between the thermal and electrical conductivity of charge carriers [18]. At high temperatures the Wiedemann-Franz law [18] holds, as the electron scattering is isotropic and independent of their energy. At low temperatures a momentum transfer from the phonon to the electron system (phonon-drag) lead additional to a pile up of electrons density enhancing the Seebeck coefficient [18].
The crystal lattice transports the thermal energy via waves that can be described by a bosonic quasi-particle concept, the phonon [16, 17]. The phonon results from the strong elastic interaction between neighboring atoms in the crystal lattice. A thermal excitation of one lattice atom out of the equilibrium position leads to a coupled response. A semi-quantum mechanical treatment of a coupled three dimensional lattice [18] derives the following notation for the phonon heat conductivity

$$\vec{\kappa}_p = -\frac{\dot{\vec{Q}}}{\vec{\nabla} T} = 1/3 \int_0^{\theta_D/T} C(x) v \lambda(x) dx, \quad x = \frac{\hbar\omega}{k_B T}, \tag{2.1}$$

where $C(x)$ marks the specific heat of the lattice within the Debye approximation, θ_D the Debye temperature, ω, v and $\lambda(x)$ the phonon frequency, velocity and mean free path. The derived formulae for thermal conductivity and mean free path obey a complex temperature dependence, which can be best explained by a graphical illustration, as shown in Fig. 2.3 for the case of crystalline insulator. For high temperatures the mean free path of the phonons is mainly limited by scattering processes with other phonons, causing the so called Normal and Umklapp scattering. The latter process describes a phonon-phonon interaction with energy high enough to invert the momentum of the phonon. Decreasing the temperature increases the mean free propagation path for the phonons, since less energy and phonons for the scattering processes are available.

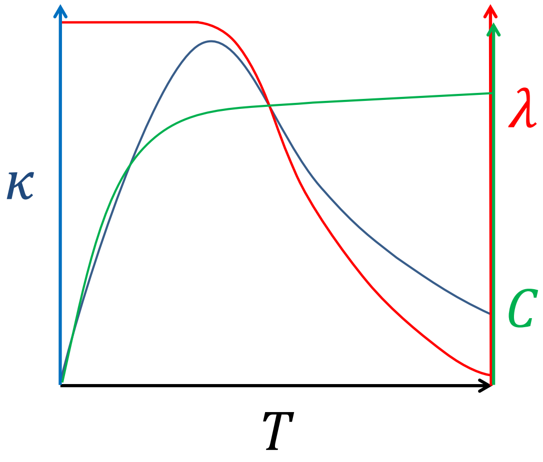

Fig. 2.3: Thermal conductivity κ, mean free path λ and specific heat C of the crystal lattice as a function of temperature for a crystalline insulator with logarithmic y-axes. The plot follows an illustration of [18].

The thermal conductivity therefore follows the increase of the mean free path. At even lower temperature the mean free path approaches a limit governed the boundary and defect scattering of the phonons. For thin films the boundary can be given by the film thickness itself, as the phonon propagation length matches the film thickness. Around the temperature where the boundary and defect scattering start to dominate, the thermal conductivity reaches a maximum. For lower temperature one additionally has to consider that the thermal capacitance $C(x)$ roughly follows $C(T) \propto T^3$ causing a decrease of the thermal conductivity in this temperature range. Thus the peak for the thermal conductivity of the lattice can be well explained by the quasi-particle concept of the phonon, arising from a propagation and interaction within the lattice. In Sec. 4.3.2, we will see that this argumentation can also be applied to the temperature dependence of the SSE to derive its origin.

Based on the earlier discussed phonon-electron interaction, the peak within the thermal conductivity of the crystal lattice leads additionally to a peaking of the Seebeck effect, the so called phonon-drag [27].

2.1.4 Nernst effect and magnetoresistance effect

In conductors the presence of external magnetic field, applied perpendicular to the current flow, leads to the accumulation of charge carries perpendicular to current flow and magnetic field, which is called ordinary Hall voltage [17]. The effect occurs due to the Lorentz force on the conduction electrons causing a directed deflection of the charge carrier transverse to the current flow, which gives rise to a transverse magnetoresistance. By replacing the conventional current with a thermally excited charge carrier flow, we obtain the configuration described by the Nernst effect [27]. The inverse effect of a thermal flow caused by a charge carrier flow within the magnetic field is called Ettingshausen effect [27]. In magnetic conducting materials further contribution to the Hall voltage can be detected, which depends on the magnetization of the material, the anomalous Hall effect (AHE) [28]. The analog to this the thermoelectric counterpart is called anomalous Nernst effect (ANE) [29], shown Fig. 2.4a). The origin of the AHE / ANE effect is explained on basis of a spin-orbit interaction dependent scattering theory [28], which gives rise to an additional magnetoresistance component in the transverse configuration.

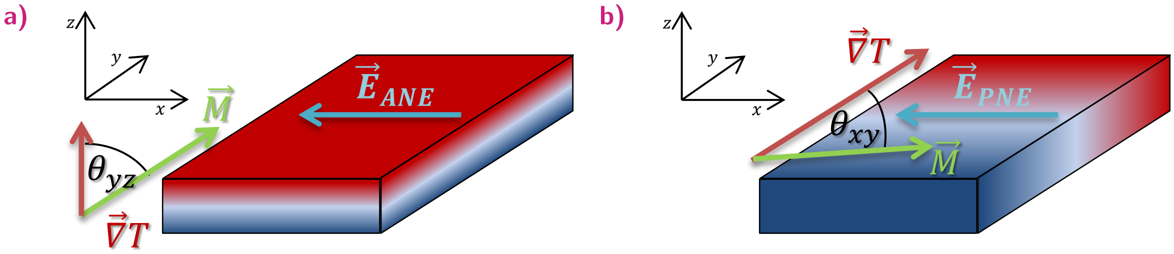

Fig. 2.4: Schematic of the angular dependence between magnetization $\vec{M}$ and electric field $\vec{E}$ for a) anomalous Nernst and b) planar Nernst configuration.

The angle dependence of the ANE can be described by

$$\vec{E}_{ANE} \propto \vec{M} \times \vec{\nabla}T, \tag{2.2}$$

revealing a sinusoidal dependence on the angle θ between magnetization and thermal gradient. As depicted in Fig. 2.4a) the ANE can be measured if the temperature gradient is applied in the out-of-plane direction with an in-plane magnetic field and voltage contacts on top of the material. Fig. 2.4b) illustrates the situation by changing the out-of-plane temperature gradient to an in-plane. For this geometry one expects a vanishing ANE effect, as the resulting $\vec{E}_{ANE}$ points out-of-plane. In contrast to this expectation one will detect in this geometry a thermal voltage, which is described as transverse thermopower or planar Nernst effect (PNE) [30, 31]. The PNE follows a second order angular dependence of

$$\vec{E}_{PNE} \propto \vec{M} \times (\vec{M} \times \vec{\nabla}T), \tag{2.3}$$

which yields $V_x \propto \sin(2\theta_{xy})$. The combination of both thermal voltages, which are unavoidably present in magnetic conductors means that only in situation of $\vec{M} \parallel \vec{\nabla}T$ no magnetic field dependent thermal voltage should be detected [32]. The corresponding Hall effect for the PNE is called pseudo or planar Hall effect, which arises due to anisotropic scattering and is related to the anisotropic magnetoresistance (AMR). The origin of this AMR effect results from the spin orbit interaction caused energy band mixing, which depends on the magnetization of the material [33].

2.2 Magnetostatic and magnetodynamic concepts of magnetism

Materials can be separated into two groups depending on their reaction on a magnetic field, described by the magnetic susceptibility $\chi = M/H$. Diamagnetism categorizes materials which show an induced magnetic moment opposite oriented to the applied magnetic field ($\chi_D < 0$, $|\chi_D| < 1$), illustrated in Fig. 2.5a). The effect is present in all materials but dominates only for materials which have no unfilled electronic shells [16].

The second category consists of materials with a finite magnetic moment, which couples positively with an external magnetic field ($\chi > 0$). In case of a negligible coupling between the individual magnetic moments the material is described as a paramagnet ($|\chi_P| << 1$), leading to an in average zero magnetic moment of the whole material in absence of a magnetic field. A quantum mechanical treatment of the system shows that the magnetization follows the Brillouin function as reaction to the external magnetic field for a given temperature [16].

In case of a finite coupling between the moments the material establishes a collective magnetism causing a magnetic ordering at zero magnetic field. The ordering allows to further classify the materials into ferromagnetic, ferrimagnetic and antiferromagnetic. Magnetic moments of a ferromagnet possess a positive interaction coupling, favoring a parallel alignment of the moments($|\chi_F| >> 1$). The magnetic field dependence of a ferromagnet, illustrated in Fig. 2.5a), shows that the material can maintain a finite magnetic moment without external field, the Remanence.

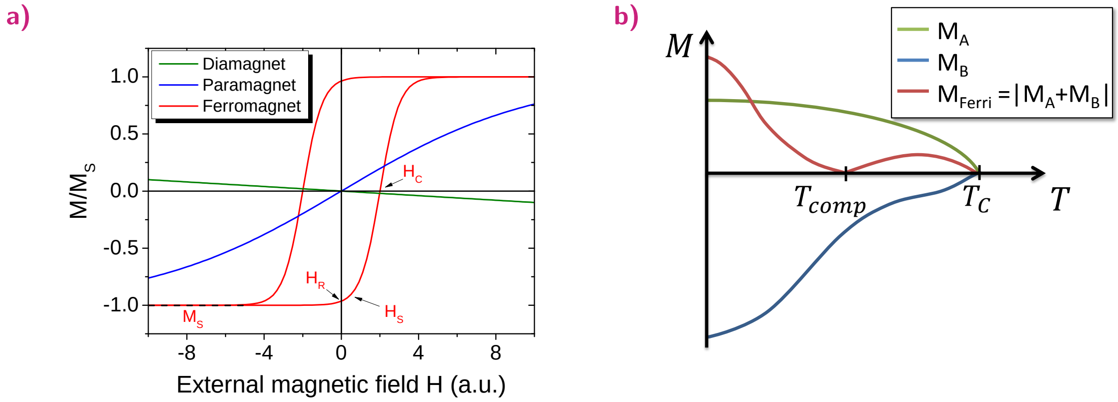

Fig. 2.5: a) Illustration of the magnetization of diamagnetic (green), paramagnetic (blue) and ferromagnetic (red) material. b) Temperature dependence of a ferrimagnetic material (red) and the two antiferromagnetically coupled sub-lattices (green and blue).

The coupling between the individual moments can cause collective switching of the magnetization (H_S, switching Field) into the saturated state at which all moments are aligned with the magnetic field (saturation magnetization M_s).

Antiferromagnets have a negative neighbor interaction causing an antiparallel alignment of the neighboring moments ($|\chi_{AF}| < |\chi_P|$). Since the moments are equal in magnitude, the moments within the material compensate one another, allowing only possible uncompensated moments at the surfaces. The last class of ferrimagnets describes materials with a more complicated substructure. In contrast to both previous classes, ferrimagnets must consist of at least two individual ferromagnetic sub-lattices with different moments in magnitude. The two sub-lattices couple antiferromagnetically causing a reduced moment for the whole material.

The coupling strength of the lattice in a ferromagnet (antiferromagnet) determines its Curie temperature T_C (Néel temperature, T_N) at which the thermal excitation is too high to allow any collective ordering of the moments. At T_C the lattice undergoes a second order phase transition to a paramagnetic ordering, causing the loss of any order due to the ferroic coupling. The competition between two different sub-lattices, which have an different temperature dependence, can lead in ferrimagnets to the occurrences of a compensation point T_{comp} of the magnetization, at which the moments of both sub-lattices compensate another, as shown in Fig. 2.5b). The magnetic interaction not only defines previous presented magneto static properties but also determines the magnetodynamic properties of the ferromagnet. We will use the concept of the magnetic free energy, which is defined as the sum the internal energy of the system plus the energy obtained in external magnetic field, to explain the main contributions to our following description of the magnetization dynamics.

2.2.1 Magnetic free energy

A ferromagnetic material, placed in external magnetic field, tries to minimize its free energy $F = \int_V \epsilon(\vec{r})\mathrm{d}\vec{r}$ across the whole sample volume V by aligning its magnetic moments into the direction of the minimum of the free energy, where ϵ represents the free energy density. Depending on the contributing terms, this minimum does not have to be parallel to the external field. The free energy density can be decomposed into

$$\epsilon = \epsilon_{ex} + \epsilon_{dipol} + \epsilon_{Cryst} + \epsilon_{uni} + \epsilon_{mag.el} + \epsilon_{Zeeman} + \ldots, \tag{2.4}$$

where the first term ϵ_{ex} labels the usually isotropic energy resulting of the exchange coupling. The four following terms, ϵ_{dipol}, ϵ_{Cryst}, ϵ_{uni}, $\epsilon_{mag.el}$, mark anisotropic energy terms, which despite their small contribution are the origin of the magnetic anisotropy of the macroscopic system. The last term ϵ_{Zeeman} describes the energy contribution resulting of the Zeeman effect [34]. Fig. 2.6 illustrates the coordinate system which will be used in the following definition of the individual terms. It is important to point out that the axes of the system need to resemble the lattice structure of investigated system. For our later discussion we will describe the terms on a basis of a cubic crystal with the [001] direction pointing out-of-plane.

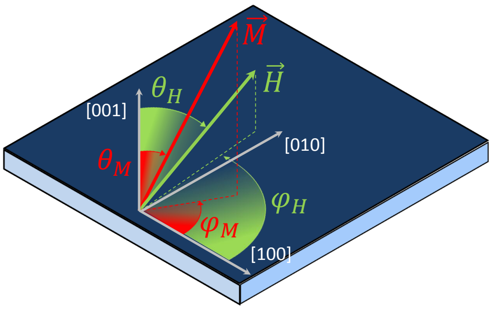

Fig. 2.6: Coordinate system used for the description of the free energy density in a [001] oriented system. θ_M (θ_H) marks the polar angle between out-of-plane [001] direction and the magnetization M (external magnetic field H). φ marks the azimuth angles between the [001] in-plane direction and M or H.

Exchange coupling

The exchange or so called spin-spin interaction results from the Pauli exclusion principle requiring an anti-symmetric total wave function for the electrons regarding the spin flip operator. This leads to a neighbor S_i neighbor S_j spin-interaction causing an energy difference between the parallel and antiparallel alignment for neighboring spins. The exchange interaction in an n-electron system can be described by the Heisenberg Hamiltonian model

$$\mathcal{H}_{ex} = -2\sum_{i>j}^{n} J_{ij}^{ex}\vec{S}_i \cdot \vec{S}_j, \tag{2.5}$$

where J_{ij}^{ex} marks the isotropic exchange constant. A positive value for J_{ij}^{ex} favors a parallel alignment of $\vec{S}_i$ and $\vec{S}_j$, which corresponds to ferromagnetic coupling, while a $J_{ij}^{ex} < 0$ causes an antiparallel orientation and thus marks an anti-ferromagnetic coupling. Based on its quantum mechanical origin the exchange interaction presents an interaction only relevant on short length scale, which allows to apply the approximation of the next neighbor interaction. The resulting formula for the free energy is in the continuum approximation for a slowly changing magnetization $\vec{M}(\vec{r})$ given by

$$\epsilon_{ex}(\vec{r}) = \frac{A}{M_s^2}(\vec{\nabla} \cdot \vec{M}(\vec{r}))^2, \tag{2.6}$$

where A labels the exchange constant that follows the same sign dependence as the exchange integral. From the equation one can see that the exchange energy shows an isotropic behavior and thus cannot give by itself an explanation for the occurrence of favored axis for the magnetization. The exchange coupling represents the highest energy contribution to the free energy with $10 - 1000\,$meV per atom [35] and thus for Curie Temperature.

In the later description we will encounter more complex systems. Especially in the case of magnetic oxides the exchange between different sub-lattices cannot be explained by a direct exchange as the separation between the lattice sites is too large. In these ionic solids the so called superexchange [36] allows an indirect interaction between two metal ions bond to the same non-magnetic oxygen ion. In most cases the oxygen ion mediates an anti-ferromagnetic coupling between the two sub-lattices as will be later seen for Yttrium Iron Garnet (YIG) (see Sec.3.2.1).

Dipolar coupling

A magnetic moment can be described as a magnetic dipole μ_1 and has in presence of another dipole μ_2 an energy of

$$E_{dipol}(\vec{r}) = -\frac{\mu_0}{4\pi r^3}\left[\vec{\mu}_1 \cdot \vec{\mu}_2 - \frac{3}{r^2}(\vec{\mu}_1 \cdot \vec{r})(\vec{\mu}_2 \cdot \vec{r})\right], \tag{2.7}$$

where r marks the separation between the dipoles and corresponds to the vacuum permeability $\mu_0 = 4\pi * 10^{-7}$ [36]. The $1/r^3$ dependence of the energy term shows that compared to the exchange interaction the dipole-dipole coupling presents a long range interaction from one might think that it is also relevant for paramagnets. A rough estimation of the order of magnitude for the energy yields $\sim$ 60 µeV, which corresponds to 1 K temperature [36] and thus illustrates that dipole-dipole by itself, plays only an important role for the magnetic ordering at low temperatures. Since the dipolar coupling is a long-range effect, it can lead to an effective magnetic anisotropy. To understand this behavior we assume the situation where all spins are parallel aligned within the material. In this configuration neighboring dipoles compensate one another leading to the fact that only the dipoles at the surface of the material are uncompensated and generate stray fields. These stray fields are responsible for the shape anisotropy. By using the Maxwell equations for electrostatic case one obtains a correlation between the stray field H_d and the magnetization M of

$$\vec{H}_d(\vec{r}) = -\overline{N} \cdot \vec{M}(\vec{r}). \tag{2.8}$$

$\overline{N}$ describes the demagnetization tensor and resembles the shape of the sample with tr($\overline{N}$)$= 1$. Since our studies are limited to thin film samples, where the in-plane expansion of the film can be treated as infinite surface compared to the film thickness, only the out-of-plane component needs to be considered ($\overline{N} = N_{[001]} = 1$). Thus the free energy of the dipole coupling can be expressed as $\epsilon_{dipol}(\vec{r}) = -\frac{\mu_0}{2}\vec{M}(\vec{r}) \cdot \vec{H}_d(\vec{r})$. For a homogeneous magnetized sample the equation can be simplified to

$$\epsilon_{dipol}(\vec{r}) = \frac{\mu_0}{2} M_s^2 \cos^2(\theta_M), \tag{2.9}$$

illustrating that the dipole coupling causes an in-plane orientation of the magnetization, since the energy gets minimized for $\theta = 90\,°$.

Crystalline and uniaxial anisotropy

Most materials show a complex magnetic anisotropy, which cannot be explained solely by the shape of the material. Especially for the case of crystalline materials the ordering of the magnetic moments within the crystal lattice structure induces a favoring of certain directions. In the case of ferrimagnetic insulating oxides, the so called single-ion model [37–39] is able to explain most occurring anisotropies within these materials. The model is based on an interplay between a crystal field and the orbital state and exchange interaction of the magnetic moments [37, 40]. The model derives a uniaxial K_u and cubic K_1 anisotropy constants [37, 41] for these systems, showing an agreement with experimental bulk material studies [42].

Phenomenologically one can describe the anisotropies by a power series which yields for the uniaxial anisotropy

$$\epsilon_{uni}(\vec{r}) = K_u \sin^2(\varphi_M) + K_{u4} \sin^4(\varphi_M) + \dots, \tag{2.10}$$

where $sin^2(\varphi_M)$ assumes an in-plane easy axis along the [100] direction. Depending on the orientation of the uniaxial anisotropy the angle of eq. 2.10 has to be adapted to match the experimentally encountered orientation of the anisotropy. For the cubic anisotropy the power series can be written in the form

$$\epsilon_{cubic}(\vec{r}) = K_1(\alpha_1^2\alpha_2^2 + \alpha_2^2\alpha_3^2 + \alpha_3^2\alpha_1^2) + K_2\alpha_1^2\alpha_2^2\alpha_3^2 + \dots, \tag{2.11}$$

where $\alpha_i = M_i(\vec{r})/M_s$ presents the direction cosines of the magnetization. For an in-plane cubic anisotropy in the system defined by Fig. 2.6, the first term of eq. 2.11 can be rewritten as

$$\epsilon_{cubic}(\vec{r}) = \frac{1}{4}K_1(\sin^2(2\theta_M) + \sin^4(\theta_M)\sin^2(2\varphi_M)) + \dots, \tag{2.12}$$

where a positive value for K_1 corresponds to an easy axis along the [010] and [100] direction and a negative value to a by $45\,^\circ$ rotated easy axis along [110]. The anisotropy can be either determined by ferromagnetic resonance measurements, which will be explained in Sec. 2.2.2 and 3.1.5, or extracted from hysteresis measurements. Fig. 2.7 shows two examples for the shape of the hysteresis obtained when the system is probed along the easy and hard axis in case of a) uniaxial and b) cubic anisotropy.

The characteristic difference between both types of anisotropy can be best seen by probing the magnetization along the hard axis, revealing a higher remanence for the cubic anisotropy. It can be shown [37] that saturation field H_K can be used to calculate the anisotropy constant $K_{u/1}$. Tab. 2.1 gives a list of the anisotropy field formulae used in this thesis.

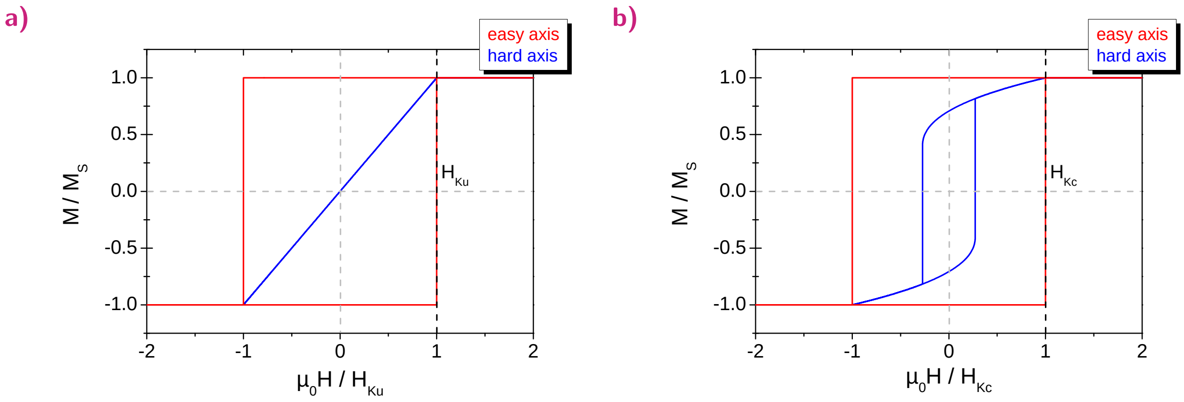

Fig. 2.7: Illustration of magnetic hysteresis loops for the easy (red) and hard axis (blue) for system with a) uniaxial and b) cubic anisotropy, draw for the Stoner–Wohlfarth model [36].

{Plane}	<Axis> (in-plane direction)	H_K (in-plane)
{100}	<100> $(0°, 90°)$	$2K_1/M_s$
	<110> $(45°)$	$-2K_1/M_s$
{111}	$<2\bar{1}\bar{1}>$ $(0°, 60°)$	$-K_2/3M_s$
	$<01\bar{1}>$ $(30°, 90°)$	$-K_2/3M_s$
Uniaxial		$2K_u/M_s$

Tab. 2.1: Magnetocrystalline anisotropy fields for a cubic and uniaxial symmetry, taken from Ref. [37].

In case of an occurrence of a combined uniaxial and cubic anisotropy, which match in their orientation for the hard axis, the anisotropy field represents the combination of both fields ($H_K = H_1 + H_u$).

Zeeman energy and electron paramagnetic resonance

Up to now we considered only internal magnetic fields, which result from the interaction of the magnetic moments. The Zeeman effect [34] term describes the response of the magnetic moments to the external magnetic field. The field causes a splitting of the energy levels between the spin orientations of $\Delta E \propto H$. The Zeeman free energy term is equal to $\epsilon_{Zee}(\vec{r}) = -\mu_0 \vec{M}(\vec{r}) \cdot \vec{H}(\vec{r})$, illustrating that its contribution gets minimal for a parallel alignment of magnetization and external field. For a homogenous magnetized sample one can simplify the equation to

$$\epsilon_{Zee}(\vec{r}) = \mu_0 H M_s (\cos(\theta_H)\cos(\theta_M) + \sin(\theta_H)\sin(\theta_M)\cos(\varphi_H - \varphi_M)). \qquad (2.13)$$

In absence of the other contributions to the free energy, this term describes the paramagnetic response of the magnetic moments to the external field. For a single electron the energy difference between the spin up and down state is given by $\Delta E = g_J \mu_B \mu_0 H$ [34], where

g_J marks the Landé g-factor and μ_B the Bohr magnetron. One can now make use of this transition and resonantly excite the paramagnet by a second weaker electromagnetic microwave field $\Delta E = \hbar\omega_{Larmor}$. The resonance frequency is described as the Larmor frequency, which drives the transition between spin up and down state. This technique is called electron paramagnetic resonance (EPR) and is used for the spectroscopy of elements.

2.2.2 Landau-Lifshitz equation for magnetization dynamics and ferromagnetic resonance

The magnetization dynamics of a ferromagnet can be described like the EPR, using two simplifications. At first we can treat the combination of the external field and the internal ($\vec{H}_{int} = -1/\mu_0 \vec{\nabla}_{\vec{M}}\epsilon$) as an effective field $\vec{H}_{eff} = \vec{H}_{ext} + \vec{H}_{int}$. Further the magnetic moments will not be considered independently but as the whole coupled magnetization $\vec{M}$, due to the exchange interaction.

The concept of the magnetic free energy has already illustrated that a minimum for the energy is achieved when the magnetic moments are aligned parallel to the effective magnetic field. Thus an applied effective magnetic field causes a torque on magnetic moments, leading to a precession of the moment around the field vector. The precession of magnetization can be derived from a classical model resulting in the Landau-Lifshitz (LL) equation

$$\frac{\partial \vec{M}}{\partial t} = -\gamma\mu_0 \left[\vec{M} \times \vec{H}_{eff}\right], \tag{2.14}$$

which describes a Larmor precession of the whole magnetization [37] using the gyromagnetic ratio γ of the electron. Like the Larmor frequency this precession possesses an eigenfrequency, at which the system can be excited, known as the ferromagnetic resonance (FMR). To calculate the FMR from eq. 2.14 one can make use of the angle definition presented in Fig. 2.6. Using the polar and azimuthal angle it has been shown [35, 43] that the FMR can be expressed as a function of second derivatives of the free energy density of the system by

$$f_{FMR} = \frac{|\gamma|}{2\pi M_s \sin(\theta_M)} \left[\frac{\partial^2\epsilon}{\partial\theta_M^2}\frac{\partial^2\epsilon}{\partial\varphi_M^2} - \frac{\partial^2\epsilon}{\partial\theta_M\partial\varphi_M}\right]^{\frac{1}{2}} \tag{2.15}$$

with $|\gamma|/2\pi \approx 28\,\mathrm{GHz/T}$. As an example we introduce the Kittel equation, which is the solution for an anisotropy free system under the assumption that the exchange contribution can be neglected, since we assume a uniform precession of the material [44]. Thus the free energy only contains the dipole and Zeeman term $\epsilon = \epsilon_{Zeeman} + \epsilon_d$. Furthermore we only consider the case of an in-plane ($\theta_H = 90\,^\circ$) oriented external magnetic field along the [100] axis ($\varphi_H = 0\,^\circ$). For an external field high enough to saturate the material, we can further simplify the formula by assuming $\theta_H = \theta_M$ and $\varphi_H = \varphi_M$.

These boundary conditions yield the so called Kittel equation

$$f_{FMR}(H_{ext}) = \frac{|\gamma|}{2\pi}\mu_0\sqrt{(H_{ext})(H_{ext}+M_s)}, \tag{2.16}$$

which describes the FMR f_{FMR} as a function of the external magnetic field H_{ext}. By adding a cubic F_{cub} and uniaxial in-plane magnetic anisotropy ϵ_{uni} to the free energy density, solving eq. 2.14 for the same direction results in

$$f_{FMR}(H_{ext}) = \frac{|\gamma|}{2\pi}\mu_0\sqrt{(H_{ext}+H_{K1})(H_{ext}+H_{K1}+M_s-H_{Ku})}, \tag{2.17}$$

where H_{K1} corresponds to the cubic and H_{Ku} to the uniaxial anisotropy field, presented in Tab. 2.1. Eq. 2.17 illustrates that a magnetic anisotropy of a material causes a deviation from eq. 2.15, allowing to use FMR as a probing tool for the anisotropy. The FMR resonance frequency can be, as the EPR, excited by an additionally applied microwave frequency field, which needs to be perpendicular oriented to the external field, since the excitation uses a dipole transition. The experimental realization is discussed in Sec. 3.1.5.
The precession we discussed so far represents a dissipationless motion, which alters the azimuthal angle of M but will never align along H_{eff}. This description is not in agreement with the experimental observation, which finds a decay of the excited precession over time.

2.2.3 Landau-Lifshitz-Gilbert damping

To consider the energy loss of the precession motion over time, the original equation has been extended by a phenomenological damping term, which takes this discrepancy into account. The extended formula is called Landau-Lifshitz-Gilbert equation [45] and has the form

$$\frac{\partial \vec{M}}{\partial t} = -\gamma\mu_0\left[\vec{M}\times\vec{H}_{eff}\right] + \frac{\alpha}{M_s}(\vec{M}\times\frac{\partial M}{\partial t}), \tag{2.18}$$

where α labels the dimensionless Gilbert damping parameter. The motion of the magnetization is illustrated in Fig. 2.8a), highlighting the contributions of the first and second term.

Phenomenologically the damping can be understood as an energy and angular momentum transfer from the main uniform FMR to phonons of the crystal lattice via spin orbit coupling, scattering with electrons, excited eddy currents within conducting systems and the decay into non-uniform magnetic spin waves [46, 47].
Following a description of Ref. [37], it can be shown that the response function of the magnetization on the applied excitation field can be expressed by the complex susceptibility tensor $\overline{\chi}$. The additional damping term leads to broadening of this response function at FMR, which can be decomposed into a real and imaginary part. The real part of the tensor

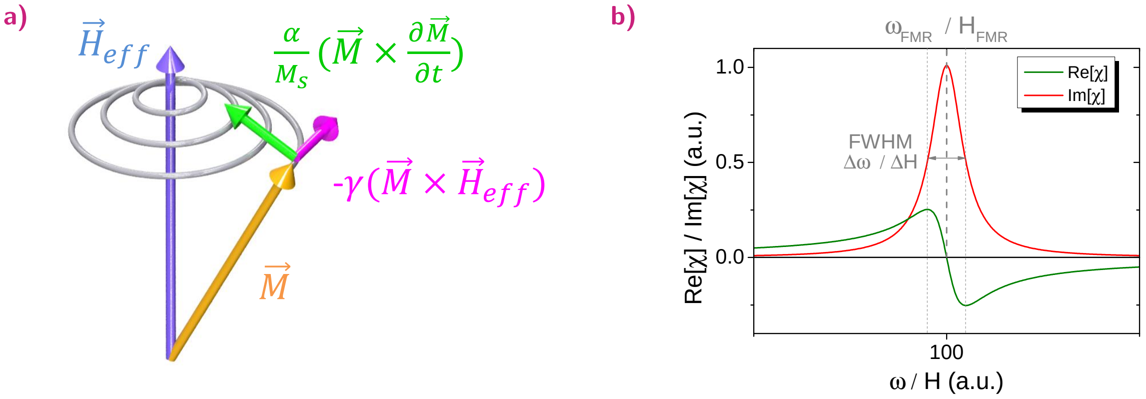

Fig. 2.8: a) Illustration of the precession of the magnetic moment due to the effective magnetic field H_{eff}. The first term of eq. 2.18 is represented by the pink arrow, which marks the identical precession as described in eq. 2.14. The green arrow indicates the second term of eq. 2.18, which illustrates damping causing a alignment of M parallel to H_{eff}. b) Real (green) and imaginary (red) part of the susceptibility tensor $\overline{\chi}$ as a function of applied field / frequency.

corresponds to the derivative of a Lorentz profile, while the imaginary part is expressed by Lorentz profile, shown in Fig. 2.8b) [37]. The response profile is valid for probing the FMR either as a function of the applied field for a static excitation frequency [37] or for a fixed external field and a variable excitation frequency [48].

Since the FMR FWHM line width is directly related to the decoherence rate of the system, it is possible to correlate FWHM with the Gilbert damping parameter [37, 48]

$$\Delta H \cong \frac{4\pi\alpha f_{FMR}}{|\gamma|\mu_0}. \tag{2.19}$$

This formula provides only a limited description of the line width broadening due to the damping and only holds for materials of high homogeneity [37]. A better approximation is provided by the empirically [49, 50] found formula dependency

$$\Delta H(f_{FMR}) = \Delta H_0 + \frac{4\pi\alpha f_{FMR}}{|\gamma|\mu_0}, \tag{2.20}$$

that includes an additional offset contribution to damping ΔH_0. α describes the intrinsic magnetic damping, attributed to above mentioned mechanisms. ΔH_0 is considered to be an extrinsic contribution to the damping attributed to frequency independent scatter mechanism like defects or inhomogeneities within the sample, which cause an inhomogeneous broadening.

2.2.4 Magnons

For FMR we have used the macrospin model to derive the dynamics for the whole ferromagnetic lattice. Like the phonon for crystal lattice, we can introduce a quasi-particle, the magnon, which describes quantized spin waves of the magnetic lattice. At zero Kelvin the magnetic lattice is completely ordered. Higher temperatures can now lead, as in the case of crystal lattice, to coupled excitations of the magnetic lattice which carry energy and, due to the dipole nature of the magnetic lattice, an angular momentum. This concept is based on an idea of Bloch [51], who illustrated that a bosonic spin-wave model for coupled excitations in magnetic lattice results in a temperature dependence of magnetization similar to the Heisenberg model, depending on the exchange interaction and ordering of the lattice. The model leads to a temperature dependence of the spontaneous magnetization $\propto T^{3/2}$, which describes well the behavior for low temperatures.

The wavelength of a magnon is defined as the phase difference between neighboring spins, which precess with the same frequency. This allows to classify two types of magnons, depending on range of the important interaction, as shown in Fig. 2.9.

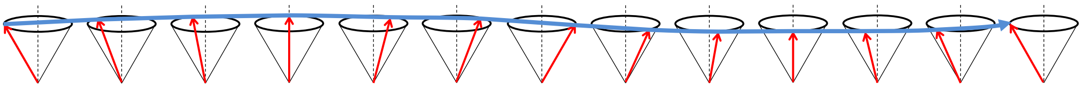

Fig. 2.9: Illustration of a magnon in a one dimensional lattice. The red arrows present the precessing individual spin, while the blue arrow indicates the wavelength of the magnon.

Short wavelength magnons are defined as exchange-dominated spin waves, since the energy resulting from the displacement of neighboring spins mainly originates from the exchange interaction. The energy of long wavelength magnons results of the dipole interaction as the phase difference for neighboring spins can be neglected.

Our later discussion of the SSE focuses on experimental geometry with in-plane magnetic field and expects a magnonic wavevector in the out-of-plane direction perpendicular to the applied field. For dipole modes this situation only allows the excitation of surface spin waves [52]. For theoretical description of the SSE we will present an atomistic magnonic model, which only considers the exchange interaction since it is limited to only a few unit cells, where contributions of dipoles mode with typical wavelength in order of µm [53] are negligible. Thus the investigated system differs significantly from microwave spin pumping experiments where in most cases dipole modes play a dominate role [53]. Furthermore, the thermal excitation causes a locally limited perturbation of the magnetic lattice, therefore only a significant contribution is expected to result from the short range exchange interaction.

In contrast to phonons, which show a linear dispersion relation $\omega \propto k$ [16], exchange-dominated spin-waves follow

$$\hbar\omega(k) = 4J|S|(1 - \cos(ka)), \tag{2.21}$$

where J denotes the exchange constant, $|S|$ the magnetic moment of the spin and a the lattice constant [36]. A magnetic anisotropy will contribute as offset for zero k [54] while the magnetic field will add a linear term to dispersion relation [37], opening an energy gap $\Delta E = g\mu_B\mu_0 H$ [55]. Taking both contributions into account it is most likely that phonon and magnon dispersion will show a crossing-point at low temperatures $< 1\,\mathrm{K}$ allowing direct magnon-phonon scattering [56, 57] besides higher order effects. At low temperatures this strong interaction leads to significant contribution of the magnetic lattice to the thermal transport in the system [55, 56, 58, 59] [p9]. To determine the magnonic contribution to the thermal conductivity one can make use of the dispersion relation, which allows one to suppress the thermal excitation of magnons by increasing their energy by a high external magnetic field. Thus the difference between thermal conductivity with and without magnetic field can reveal the magnonic thermal conductivity [55, 56, 58, 59] [p9].

Furthermore the thermal conductivity of magnons shows the same temperature dependence as the one observable for phonons, revealing a peak for bulk films around $10\,\mathrm{K}$ [59] and a slightly higher peak for µm thick films at $15\,\mathrm{K}$ [p9]. These results hint to complex temperature dependence of the thermal magnon propagation length caused by further scatter mechanism such as the magnon-magnon interactions [59].

2.3 Spintronic effects and concepts

In the first part of the theory we focused on the interplay between electrons and phonons, only considering the electrical charge of the electron. The field of spintronics represents the expansion of the classical electric concepts by considering additionally the spin of the electron and magnetic lattice for an explanation of transport phenomena.

In the following section we will present a brief overview of the effects and concepts within the field of spintronics, which are relevant for SSE and theories discussed in this thesis. As a first concept, we present the idea of spin pumping, which is used to describe the interaction between a precessing ferromagnet in proximity with a non-magnetic layer. Ideas and models from coherent spin pumping have been transferred and adapted in order to describe spin caloritronic phenomena and are therefore fundamental to understand the later theories. Afterwards we introduce the SHE and ISHE, which are closely related to spin pumping, as these effects can be used for excitation and detection spin currents. Especially the ISHE marks an important effect for this thesis as its development and understanding is strongly related to the one of SSE. The last effect that will be presented in this section is the SMR, which represents a magnetoresistance arising due to the SHE. Since its origin and actual mechanism are topic of current research it is unclear if it can be solely attributed to SHE. To highlight its importance for the SSE we present a more detailed description.

2.3.1 Spin pumping

Spin pumping (SP) is defined as the generation of spin currents due to precision of the magnetization, which identifies SP as the reciprocal effect of the spin transfer torque (STT) [6, 60], where the angular moment of a magnonic or electric current is acting as torque on the magnetization. In the following we will present a phenomenological overview of SP, while a comprehensive theoretical description can be found in Ref. [61].

The concept of SP has been motivated by experimental observations of an enhanced Gilbert damping, which occurs if a ferromagnetic material (FM) is in contact with a non-magnetic metal [62]. The original idea of Tserkonvyak *et al.* [63] was to explain this phenomenon by an additional damping term $\Delta\alpha$ in the LLG eq. 2.18, originating from a pumped spin current from the ferromagnet into the normal metal (NM). In this macrospin model the precessing magnetization excites a spin current oriented perpendicular to magnetization within the NM due to the exchange interaction at the interface [6, 60]. The conductance electrons of the NM thus absorb an angular momentum from the FM and become spin polarized, depending on the orientation of the FM as illustrated in Fig. 2.10.

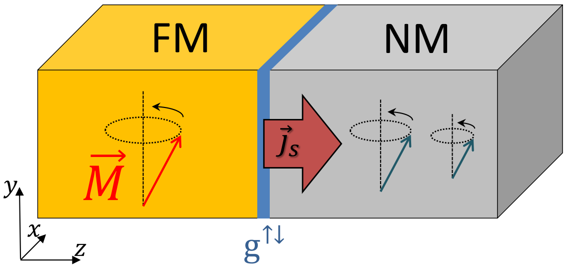

Fig. 2.10: Schematic of the spin pumping process in a ferromagnetic normal metal bilayer. The ferromagnet, precessing in the xy-plane, injects a spin current j_s into the attached normal metal layer, due to a exchanged coupled interface, whose coupling strength is defined by the spin mixing conductance $g^{\uparrow\downarrow}$.

One spatial component, of the dc part of the excited spin current density of $\vec{j}_s$ can be described [64, 65] by

$$j_s = \frac{f\hbar}{4\pi M_s^2} \int_0^{1/f} g^{\uparrow\downarrow} \left[\mathbf{M}(t) \times \frac{d\mathbf{M}(t)}{dt}\right]_y \mathrm{d}t, \tag{2.22}$$

where $\left[\mathbf{M}(t) \times \frac{d\mathbf{M}(t)}{dt}\right]_y$ marks the y component, which is oriented along the magnetic precession direction (see Fig.2.22), and f its frequency. The important parameter of this formula is the real part of spin mixing conductance $g^{\uparrow\downarrow}$, which is the sum over a scattering matrix for the reflection and transmission channels at the interface [63]. In most experimental situations, the transmission channels can be neglected, allowing one to only consider the real part [63], although this assumption might not hold for magnetic insulators [66]. Since excited spin current in the NM is proportional to $g^{\uparrow\downarrow}$, the spin mixing conductance experimentally represents a measure of the interface quality.

As can be seen from the form of eq. 2.22, this transfer of angular momentum from the ferromagnetic towards the normal metal can be taken into account by using an effective damping $\alpha_{eff} = \alpha_0 + \Delta\alpha$ in the description of the LLG eq. 2.18, where α_0 labels the original damping of the material.

In cooperation with the University of Kaiserslautern this theory of additional damping due to proximity between ferromagnet and normal metal has been tested within this thesis [p1]. Our results show that the theoretically predicted thickness dependence of the additional damping term, determined by spin pumping experiments, follows the theoretical model of

$$\Delta\alpha = \frac{g\mu_B}{4\pi M_s d} g^{\uparrow\downarrow}, \tag{2.23}$$

where d labels the thickness of the FM. Additionally we observe a nonlinear power dependence of the spin pumping signals with increasing film thickness, which we attribute to magnon-magnon interactions that are suppressed in thinner films. Since the derived results are not related to the main topic of this thesis we refer the interested reader to Pub. [p1]. Most spin pumping experiments make use of the ISHE, as it allows to detect the injected spin current by converting it into a detectable voltage. In the following section we will explain this effect together with a related variant, the SHE.

2.3.2 Spin Hall effect and inverse spin Hall effect

A spin dependent separation of a charge current perpendicular to its direction of flow in a non-magnetic material is called spin Hall effect (SHE) [67], shown in Fig. 2.11a). The effect occurs in the absence of a magnetic field and can be used to generate a pure diffusive spin current if the emitting material is in contact with a further conductor. The inverse case of a conversion of an injected spin current into a charge carrier separation and by this detectable voltage is the inverse spin Hall effect (ISHE) [68], shown in Fig. 2.11b).

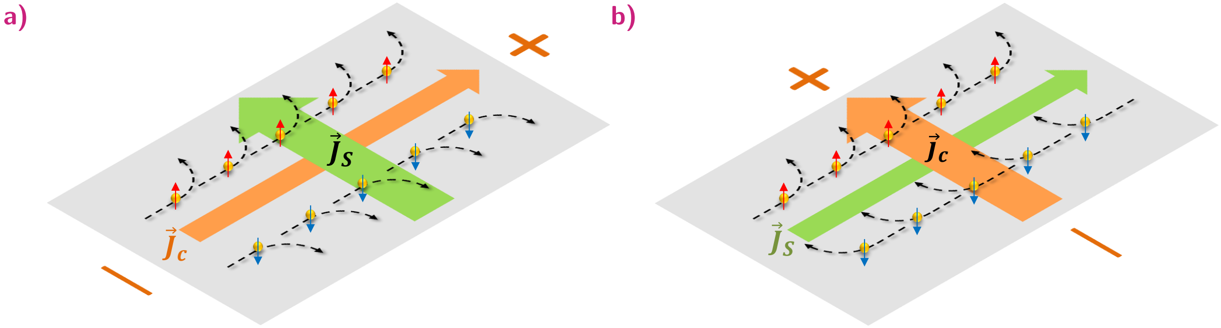

Fig. 2.11: Illustration of the a) SHE and b) ISHE. A charge carrier current j_c encounters a spin dependent scattering towards the boundaries of the material. Vice versa a spin current j_s is converted into charge current j_c, which gives rise to an electric potential difference E_{ISHE} depending on the polarization of the charge carriers σ and propagation direction of j_s.

The progress within the theoretical description of the AHE [28] allows us to split the effect into an intrinsic and extrinsic contribution. A similar approach using the same theoretical concepts of Berry Phase theory for the intrinsic and Mott scattering for the extrinsic contribution can be applied on the SHE / ISHE [69]. An explanation of the important mechanism extends the length of this thesis and does not contribute to the understanding of the SSE. Therefore we recommend the review articles [69, 70] for a deeper understanding. In the following we will present only the empirical derived results for the ISHE, which have an impact on our measurements of the SSE. The dependence of the resulting charge current by the ISHE can be described [65] by

$$\vec{j}_c = \frac{2e}{\hbar}\theta_{SHE}\,\vec{j}_s \times \vec{\sigma}, \tag{2.24}$$

where $\vec{j}_s$ marks the spatial diffusion direction of the spin current density and $\vec{\sigma}$ its polarization vector. θ_{SHE} marks the dimensionless material dependent parameter, the spin Hall angle, that labels the conversion efficiency of the spin current. The absolute value of the parameter is roughly proportional to the atomic order parameter $|\theta_{SHE}| \propto Z^4$ [71] as it labels the strength of the spin orbit coupling. For a more accurate estimation one has also to take the d-orbital configuration [72] into account, which can also explain the appearance of negative spin Hall angle for Tantalum and Tungsten compared with one for Pt [71].

While the scaling and sign for the ISHE can be explained and predicted by this model, the absolute value derived from different experimental methods shows a broad variety. Only for Pt, the absolute value of θ_{SHE} differs more than one order of magnitude, since values from 0.01 up to 0.1 have been determined [70, 73]. This can be understood by taking into account that experimental approaches, like spin pumping experiments, rely on a proper estimation of $g^{\uparrow\downarrow}$ as well as on the spin diffusion length. The first parameter is strongly influenced by the interface quality, the deposition method and additionally the emitting material, while the second parameter is highly sensitive to the quality of the ISHE material itself and leads to an exponential thickness dependence of the penetration depth of the spin current in the NM [65, 74–76].

Thus one has to consider that, beside the material, the interface, its thickness and additionally measurement geometry influence the signals. The last point originates from the fact that the experimental detected voltage results [65] of

$$V_{ISHE} = \frac{\rho l}{A} I_c = \frac{\rho l w}{A}\theta_{SHE}\frac{2e}{\hbar}\lambda\, tanh(\frac{d_N}{2\lambda}) j_s^0, \tag{2.25}$$

where ρ marks the resistivity, l the length, w the width and $A = d_N w$ the cross section area of the used geometry. d_N labels the thickness of the ISHE layer, λ the spin diffusion length and j_s^0 the spin current density at the interface.

2.3.3 Spin Hall magnetoresistance effect

Like the AHE, the SHE possesses a resulting intrinsic resistance [69], which should not be mistaken with the following spin Hall magnetoresistance effect (SMR). The SMR only occurs, in contrast to all other magnetoresistance effects, only in bilayer systems, consisting of a spin Hall layer in contact with a ferromagnet. The first experimental report, which was interpreted as the SMR, was the detection of magnetoresistance effect in Pt in proximity with YIG [77].

Up to now its origin is topic of current research, since Pt marks a special material. Pt is near the Stoner ferromagnetic instability, which allows to magnetize Pt in contact with a ferromagnet, known for Pt/Fe [78]. This induced magnetic moments would give rise to a proximity induced conventional AMR effect in the Pt as discussed by the community [14, 15]. X-ray magnetic circular dichroism measurements of the YIG/Pt bilayer contradict one another. Lu *et al.* [79] observe a proximity induced moment while Geprägs *et al.* [80] do not find any evidence for such an induced moments at the interface. Further studies reveal a dependence of the magnetoresistance (MR) signals on the deposition method [81], hinting towards an interface induced origin.

Experimentally the key point to distinguish the AMR from the SMR effect is to perform out-of-plane angle dependent measurements of the MR. As described in eq. 2.3 the AMR follows a double cross product relation, leading to $\rho_{xx} \propto cos(2\gamma)$ dependence of the longitudinal resistance ρ_{xx} if probed as a function of the out-of-plane angle γ in the xz-plane, as illustrated in Fig. 2.12a). In contrast to this the SMR effect shows a constant signal with no angular dependence. All further angular dependences are identical for both effects. Nakayama *et al.* [77] highlighted this elemental difference between both effects and additionally were able to show that the MR does not vanish even if a copper layer is inserted in between YIG and Pt making a proximity induced magnetization impossible.

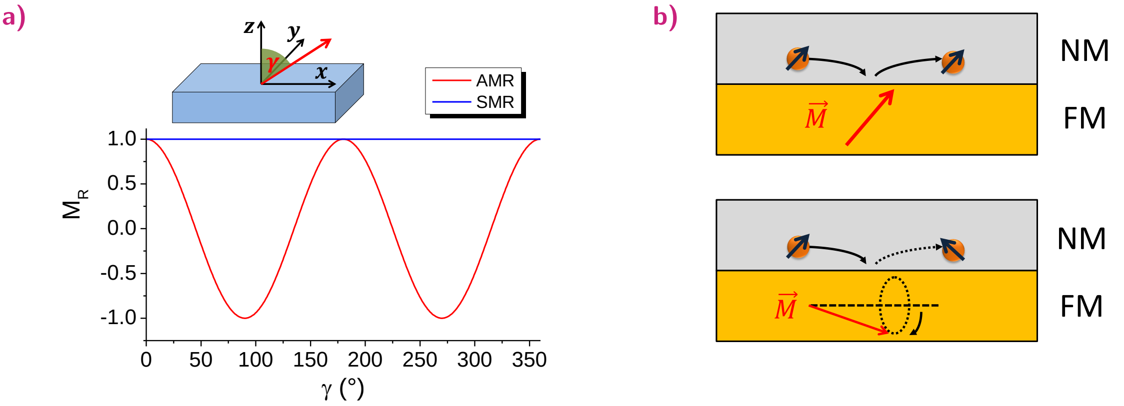

Fig. 2.12: a) Angular dependence of the AMR and SMR of the MR measured in the xz-plane as illustrated in the schematic above the graph. b) STT between magnetization and spin current in the NM|FM bilayer for two different alignments of the magnetization of the ferromagnet.

Phenomenologically one can understand the effect by a STT between the magnetization of the ferromagnet and the spin current, resulting of the SHE. The SHE leads to spin dependent separation of the charge carriers at the edges of the sample, as illustrated in Fig. 2.11a) and 2.12b). If this spin current at the interface with the ferromagnet experiences a STT, due to the exchange interaction, this current is either absorbed or reflected, depending on the orientation of magnetization of the ferromagnet, as shown in Fig. 2.12b). Since the spin current flow is connected to the charge carrier flow, the absorption of one spin channel raises also the longitudinal resistivity [77, 82]. A STT is only possible in a non-parallel configuration between magnetization and polarization of the spin current, leading to no resistance change for the longitudinal out-of-plane configuration. From a phenomenological point of view its concept matches with the observation of a STT induced by the SHE in FMR experiments [6, 83].

The development of the concept of the SMR and its origin proceeded in parallel to the work of this thesis. In the next section of spin caloritronics we explain why research of the SMR effect was originally triggered by the spin caloritronic community as a MR effect in the ISHE layer raises fundamental questions about the origin of the SSE.

2.4 Spin caloritronics

The development of research topic of spin caloritronics is closely related to the one of the SSE. The initial experiments of Uchida *et al.* in 2008 [7] meant a breakthrough for the field and triggered the discovery of many other effects. Up to now the spin dependent Seebeck [84] and Peltiers effect [25], the magneto-Seebeck [85] and Peltier effect [86] as well as the spin Seebeck [7] and the possible reciprocal spin Peltier [87] effect have been discovered. The spin dependent and magneto-effects are limited to magnetic conductors as they represent the spin dependent expansion of the classical thermoelectric charge effects [19]. The SSE has been observed in conductors as well as in insulators [88], while the spin Peltier [87] has been recently discovered in magnetic insulators. Since the origin of the SSE is still topic of current research, it is unclear whether the spin Peltier effect can be solely described as the reciprocal effect.

In the beginning of this section, we will give a brief introduction to spin dependent and magneto-Seebeck effect and illustrate that the effects can be understood by including the spin of electrons into the concept of the Onsager reciprocity. Compared to the spin dependent effects, the SSE represents a novel thermoelectric effect, which cannot be described by a charge carrier model. Its origin is debate of current research and motivated the work presented in this thesis. As the development of the research of this effect reflects very well its up to now controversially discussed origin, we will first give a brief overview about first results and current state of the research on the SSE. As a last point of this section we present an overview of the main theoretical model that has been used to describe our obtained results of the magnonic origin of the SSE.

2.4.1 Spin dependent and magneto-thermoelectrics

The magneto-thermoelectric effects represent an expansion of the classic thermoelectric effect by a two current model for spin up and down electrons [19]. Thus the magneto-

Seebeck effect can be most efficiently measured in magnetic tunnel junctions [85,89], where it is possible to suppress one type of spin polarization of the tunneling currents by the respective alignment of FM|I|FM junctions. The magneto-Peltier effect thus presents the magnetoresistive dependent thermal transport, which as well can be observed easiest in tunnel junctions [86], where the thermal flow carried by the tunneling electrons can be blocked depending on their spin polarization.

The spin dependent Seebeck effect (SDSE) describes a more complex situation where only an electron mediated spin current is thermally excited, without a net charge current. The first detection of such a thermal diffusive spin current has been achieved in a lateral spin value structure [84]. A high density charge current is applied to the FM, in order to generate a temperature gradient along a FM|NM junction perpendicular oriented to the charge carrier flow. Since the conductivity and density between different spin states differ in the FM, a Seebeck current excited by the thermal gradient is spin polarized. In the spin valve geometry of the FM|NM junction, the spin polarized charge current flowing from the FM to the NM is compensated by a non-spin polarized current from NM to FM. Thus only a thermally excited diffusive spin current flows into the NM. This spin current can be detected by a second ferromagnet attached to the NM, by probing the pin accumulation due to a voltage difference. The length scale of the SDSE depends on the spin diffusion length of the material. In the ferromagnet the diffusion length limits the effect to a length scale of several nm, while the diffusion into the NM allows detecting the effect on a length scale of $100\,\mathrm{nm}$ [90].

The reciprocal effect, the spin dependent Peltier effect, has been detected in lateral spin value FM|NM|FM structure combined with an electrically isolated thermocouple thermally attached to one of the ferromagnets [25]. A current sent through this junction will cause a conventional Peltier effect within the stack. By comparing the parallel and antiparallel configuration for the spin value, it is possible to determine a temperature difference, which can solely be attributed to the heat current only carried by the spin current. Thus the magneto-and spin dependent effects only differ as a net charge carrier flow is needed to be taken into account for the magneto-thermoelectric effects, while the spin dependent effects are solely attributed to the spin current. All four above described effects can be described by the expanded two current model concept for thermoelectric effects, which as well as the classical model fulfills the Onsager reciprocity [19,26].

2.4.2 Introduction to the spin Seebeck effect

The first report of the SSE was the measurement of a thermally excited spin current in a $\mathrm{Ni}_{81}\mathrm{Fe}_{19}$ (Permalloy, Py) film detected by the ISHE signal in a Pt layer [7] in 2008. In this first report the authors presented the concept, as shown in Fig. 2.13a), that a thermal gradient applied along a ferromagnetic metallic layer leads to the excitation of a pure spin current within the ferromagnet, similar to the later discovered spin dependent Seebeck effect. This measurement geometry for the SSE was later denoted as the 'transverse geometry' or transverse spin Seebeck effect (TSSE) as the temperature gradient is applied in the plane of the sample. Fig. 2.13b) shows the principle of the transverse geometry measurement method, while a detailed explanation of the experimental realization and challenges of SSE measurements is given in Sec. 4.1.1.

Phenomenologically the temperature gradient excites a parallel directed spin current that partially diffuses into Pt stripes, where it is converted into a detectable voltage. In contrast to the SDSE, the TSSE shows a dependence on the probing position over several mm, as illustrated in Fig. 2.13c). The signal amplitude linearly changes as a function of the probing position on the sample, leading to an opposite signal sign between hot and cold side and a vanishing signal in the middle of the sample. Based on the model of the SDSE one would expect a signal amplitude depending on the temperature of the Pt layer, which would in case of the presented geometry lead to a position independent signal.

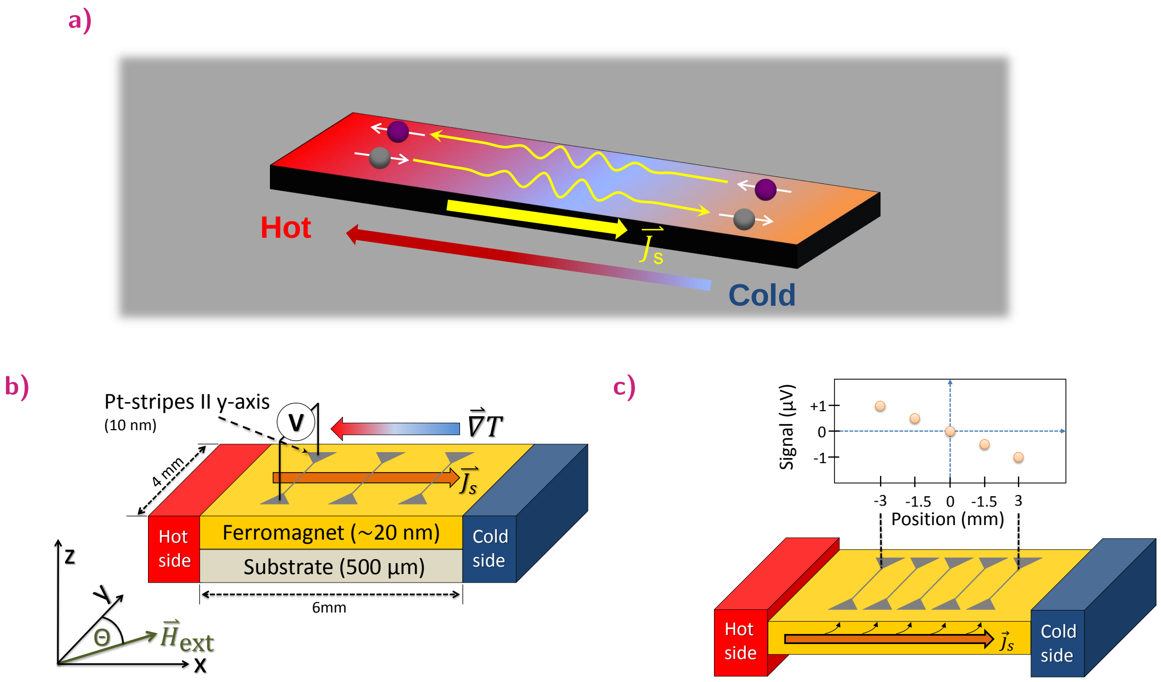

Fig. 2.13: a) Illustration of the spin Seebeck effect. A temperature gradient $\vec{\nabla}$ excites a thermal spin current $\vec{J}_s$ antiparallel to it. b) Sketch of the measurement geometry used for detection of the TSSE, which uses an in-plane temperature gradient. c) Position dependent signals of the TSSE, sketched according to the measurements of Uchida *et al.* [7].

To probe the spin current origin of the signal, it was shown that the signal vanishes without the ISHE layer and that the signal is correlated to the magnetization of the sample and heat flow within the system. Originally the same theoretical concept as for the explanation of the SDSE was used to describe the TSSE, which does not hold as the length scale for the usual spin diffusion length of electrons is of the order of several nm in magnetic metals [90] in contrast to the observed mm.

After these first experiments other groups [31, 32, 91, 92] were not able to reproduce the initial data in similar samples and geometries. Instead it could be shown that measurements in metallic systems can be accounted by signals of the PNE, which shows an identical dependency on the temperature gradient. Sec. 4.1.1 describes in more detail that transverse geometry is additional very likely accompanied by out-of-plane temperature gradients [91,93], which cause thermoelectric signals by the anomalous Nernst effect (see Sec. 2.1.4). Since ANE and TSSE show the same dependence on $\vec{M}$ and ΔT, only comparison measurements in samples with and without Pt detection layer allow to distinguish between both effects, which beside the initial results could have never been reproduced.

While partially the community focused on the measurements in magnetic metals, in later experiments the SSE was also measured in Heusler compounds [94], magnetic semiconductors [95,96] and even magnetic insulators [88], raising doubts about the electron based origin of the effect. Since the signal in insulators should in principle not be superimposed by signals from the ANE, like in metallic systems, it was possible to change the measurement geometry from an in-plane temperature gradient to an out-of-plane geometry, the longitudinal SSE (LSSE) [97] shown in Fig. 2.14. In Sec. 4.1.1 we explain in detail that the LSSE provides a more robust concept, as an in-plane heat flow can be neglected. In contrast to TSSE, the thermally excited spin current directly propagates into the detection layer in the LSSE configuration, as it is parallel oriented to the heat flow direction. Therefore one can think of the TSSE as the non-local detection of the LSSE.

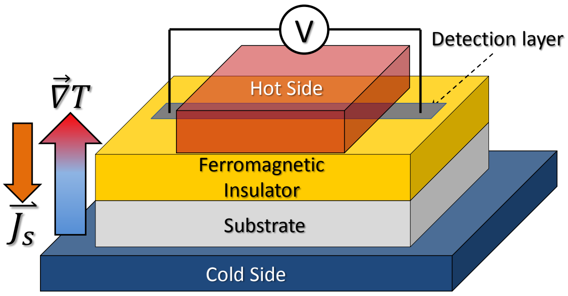

Fig. 2.14: Illustration of the LSSE. In the LSSE configuration $\vec{\nabla}$ is applied out-of-plane, causing a direct flow of $\vec{J}_s$ into the detection layer.

The discovery of the SSE in magnetic insulators inspired theories based on a magnon interpretation of the thermally excited spin current [12,13,19,60,66,98–104], since contributions to the SSE by conduction electrons should be negligible in insulators. The list of theories is not complete and can only illustrate the huge variety of approaches to explain the SSE. Further experiments in semiconductors [95] and metals [105] revealed, that TSSE mains its position dependence over several mm, although the ferromagnetic layer on top of the substrate had been separated by gaps, pointing towards a more complicated phonon interaction of the effect. The same conclusion resulted from the observation of a peak in the SSE signals [106–108] if probed as a function of temperature. The measurements were performed in the TSSE [96,106,108] and LSSE configuration [104,107,108]. Since the SSE signal peak temperature below $100\,\mathrm{K}$ is close to the peak temperature of the phonon thermal conductivity, it is currently being attributed to a drag effect between magnons and phonons [104, 106]. As our own results discussed in Sec. 4.3.2 will show, this first interpretation of a direct magnon-phonon drag needs to be further expanded to explain our observations.

Up to now most magnonic theoretical approaches [12, 66, 101], which partially consider the phonon heat bath in order to explain the gap and drag experiments, can explain most room temperature experiments for the LSSE. In contrast to this the theories cannot derive the observed length scale for TSSE of several mm, which has been observed for metals [7] and insulators [97]. An optical experiment [109] tried to directly probe the theoretically predicted difference between the magnon and phonon lattice temperature in YIG [66]. The experiment did not find a difference between the two temperature bathes and was thus only able to provide an estimate for the upper limit of the length scale of the TSSE of 0.47 mm, which marks an order of magnitude lower value than predicted by theory and TSSE experiments.

The non-reproducibility of the initial experiments and the incompatibility with magnonic theories and the length scale of the TSSE raised the question in the community whether the TSSE can be treated as a special case of the LSSE or can even be solely explained by thermal artifacts in the system, causing a local occurrences of the LSSE [110]. Therefore a better understanding of the easier to determine LSSE can give an answer to the fundamental questions of the existence of the TSSE.

Although the magnonic theories can give explanations for the experimentally obtained signal dependences of the LSSE, the physical origin of the effect is still under discussion. The magnonic theories can currently be separated into two groups. The first group attributes the SSE to magnons emitted from the bulk of the ferromagnetic material [13, 54, 66, 102, 103], while the second group assumes only thin interface layers [12, 101] between ferromagnet and detection material as the origin of the effect. Up to now a direct measurement of the magnonic origin of the SSE has not be possible, which even led to discussion of existence of the LSSE.

While the discussion about a parasitic superposition of the SSE signal with Nernst effects in metals is unavoidable, the signals determined in magnetic insulators seemed to be unaffected by this. In 2012 the detection of a MR effect in Pt [14, 111], obtained in the proximity with YIG, led to the discussion if a Nernst effect(see Sec. 2.1.4) causes or superimposes the SSE even in insulators. Recent experiments could show that this novel MR effect, partially described by the community as the spin Hall magnetoresistance [77] (SMR, see Sec. 2.3.3) does not follow the expected angular dependence of a typical AMR effect, which allows to distinguish between both. Still its origin and contribution to the SSE is under discussion, raising the question if not all observed signals can be explained by a Nernst effect of the interface [14, 15]. To eliminate the Nernst contribution, experiments using Au as detection layer have been performed [112], while other experiments tried to estimate the Nernst signals by a comparison of the transverse and longitudinal case of the temperature gradient [113]. Both types of experiments could, in parallel to our own experimental approach presented in Sec. 4.2, show that observed signals cannot be explained by an ANE effect of the detection layer but must have a different origin as shown in Chapter 4.2. Using our approach it was not only possible to show the negligible contribution of the Nernst effect but also to determine this origin by probing the SSE as a function of the ferromagnetic material thickness, revealing a novel signal feature that can be attributed to a magnonic spin current from the bulk of the material.

2.4.3 Numerical approach for the magnonic spin Seebeck effect

For the theoretical description of the SSE we work in collaboration with the group of Prof. Ulrich Nowak from the University of Konstanz. The following theoretical description reproduces the work of U. Ritzmann [114]. The group of Prof. Nowak specialized on the numerical simulation of the stochastic Landau Lifshitz Gilbert equation (see. Sec. 2.2.3) in either macro- [115] or atomistic spin models [54]. In the following we give a brief introduction to their work and principles of their simulations.

For our description of the intrinsic origin of the SSE we use the atomistic model, where each unit cell of the material is represented by a localized, normalized spin $\mathbf{S}_i = \boldsymbol{\mu}_i/\mu_s$, where μ_s marks the magnetization of one cell. The spins are placed in a three dimensional simple cubic lattice, with a spacing of a reflecting the crystal lattice constant, as shown in Fig.2.15. The system boundaries in the yz- and xz-planes are treated as open, while the xy-planes at the beginning and end of the system absorb incoming waves.

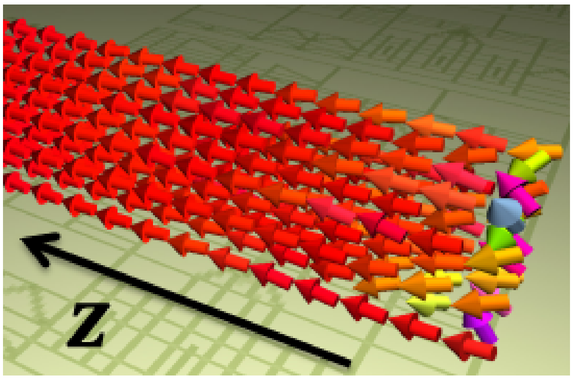

Fig. 2.15: $3D$ render image of the spin configuration for $4 \times 4 \times 512$ system, having a temperature step after the first layer. The image has been taken from Ref. [114], by kind permission of the publisher.

The dynamic precession of the individual spins is described by the LLG eq. 2.18, including the phenomenological damping term α and the effective magnetic field H'_{eff}. The effective magnetic field consists of

$$H'_{eff} = -\frac{\partial \mathcal{H}}{\partial \mathbf{S}_i} + \xi_i(t), \tag{2.26}$$

where the first term is the derivative of the interaction Hamiltonian $\mathcal{H}$. For the study of thermally excited magnons we only consider the exchange interaction, a uniaxial anisotropy parallel to the longest axis of the system and the Zeeman energy due to the external magnetic field. The second term $\xi_i(t)$ is the thermal white-noise contribution, which introduces the temperature influences to the system. The white-noise term fulfills the condition of $\langle \xi(t) \rangle = 0$ and

$$\left\langle \xi_\eta^i(0)\xi_\theta^j \right\rangle = \frac{2k_B T_p(z)\alpha\mu_s}{\gamma}\delta_{ij}\delta_{\varphi\theta}\delta(t), \tag{2.27}$$

where i and j denote the lattice sites and φ and θ Cartesian components of the spin, as shown in Fig. 2.6. $T_p(z)$ describes the phonon temperature for the spins in the xy-layers along the z-axis of the lattice, which allows to include different temperature profiles to the system such as a step function [54] or a linear temperature gradient, see Fig. 4.12a). Thus the phonon heat bath provides a constant temperature background, which interacts with the magnetization but not vice versa. The lateral size of phonon distribution must be chosen small enough to minimize influences by the finite size of the system.

The stochastic LLG equation is solved numerically by the Heun method [116]. In order to determine the thermal fluctuation of the system, the system is initialized in parallel state to the easy axis along the z-axis, which allows to define a starting magnetization $m_0(z)$ per xy-plane. In the higher temperature levels of the system, thermal magnons are excited, which propagate through the system. The initial aligned moments get perturbed by these magnons, leading to a relaxation of the system into a quasi-stationary state. In this state the mean fluctuation of the individual spins gets time independent for the investigated timescale, which allows to determine its deflection $\Delta m(z)$ as

$$\Delta m(z) = m_0(z) - m(z), \tag{2.28}$$

where $m(z)$ denotes the averaged magnetization per xy-layer. Using the $\Delta m(z)$, it is possible to calculate a magnon temperature of the system $\Delta m = \beta/T_c T_m$, where β is the critical exponent obtained by fitting the system magnetization as a function of temperature using $m(T_m) \approx 1 - \frac{\beta}{T_c}$ [57]. T_c describes the Curie temperature, which is as well determined from the simulations. Thus one obtains from the numerical calculation the essential parameters T_m, T_p, also derived from the linear response theory of Xiao *et al.* [66]. This theory attributes the temperature difference $\Delta T = T_m - T_p$ as the origin for the thermally excited magnons and derives, using the spin pumping model (see Sec. 2.3.1), a functional dependence between the experimentally detected ISHE voltage in the NM and the temperature difference between magnon and phonon bath in the ferromagnet or respectively the normal metal, whose electron and phonon heat baths are assumed to be in equilibrium with the one of phonons in the ferromagnet.

Materials and fabrication techniques

3

The introduction already pointed out that the SSE presents a novel yet up to now not well understood spincaloric effect, whose origin is attributed to thermally excited magnons. Many studies of the SSE focus on specific topics and neglect to present a comprehensive picture of the material and its magnetic or crystalline properties. As the origin of the SSE and its dependence on the material is still under discussion, these studies are essential to provide insights. An example for this is given by the fact that the SSE has been reported for bulk as well as for thin films of the same material. While the material properties vary for different thicknesses, the SSE maintains a similar amplitude of signal. For a comprehensive study of the origin and the dependence of the SSE, it is therefore necessary to know and to be able to control the material parameter. Having access to the growth of the investigated material provides an ideal opportunity for this possibility.

Due to this it was part of this PhD thesis to establish the growth of the material class of garnets by pulsed laser deposition in Mainz in collaboration with the Massachusetts Institute of Technology (MIT) in Boston. This allowed to specifically study the influence of the thickness and modification of the material on the SSE. To provide a comprehensive picture of the material properties for theses studies, the possibilities for sample characterization already available in Mainz were extended by a Vector Network Analyzer-FMR (VNA-FMR) setup. The development and construction of the setup was also part of the thesis. In the following chapter will therefore provide an overview of the growth techniques for our investigated stack of material and describe the used methods for the analysis of the material properties.

We will describe in detail the technique of pulsed laser deposition used for the growth of the ferromagnetic material and magnetron sputtering for the growth of the detection layer. An introduction to the analysis of the crystal structure by x-ray diffraction is given as well as example measurements and evaluations of magnetic properties by SQUID magnetometry and VNA-FMR. In the last part of this section focuses on the to magnetooptic characterization, which allowed not only to study the magnetic structure of the material, but will also be of use for future experiments following this PhD thesis.

In the next section we will make use of the techniques and methods described in this section and present the results of our material development.

3.1 Characterization and deposition techniques

3.1.1 Pulsed laser deposition

The research within the field of spin caloritronics led to the need of high quality thin films of an insulating magnetic material. For our research we choose magnetic garnets, as they are highly insulating and possess a Curie temperature $\sim 280\,\mathrm{K}$ above room temperature, which makes them easy to handle (see Sec. 3.2). The drawback of magnetic garnets is their complex stoichiometry, which necessitates a long optimization process for deposition methods like radio frequency sputtering. Pulsed laser deposition (PLD) describes a thin film deposition method, which is making use of an instant ablation of target material by a laser pulse. This instant ablation allows nearly exact stoichiometric transfer of the target material onto the substrate. Further advantages of this method are its high flexibility, as usually only one target per material is required, and the high achievable crystalline quality especially for oxide materials [117], such as garnets.

Two different PLD chambers have been used for the deposition of the garnet materials, presented in this thesis. Both chambers, the one at the MIT, a commercial system by Neocera [118], and the custom build system in Mainz [119], use the same model of ablation laser and only differ in the heating method for the substrate. Thus, we will only discuss the basic principles of PLD, based on the chamber concept in Mainz. Fig. 3.1a) shows a sketch of the basic components of the PLD chamber in Mainz. The chambers use two stage pumping systems, to reach a base pressure of $\sim 10^{-8}$ mbar and allow to control the processes gas pressure by mass flow controllers. A KrF ($\lambda = 248\,\mathrm{nm}$) excimer laser (CompexPro 205, Coherent) generates a high energy laser pulse in the energy range of $250\,\mathrm{mJ}$ to $450\,\mathrm{mJ}$ with a pulse length of $20\,\mathrm{ns}$. The laser pulse is guided by a mirror system to the PLD chamber and is optimized on its path by beam optics, such as an aperture to block divergent parts and a lens system to focus the laser on the ablation target. As the CompexPro initially provides a rectangular shaped spot profile, with sharp intensity boarders, an optimized beam optics should reproduce the rectangular sharped spot on the ablation target. This way the final spot on the target has a uniform intensity distribution, leading to a uniform ablation of the material. Depending on the area and selected energy of the pulse, the energy density on the target can be varied between $0.2\,\mathrm{J/cm^2}$ and $20\,\mathrm{J/cm^2}$.

In order to provide a high exploitation of the target and to prevent the occurrence of droplets on the film [117], the target is rotated during the deposition. This rotation is coordinated with the repetition frequency of the laser.

The high energy density of the laser leads to heating rates of up to $10^{11}\mathrm{K/s}$ [120, 121] within the vicinity of the spot on the surface. Most energy is absorbed in the upper layer of the target material, leading to only little thermal damage in the surrounding. However the extreme conditions within the spot, cause an element independent ablation. This process should not be mistaken as evaporation, which would occur at different rates for the different target elements. All components of the target material are removed forming a plasma, which contains a mixture of molecules, atoms and ions, allowing for a stoichiometry transfer [121]. The plasma expands adiabatically perpendicular to the target surface into the direction where the substrate is placed. Depending on the working pressure the kinetic energy of the material gets reduced due to collisions with the gas molecules. This way the gas type and pressure can influence properties of the deposited film. Especially for the case of oxides, oxygen is a preferential preferred gas as it reduces or even prevents the formation of oxygen vacancies within the film. A sketch of the plasma and film growth is shown in Fig.3.1b).

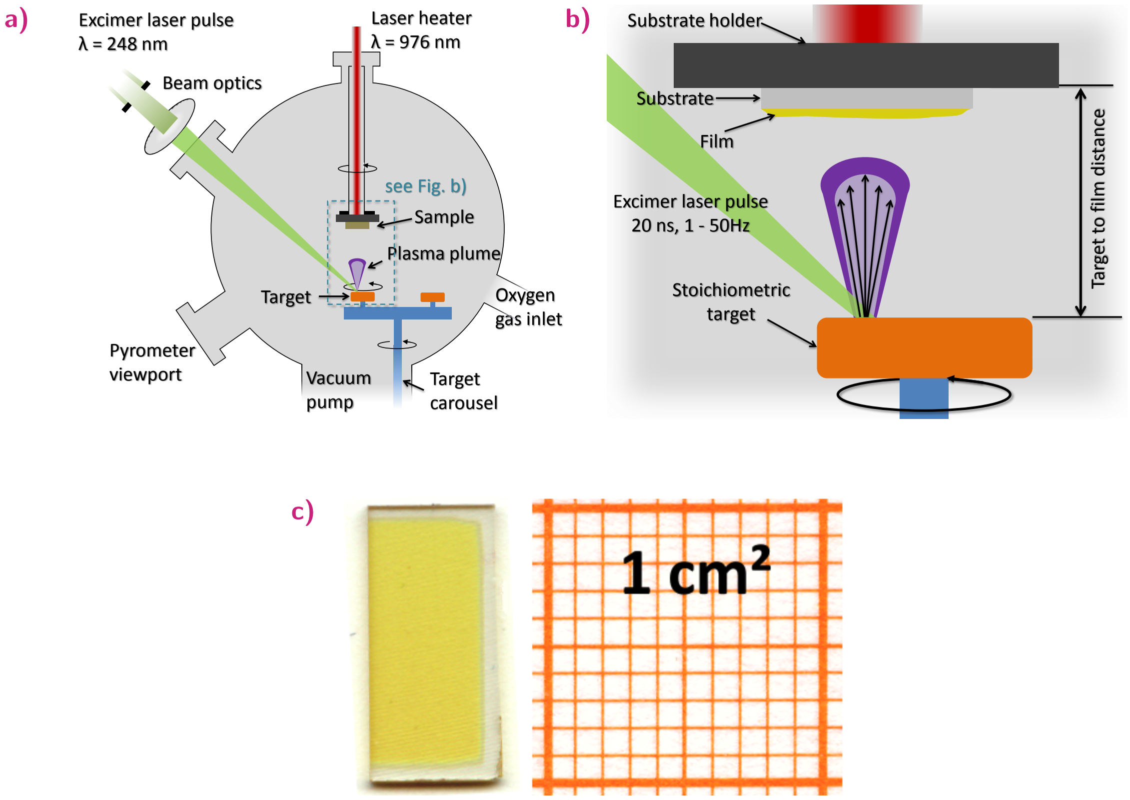

Fig. 3.1: a) Sketch of the PLD system in Mainz. b) Illustration of the marked region of a). c) Picture of a 150 nm thick YIG film on grown GGG with 1 cm^2 millimeter paper for scale.

The target material that reaches the surface of the substrate is adsorbed and starts the formation of the film. Different growth modes, classifiable in layer by layer, island growth and mixed growth, can occur, which may also depend on the substrate temperature during deposition [122]. Heating of the substrate is achieved by a second continuous wave laser ($\lambda = 976\,\mathrm{nm}$), aiming on the backside of the substrate holder. A calibrated pyrometer reads the temperature of the substrate holder and a feedback loop controls the laser power to stabilize the substrate temperature.

From the description of the laser ablation we can identify the crucial parameters for the deposition, which have also been marked in Fig. 3.1b). Important parameters of the used laser are the energy density, the wavelength and the repetition frequency. Material transfer and growth can be influenced by the type and pressure of the process gas, the target to substrate distance, the substrate temperature and finally the substrate itself. The crystallographic quality of the produced films can additionally be influenced by an annealing step after the deposition. This step can consist of a higher temperature and pressure, which the sample is exposed to, leading to a self-ordering of the crystal and a reduction of oxygen vacancies.

Partial work of this thesis was to optimize the epitaxial growth of Yttrium Iron Garnet (YIG) on Gadolinium Gallium Garnet (GGG) [p2] and to establish the growth of other interesting garnets [p3][p7][p8] by PLD, as will be described in Sec. 3.2, where we will also give details for the deposition parameters. An example for a 150 nm thick film YIG on grown GGG is shown in Fig. 3.1c). The yellow material presents the film itself, while the white areas are uncovered parts of the GGG substrate. The reason for the uncovered parts is the substrate holder at the MIT, which uses a deepening to provide a glue free mounting of the film. The drawbacks are uncovered areas and a thickness gradient of 200 µm length at the edges of the substrate.

A disadvantage of PLD is the limitation in the film thickness that can be grown. While high quality thin film samples can easily be grown with up to 100 nm thickness, the deposition time for films of 200 nm is more than 6 h. Furthermore a high amount of damage is induced to the ablation target and deposition conditions start to drift as the gas of the excimer laser fatigues. Due to this we limited our thin film grown by PLD to a film thickness of 300 nm and used liquid phase epitaxy grown samples for thicknesses beyond.

As we now have discussed the preparation of the ferromagnetic layer, we will give a overview of the deposition of the metallic layer used for the detection of the SSE.

3.1.2 Magnetron sputtering and lithography

Magnetron sputtering

While PLD presents a superior technique for the deposition of oxides, it has several disadvantages regarding the deposition of metallic materials [117]. In contrast to PLD, magnetron sputtering provides an easier and more reliable solution for the deposition of pure or simple materials. Another advantage presents the fact that the sputter chamber used in Mainz, provides the possibility to deposit up to 8 $10\,\mathrm{mm} \times 5\,\mathrm{mm}$ samples simultaneously. This presents an important feature, as an identical interface can only be ensured by a simultaneous interface preparation and film deposition. Our work in Sec. 4.2 will show that the interface strongly influences the SSE and that we can only ensure a comparability between different samples by an identical interface treatment.

As the sputter deposition and its parameters mark an important step in our material preparation, we will shortly present the principles of magnetron sputtering.

For the deposition of a conducting material we need to apply a high negative voltage ($200 - 600\,\mathrm{V}$) with respect to substrate holder and dark shield of the cathode, as shown in

Fig. 3.2a). As for the oxide PLD, the chamber is filled with an process gas. In case of the deposition of noble metals, argon is best suited. A initial ionization of a argon gas atom within the applied electric field, caused by a random event like cosmic background radiation, leads to a chain reaction. The ion gets accelerated towards the cathode due to the applied potential and collides with the cathode, causing the expel of secondary electrons. Due to their charge the expelled electrons get attracted to the substrate holder and dark shield and strike on their path other gas atoms forming more ions and by this the plasma [123]. In contrast to conventional sputtering, the excited plasma is compressed to a torus for magnetron sputtering. Magnets in the sputter cathode are used to generate a magnetic field that forces the electrons on an additional circular motion in the plane of the target surface. The increased density by the confinement, leads to a higher ionization rate and therefore allows to work at lower pressures than normal sputtering and also increases the sputtering rate. The sputtering process itself is a ballistic process, where the argon ions collide with the target surface and thus cause the erosion of the target material. Ejected target atoms diffuse to the substrate and start the formation of the film layer. Like in PLD the growth mode is strongly influenced by the substrate temperature and can be classified into the same three different types.

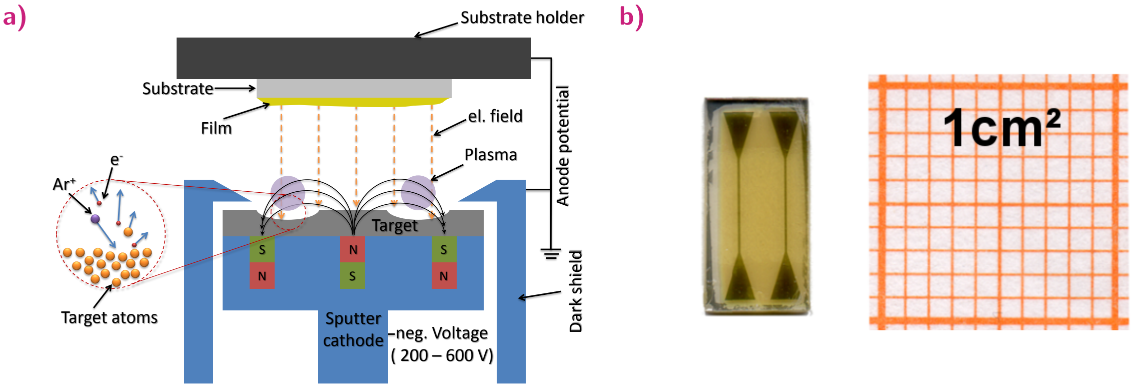

Fig. 3.2: a) Illustration of the sputter process. b) Image of a structured Pt film on YIG (Pt (6nm), YIG (190nm), GGG (sub)) with 1 cm^2 millimeter paper for scale.

For the used sputter chamber in Mainz (base pressure 5×10^{-9} mbar), we optimized the Pt deposition at room temperature. The optimal conditions were found to be argon pressure of 1×10^{-2} mbar, a target to substrate distance of $5\,\mathrm{cm}$ and a cathode current of $15\,\mathrm{mA}$ ($\sim 300\,\mathrm{V}$). For these settings we obtain a growth rate of $\sim 0.077\,\mathrm{nm/s}$ and surfaces with roughness below $0.2\,\mathrm{nm}$ (see. Fig. 3.4), which is lower than the usual surface roughness of the coated YIG films, which have a roughness below $0.5\,\mathrm{nm}$ (see Sec. 3.2.1)

The chamber furthermore allows cleaning or etching of the interface in-situ prior the deposition by a plasma source (Gen 2, Tectra). The source can be operated with oxygen and argon, where oxygen should preferentially be used for oxygen materials in order to prevent a reduction of oxygen in the surface layers. For the YIG cleaning we use a oxygen working pressure of 4×10^{-4} mbar, a plasma source current of $25\,\mathrm{mA}$, an extraction voltage of $-300\,\mathrm{V}$

($< 0.5\,\mathrm{A}$) and an accelerator voltage of $125\,\mathrm{V}$ ($5\,\mathrm{mA}$). For these conditions we find an etching rate of less than $0.5\,\mathrm{nm}$ in $20\,\mathrm{min}$ for YIG at angle $0\,^{\circ}$ of incidence. For cleaning of the YIG surface we use a angle of incidence of $45\,^{\circ}$ and an etching time of $\sim 20\,\mathrm{s}$, which allows for removing carbon contamination by oxidation from the surface. The carbon contamination can arise from the ex-situ sample transfer from PLD to sputter chamber, making the interface treatment prior the deposition important, as it ensures a similar interface for different films. Additionally the YIG is heated up prior to the oxygen etching to $200\,^{\circ}\mathrm{C}$ for 30 min to remove residual water, also caused by the ex-situ transfer.

After the deposition the Pt/YIG/GGG stack provides a robust material, as neither Pt nor the garnets show a hydrophobic behavior or show any other degradation, such a diffusion of oxygen at room temperature.

As the Pt/YIG interface needs to be as clean as possible, we have chosen not to perform a lift-off process for structuring of the Pt but a controlled etching, which we will now discuss.

Lithography

Each detection layer, for which in most cases we use Pt, is structured by optical lithography and ion etching into two separate stripes. The stripes allow to define a precise in-plane angle between the magnetic field and comparable position for voltage contacts (see Sec. 4.1.1). This is important as the ISHE has a linear dependence on the gap size between the voltage contacts (see Sec. 2.3.2). Two stripes enable us to control the SSE setup for mounting errors and also to increase the statistics of our measurements. Additionally the structuring is necessary, as not the whole sample surface is coated with YIG. Any conducting material on GGG, which is in contact with the detection layer on YIG, will inhibit the charge carrier separation but will allow a backflow of the electrons, which short circuits the ISHE-voltage (see Sec. 2.3.2). A picture of the Pt stripes is shown in Fig.3.2b), while the precise dimensions of a Pt stripes are shown in Fig. 4.1c). Additionally we use a protective layer to prevent the inner part of the stripes from scratches, which may be caused by the mechanical nature of the setup (see Sec. 4.1.2). This layer consists of a scratch resistant positive photoresist SU-8 and can be see in Fig. 3.2b) as the brighter rectangle in the middle of the sample.

Each sample is also characterized by x-ray diffraction to determine the crystallographic quality and actual layer thickness. In the following section we give a short introduction to the principles and analysis.

3.1.3 X-ray diffraction

The x-ray diffraction (XRD) analysis of our material allows us to determine structural parameters, like the dimensions of the unit cell and crystallographic quality. Most measurements present in this thesis have been done, using a commercial high-resolution x-ray diffraction (HD-XRD) device (Bruker D8 Discover). The basic principles of the devices, which operates in the Bragg-Brentano geometry are sketched in Fig. 3.3a). In this geometry the detector and emitter are placed on a circle, with the center on the sample [124]. The setup uses a copper cathode for the emission of x-rays with the wavelength of Cu-$K_{\alpha 1} = 1.5406\,\text{Å}$ and Cu-$K_{\alpha 2} = 1.5444\,\text{Å}$. The next beam element is a parabolic Göbel Mirror, which makes use of diffraction of the incoming radiation to parallelize the beam. The mirror by this not only monochromatizes the beam but also increases the brilliance, as the preferred wavelengths of the beam are corrected from a divergent beam from the source into a parallel one. Additionally a parallel beam reduces errors caused by misalignment of the sample. YIG and GGG have similar lattice constants leading to very close peak positions of the lattice reflexes. In order to be able to resolve the difference a monochromator is placed in the beam path. By selected diffraction it suppresses Cu $K_{\alpha 2}$ within the beam and by this increases the resolution [124]. The monochromatic and parallel beam is scattered at the sample and then detected by a scintillator. Variable slits on the beam path, allow to adjust the angle resolution. A XRD scan corresponds in this geometry to a combined scan of 2θ and ω, allowing the use of the Bragg equation to calculate the lattice constant from the peak position.

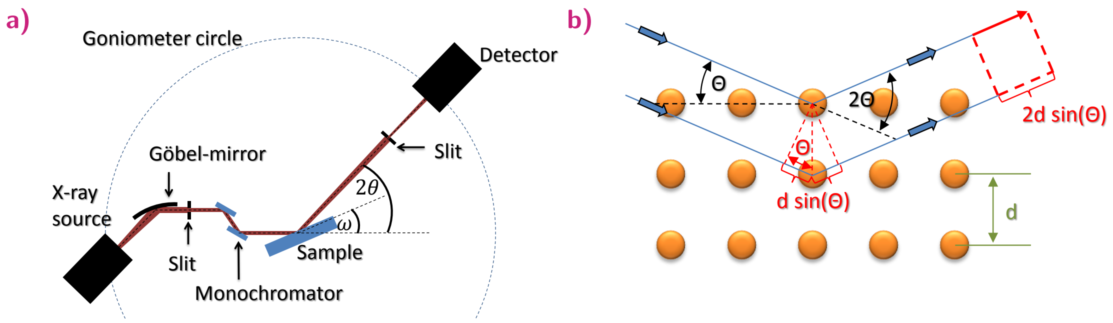

Fig. 3.3: a) Illustration of the XRD components used for HD-XRD. b) Sketch of the reflection condition for the Bragg equation.

The condition for constructive interference is given by $n\lambda = 2d_{hkl}\sin(\theta)$, where the path difference of the scattered light $2d_{hkl}\sin(\theta)$ is equal to an integer manifold n of the wavelength λ of this light. θ corresponds to the angle of incidence with respect to the lattice planes of the as marked in Fig. 3.3b), while d_{hkl} describes the lattice spacing. Fig. 3.4a) shows an example for a $2\theta - \omega$ scan of a Ce:YIG sample grown on GGG (001). The figure also contains a reference measurement of a GGG (001) substrate, which helps to identify artifacts from the substrate. From the scan we can identify the peak of the Ce:YIG (004) reflex at $28.368°$ from which we calculate an out-of-plane lattice constant of $d_{001} = 1.257\,\text{nm}$, and the GGG (004) reflex at $28.830° \mathrel{\hat{=}} d_{001} = 1.238\,\text{nm}$. The GGG substrate shows the same lattice constant as its literature value ($1.2383\,\text{nm}$ [125]), while the Ce:YIG shows a larger lattice constant, than the substrate. This combined with the knowledge of the material, (see. Sec. 3.2.2) and further information about the in-plane lattice constants of the films (see Ref. [p3]) allows us to conclude that the Ce:YIG must grow under tetragonal distortion on the GGG, leading to a strain in out-of-plane direction. The peak labeled with AF1 at $2\theta = 26°$ is the result of residuals of other wavelengths within the diffractogram. The peak position matches the wavelength of Cu-$K_{\beta 1} = 1.3922\,\text{Å}$, which we can therefore identify as the origin of the reflex. Cu $K_{\alpha 2}$ is well suppressed by the monochromator, as it would lead to reflexes slightly higher than the substrate peak at $2\theta_{GGG(004)} = 28.900$. AF2 corresponds to the reflex of (006), which should be forbidden as GGG has a cubic unit cell. Despite this, the peak can arise from a non perfect atomic ordering of the GGG substrate and due to the mere existence of a surface (surface truncation rod). No further peak can be observed within the spectra, showing that the film only consists of a Ce:YIG phase. This is an important results and will be in depth discussed in Sec. 3.2.2, which focuses on the growth of high quality Ce:YIG. In case of films of a high crystalline quality another feature can be observed from XRD scans. Fig. 3.4b) illustrates the occurrence of oscillations around the film peak, which are called Laue oscillations. These oscillations are the higher order maxima of the x-ray interference pattern of the crystal lattice. The interference pattern can only be observed if the film is highly ordered and has a smooth layer to layer interface. Like for the classical interference pattern, one can calculate from the oscillations the distance and number of the crystal layers causing the pattern and therefore the thickness of the epitaxial layer. As the discussion of the evaluation could show, we are able to obtain valuable information about the crystal structure of the film by XRD.

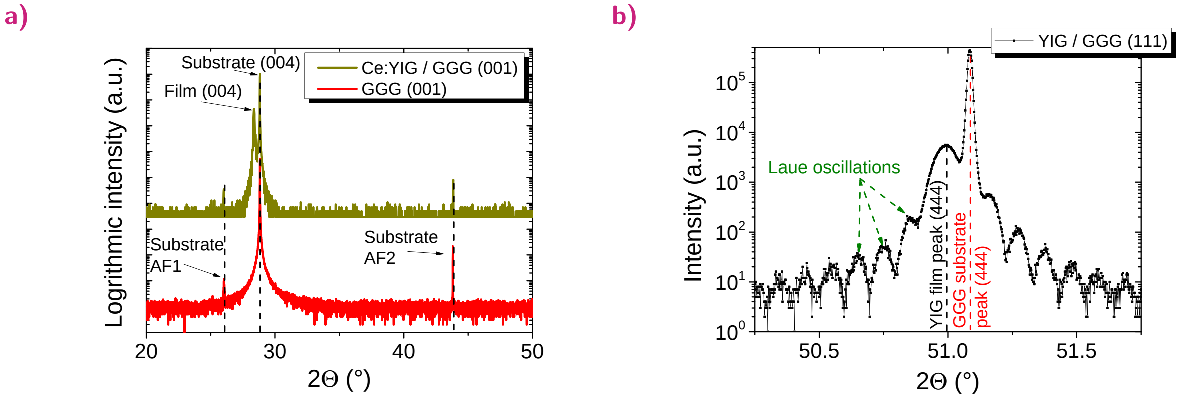

Fig. 3.4: a) $2\theta - \omega$ scan of a Ce:YIG / GGG (001) sample. The data are part of Ref. [p3]. b) $2\theta - \omega$ scan of the film and substrate (444) peak of a $100\,\text{nm}$ thick YIG / GGG (111) sample.

Rocking curve

Further information about the crystallographic quality can be determined by so called rocking curve measurements. For this measurement the detector is fixed at a certain 2θ value corresponding to a Bragg reflex, while the film is "rocked" by rotating ω. The width of a rocking curve of a reflex is influenced by the spread of the crystallite orientations within the film. This spread can be caused by dislocations, curvature of the film or a mosaicity [124]. In extreme cases this can lead to the observation of two separate peaks, which hints to two separate crystals with different orientation within the film. An example for a rocking curve is shown in Fig. 3.5a) for the Ce:YIG(004) reflex. A Gauss peak model fit, yields a FWHM of $0.0194°$, which needs to be compared to width of the rocking curve of the substrate peak of the GGG(004), which shows a FWHM of $0.0073°$. The substrate peak width represents the optimal value that can be obtained if the films growths fully epitaxial on the substrate. The found increase by a factor of 2.7 compared between Ce:YIG and GGG presents an example of a high epitaxy between film and substrate, while also the narrow absolute value highlights the good quality of the film. In the further discussion of the film quality in Sec. 3.2, we spare a detailed presentation of rocking curves, and will only discuss the interpretation of the measurements.

X-ray reflectivity

X-ray reflectivity (XRR) describes a technique that allows to determine the thickness, interface and surface roughness and density of a material. The x-ray beams hits the sample under a grazing incidence angle, leading to a partial reflection of the x-rays at the interface of film and substrate and the surface of the film [124]. The principle of this method can be compared to the light interference pattern obtained by a slit blend. Thus, the minima of the observed oscillation contain information about the thickness of the investigated material, while the decay can be attributed to the roughness of both interfaces. The critical angle is dependent on the electron density of the material. Fig. 3.5b) shows an example measurement including the curial parameters that can be obtained from the measurement. For fitting of the curve we use a commercial software (LEPTOS 7) that is based on the Parratt algorithm [126]. For the shown example of a Pt (film) / MgO (substrate) sample, used for the calibration of the Pt deposition rate, we determine a Pt thickness of $13.73\,\mathrm{nm}$ with a roughness below $0.1\,\mathrm{nm}$.

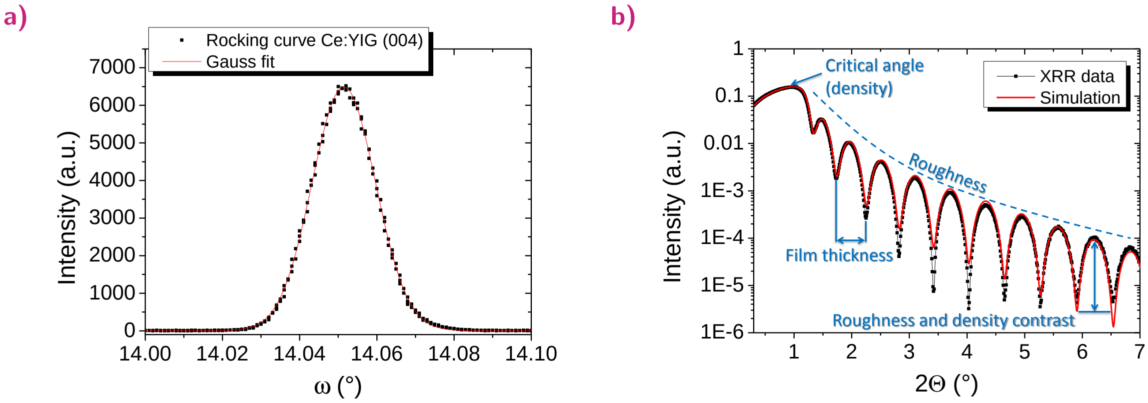

Fig. 3.5: a) Rocking curve of a Ce:YIG (004) reflex. The curve shows the fit of a Gauss model to the peak. b) XRR scan of a Pt / MgO sample. The black curve corresponds to the data, while the red curve to the XRR fit. The fit yields a thickness of the Pt $13.73\,\mathrm{nm}$ with a surface roughness of $0.23\,\mathrm{nm}$ and a interface roughness of $0.21\,\mathrm{nm}$.

3.1.4 SQUID magnetometry

For detection of the static magnetic properties, we use a commercial superconducting quantum interference device (SQUID) magnetometer (Quantum Design MPMS XL SQUID-Magnetometer). SQUID magnetometry represents one of many well established methods [127], such as vibrating sample magnetometry (VSM) and alternating gradient magnetometry (AGM), to determine the magnetic properties of a thin magnetic film. The original SQUID concept as well as magnetometry devices themselves have been further developed and optimized, leading to the point that a description of the working principles of a SQUID go well beyond the scope of this thesis. Due to this we refer the interested reader to the literature [128, 129] and only discuss the evaluation of the raw data, which is important for the understanding of the presented results.

A typical example for a hysteresis measurement is shown in Fig. 3.6a). The black curve presents the raw signal of a $130\,\mathrm{nm}$ thick YIG film grown on a GGG substrate. GGG itself has a high paramagnetic moment, leading in combination with a substrate thickness of $\sim 500\,\mu\mathrm{m}$ to a strong background signal. This paramagnetic background can be best described by a Brillouin function (see Sec. 2.2), which, for small field values, is sufficiently approximated by a linear function. Since YIG is a soft magnetic material, we can use the linear approximation to subtract the background signal by the GGG. By applying a linear fit for the region of (H » H_c), we obtain a value for the paramagnetic contribution by the GGG and can subtract this from the raw signal as shown for the red curve in Fig. 3.6a).

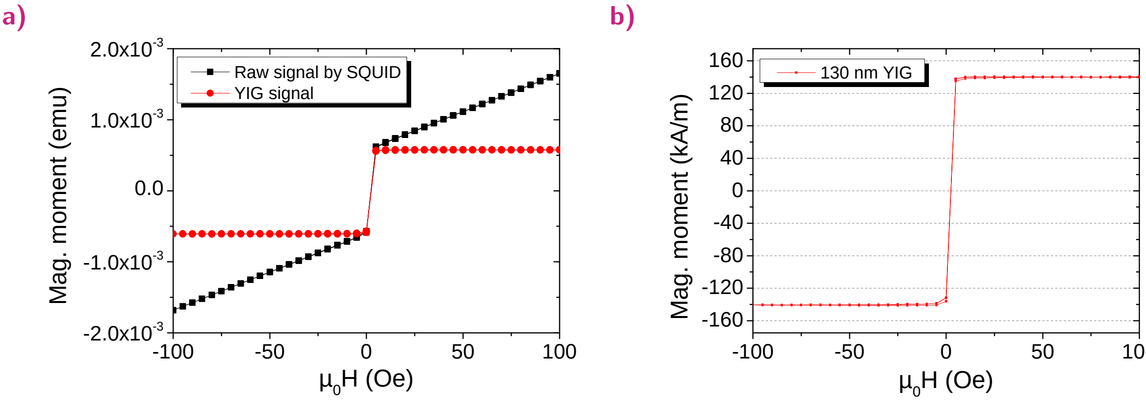

Fig. 3.6: a) The black curve presents the raw signal of a $130\,\mathrm{nm}$ thick YIG on a GGG substrate. The background signal by the GGG substrate has been subtracted for the red curve. b) Volume and shape corrected hysteresis measurement of the same sample.

Further data evaluation requires to know that SQUID magnetometry is an inductive method that detects the magnetic stray fields of a sample. These fields are shape dependent and a correction factor needs to be applied to the data in order to obtain the correct absolute moment [130]. The used SQUID is calibrated to the stray field of a point dipole making it necessary to scale the presented data by a factor of 1.14, which corresponds to a sample shape of $10\,\mathrm{mm} \times 5\,\mathrm{mm}$.

To determine the magnetization per volume, we furthermore need to estimate the real film volume. The real film area may slightly differ from $10\,\mathrm{mm} \times 5\,\mathrm{mm}$ due to deviations of the substrate size or covered areas while the deposition, as discussed in Sec. 3.1.1. We calculate the actual area using the number of pixels for the film compared to the number of pixels of reference $1\,\mathrm{cm}^2$ from a desk scanner picture as shown in Fig. 3.1c). Film thicknesses below $120\,\mathrm{nm}$ can in most cases be determined by XRR, as discussed in Sec. 3.1.3. Above $120\,\mathrm{nm}$ the film thickness can either be determined by profilometer measurements or estimated by the deposition rate. The volume estimation yields the biggest error for the later result, as the thickness and area uncertainty contribute to the volume. Using the information of the volume one can calculate the magnetization per volume, as done for the example YIG/GGG film in Fig. 3.6b). From the data we can extract a saturation magnetization of $\mathrm{M}_s = 140\,\mathrm{kA/m} \pm 5\,\mathrm{kA/m}$, which matches well with the literature value of $140\,\mathrm{kA/m}$ [131] for bulk YIG at room temperature.

Unless noted otherwise, all further saturation magnetization values have been obtained using the above described procedure.

3.1.5 Ferromagnetic resonance spectroscopy

To carry out the necessary characterization of the magnetodynamic properties such as the Gilbert damping parameter α (see Sec. 2.2), FMR is used to investigate the material. The method of ferromagnetic resonance spectroscopy allows one to study FMR by the excitation of the magnetic lattice using a microwave field. By studying the FMR, one can determine fundamental material parameters, discussed in Sec. 2.2.2, such as the saturation magnetization, the magnetic anisotropy constant and furthermore obtain an estimation for the Gilbert damping parameter. Since no appropriate setup was available in the beginning of this PhD thesis, one of the tasks of this PhD thesis was the design and construction of a setup for ferromagnetic resonance spectroscopy and to provide a model for the interpretation of the data. While the theoretical description is given in Sec. 2.2.2, we will focus in this section on the experimental realization.

For the experimental realization we have chosen a vector network analyzer FMR (VNA-FMR) setup, which presents a novel FMR detection method that became possible due to the development of the vector network analyzer (VNA). In contrast to conventional microwave sources, the VNA not only provides the possibility to emit, but also to detect, microwave signals at the same or different ports, at the same time. This feature allows a simple realization of a FMR setup [132]. A schematic of the VNA-FMR components is shown in Fig. 3.7a).

In our experiments, we operate the VNA in the transmission mode S_{21}, which means that we use port one as source and detect the incoming signal at port two. The microwave signal emitted by the VNA is fed via a high frequency, phase stabilized cable to a custom designed grounded coplanar waveguide (GCPW), optimized for frequencies up to $50\,\mathrm{GHz}$. The GCPW can be understood as a halved co-axial cable that allows for a near field interaction between the sample and the antenna of the GCPW. During the measurement, the sample is placed face down on the GCPW signal line, which leads to an interaction between the magnetic moments of the sample and the high frequency field H_{rf} generated by the microwave signal, as shown in Fig. 3.7b). Additionally, an external magnetic field H_{ext} perpendicular oriented to H_{rf} needs to be applied, to align the magnetic moments of the sample. This is necessary as H_{rf} drives a dipole Zeeman transition for the excitation of the ferromagnetic lattice, which is maximized for this configuration [34]. Depending on the measurement mode, the magnetic field or applied frequency can be tuned to fulfill the FMR condition. In the resonance condition, the transmitted signal S_{21} shows a minimum, due to the signal absorption by the ferromagnet.

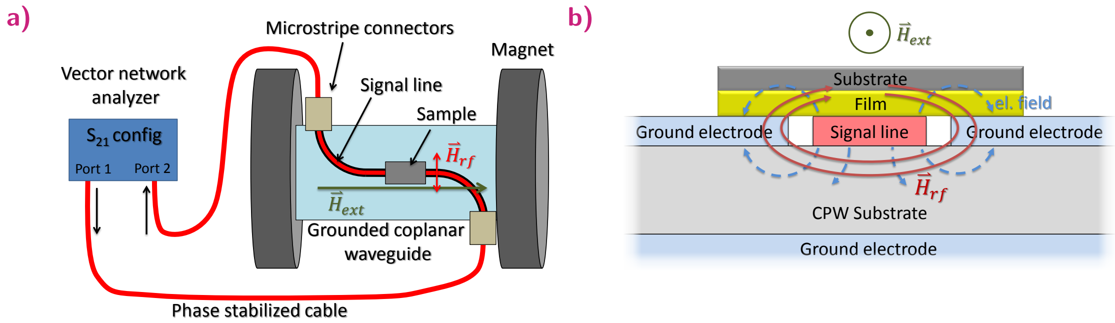

Fig. 3.7: a) Schematic of the used VNA-FMR setup, showing the basic components. b) Intersection sketch of the waveguide and sample, illustrating the electromagnetic field lines.

A VNA allows for two different, but in principle equivalent, measurement concepts of the FMR. In the first variant, the VNA is used in the continuous wave (cw) mode, providing a fixed frequency signal. The external magnetic field is swept in order to measure the resonance, which is similar to FMR cavity experiments, but not limited to certain frequencies given by the geometry of the cavity. Vice versa the VNA can sweep the frequency of the S_{21} signal, while the external magnetic field is kept constant, allowing to scan the FMR by frequency. The latter measurement method provides the advantage that the measurement time and resolution increases, since the VNA is capable of performing broad frequency sweeps in range from $10\,\mathrm{MHz}$ to $40\,\mathrm{GHz}$ with the precision of several Hz. The first method has the advantage of an easier data evaluation, as less material parameters influence the fit of the magnetic damping. At the cost of a longer measurement time and a lower resolution, as the magnetic field can only be tuned in this setup with a precision of $\sim 0.8\,\mathrm{Oe}$, which is comparably large to the normal FWHM line width of $2-3\,\mathrm{Oe}$ for YIG. Taking this into account, the frequency sweep method presents a more appropriate detection method for YIG and will be described in detail for a $80\,\mathrm{nm}$ thick YIG film.
As mentioned in the beginning, both methods can considered to be equivalent as it is possible to convert the Δf to ΔH using the following relation [132]

$$\Delta f = \Delta H \frac{\partial f_{FMR}(H_{ext})}{\partial H_{ext}}, \tag{3.1}$$

where $\frac{\partial f_{FMR}(H_{ext})}{\partial H_{ext}}$ is the derivative of eq. 2.15. An example of a frequency sweep measurement of a $80\,\mathrm{nm}$ thick YIG film grown on GGG(001), is shown in Fig. 3.8a), measured at $H_{ext} = 270\,\mathrm{mT}$. It is important to note that one needs to first subtract the background signal $S_{21/ref}$ from the FMR data $S_{21/FMR}$, in order to obtain the response signal of the ferromagnetic layer. Both raw signals are plotted in the inset of Fig. 3.8a). $S_{21/ref}$ should be measured at a higher field than $S_{21/FMR}$, to ensure an off-resonance measurement of the background signal by the system.

S_{21} consists of a set complex numbers, which allows one to obtain amplitude and phase of the signal. This allows to use different approaches to determine the line width from the resonance. The first approach, having a direct relation to the theoretically derived model is to decompose the signal into real and imaginary part. This decomposition has the problem that the real and imaginary part show a frequency dependent inter mixture. Since the VNA-FMR is preferentially designed for frequency sweep measurement, a decomposition of the signals might lead to artifacts. Furthermore a direct correlation between the scattering matrix parameters and the susceptibility tensor is only given for a completely determined set of S parameters [133]. Thus we use a simplified approach by fitting fitting $|S_{21}|$ to determine the line width. Using $|S_{21}|$ provides a good value for high magnetic fields $> 100\,\mathrm{mT}$ [133], where the shape of the signal is less influenced by inhomogeneous broadenings. For lower fields this approach might yield an overestimation from the more precise value, determined from a full set of S-parameters, of up to $10\,\%$ [133]. In order to provide a fast but precise data evaluation, we limit our FMR study to the field range from $100\,\mathrm{mT}$ to $450\,\mathrm{mT}$. Thus we determine the FWHM line width Δf and f_{FMR} by fitting of a Lorentz profile to $|S_{21}|$ for a certain magnetic field $\mu_0 H$. If we now measure f_{res} for different magnetic fields, high enough to align the magnetic moments of the sample, we can plot the resulting f_{FMR} as a function of the applied magnetic field, as shown in Fig.3.8b). The field dependence of this YIG sample is well described by the Kittel eq. 2.16, which assumes no magnetic anisotropy. From the fit we derive a M_s of $139.5\,\mathrm{kA/m} \pm 0.7\,\mathrm{kA/m}$, showing a good agreement with the value of the SQUID measurement of $143\,\mathrm{kA/m} \pm 7\,\mathrm{kA/m}$. We can use the relation of

$$\Delta f(f) = \left(\frac{|\gamma|}{2\pi} \mu_0 \Delta H_0 + 2\alpha f \right) \sqrt{1 + \left(\frac{|\gamma|\, \mu_0 M_s}{4\pi f} \right)^2}, \tag{3.2}$$

to describe the frequency dependence of the data of Δf [132, 134, 135]. This equation only provides a rough approximation as no magnetic anisotropy is taken into account. By plotting Δf for the corresponding frequency f_{FMR}, shown in Fig. 3.8c), we can apply the equation to to our data, using the M_s value of the Kittel fit as fixed value for the fit. A fixed value for M_s should always be used, due to the fact that more than one combination of α and M_s present a minimum for the fit algorithm. This leads to the necessity of an independent procedure to determine M_s like the Kittel fit or SQUID measurements. The fit yields a value for the Gilbert damping parameter α of $(2.3 \pm 0.1) \times 10^{-4}$ and $1.4\,\mathrm{Oe} \pm 0.1\,\mathrm{Oe}$ for H_0. This value for α represent one of the lowest reported values for PLD grown YIG films and highlights as

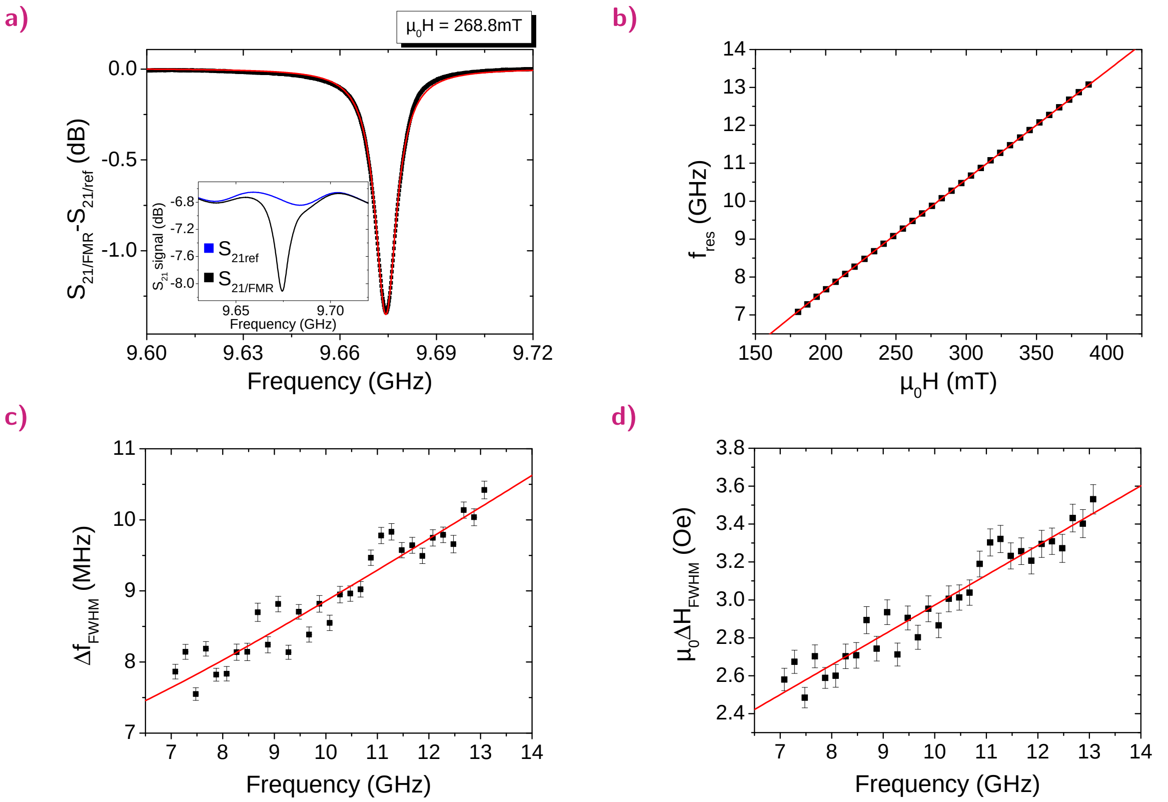

Fig. 3.8: a) Example for a frequency sweep measurement. The inset shows the raw signal data that needs to be subtracted in order separate the FMR response from the waveguide signal. b) Resonance frequency as a function of the applied magnetic field. The red curve corresponds to a fit of the Kittel eq. 2.16 for no magnetic anisotropy. c) Δf as a function of the resonance frequency. The red curve corresponds to a fit of eq. 3.2. d) Converted ΔH as a function of the resonance frequency. Eq. 2.20 has been used to obtain the fit, shown as the red curve.

well as the low value of H_0 the good sample quality. In Sec. 3.2.1 we give a more detailed comparison to other YIG films as well as in publication [p2].

To provide a complete and comparable picture of the film, we will convert the data to ΔH using eq. 3.1, as most literature sources only provide the magnetic line width value at $\sim 10\,$GHz. Fig. 3.8d) shows the converted data in combination with a fit of eq. 2.16. For H_0 the fit yields the identical value of $1.4\,$Oe$\,\pm\,0.1\,$Oe, while we obtain a slightly lower value for α of $(2.2 \pm 0.1) \times 10^{-4}$ which is within the error of the fit of eq. 3.2. This discrepancy possibly results from the numerical inaccuracy of the conversion and approximation of the model system. Therefore, we can determine a value for Δ at $10\,$GHz of $2.97\,$Oe, which again represents one of the lowest line widths for a PLD grown thin film.

3.1.6 Magnetooptic Microscopy

As a last characterization method, we introduce an optical magnetometry method, based on the magneto optic Kerr effect (MOKE) [36]. The MOKE of magnetic materials causes a rotation of the polarization of the reflected light, depending on magnetization of the material, while a rotation of the polarization of the transmitted light is called the Faraday effect [136]. Based on the longitudinal MOKE configuration, we will explain the basic concept of a MOKE setup [137], shown in Fig. 3.9a). In order to use the MOKE as a magnetometry method the light from a source (either a laser or a white LED light source) needs to be linearly polarized. As the polarized light is reflected by the surface layers of the sample, its polarization will undergo a rotation. This rotation, the Kerr rotation, depends on the magnetic orientation of the material and can therefore be used to determine magnetic properties of material. A high sensitivity for this rotation can be achieved by setting the analyzer to a perpendicular polarization with respect to polarizer. The transmitted light thus only corresponds to the Kerr effect and is afterwards detected by a photodetector [137]. In chase of the MOKE microscopy an objective is additionally mounted in front of the analyzer, allowing the use of an area resolving CCD-sensor to image the surface. MOKE measurements can be separated into three different configurations [36]. The transverse and longitudinal configuration can be used to detect the in-plane magnetization of the sample. In case of the longitudinal configuration the magnetization is aligned in-plane parallel to the path of the incoming light, while in the transverse case the magnetization is in-plane perpendicular oriented. Fig. 3.9a) shows the longitudinal configuration. If the angle of incidence for the light is close to $\chi = 0\,^\circ$ one is sensitive to the out-of-plane magnetization. This configuration is called polar MOKE configuration.

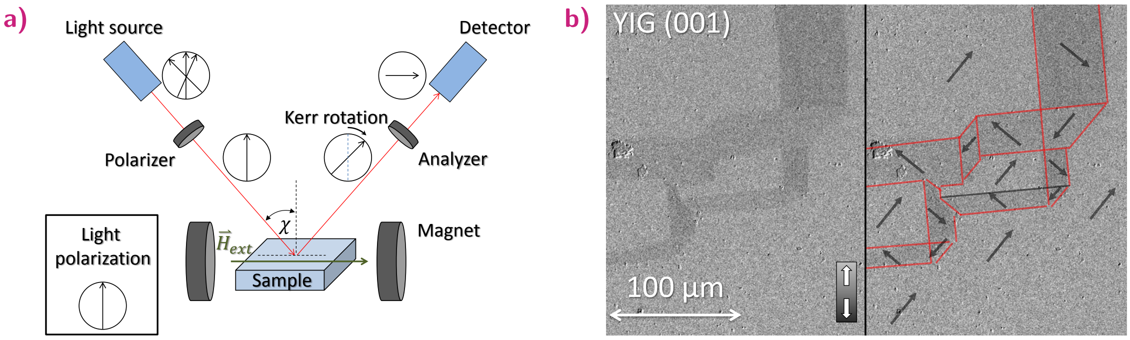

Fig. 3.9: a) Sketch of principles of a longitudinal MOKE setup. b) MOKE microscopy image of a $300\,\mathrm{nm}$ thick YIG film on GGG(001). The magnetic domain structure has been highlighted in the right picture.

The MOKE magnetometry measurements presented in Sec. 3.2.2 were carried out at the University of Bielefeld using an extended longitudinal MOKE setup [138] and a rotatable Wollaston prism combined with two photo-diodes for polarization detection [139]. For the presented MOKE microscopy imaging of the surface domain structure, we used a EVICO-ZEISS Imager (D2m). The microscope uses a white light LED source, which provides a continuous spectrum of light in the visible range. The magnetic contrast in the MOKE microscopy images is obtained by digital image processing. A background image is taken in the saturation state of the ferromagnet and subtracted from the image of remanent state. Fig. 3.9b) shows an example for such a differential MOKE microscopy image of an $300\,\mathrm{nm}$ thick YIG film grown on GGG (001). YIG possesses in general a small Kerr rotation for optical wavelengths, but a large Faraday rotation. The shown image exploits this effect, as the analyzed film was coated with a reflecting Pt-layer. As YIG is transparent at optical wavelength, the light crosses the YIG film twice, allowing to use the Faraday effect to detect the magnetic domain structure. The domain structure shows three different magnetic contrasts and a clear $45\,^\circ$ shaped pattern. Both features hint to a cubic magnetic anisotropy of the sample, which is to expected from YIG sample grown on a GGG (001) substrate, as well be discussed in the following section 3.2.1. Later in chapter 4 we will present SSE measurements of the same sample in Sec. 4.1.5 and Fig. 4.6a), which can also confirm this cubic anisotropy within the sample. In Sec. 3.2.2 we will show that a Cerium substitution into YIG increases the MOKE, which then allows to directly use the Kerr effect to image the magnetic domain structure in even thinner samples.

3.2 Materials development

In the last section we established the growth and evaluation methods for the material, which we use in the SSE experiments. Within this section we will give an introduction to the important magnetic garnets that have been studied and present our results of the growth and optimization of these materials.
First we will present our results obtained for the growth of Yttrium Iron Garnet (YIG), which is considered as the model system for magnetic insulators. Using the previous described magnetometry and structure analysis methods we can show that we are capable of growing high quality epitaxial thin films, which exhibit comparative quality to those reported in literature [p2]. These films will be later used in the SSE experiments, where an exact knowledge and control of the material properties are crucial to rule out influences of other sources. After the description of YIG, we will discuss how a substitution of Yttrium by Cerium (Ce:YIG) affects magnetic and magnetooptic properties. The shown enhancement of the MOKE in Ce:YIG will be of further use for future spin caloric experiments, as it allows for easy imaging of thermally driven domain wall motion. As a last material we will introduce Gadolinium Iron Garnet (GIG), which in contrast to YIG shows a ferrimagnetic magnetization behavior. The more complex temperature dependence of the magnetization of this material enables us to show correlations of the SSE with the magnetic sub-lattices of the material, showing limitations of current theories which only consider the total magnetization of the material.

3.2.1 Yttrium iron garnet

$Y_3Fe_5O_{12}$ or YIG is an artificial created insulating magnetic garnet, synthesized as a bulk material first in 1956 [140, 141]. Its discovery meant a milestone for microwave research and helped to advance many concepts and applications in magnetism. Kittel called it "the fruitfly of magnetism" pointing out its importance for the community [142]. After this boom in the investigation of garnets the interest decreased over the years. Recent discoveries in the field of spintronics led to a revival in the investigation and optimization of the YIG growth. Among those was the first magnonically transmitted electric signal [6] and by thermal excitation generated pure magnonic spin currents, the SSE.

For commercial application the growth of YIG has been optimized by using liquid phase epitaxy (LPE). As the name of the process implies, the film is grown by dipping a garnet substrate, in most cases Gadolinium Gallium Garnet (GGG , $Gd_3Ga_5O_{12}$) into a saturated melt of Fe_2O_3/Y_2O_3 and PbO/B_2O_3 at temperatures around $1000°C$ [143–145].

The progress in the development of thin film deposition techniques like PLD, makes it nowadays possible to produce high quality YIG films with thicknesses of only a few unit cells [146]. For the research on the SSE it is crucial to have access to both, µm and only few nm thick YIG films to investigate the origin and dependence of the SSE. Additionally the films need to be of comparable quality in order to avoid influences on the SSE by changes in the material properties.

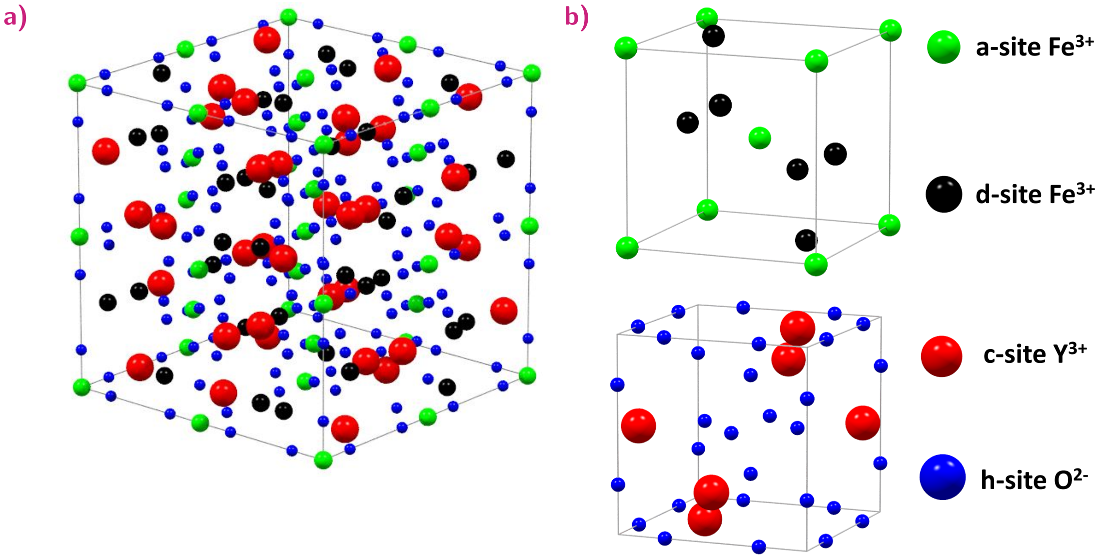

Fig. 3.10: a) Illustration of an YIG unit cell. b) Schematic of the different lattice site within the eighth of a YIG unit cell.

With its large cubic unit cell of $1.2376\,\mathrm{nm}$ [147, 148], containing 160 atoms, YIG is a complex material to grow. Four different sub-lattices $\{c_3\}[a_2](d_3)\langle O_{12}\rangle$ can be identified based on the symmetry group (230) $Ia\bar{3}D$ for the garnets. 96 O^{2-} ions are located within each cell leading to a part-ionic and part-covalent character of the chemical bonds [149]. The high oxygen concentration easily allows for the occurrence of oxygen vacancies as a defect, which influences the lattice constant and the electrically insulating properties of YIG [150](bandgap of $2.66\,\mathrm{eV}$). Y^{3+} is non magnetic and is placed on the dodecahedral $\{c_3\}$ lattice site, leading to 24 atoms within a unit cell. The Fe^{3+} ions occupy the octahedral $[a_2]$ site with 16 atoms and tetrahedral (d_3) site with 24 atoms. Each Fe^{3+} has a magnetic moment of $5\mu_B$. Since the [a_2] and (d_3) site are antiferromagnetically coupled via superexchange by an O^{2-} ion, the net moment is reduced. Fig. 3.10b) illustrates the arrangement of the different lattice sites with respect to one another. The net moment of a unit cell thus consist of $40\mu_B$, which corresponds to a volume saturation magnetization of $M_s = 191$ kA/m at 4.2 K [131] and $M_s = 140$ kA/m [131] at 300 K. Due to the ferrimagnetic lattice character, YIG shows slightly different temperature dependence of the magnetization [37] compared to the $M(T) \propto T^{-3/2}$ of a ferromagnet, with a Curie temperature at around 560 K [131, 151]. Bulk YIG in general possess only a very weak cubic magnetic anisotropy with the easy axis along the $\langle 111 \rangle$ direction [37, 152]. The origin of this cubic anisotropy cannot directly be linked to the lattice structure, due to the ferrimagnetic sub-lattices. The antiparallel oriented sub-lattices show no simple arrangement for magnetic moments along the simple cubic axes $\langle 100 \rangle$,$\langle 110 \rangle$ or $\langle 111 \rangle$ [37], as shown in Fig. 3.10b). Substitution experiments of bulk material could show that the anisotropy can be easily disturbed and thus results from a complex interplay of all lattice sites [37].

The most important of all material properties is the low Gilbert damping α, which is for bulk material in the order of $\alpha = 10^{-5}$ [151]. This marks the lowest reported value of the damping parameter for all magnetic materials, being the reason that most studies of magnons are carried out in YIG [53]. Thus YIG represents also an ideal material for the investigation of thermally excited magnons, as a long magnon propagation length enables a simplified study of the possible correlation between SSE and the magnetic lattice.

To make use of this opportunity, one needs to have access to thin YIG films. This requirement resulted in one of the main subjects of this thesis, to establish the YIG growth by PLD in Mainz and to optimize its properties. In collaboration with the group of Prof. Ross at MIT we were able to publish a paper about high quality epitaxial YIG thin films, with near bulk film properties [p2]. The results of this paper will be presented in the following.

YIG growth by PLD

A stoichiometric YIG target[1] with 1" diameter is used for the deposition of the films. The target itself is prepared by mixing Y_2O_3 and Fe_2O_3 powder in the stoichiometric ratio of YIG, followed by mixing and milling using ZrO_2 balls for 24 hours and consecutive sintering at 1400 °C for 10 h. The last heating step consists of a calcination of the target at 1150 °C for 24 h, causing a formation of the YIG phase. The films are deposited on single crystalline GGG substrates, chosen because of the small lattice mismatch between bulk YIG and GGG (1.2383 nm [125]) of 0.05 %. For the deposition the substrate is heated to 650 °C at an oxygen pressure of 2.67×10^{-2} mbar. A laser energy of 400 mJ, repetition rate of 10 Hz and a target to substrate distance of around 6 cm yields a growth rate of ~ 3 nm/min. After the deposition the films are annealed ex-situ by rapid thermal annealing (RTA) for 120 s at 800 °C, which

---

[1] The target has been produced by D. H. Kim from the MIT.

reduces the amount of oxygen vacancies.

We chose for our studies films with thicknesses ranging from 17 nm to 190 nm, in order to control relaxation induced processes in the crystal lattice. First we will take a look at the crystal structure by evaluating the XRD scans of the film peaks. Fig. 3.11a) shows three examples for YIG films grown on GGG (001) substrates. From the scans one can see that for each film Laue oscillations of the YIG reflex are observed.

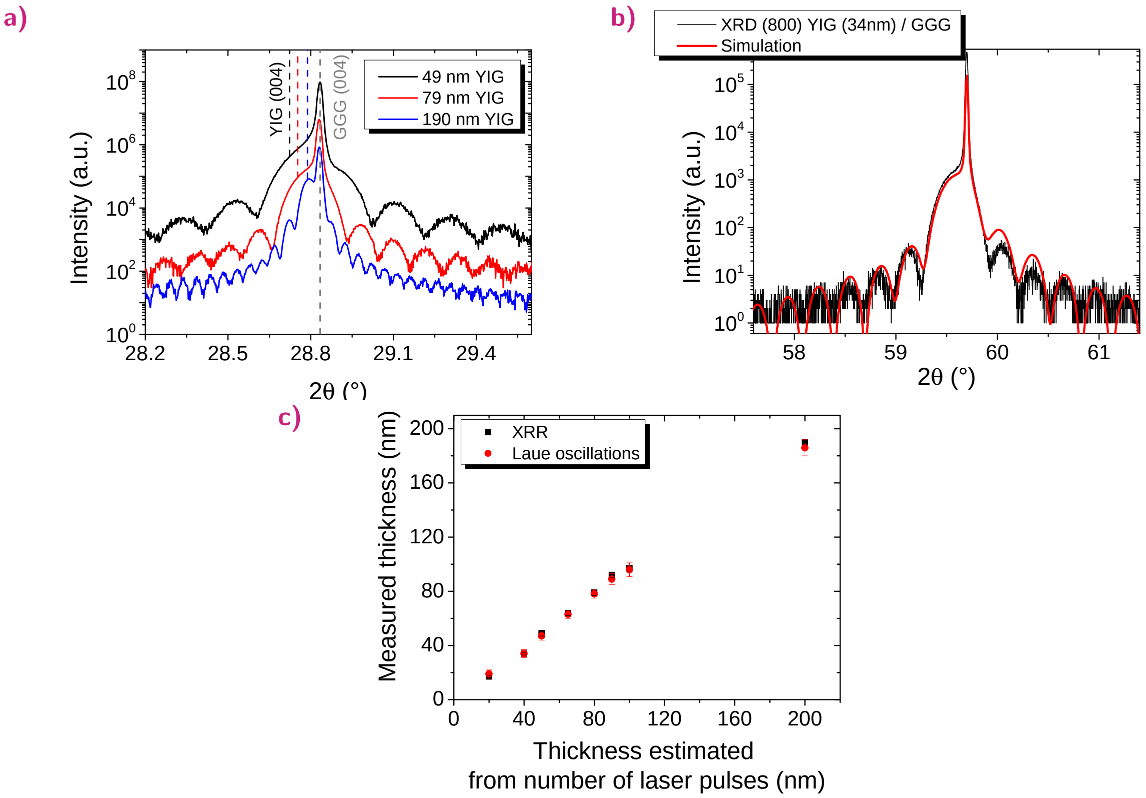

Fig. 3.11: a) $2\theta/\omega$ scan of three YIG films and GGG substrates peak. b) $2\theta/\omega$ scan (black curve) of the YIG film peak and the GGG substrate combined with a simulation scattering on the different lattice layers (red curve). c) Film thickness determined by XRR and the Laue oscillations for the estimated film thickness by the number of laser pulses. A slight decrease of the deposition rate can be detected due to a deposition of material on the view port of the ablation laser.

Thus the presence of these oscillations marks an epitaxial layer by layer growth of the material and indicates a high crystalline quality. A simulation model derived by Gerhard Jakob allows one to calculate the average lattice parameter and the thickness of the epitaxial layers from the separation of the fringes. Fig. 3.11b) shows an example of such a simulation for a 34 nm film. Using this simulation method, for our samples grown in optimized conditions, we derive a thickness of the epitaxial lattices. The determined value agrees within the error with the film thicknesses obtained by XRR, corroborating the high crystalline quality without the presence of a dead interface layer, shown in Fig. 3.11c). The simulation model enables us to estimate the film peak position despite the fact that actual reflex is too close to the substrate peak to be separately resolvable, as presented in Fig. 3.11a). Furthermore the model can include growth induced strain, which will lead to a shift and asymmetry of the film peak. An example for such a growth induced strained sample, possibly caused by oxygen vacancies, is shown in Fig. 3.12a). As can be seen in Fig. 3.11a) our films grown at the optimized conditions exhibit only a small compressive in-plane strain, possibly originating from epitaxial growth on the GGG substrate.

Our results reveal that the film's out of plane lattice constant exhibits a $0.005\,\text{Å}$ variation around $12.400\,\text{Å}$, indicating a stable crystal growth without any lattice relaxation for high film thicknesses. This behavior is contrary to findings for YIG grown on Yttrium Aluminum Garnet, where the larger lattice mismatch leads to lattice relaxation for films with a thickness of even $40\,\text{nm}$ [153].

The surface roughness has been analyzed by Atomic Force Microscopy (AFM) measurements revealing a RMS roughness around $0.2\,\text{nm}$, which is in agreement with results from the XRR measurements that can only detect a surface roughness below $0.5\,\text{nm}$. Fig. 3.12b) shows an example measurement for a $79\,\text{nm}$ thick YIG film. More information about the crystallographic structure and additional x-ray analysis are given in Pub. [p2]. In summary the x-ray analysis demonstrates the high crystal quality of the films and allows us to obtain a detailed knowledge about the crystalline sample structure.

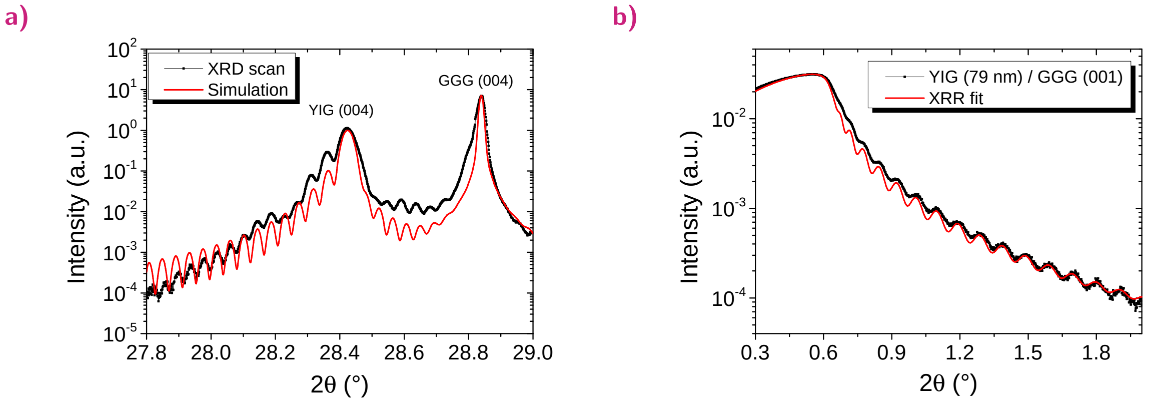

Fig. 3.12: a) $2\theta/\omega$ scan (black curve) of the highly strained YIG film. The red curve simulates a $216\,\text{nm}$ thick YIG film, with a strain relaxation of over $\sim 28\,\text{nm}$ and largely expanded lattice constant of $1.2546\,\text{nm}$. b) XRR measurement of a $79\,\text{nm}$ thick YIG film on GGG (001) indicate a smooth surface with a roughness below $0.5\,\text{nm}$.

The thickness information gathered by XRR are used to calculate the volume magnetization from the magnetometry measurements with SQUID (see Fig. 3.13a)). The films show a constant, bulk like saturation moment of $140\,\text{kA/m} \pm 5\,\text{kA/m}$. Only the $17\,\text{nm}$ film shows a $14\,\text{kA/m}$ lower value. Later experiments showed that a higher moment can be achieved by a slower growth rate, from which we conclude that the deposition rate of $\sim 3\,\text{nm/min}$ is too high to allow a proper rearrangement of the material within the first layers. Our FMR investigation of the samples is based on the techniques presented in Sec. 3.1.5. Fig. 3.8 shows an example evaluation of a $80\,\text{nm}$ thick YIG film, discussed in the same section. A summary of all measured M_s values is shown in Fig. 3.13a), which confirm the bulk like saturation magnetization and the trend of a smaller value for the thinnest sample. To obtain these values we used the Kittel eq. 2.16 without magnetic anisotropy. The good agreement with the SQUID values reveal that the samples can only possess a small magnetic anisotropy similar to bulk material.

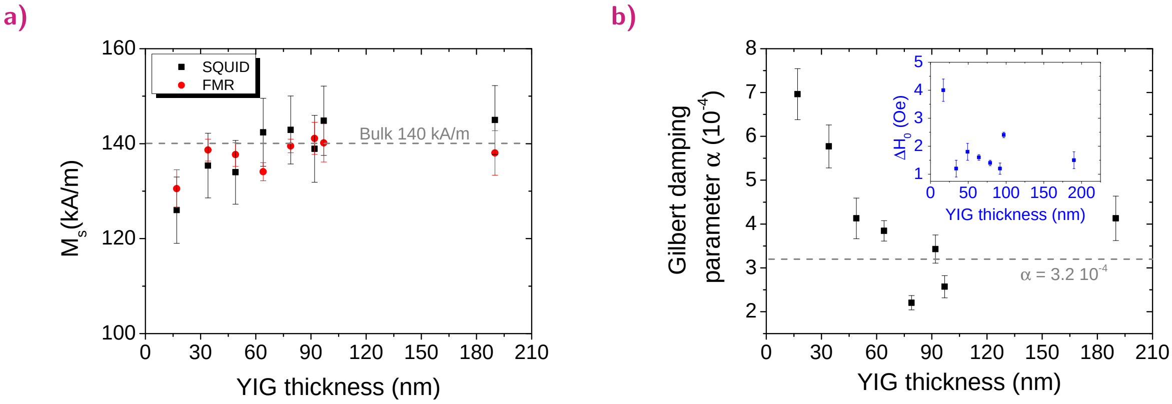

Fig. 3.13: a) M_s values obtained by SQUID and FMR as a function of the YIG film thickness. b) Gilbert damping constant α as a function of the film thickness. The inset shows the ΔH_0 as a function of film thickness.

The evaluation of the Gilbert damping parameter α reveals a decrease with increasing film thickness up to $50\,\mathrm{nm}$. Thicker films show an arbitrary variation without correlation to the film thickness (see Fig. 3.13b)). One determines an average value of $\alpha = 3.2 \pm 0.8 \times 10^{-4}$ for this thickness range, pointing out that the films are among the highest quality thin films grown by PLD [154, 155] and possess a damping comparable to the thinnest LPE grown films of $\sim 200\,\mathrm{nm}$ [156, 157]. As discussed in Sec. 3.1.5, ΔH_0 allows to estimate the density of magnetic defects in the sample, as it marks the intrinsic contribution to the damping (see Sec. 2.2.2). From our measurements, shown in the inset of Fig. 3.13b), we can only observe an arbitrary scattering around $1.6\,\mathrm{Oe} \pm 0.4\,\mathrm{Oe}$ for the films thicker than $34\,\mathrm{nm}$. Since extrinsic and intrinsic damping are both higher for the $17\,\mathrm{nm}$ film, we can conclude that the influence of strain or surface roughness induced by the GGG starts to worsen magnetic properties. Despite this, the small absolute value for the thick films confirm the good sample quality and allows us to use these samples for our SSE measurements. It is important to point out that thickness independent values for the saturation magnetization as well for α, are requirements for the interpretation of our thickness dependent SSE data that will be presented in Sec. 4.2.1.

Thus we could show that our optimization of the YIG film growth allows us to produce high quality epitaxial YIG films. Furthermore, the investigation of the magnetic properties revealed that neither M_s nor α scale with the film thickness. Further information on the magnetic coercivity and the in-plane relaxation of the lattice, is given in Pub. [p2]. We will now discuss the effect of substituting Cerium in YIG, as this turns out to be a way to tailor the magnetic anisotropy of the material and to enhance the magnetooptic properties.

3.2.2 Cerium substituted Yttrium Iron Garnet

For our future studies of the thermally driven domain wall motion by the SSE, a material with a higher magnetooptic effect than YIG is desirable, since the magnetooptic properties of YIG complicate a magnetooptic imaging of domains in thin films [37]. It is known for bulk as well as for thin films that the substitution of Yttrium by Cerium leads to an enhancement of the Faraday effect in Ce:YIG [158–162]. While the probing method by the Faraday effect provides an elegant solution for magnetometry measurements, the magnetooptic Kerr effect is more robust and allows to study thin films independent of the used substrate (see Sec. 3.1.6). Using MOKE microscopy of thin films furthermore enables one to probe the magnetic domain wall motion even in structured geometries and by this to obtain more information than provided in proof of principle experiments in μm thick material [163]. The magnetodynamic properties of Ce:YIG have only be sparsely studied in literature but they are essential for a deeper understanding of the SSE in this material. Thus, we present a detailed study of the magnetooptic and magnetic properties of epitaxial Cerium substituted YIG thin films, in order to assess, if the material is suitable for further spin caloritronic experiments. In the following we will show that the substitution by Cerium does not only increase the MOKE but also increases the magnetic anisotropy, making it possible to tailor the properties of the garnet by the amount of substitution. The presented work is part of the joined publication [p3] between the MIT, the University of Bielefeld and the University of Mainz.

Analogous to the YIG deposition by PLD, we use a mixed powder target in the stoichiometry $Ce_1Y_2Fe_5O_{12}$, which is identically prepared. While the laser parameters are identical, we use a heater temperature of $815\,°C$ and a lower oxygen pressure of 6.67×10^{-3} mbar. The RTA treatment is left out, to preserve a homogeneous Cerium distribution in the film.

The XRD analysis for films grown under these conditions is shown in Fig. 3.14. The substrate surface orientation either (001) or (111) is transferred to the deposited film. Like the YIG samples, the Ce:YIG films show, independent of their crystalline orientation, Laue fringes indicating a highly coherent scattering from the epitaxial film. From the peak position of the films, we extract a lattice constant of 1.257 nm for both films. A reciprocal space map (RSM) of non-specular reflexes enables us to determine the in-plane and out-plane lattice constants with respect to the substrate. Fig. 3.14d) shows the RSM of the (228) peak of a Ce:YIG / GGG (001) sample. Mismatched different in-plane lattice constants for film and substrate indicate a relaxation of the film. Additionally the scan finds a larger in-plane constant compared to the out-of-plane constant for Ce:YIG revealing a tetragonal distortion of the cubic unit cell. The $2\theta/\omega$ scan shows no formation of a secondary Ce_2O phase, which is important since this phase would influence the magnetic film properties negatively [159, 164]. An example for a wide range $2\theta/\omega$ scan for one of Ce:YIG film orientations is shown and discussed in Sec. 3.1.3. From the rocking curves we derive a FWHM of around $0.022°$ for both orientations, which is as narrow as our YIG films, confirming a high quality epitaxial structure of the films. Both surface evaluation techniques, XRR and AFM, indicate a surface roughness below 0.7 nm. Fig. 3.14c) shows the corresponding XRR measurements, while more detailed information about the AFM measurements and the rocking curves are given in publication [p3].

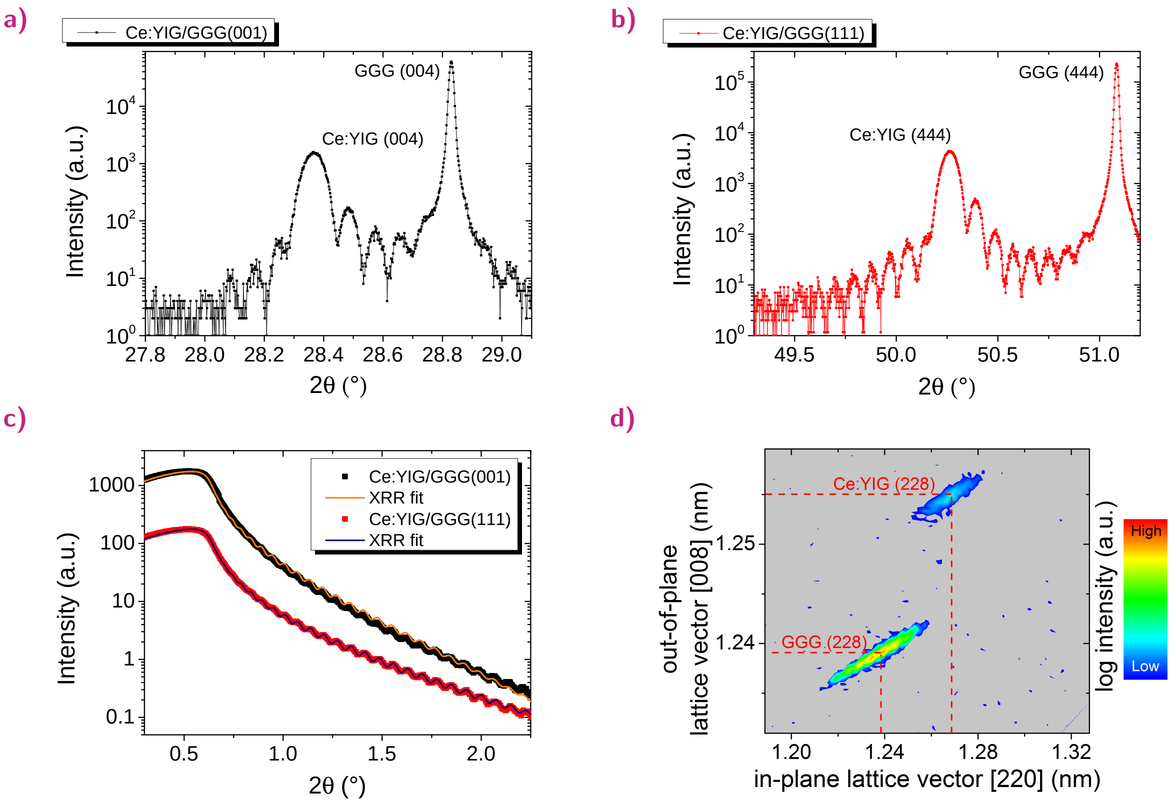

Fig. 3.14: $2\theta/\omega$ scan of Ce:YIG grown on GGG (001) a) and GGG (111) b). c) XRR measurements of Ce:YIG (001), black curve, and (111), red curve, with the corresponding XRR fit curves deriving a thickness of 111 nm and 112 nm. The fits have been performed assuming a stoichiometry of $Ce_1Y_2Fe_5O_{12}$. d) RSM of the (228) substrate and film reflex.

From the lattice structure analysis we can see that despite the high Cerium substitution, the samples show an epitaxial growth on the substrate. Next we will investigate the influence of the Cerium on the magnetic properties. We can use the thickness values obtained by the XRR measurements, of around 110 nm, to calculate the volume magnetization from our SQUID measurements, shown in Fig. 3.15. The measurements reveal only a slightly increased M_s 155 kA/m for both Ce:YIG films. This increase by 15 kA/m, compared to undoped YIG, results from the substitution by Cerium. Ce^{3+} in contrast to Y^{3+} possesses a magnetic moment, which couples ferromagnetically to the d-site Fe^{3+} ions [159,165,166]. This coupled moment increases the net magnetic moment and furthermore confirms the absence of a Ce_2O phase, as that would lead to a reduction of the moment [159].

The magnetic coupling of the Ce^{3+} influences also the magnetodynamic properties. Our VNA-FMR can show that the line width increases by two orders of magnitude due to the substitution, resulting in a Gilbert damping of $\alpha \sim 10^{-2}$ for both films. Compared to normal YIG, this means an enhancement of α by two orders of magnitude, which indicates that the films have a magnetic damping comparable to magnetic metals. The corresponding frequency line width as a function of the resonance and the fit of eq. 3.2 are shown in Fig. 3.15c). In addition to the irregular magnetic perturbation of the Fe sub-lattice by the Ce^{3+}, also the tetragonal lattice distortion contributes to the increased magnetic damping. A more detailed analysis of the VNA-FMR data of Ce:YIG is presented in Pub. [p3]

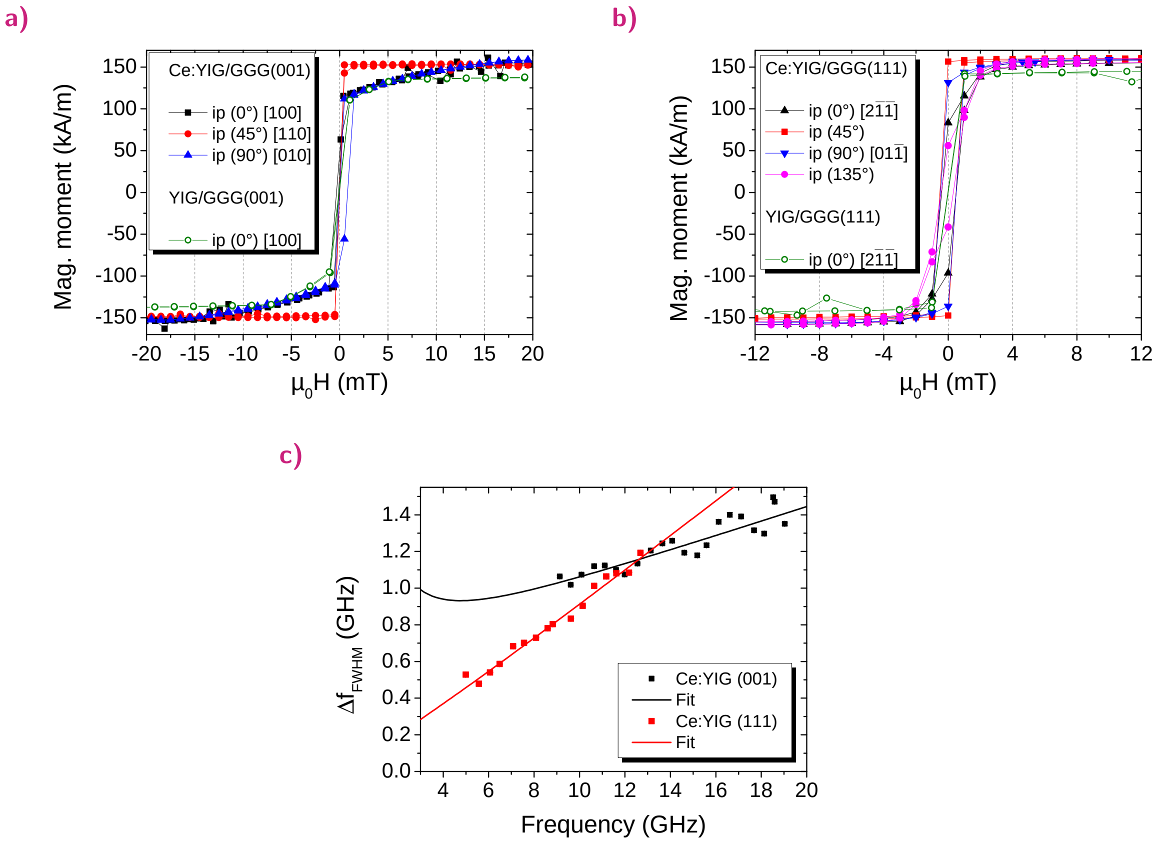

Fig. 3.15: SQUID hysteresis loops for Ce:YIG (001) a) and CeYIG (111) b) together with measurements of normal YIG. The graphs additionally show SQUID loops along different in-plane orientations of the Ce:YIG samples. c) Frequency line width as a function of the resonance frequency for both Ce:YIG samples. The lines correspond the fit using eq. 3.2.

Our study of the magnetic anisotropy in the films strengthens the conjecture of a strong influence of magnetostrictive contribution to the anisotropy. Using angle dependent SQUID measurements, shown in Fig. 3.15, we find for both crystalline orientations an increased magnetic anisotropy compared to undoped YIG. For Ce:YIG grown on GGG(001), we observe a hard magnetic axis for $0\,^\circ$ and $90\,^\circ$ and an easy axis for $45\,^\circ$, as shown in Fig. 3.15a). This behavior corresponds to a fourfold symmetry, which we can attribute to an in-plane cubic anisotropy. $45\,^\circ$ corresponds to the [110] direction, which shows that the cubic anisotropy of Ce:YIG is identical oriented to the one of the unsubstituted YIG thin films. In these thin film samples, the shape anisotropy causes a shift of the bulk cubic easy axes along the $\langle 111\rangle$ direction towards an in-plane projection along the $\langle 110\rangle$ directions. Using eq. 2.1, we extract from the saturation field of $H_k = 175\,\mathrm{Oe}$, a cubic anisotropy constant of $K_1 = -1.3\cdot 10^3\,\mathrm{J/m^3}$.

For our pure YIG thin film, we derive a value of $K_1 = -0.5 \cdot 10^3$ J/m^3, being a factor of 2.6 smaller.

The film grown on GGG substrate along the [111] direction exhibits a more complex anisotropy behavior. Based on the symmetry of the crystal, one would expect a sixfold in-plane anisotropy, since the film is grown on the $\{111\}$ plane. Our SQUID hysteresis measurements cannot confirm this type of anisotropy, but reveal a magnetic hard axis along $135\,^\circ$ and a magnetic easy for $45\,^\circ$, shown in Fig. 3.15b). This two fold symmetry corresponds to a uniaxial anisotropy, which is not oriented along any of the high symmetry axes of the crystal. The origin of the uniaxial anisotropy can be explained by a further x-ray analysis of the sample, shown in the supplementary information of Ref. [p3]. The ω-scan of the substrate peak with respect to the surface normal of the sample reveals the presence of a miscut. The measurements find a maximum of this miscut perpendicularly oriented to the easy axis, which confirms our assumption of substrate induced anisotropy. A miscut of the substrate leads to the formation of terraces on the surface of the sample, oriented along the direction of the miscut. As the terraces can be compared to a structured surface, the magnetic free energy is minimized if the magnetization is perpendicularly to the steps of the terraces. Thus we can explain the origin of the unusual anisotropy being caused by the substrate. As this type of anisotropy results from the substrate quality we forego a detailed comparison with YIG (111). However, from a comparison of the coercive fields for the $[2\,\overline{1}\,\overline{1}]$ axes of both (111) oriented samples, one would again expect a higher anisotropy for Ce:YIG than for the unsubstituted YIG. In Sec. 4.1.5 we will show that also the SSE can be used as a tool to investigate the magnetic anisotropy of the material, confirming and expanding our results obtained by the SQUID measurements.

Next we investigate the change of magnetooptic properties resulting from the Ce substitution. In Fig. 3.16 we show longitudinal MOKE hysteresis of YIG and Ce:YIG measured with two different wavelengths. First we take a look on the results for a laser wavelength of 406 nm, which represents a higher energy than the bandgap of $2.66\,\mathrm{eV} \mathrel{\hat{=}} 466\,\mathrm{nm}$ for pure YIG. From the MOKE measurements, shown in Fig. 3.16a), we obtain a Kerr rotation of 16 mdeg for both YIG crystalline orientations. For Ce:YIG we find a twofold larger Kerr rotation of 37 mdeg for Ce:YIG (001) and 46 mdeg for Ce:YIG (111). These results show that the enhancement of the magnetooptic effect by Cerium is not only valid for the Faraday effect but also the magnetooptic Kerr effect. To emphasize the exceptional feature obtained by the Cerium substitution, we additionally study the MOKE at 635 nm, which represents a wavelength with an energy lower than the bandgap of YIG. The MOKE for pure YIG is vanishing at this wavelength as can be seen in Fig. 3.16b). We can only detect a Kerr rotation of around 2 mdeg, while the Kerr effect in Ce:YIG shows a high signal of up to 26 mdeg for (001) and 38 mdeg for (111). 635 nm presents a wavelength more suited for most nonreciprocal magnetooptic devices than 406 nm, highlighting that this material is well suited for applications. A more detailed spectral analysis is required to obtain a better understanding of the wavelength dependence for this material and will be done in the future collaboration with the University of Bielefeld.

Despite the change in stoichiometry, Ce:YIG maintains the good insulating properties of YIG, which, in combination with the enhancement of the MOKE for optical wavelength, allows to study the influence of thermally excited magnons on magnetic structures.

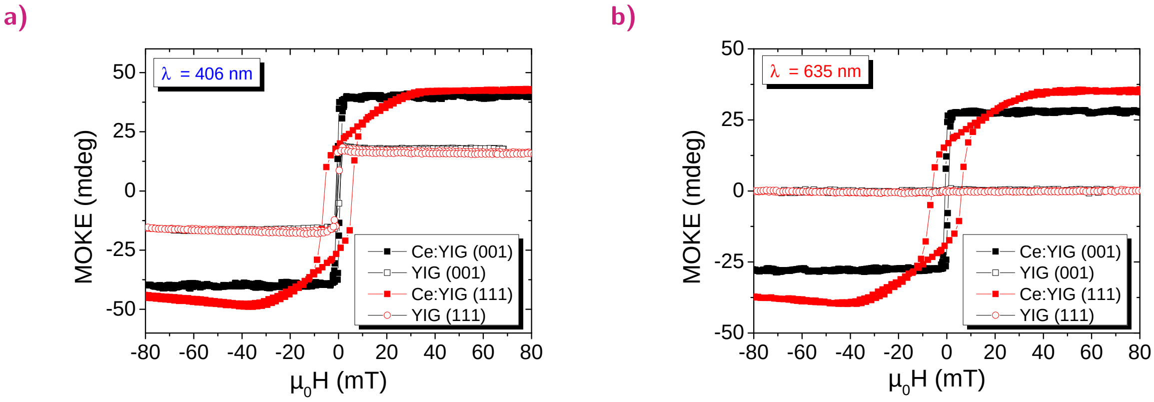

Fig. 3.16: a), b) Kerr rotation for Ce:YIG and YIG as a function of the magnetic field for two different wavelength a) $\lambda = 406\,\mathrm{nm}$ and b) $\lambda = 635\,\mathrm{nm}$.

As an example measurement we present two MOKE microscopy measurements for both Ce:YIG samples in Fig. 3.17. The differential image of Ce:YIG (001), taken in the remanent state in the longitudinal in-plane MOKE configuration, exhibits a clear magnetic contrast, although the sample has only a thickness of $110\,\mathrm{nm}$. This is not possible for pure YIG films, as discussed in Sec. 3.1.6. Magnetic domains with three different contrasts can be distinguished, the shape of which hints to a more complex anisotropy than derived from the SQUID measurements. Moreover the pattern indicates a combination of cubic and uniaxial anisotropy, which can be verified by further magnetometry measurements using the SSE discussed in Sec. 4.1.5. For Ce:YIG (111) we are able to detect a magnetooptic contrast in the polar MOKE configuration, as shown in Fig. 3.17b). The triangular shaped domain pattern hints to a uniaxial anisotropy in the sample, which seems to be partially oriented out-of-plane, allowing to obtain a contrast in this configuration. For a more comprehensive statement about the anisotropy of this sample, a full in- and out-of-plane magnetometry measurement would be required which is beyond the scope of our work.

With the presented work we are able to show that the Cerium substitution allows one to modify the magnetic and magnetooptic properties of YIG. Besides the enhanced total magnetic moment, one can also use Cerium to tailor the magnetic anisotropy, which presents a desirable opportunity for magnetooptic applications, such as sensors [167,168]. Furthermore, our results demonstrate that the magnetooptic Kerr effect is strongly enhanced by Ce-doping, thus enabling MOKE magnetometry measurements even at optical wavelengths, which is not possible for conventional YIG. This allows us to determine the magnetic domain structure by MOKE microscopy, which will be of further use for the study of thermally induced domain wall motion.

In this section we have shown the effect of a partial substitution of Yttrium by Cerium in YIG.

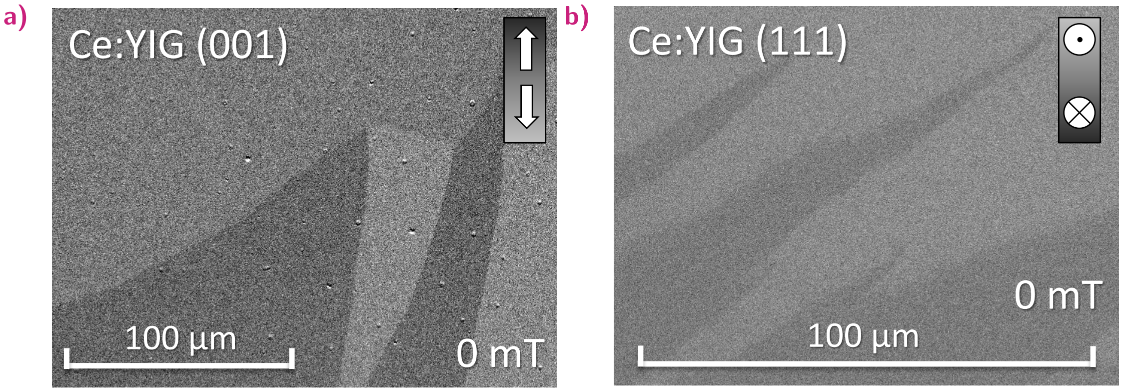

Fig. 3.17: a), b) MOKE microscopy images of both Ce:YIG samples. The picture presented in a) has been recorded in the longitudinal MOKE configuration and b) in the polar MOKE configuration.

In the following section we will show the outcome of a complete exchange of Yttrium by Gadolinium.

3.2.3 Gadolinium Iron Garnet

Despite its antiferromagnetic oriented two Fe sub-lattices, YIG possesses a net magnetization, which shows a roughly ferromagnetic temperature dependence [37]. By exchanging the Yttrium on the $\{c_3\}$ lattice site with Gadolinium one obtains a ferrimagnetic material ($Gd_3Fe_5O_{12}$, GIG). Bulk GIG maintains the Néel temperature at around $550\,K$ and shows a magnetic compensation point at $T_{comp} = 288\,K$ [37, 169, 170]. The complex temperature dependence of the magnetization enables us to study the influence of the competing interactions of the magnetic sub-lattices on the SSE. We will show in Sec. 5 that our temperature dependent SSE measurements in GIG reveal that the assumption of a simple correlation between the SSE and total magnetic lattices of the samples does not hold. Our analysis will show that only a model, which considers the magnetization as result of interacting magnetic sub-lattices can give a description of the observed behavior, pointing out its relevance for other SSE experiments.

In this section we will introduce the material and discuss its growth and optimization. We also present our results for temperature dependent magnetization measurements of the material, which reveal an unexpected influence of the film thickness on the magnetic compensation point.

As for YIG and Ce:YIG we grow our GIG films by PLD using a pressed powder target of $Gd_3Fe_5O_{12}$ stoichiometry. Compared to YIG we find a wider range of the oxygen pressure from 0.5 to 1×10^{-1} mbar allowing the growth of high quality films. For the deposition we use a $\sim 200\,K$ higher substrate temperature of $820\,°C$ and a lower laser pulse energy of $1\,J/cm^2$. The outcome is a slow growth rate of around 2000 pulses per unit cell at a target to substrate distance of 7 cm. An annealing step after the deposition does not change the magnetization, and only slightly decreases the lattice parameter, indicating that our GIG films, in contrast to YIG have no significant oxygen vacancies.

Using these deposition conditions we obtain an epitaxial film growth, indicated by the Laue fringes observed in the XRD scan. In Fig. 3.18 we present multiple XRD scans of the (004) reflex of GIG films of different thicknesses.

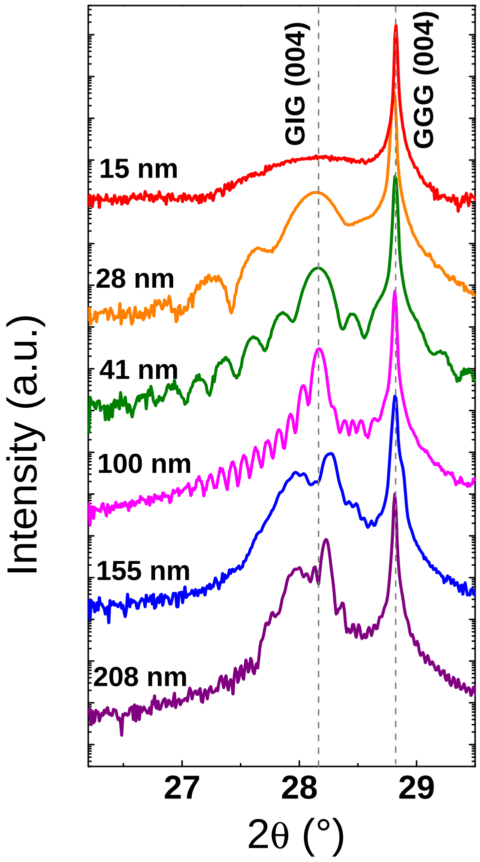

Fig. 3.18: $2\theta/\omega$ scans of GIG films with varying thickness grown on GGG (001) substrates.

The (004) GIG film peak for films thinner than $150\,\mathrm{nm}$ corresponds to an out-of-plane lattice constant of $1.2665\,\mathrm{nm}$, which is $\sim 0.02\,\mathrm{nm}$ larger than the literature value of $1.2472\,\mathrm{nm}$ [171]. Reciprocal space maps show a match with the GGG substrates, as shown for the (228) of GIG / GGG (001) in Fig. 3.19a).

This result illustrates that the GIG growth takes place under a compressive in-plane strain, causing a tetragonal distortion of the film. For samples thicker than $150\,\mathrm{nm}$ we can observe a shift of the out-of-plane lattice constant to smaller values of around $1.2635\,\mathrm{nm}$ indicating a relaxation of the film. Under the assumption of volume conservation the tetragonal growth on GGG, should lead to an out-of-plane lattice constant of $1.2652\,\mathrm{nm}$, using the bulk value for GIG and GGG. Our derived lattice constant agrees with this value within less than $0.2\,\%$, highlighting that an off stoichiometry of our samples is unlikely.

The presence of high concentration of oxygen vacancies can be excluded as an annealing

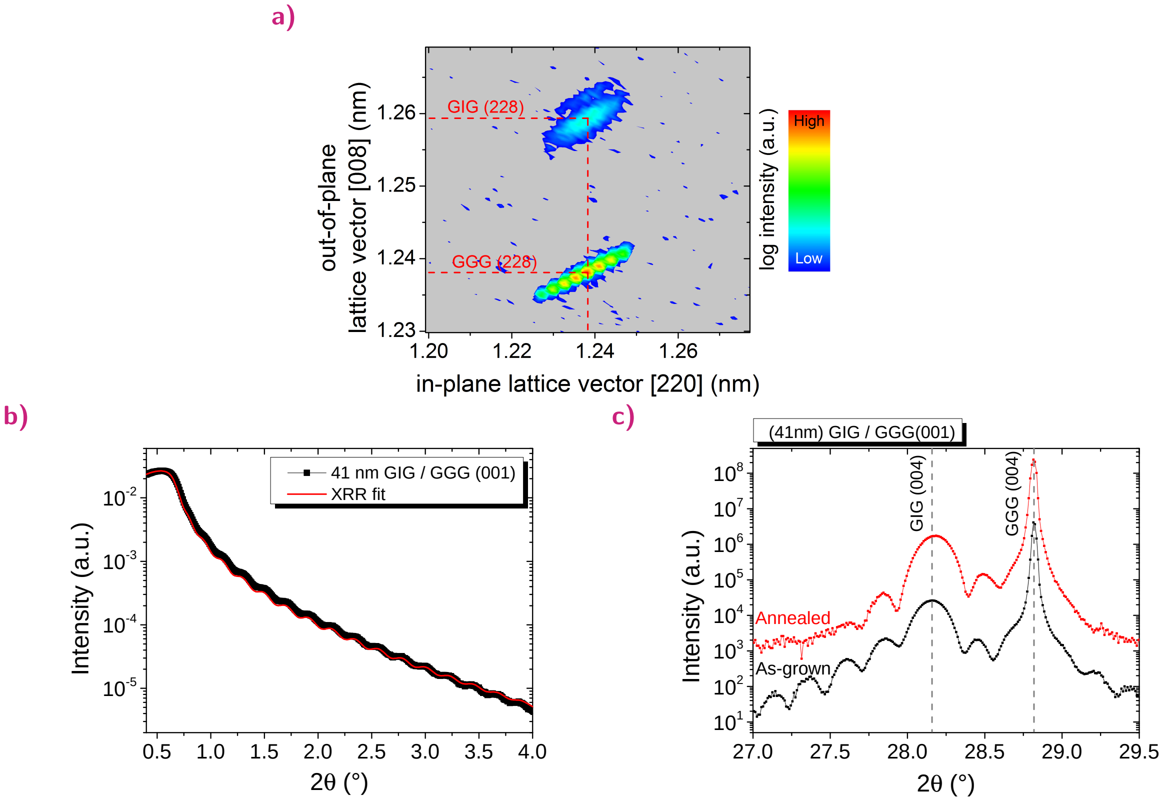

Fig. 3.19: a) RSM of a 41 nm thick GIG film grown a GGG (001) substrate. b) XRR measurement of a 41 nm thick GIG sample combined with a XRR fit using the material density of $Gd_3Fe_5O_{12}$. c) $2\theta/\omega$ scans of a 41 nm thick GIG film before and after annealing.

after the deposition at $950\,^\circ$ for 3 h shows only a small influence on the lattice constant, as shown in Fig. 3.19c). This description of the film stoichiometry will provide a background for the further analysis of the SQUID results.

From our XRR measurements, we can observe oscillations even for high angles, demonstrating the smooth surface of the film, which can be quantified by the fit to less than 0.5 nm roughness, similar to the other garnets. An example XRR measurement for a 41 nm thick GIG film is shown in Fig. 3.19b).

Next we will discuss the magnetic properties of the GIG. In contrast to Y^{3+}, Gd^{3+} possesses a magnetic moment, due to the partially filled $4f^7$ shell. In contrast to Ce^{3+} the Gd^{3+} ions are antiferromagneticlly oriented to the Fe^{3+} on the d-lattice site and only weakly exchange coupled to the Fe^{3+} on the a-side [172]. At room temperature this leads to a reduction of the total magnetic moment, as shown in the SQUID measurement of Fig. 3.20a). For 300 K we obtain a saturation magnetization of around 28kA/m $\pm$ 4kA/m. As we decrease the temperature also the saturation moment decreases, with a minimum at 145 K. We identify this temperature as the compensation point T_{comp} of the material, where the net magnetization of the sample vanishes for bulk material. For our thin films the signal to noise ratio is influenced by the background signal of the GGG substrate, which at this temperatures is three orders of magnitude larger than the film's contribution. Due to the strong temperature dependence of the GGG signal, even a small drift in temperature of $0.1\,\mathrm{K}$ leads to a large change in moment compared to the absolute moment of the GIG film. At temperatures lower than the magnetic compensation point M_s increases again, as shown in Fig. 3.20b) where we plot the extracted M_s values as a function of the temperature.

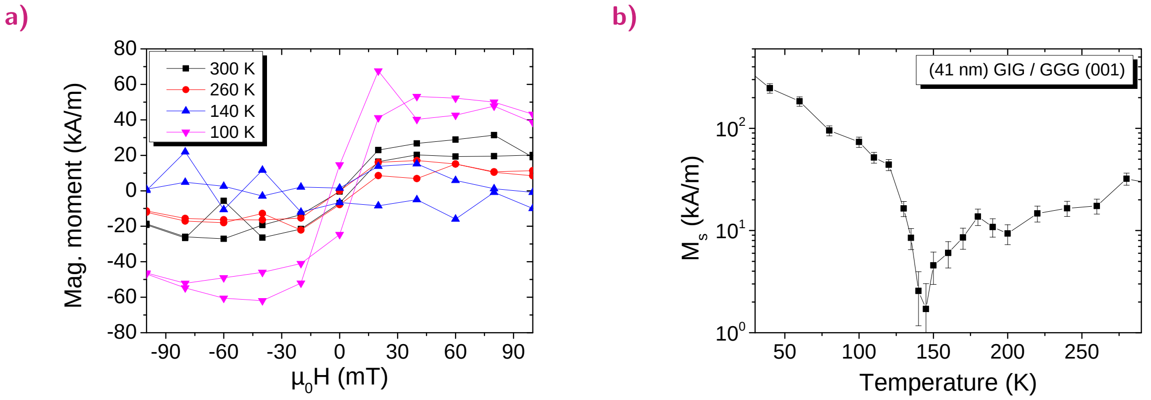

Fig. 3.20: a) SQUID hysteresis measurements for a $53\,\mathrm{nm}$ thick GIG/GGG(001) sample at different temperatures. b) Saturation magnetization M_s as a function of temperature.

In order to understand the temperature dependence we have to take an independent look at the three magnetic sub-lattices, illustrated in Fig. 3.21. For high temperatures $T >> T_{comp}$ the net magnetic moment is dominated by the two Fe^{3+} sub-lattices, leading to a Néel temperature ($T_N = 556\,\mathrm{K}$) similar to the Curie temperature ($T_{Curie} = 551\,\mathrm{K}$) of the YIG. Decreasing the temperature increases the magnetic moment of the Gd^{3+} ions [172].

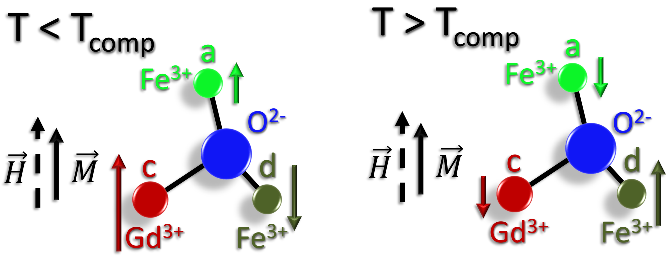

Fig. 3.21: Illustration of the three magnetic sub-lattices in GIG for $T < T_{comp}$ and $T > T_{comp}$. The picture shows the magnetization $\vec{M}$ in the presence of a finite external magnetic field $\vec{H}$.

At a certain temperature the combination of the parallel oriented Gd^{3+} and Fe^{3+} on the a lattice site equals the magnetic moment of the Fe^{3+} ions on the d-site. At this temperature, the compensation temperature (T_{comp}), the magnetic moments compensate one another, leading to a total magnetic moment of zero for the whole material. By decreasing the temperature further the total magnetic moment is dominated by the Gd on the c- and the Fe on the a-lattice, leading to an inversion of the magnetization of GIG [169, 172]. In a finite magnetic field, magnetic moments of the material have to reorient as the material itself maintains its ferromagnetic coupling, indicated in Fig.3.21 for $T > T_{comp}$ and $T < T_{comp}$. A further decrease of the temperature causes an increase of the magnetic moment beyond the one of YIG. This increase indicates that the main contribution to the magnetization at low temperatures is given by the magnetization of Gd^{3+}.

In our thin film samples we find a dependence of the magnetic compensation on the thickness of the GIG film and deposition conditions. The compensation point is at lower temperatures than the reported literature value of $288\,\mathrm{K}$ for bulk material [169–171]. Fig. 3.22a) shows an example for three different samples with varying GIG thickness. The SQUID measurements indicate a shift of the compensation towards the bulk value the thicker the GIG films are. Furthermore the T_{comp} can be influenced by the oxygen pressure during the deposition, with higher pressures leading to increased T_{comp} for the identical thickness (see Fig. 5.6a)). From our x-ray analysis we can conclude that only a negligible amount of oxygen deficiency is present for films deposited at lower pressures, as an additional annealing of the sample showed only a minor influence on the out-of-plane lattice constant 3.19c). The presence or lack of oxygen is a crucial property of magnetic garnets, since the orbital superexchange of the Fe^{3+} and Gd^{3+} over the O^{2-} ions determines the magnetic properties of these materials. To strengthen our conjecture of a negligible difference in the oxygen concentration between both deposition pressures, we compare the magnetization of a sample deposited at a lower oxygen pressure before and after the annealing. The corresponding SQUID magnetometry measurements are shown in Fig. 3.22b). This direct comparison of T_{comp} reveals no influence of the annealing within the resolution of our measurement. Since the difference for T_{comp} between both deposition pressures marks $100\,\mathrm{K}$ for these film thicknesses (see Fig. 5.5), the origin cannot be the amount of oxygen within the samples.

Taking the tetragonal distortion into account, we assume that the lattice expansion in the out-of-plane direction causes a finite size effect combined with a slight off-stoichiometry of Gd$_{3-x}$ and Fe$_{5-y}$. Both effects in combination might lead to the observed behavior, although studies of the influence of strain on the compensation point in GIG are yet to be

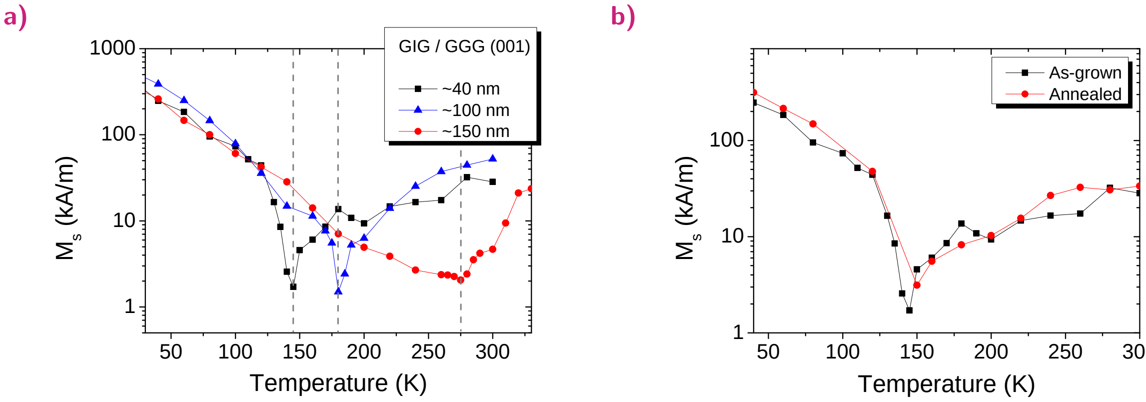

Fig. 3.22: a) SQUID magnetization measurements for three different GIG/GGG samples with different film thicknesses. b) SQUID hysteresis before and after the annealing of the sample.

done. It is known that a Nd doping leads to a reduction of the compensation point in bulk material [171], which is comparable to our assumption of a small off stoichiometry. For our thin films we can verify a lack of Fe by probing the Néel temperature for the films, where a reduced Fe concentration will lead to a deviation from the literature value. Currently we have not probed the stoichiometry of the Gd concentration. Our usually used energy-dispersive x-ray spectroscopy (EDX) has a probing depth in the range of 2 μm, meaning that we also measure the $Gd_3Ga_5O_{12}$ substrate.

Although we cannot fully explain the origin of the thickness dependence of the compensation temperature, this behavior offers a unique possibility for our SSE measurements, as it allows us verify the correlation between the magnetic compensation point and the SSE, shown in in Sec. 5.

3.3 Conclusion of the materials development

In this chapter we presented our work on the growth, the characterization and optimization of magnetic, insulating garnets by PLD. In collaboration with the group of Prof. Ross at MIT we investigated the deposition of epitaxial YIG thin films and presented optimized growth parameters. As a result we were able to deposit samples with identical magnetostatic and magnetodynamic properties independent of the thickness of the thin film. Furthermore the investigated samples possess a high crystalline quality and bulk like magnetostatic properties in addition to Gilbert damping values in line with the best reported films in literature. Our results on the investigation and growth of epitaxial Ce:YIG thin films have shown that the substitution by Cerium enhances the magnetic anisotropy. Furthermore MOKE measurements carried out by T. Kuschel from the University of Bielefeld revealed that the magnetooptic Kerr effect is enhanced by a factor of 20 compared to YIG at optical wavelengths. Both properties are desirable for future spintronic applications and will be of use for further research in the field of spin caloritronics. In the last part of this chapter we presented a detailed study of the growth of GIG, which exhibits as the bulk material a magnetic compensation point. Like the other garnets, our by PLD grown GIG thin films show a high crystalline quality in addition to a smooth interface, which is important for the reproducibility of our spin caloritronic experiments. SQUID magnetometry finds a thickness and deposition pressure dependence of the compensation point.

The knowledge about the thickness independence of the magnetic material parameters of YIG enables us to study the SSE as a function of the film thickness in order to investigate its origin in the following chapter.

4

Spin Seebeck effect in Yttrium Iron Garnet

In the last chapter we introduced the insulating magnetic garnets, which provide an ideal material for the investigation of the magnonic origin of the SSE. YIG represents one of the most simple material combinations for magnetic garnets, as it can be sufficiently described by a simplified ferromagnetic model, which allows us to explain basic principles of the SSE. Its insulating properties furthermore allow us to neglect contributions of the Nernst effects caused by the material itself and to focus on the magnonic picture, which will be used to explain the observed experiential dependences.

In the beginning of this chapter we will explain the measurement principles of the SSE and influences on the signals, which can solely arise caused by the setup and not the effect. Following the measurement methods, we will introduce the basic dependences of the SSE on the magnetic field and the applied temperature gradient in Sec. 4.1. Afterwards a detailed analysis of the low magnetic field dependence of the SSE will demonstrate that the effect can be used as a novel probing tool for the magnetic anisotropy of the emitting ferromagnet. In Sec. 4.1.5 we will explain this application based on several examples.

Having established the basic principles of the SSE, we present studies probing more complex dependences of the effect, which enables us to test the concepts of its magnonic origin. A main result of this thesis is the observed dependence of the SSE on the thickness of the emitting ferromagnet, shown in Sec. 4.2. Experimentally we derive a finite length scale of the SSE, which we explain solely by using a atomistic magnetic model (see Sec. 2.4.3). From this, we derive the conclusion that the effect is based on magnons from the bulk of the ferromagnetic material. To exclude further influences by other sources like the interface or material variation, we present a comprehensive analysis of the corresponding material and interface parameter.

To extend our understanding of the effect and to further test the magnonic concept, we probe the SSE as a function of temperature in Sec. 4.3. Our results highlight that the so far established model of the magnon-phonon drag cannot give sufficient description of the observed behavior. Based on the magnonic origin we discuss other possible mechanisms. The last part of the chapter illustrates the high magnetic field suppression of the SSE (Sec. 4.4), which as well as the other found dependences must originate from a magnonic origin.

4.1 Principles of the SSE and application as a probing tool for the sample magnetization

So far, the SSE has only been described as an thermoelectric effect which leads to the excitation of a spin current detected by the ISHE. In the following sections we present a more detailed picture of the SSE, using the later derived magnonic model to explain the observed dependences on the sample magnetization and the applied temperature gradient. Since these measurements require a detailed knowledge about the used experimental setups to exclude contributions of parasitic effects, we will first give an introduction to the used setups and measurement principles of the SSE. The explanation of the two different measurement geometries used will additionally highlight that the LSSE geometry presents a more robust and reliable measurement geometry for the effect. Using this geometry we will show, that it is possible to use the SSE to investigate the magnetic anisotropy of the sample itself. The last part of this section addresses the difficulty in determining an absolute value for the SSE and comparing the effect in different setups, which relies on the knowledge of the actual temperature gradient applied to the YIG layer. We will present our approach to solve this problematic topic and derive the order of magnitude of the absolute SSE signal.

4.1.1 Measurement concepts for the spin Seebeck effect

Measurement geometries for the SSE can be divided into two basic concepts. The first concept is the so called transverse spin Seebeck effect (TSSE) [7]. In this geometry the temperature gradient is applied along the ferromagnetic layer, which leads to an excitation of a spin current [101], as shown in Fig. 2.13b). In order to generate an in-plane temperature gradient, the sample needs to be mounted at its edges so one side can be heated while the other one is cooled. To generate only an in-plane temperature gradient without contributions from an out-of-plane gradient has proven to be hard to achieve experimentally. This is of major importance as an out-of-plane temperature gradient will lead to the generation of signals by the ANE in metallic systems (see Sec. 2.1.4) or to contributions by the LSSE in the case of insulators [110]. Both additional effects cannot be distinguished from the TSSE in this geometry. Systematic studies of the TSSE have shown that a small misalignment of the sample can lead to noticeable changes in the signal due to the formation of an out-of-plane temperature gradient [91, 92]. Another source for an out-of-plane gradient is the mismatch between thermal conductivity of the substrate and the thin ferromagnetic film. As the substrate is usually four orders of magnitude thicker ($\sim 500\,\mu\mathrm{m}$) than the ferromagnetic layer ($\sim 50\,\mathrm{nm}$), its thermal conductivity is dominating the thermal flow of the setup [30, 31]. A large contrast in the thermal conductivity, will cause the ferromagnetic layer at the surface to either function as a heat sink or as an thermal insulator. Both lead to the formation of an out-of-plane gradient [91]. Another source for an unintentional temperature gradient [93] is temperature difference between sample and environment, which is of most relevance for setups operating in cryostat using a He-flow cooling. The situation of thermal mismatch of substrate and film, as well as temperature difference with the environment, are illustrated in Fig. 4.1a).

If we now only consider the case of an in-plane temperature gradient, the thermal excitation is meant to generate a spin current $\vec{J}_s$, which partially diffuses into the detection layer at the surface of the ferromagnet. The detection layer consists of a nonmagnetic material with a spin Hall angle, for which Pt is very well known (see also Sec. 2.3.2). The Pt layer is structured into stripes oriented perpendicular to the temperature gradient, in order to avoid influences of the position dependence of the TSSE. An external magnetic field $\vec{H}_{\mathrm{ext}}$ needs to be applied in-plane to align the magnetization of the sample. Similar to the thermal gradient, a misalignment or inhomogeneity of the magnetic field with small out-of-plane components will cause contributions by the ANE.

The above mentioned experimental challenges, as well as the current interpretation of the SSE as a magnonic effect, led to the decision to investigate the SSE only in magnetic insulators in the more robust longitudinal geometry. Furthermore the experimentally found issues raised the question, if the experiments of the TSSE might actually be measurements of the LSSE in a non-local geometry [110] (see Sec. 2.4.2).

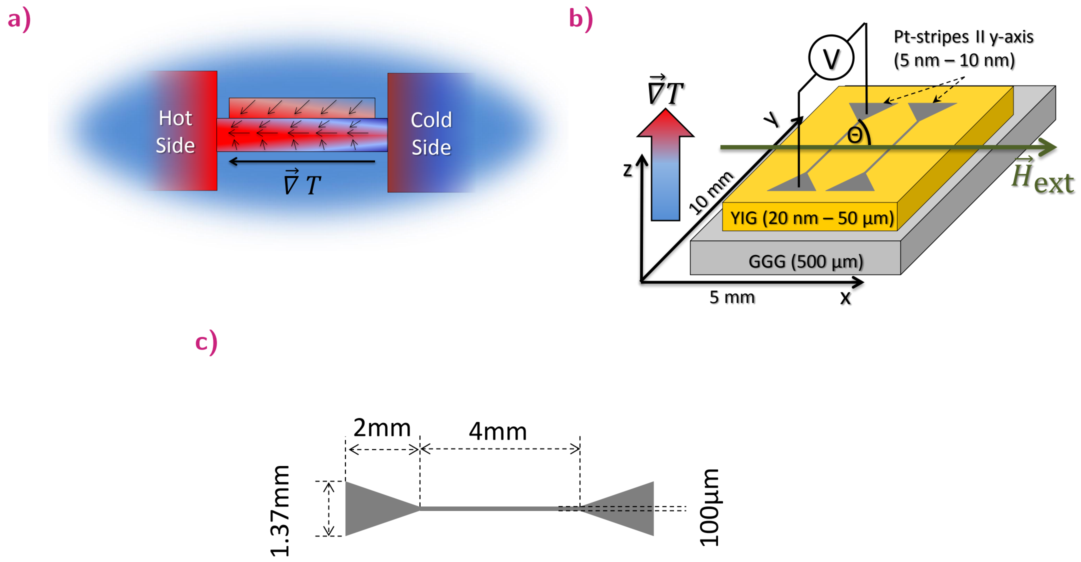

Fig. 4.1: a) Sketch of the out-of-plane temperature gradients generated by the environment or mismatch in the thermal conductivity. The arrows indicate by this mechanism caused additional components of the thermal gradient in film and substrate. b) Illustration of the measurement concept of the longitudinal SSE. c) Technical drawing of a Pt stripe used for the detection of the SSE.

The so called longitudinal geometry [97] makes use of an out-of-plane temperature gradient. While in the transverse geometry the direction of the spin current is still under discussion, the situation is simpler for the LSSE. The thermally generated magnon flow is considered to be antiparallel to the temperature gradient and thus parallel to the heat flow of the phonons within the system, as depicted in Fig. 4.1b). In this simple picture the thermal magnons are directly pumped into the detection layer. As the ISHE signal scales linearly with the length of the detection layer (Sec. 2.3.2), also the SSE signal can be enhanced by a simple increase of one dimension of the sample size. In all following experiments we use a sample size of $5\,\mathrm{mm} \times 10\,\mathrm{mm}$, with the two Pt stripes structured in parallel to the long side of the sample. Fig. 4.1b) shows an illustration. Sec. 3.1 gives a further description of the deposition of the YIG and Pt detection layer. Each Pt stripe has a width of $100\,\mu\mathrm{m}$ and a length of $4\,\mathrm{mm}$ with a triangular shaped contact pad at the end of the stripe, as shown in Fig. 4.1c). Two separate detection stripes allow us to control the heat flow within the setup, the interface preparation and homogeneity of the sample, since a difference in the signal amplitude between both stripes is caused by one of the listed effects. The usage of stripes facilitates the alignment of the voltage contacts with respect to the external magnetic field $\vec{H}_{\mathrm{ext}}$.

Having established the fundamentals necessary to detect the SSE, we will introduce the measurement setup, which was designed and constructed to perform room temperature measurements of the longitudinal SSE.

4.1.2 Room temperature measurement setup for the longitudinal SSE

One challenge of the measurement concept for the LSSE is to allow a four point measurement of the Pt stripes, while having an effective heat flow through the sample. Furthermore the heat flow needs to be invertible in order to validate basic features of the SSE. Figure 4.1b) presents the concept of the LSSE, while Fig. 4.2a) illustrates the basic components of the room temperature setup, that are necessary to understand the working principle of the design.

To allow an out-of-plane uniform heat flow through the sample, it is sandwiched in between two copper blocks, which can be heated and cooled independently. The cooling is achieved via mechanical connection of the copper blocks to the surrounding poles of a water cooled magnet, while a cartridge heater ($25\,\mathrm{W}$) embedded in each block is used for heating. Pt-100 elements attached to each copper block provide an accurate temperature measurement, which are read by Lakeshore 330 controllers that regulate the power of the cartridge heaters to drive the temperature of the system. As the cooling of the setup is provided by the water cooling of the magnet, the lower temperature of the system is given by the temperature of the cooling water, and stabilized by the heater. $500\,\mu\mathrm{m}$ thick sapphire substrates above and below the sample insulate the copper blocks electrically from the sample and provide a smooth surface for mounting. Additionally, thermal conductive tape or thermal grease is used to compensate misalignments occurring from the assembly and to reduce damage of Pt stripes due to mechanical contact of the sample surface. As the thermal conductivity across the whole stack is very sensitive to the applied pressure while mounting, the complete setup is pressed together by four springs to guarantee reproducible conditions, as shown in Fig. 4.2b). Depending on the sample size the setup can generate a stable temperature difference of up to 15 K between the copper blocks. Higher temperature differences are inefficient and hard to control, due to the thermal connection of the brass rods between the top and bottom block, which act as a thermal shortcut. This temperature difference is used as a reference for the system and for the calculation of the spin Seebeck coefficient in Sec. 4.2. The actual temperature difference generated through the YIG film is expected to be smaller and is discussed in detail in Sec. 4.1.6

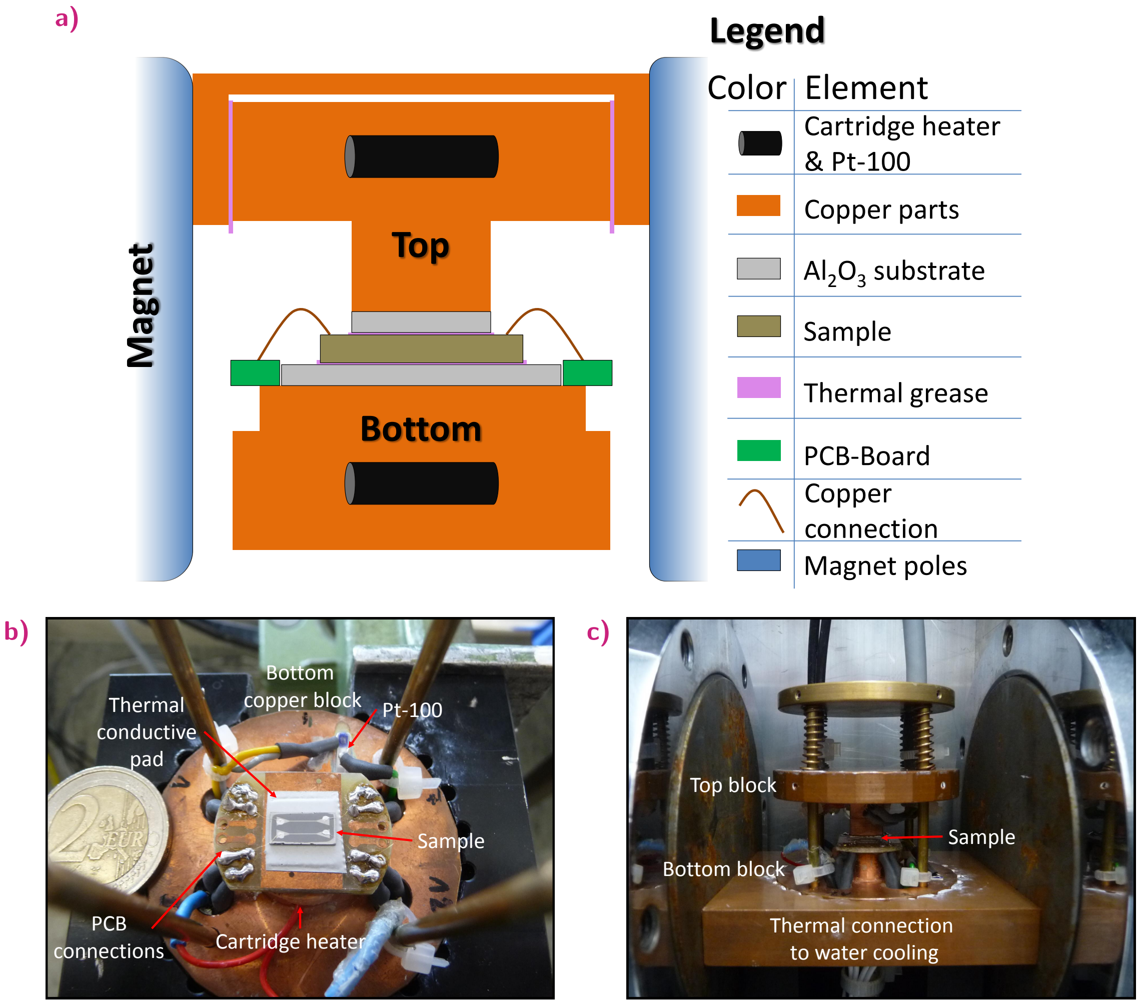

Fig. 4.2: a) Concept sketch of the setup for LSSE at room temperature. b) Picture of a 50 µm thick YIG film with two connected Pt stripes on the bottom block. c) Picture of the mounted setup attached to the magnet.

The mechanical connection with the water cooled magnet does not only provide the heat sink for the system but also serves as an alignment of the setup with respect to the external magnetic field. Using guiding grooves it is possible to rotate the setup in-plane in reproducible 15 ° steps, which allows one to identify the in-plane dependency of the SSE and the magnetic anisotropy of the samples, discussed in Sec. 4.1.4. As indicated in Fig. 4.1b), Θ denotes the in-plane angle between the Pt stripes and the external magnetic field $\vec{H}_{\text{ext}}$. $0\,°$ marks parallel and $90\,°$ perpendicular in-plane alignment of external magnetic field with the Pt stripes, respectively.

A PCB, mounted on the lower half of the sample holder, allows for contacting of up to twelve coaxial connections. For this purpose copper wires are soldered on the board, while the contact to the Pt pads is established with conductive Silver epoxy glue. As shown in Fig. 4.1b) and Fig. 4.2b), a two terminal configuration is used to detect the thermally generated voltage with a Keithley 2182a nanovoltmeter. For all shown resistances a four terminal measurement is performed using a Keithley 2400 sourcemeter, unless indicated otherwise. All devices are computer controlled via VEE HP Lab programs, which provide an automatic measurement scheme for the MR and the SSE at selectable magnetic field strengths and temperature differences.

4.1.3 Dependence of SSE on applied temperature differences

As a thermally driven effect the SSE shows a characteristic dependency on the applied temperature difference of the system and is not existing if the sample is in thermal equilibrium. Using a standard measurement procedure for the SSE, we will give examples for these key characteristics.

In the case of the room temperature setup a stable temperature difference between the two copper blocks and thus over the sample is generated by heating one and cooling the other copper block. When the temperature difference is stable within a range of $5\,\text{mK}$ the external magnetic field is swept in both field directions, until a saturation of the thermal voltage signal can be observed. As a consequence the obtained signal shows a hysteresis like shape, as shown in Fig 4.3a) for a temperature difference of $\Delta T = 11\,\text{K}$. The hysteresis shape of the signal already points towards a correlation between the SSE and the magnetization of the sample, which will be explained in Sec. 4.1.5. For now we will first discuss the origin of the saturated signals. The shown measurements were carried out using a $200\,\text{nm}$ thick YIG sample and perpendicular in-plane orientation between the external magnetic field and the voltage contacts ($\Theta = 90\,°, 270\,°$). For this alignment, the SSE obtains a maximal voltage in saturation of the sample, as will be explained in detail in Sec. 4.1.4. The ISHE-voltage (V_{ISHE}) generated by the SSE is defined as

$$V_{\text{ISHE}} = \Delta V/2, \tag{4.1}$$

where ΔV denotes the difference between the signal amplitude measured in saturation of the signal for both magnetic field directions, as indicated in Fig. 4.3a). The measurement measured voltage has a constant offset of $\sim 150\,\text{nV}$. This voltage can have several origins.

As different metals are used to contact the sample, a conventional SE can be generated by temperature differences along the two point connections. The second source can be a small offset voltage in the electrical ground connection of the setup, which serves as a reference for the voltmeter. The third source can be the calibration of the Keithley 2182A itself. In order not to measure a thermal offset voltage generated by the device itself, a calibration measurement at a stable room temperature is needed. Any difference in room temperature between the time of calibration and measurement causes an offset. Since an offset is independent on the magnetic field, it is not related to the signals originating from the SSE and can be neglected. If present, any offset of this kind was subtracted from the data, which has no influence on ΔV.

If we now probe the SSE as a function of ΔT applied to the system, we observe a linear increase of the signal difference ΔV. Fig. 4.3b) shows six measurements for different temperature differences. The measurements show that the signal strength is increasing with increasing temperature difference and vanishes at zero temperature difference of the setup. A key feature of an ISHE-signal is its sensitivity to the direction of the converted spin current $\vec{J}_s$ (see eq. 2.24). If the propagation direction of the spin current changes from parallel to antiparallel, the detected ISHE-voltage should also change sign. In the case of the thermally excited spin currents of the SSE, this situation resembles the inversion of the thermal gradient.

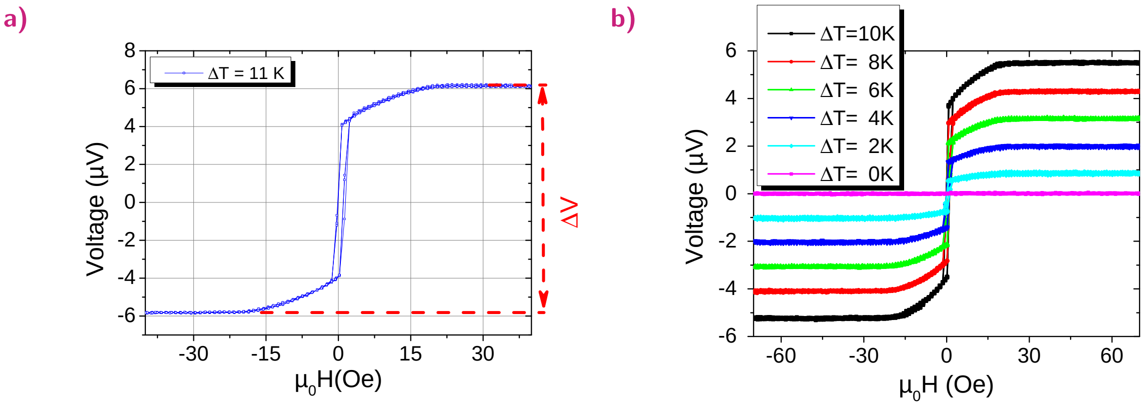

Fig. 4.3: a) Thermally generated voltage as a function of the applied external magnetic field, example for an SSE hysteresis measurement. The signals that can be attributed to the SSE have been marked by ΔV. b) SSE hysteresis loops for six different temperature differences between the copper blocks. Each color represents one stable temperature difference. The measurements were performed for $\Theta = 90\,^\circ$ and with the hotter block above the sample. All signals have been measured on the same sample (Pt($8.5\,\mathrm{nm}$)/YIG($200\,\mathrm{nm}$) grown on a GGG(001) substrate).

To understand this behavior we make use of the magnonic model [13] for the SSE, which identifies thermally excited magnons as the spin current. At finite temperatures, thermal magnons are generated in every part of the ferromagnetic layer and diffuse randomly. The higher the temperature the higher is the number of thermally excited magnons (See Sec. 2.2.4). If a temperature gradient is applied over a ferromagnet, the magnon density will be higher in the hotter part, leading to a diffusion of the majority of the thermally excited magnons from the hotter to the colder part. This diffusion thus defines the direction of the thermal spin current $\vec{J}_\mathrm{s}$, which is antiparallel to the temperature gradient $\vec{\nabla}T$. The dependence derived from the magnonic model [13] agrees with expectations based on the energy equilibrium picture [13] and matches the concept of a macrospin model, which only assumes a magnonic origin [12,66,101]. Using the idea of thermally excited magnons it is now easy to understand, why an inversion of the temperature gradient then also leads to an inversion of the SSE signal, as shown in Fig. 4.4a).

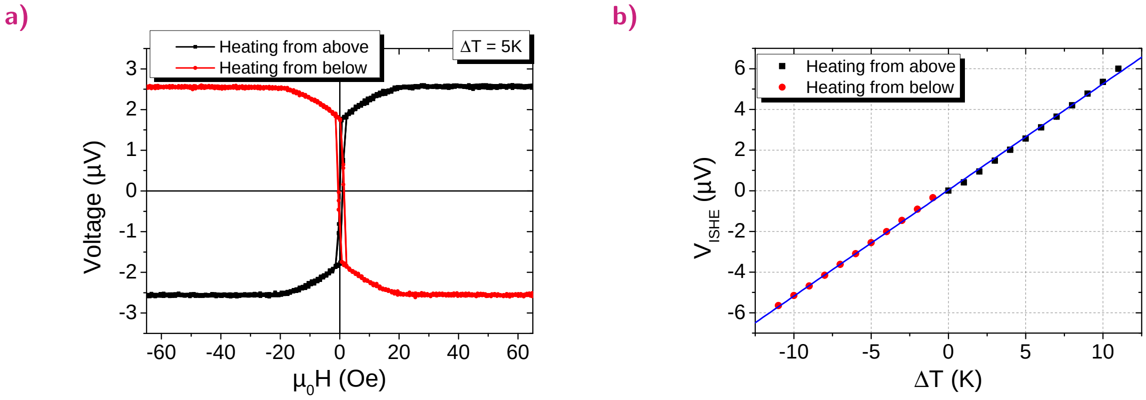

Fig. 4.4: a) Two SSE hysteresis for parallel and antiparallel heat flow, using a temperature difference of $5\,\mathrm{K}$. b) SSE voltage for each used temperature difference, for both direction of the thermal gradient. The blue function indicates the linear fitting function of $y = 0.037 + 0.52 * x$. All signals have been measured on the same sample (Pt($8.5\,\mathrm{nm}$)/YIG($200\,\mathrm{nm}$) grown on a GGG(001) substrate).

If one now plots the extracted ISHE-voltage of the SSE as a function of the applied temperature difference, one obtains a linear dependency between the signal amplitude and the temperature difference of the system, as shown in Fig. 4.4b). This dependency can be described by

$$V(\Delta T)_\mathrm{ISHE} = a_\mathrm{SSC}\Delta T + \Delta T_0, \tag{4.2}$$

where the slope a_SSC defines the spin Seebeck coefficient (SSC). It describes the thermal voltage generated per degree of temperature difference ΔT in the out-of-plane direction and thus represents the efficiency of the SSE. The intercept ΔT_0 marks the quality of the setup, as a non zero value indicates a systematic error in the temperature calibration of the setup. For the shown $200\,\mathrm{nm}$ thick YIG sample with a Pt detection layer of $8.5\,\mathrm{nm}$, the linear fit yields an SSC of $0.522\,\mu\mathrm{V/K} \pm 0.003\,\mu\mathrm{V/K}$ and an intercept of $0.04\,\mu\mathrm{V} \pm 0.02\,\mu\mathrm{V}$. The obtained value for the SSC is in line with SSE measurements reported by other groups [8,88,97,106,111]. The intercept value indicates a small and compared to the SSC signal negligible error in the system, either due to a small deviation in the calibration between the two used thermocouples or a small deviation between the parallel and antiparallel case for the heat flow in the out-of-plane direction. The SSC shows that the setup as well as our sample fabrication and preparation yield SSE signals of the same magnitude compared to measurements of other groups [11,104,111] using similar setups and samples. In Sec. 4.1.6 we explain the challenges of a direct comparison of the SSE signals obtained by different setups.

It is interesting to note at this point, that the found linear correlation for the SSE and the temperature difference applied to the setup is not obvious. Other experiments using different heating methods and therefore different scaling values, like the applied heating power of the Laser [111], or the power of the heating current [173] to calculate the SSC, derive the same linear dependence. Up to now no deviation from this linear behavior could be observed, even at low temperatures, as shown in Sec. 4.3. Based on the theory of a magnonic excitation, one would expect a deviation from this behavior, for high temperature differences $\Delta T > 50\,\mathrm{K}$ or measurements of the SSC close to the Curie temperature [174]. These deviations are expected since the amount of thermally created magnons follows the Bose Einstein distribution of exchange magnons, which have the dispersion relation $\propto k^2$ (see eq. 2.21). Therefore we assume that the linear increase only represents an good approximation for small ΔT, while for higher ΔT we expect an deviation from this behavior.

4.1.4 Low magnetic field dependence

Each thermal magnon carries a certain angular momentum and hence a polarization $\vec{\sigma}$ obtained by the emitting ferromagnetic lattice. Due to the momentum conservation, the polarization of the momentum of the magnon is negative with respect to the lattice momentum. As the magnetization of the sample switches by inverting the magnetic field, also the polarization $\vec{\sigma}$ of the magnons is inverted and the thermal voltage switches as seen in the SSE hysteresis loops in Fig. 4.5a). Furthermore the detection mechanism of the ISHE is sensitive to the angle Θ between the polarization vector $\vec{\sigma}$ (for magnetic fields high enough to saturate the magnetization of the film) and the voltage contacts $\vec{E}_{\mathrm{ISHE}}$, as defined in eq. 2.24. The highest signal amplitude is measured for a perpendicular alignment of the voltage contacts (Pt stripe) with respect to the external magnetic field ($\Theta = 90\,°$). Since the electric field vector $\vec{E}_{\mathrm{ISHE}}$ follows the polarization of the spin current and thus the orientation of the external field, a deflection from $90\,°$ causes a weaker signal. Fig. 4.5a) shows this dependence. It can be seen that the measurements for a smaller angle between the field and the Pt stripes yield a smaller saturated signal amplitude above $50\,\mathrm{Oe}$. In agreement with the assumption of a signal caused by a spin current converted by the ISHE, we detect a minimal signal for parallel alignment of Pt stripe and magnetic field ($\Theta = 0\,°$). The cross product correlation between the spin current $\vec{J}_s$ and its polarization vector $\vec{\sigma}$ (see also Sec. 2.3.2) leads to an inversion of the signal when the sample is rotated by $180\,°$ in-plane. Fig. 4.5b) shows an example for this case. The complete in-plane angular dependency of the V_{ISHE} for a fixed temperature gradient is shown in Fig. 4.5c). Each data point represents a complete SSE hysteresis measurement. The signals follow the expected sinusoidal behavior based on the assumption of a converted spin current detected by the ISHE.

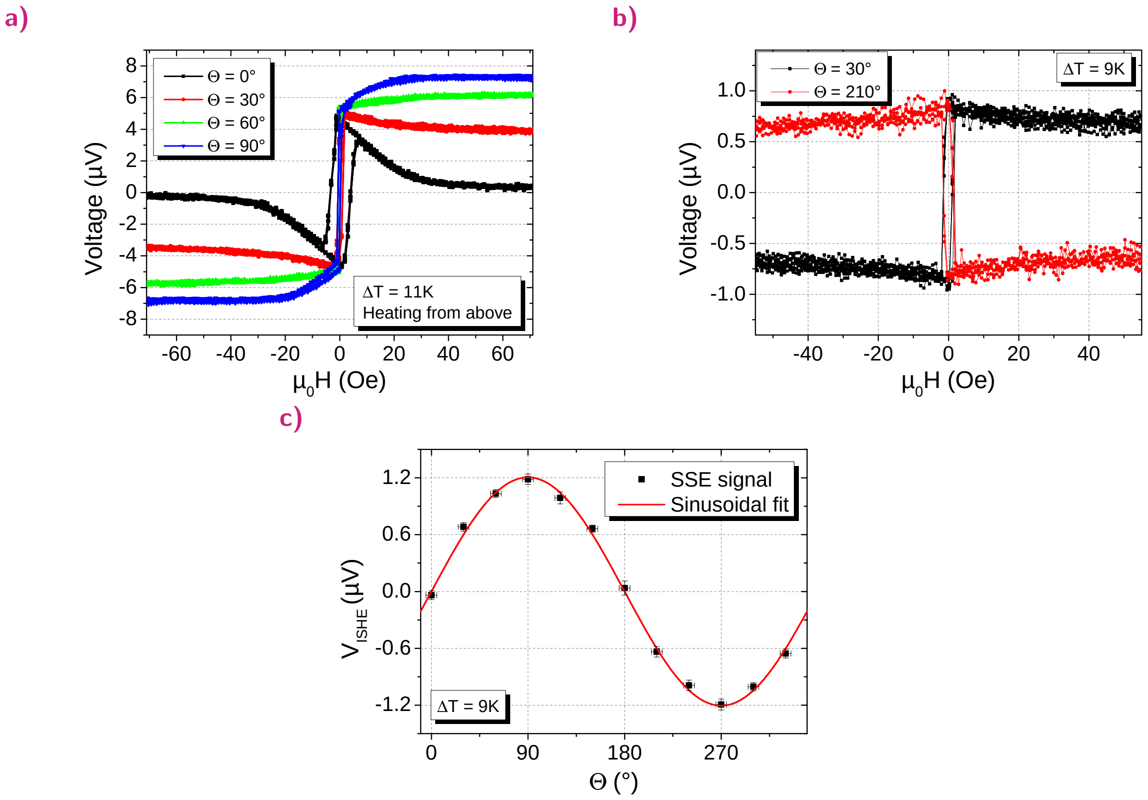

Fig. 4.5: Illustration of the magnetic field angle dependency of the SSE. a) SSE measurements for four different in-plane orientations of the sample (Pt($8.5\,$nm)/YIG($200\,$nm) grown on a GGG(001) substrate). b) SSE hysteresis measurements for $30\,^\circ$ and $210\,^\circ$, highlighting the signal inversion resulting of an in-plane sample rotation by $180\,^\circ$. c) V_{ISHE} as a function of the in-plane angle between the voltage contacts and the external magnetic field. b) and c) have been measured on the same sample (Pt ($8\,$nm)/YIG ($300\,$nm) grown on a GGG(001) substrate).

4.1.5 Probing the sample magnetization

Up to now we have only discussed the behavior of the SSE signals for magnetic fields high enough to align all magnetic domains of the ferromagnetic layer for which the SSE generates a constant signal. In the following we will show that the SSE can be used as a magnetometry method to probe the magnetic anisotropy of a sample by investigating the low field behavior of the SSE signals, which is subject of the publication [p4]. In the magnonic SSE picture, this feature results of the spin polarization $\vec{\sigma}$ of the thermally excited magnons that follow the orientation of the magnetization of the emitting ferromagnet (see Sec. 4.1.4). Thus the field and angle dependence of the SSE signals below the saturation field can be used to probe the magnetization of the sample. Like for magnetometry measurements different characteristic fields can be determined from hysteresis measurements and used to determine the rotational symmetry and thus magnetic anisotropy of the sample.

First we will use the SSE signal at zero external field S_R to illustrate its dependence on the sample magnetization, indicate in Fig. 4.6a). Coming from the saturated state, the magnetization of the sample will partially relax to the magnetic easy axes zero external magnetic field and form a multidomain state, depending on the direction of the saturated state. YIG marks a special material, since it is a very soft magnetic material with a coercive field of only a few Oe [37]. Thus the magnetization has to overcome no higher energy to partially relax to easy axis, which enables us to interpret SSE signals S_R at zero magnetic field to give an estimation for alignment of the easy axes of the sample.

As an example we will discuss the properties of the $300\,\mathrm{nm}$ thick YIG shown in Fig. 4.6a). Independently from the in-plane angle Θ, the amplitude of the S_R yields a non-zero value of $S_R = 0.88\,\mu\mathrm{V} \pm 0.06\,\mu\mathrm{V}$. Considering a simple model for the magnetization (see Fig. 2.7), one would expect a minimum for S_R in an angular range of $90\,^\circ$ induced by either a uniaxial or cubic anisotropy. The observed behavior therefore indicates the decay of the magnetization into a multidomain state at zero field. Within the resolution of our measurement we cannot determine a clear minimum in the an angular range from $\Theta = 0\,^\circ$ to $\Theta = 90\,^\circ$, which would hint to a cubic or similar anisotropy. By comparing the value of S_R with the value measured for the saturated signal at high fields, one can estimate the orientation of the remanent magnetization with respect to the Pt stripes. The complete in-plane angle scan of this sample is shown in Fig. 4.5c), and has been recorded for the same temperature difference as the data in Fig. 4.6a). Using the sinusoidal fit that has been used to highlight the angular dependence of the data, we obtain an angle of $\Theta = 47\,^\circ \pm 3\,^\circ$, yielding the same signal amplitude as the remanent state. The value $\Theta = 45\,^\circ$ corresponds to the in-plane lattice vector of $\langle 110 \rangle$, as the YIG film is grown on a GGG (001) substrate with primitive cubic axes along the edges of the sample ($\Theta = 0\,^\circ$ corresponds to $\langle 100 \rangle$). It has been shown in Sec. 3.2.1 that magnetic garnets in general possess a cubic magnetic anisotropy along the $\langle 111 \rangle$ axes [37]. In particular it is expected for thin film samples, that the additional shape anisotropy causes the cubic anisotropy to favor an in-plane with the easy axes along $\langle 110 \rangle$, as discussed for the Ce:YIG in Sec. 3.2.2. Thus we exclude an out-of-plane orientation as the reason for the smaller S_R and assume that S_R results from an easy axes along of $\Theta = 45\,^\circ$

Another method to probe the magnetic anisotropy of a sample is using the coercive field of SSE signal S_C for different angles. For the sample shown in Fig. 4.5c), a clear difference between the $\Theta = 0\,^\circ$ coercive field and the other directions can be identified. From the measurements, we can determine a field of $\sim 15\,\mathrm{Oe}$ necessary to reach the coercive field point S_C compared to $\sim 1.5\,\mathrm{Oe}$ for the other probed directions. The higher coercive field and the signal shape hints towards a uniaxial magnetic hard axis along $0\,^\circ$. To understand this behavior one has to be reminded of the soft magnetic character of YIG, usually leading to small coercive fields [37]. Using the SSE as a probing tool, we have to consider that the ISHE signals we detect have a sinusoidal in-plane dependence. Furthermore we know from the previous discussion, that the investigated sample has an easy axis along $45\,^\circ$. Starting at S_R, the magnetization will be rotated to the direction of the increasing external magnetic field and switch into the direction of the magnetic field. For a hard axis, higher magnetic fields are needed to align the magnetization along the applied field direction. For this reason, also the SSE signal shows a switching and saturation of the signal at higher magnetic fields. In the case of a perfect alignment along the hard axis of the uniaxial anisotropy, one expects no switching of the SSE signal but a signal shape similar to the absolute value of the magnetization of the hard axis (see Fig. 2.7a)). Therefore our $\Theta = 0\,^\circ$ measurements indicate a slight misalignment between the hard axis of the uniaxial anisotropy and the probing direction.

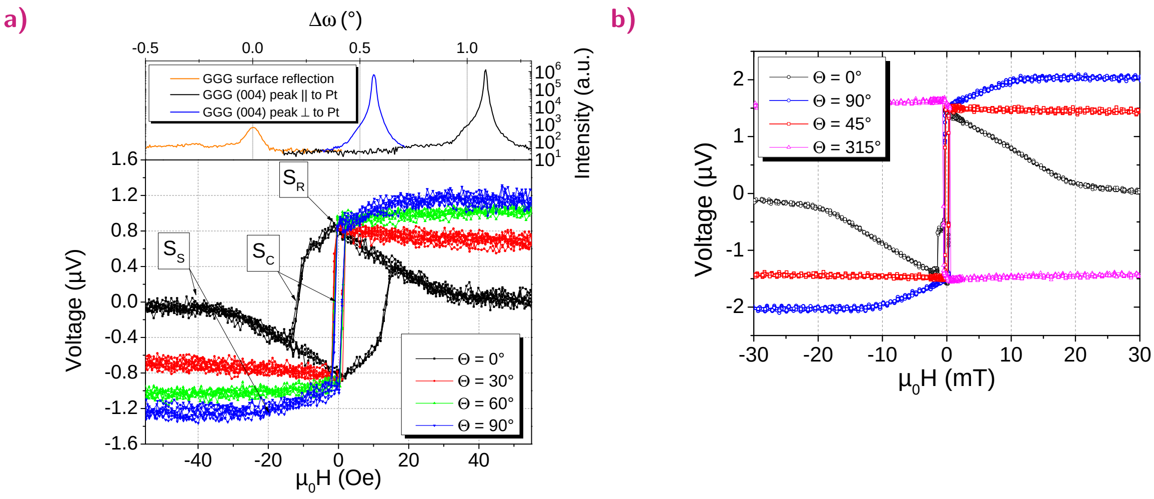

Fig. 4.6: Example measurements showing the possibility to probe magnetic anisotropy by the SSE. a) Measurements for a $300\,\mathrm{nm}$ thick YIG grown on GGG (001) showing a pronounced uniaxial anisotropy combined with a cubic anisotropy of the crystal lattice. The upper graph shows the miscut of the substrate with respect to the surface normal, which can give an explanation for the observed uniaxial anisotropy. The data are part of Ref. [p4]. b) SSE magnetometry measurements in a Ce:YIG sample showing the same magnetic anisotropy as observed for other magnetometry methods as discussed in Sec.3.2.2.

Thus using the saturation fields S_S presents, like for magnetometry, a possibility to determine the anisotropy from the SSE hysteresis loops. Compared to the other orientations we observe for $\Theta = 0\,^\circ$ higher fields necessary to saturate the SSE signal. In combination with the discussed higher coercive field this hints to a uniaxial anisotropy. Taking the found cubic easy axis along $\Theta = 45\,^\circ$ into account, $\Theta = 0\,^\circ$ corresponds to a combined hard axis for cubic and uniaxial anisotropy. Using the values $S_S = 20\,\mathrm{Oe}$ and $S_S = 40\,\mathrm{Oe}$ for $\Theta = 90\,^\circ$ and $\Theta = 0\,^\circ$ respectively, we can estimate the cubic K_1 and uniaxial anisotropy constants K_u. S_S for $\Theta = 90\,^\circ$ can solely be attributed to the cubic anisotropy and derives a value of $K_1 = 112\,\mathrm{J/m^3}$, using eq. 2.1 and $\mathrm{M}_s = 112\,\mathrm{kA/m}$ (measured by SQUID). To determine K_u, we need to subtract the value obtained for K_1 from the determined anisotropy field for $\Theta = 0\,^\circ$, yielding a value of $K_u = 112\,\mathrm{J/m^3}$ for the uniaxial anisotropy constant.

While the origin of the found cubic anisotropy can be explained by the crystal symmetry, the uniaxial anisotropy might result of a miscut from the substrate. The upper graph in Fig. 4.6a) shows rocking curves with respect to surface normal of the substrate along the two orientations perpendicular to another. As already discussed for Ce:YIG samples in Sec. 3.2.2, a miscut can lead to the formation of terraces on the sample surface causing preferential

orientation of the domains along them. The miscut measurements for this sample do not reveal a clear preferential orientation as for the Ce:YIG(111) sample but indicate an irregular surface structure. Both found angles for the miscut of $0.6\,^{\circ}$ and $1.1\,^{\circ}$ are large compared to substrates of good quality. Additionally further x-ray measurements reveal an increase of the out-of-plane lattice constant by 1.17% compared to bulk leading to an tetragonal distortion of the lattice. As a source for the uniaxial anisotropy one has to mention that YIG is likely to suffer a oxygen deficiencies within the growth process. The deficiencies, as well as a lattice distortion, are known to cause a growth-induced uniaxial anisotropy in garnets [38, 39].
As a next example, we discuss the SSE in Ce:YIG, which shows a more pronounced magnetic anisotropy due to the Cerium substitution (see Sec. 3.2.2). Fig. 4.6b) shows an example measurement for a $\sim 100\,$nm thick Ce:YIG sample grown on a GGG(001) substrate. From the measurements one can see that the SSE for $\Theta = 45\,^{\circ}$ and $315\,^{\circ}$ yields the same signal shape, showing only a switching of the signal but no further increase or decrease of the signal for higher magnetic fields. Combined with the signal amplitude for zero field we can identify this behavior as a cubic in-plane magnetic anisotropy that has also been found to be pronounced in other Ce:YIG(001) samples. The difference between the saturation field for $0\,^{\circ}$ and $90\,^{\circ}$ resembles the situation observed for YIG in Fig. 4.6a). Using this knowledge we can identify this behavior as uniaxial anisotropy with magnetic hard axis close to the $0\,^{\circ}$ orientation. As expected for Ce:YIG, the anisotropy is larger by a factor of ~ 20 compared to YIG, possibly due to the larger tetragonal lattice distortion.

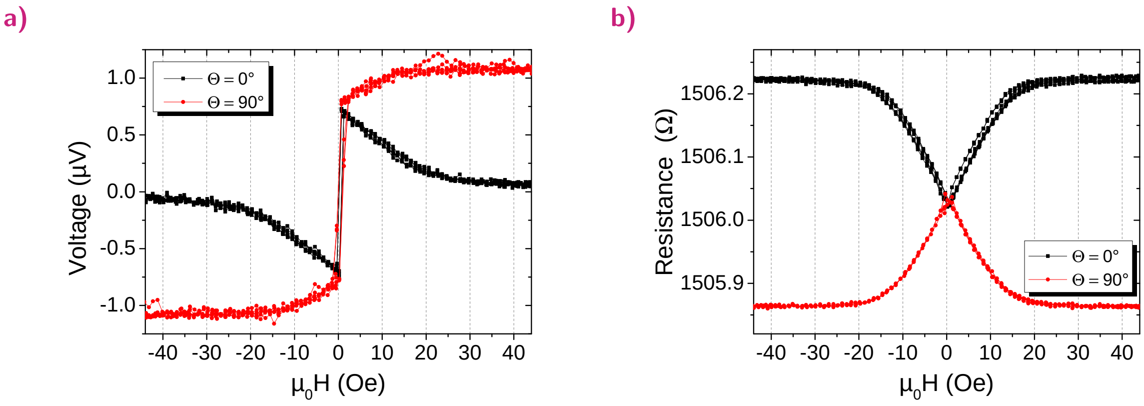

Fig. 4.7: SSE magnetometry measurements of a $20\,$nm thick YIG showing the agreement between SSE and MR measurements. a) Thermally generated voltage as a function of the applied external magnetic field for parallel and antiparallel in-plane orientation for a temperature gradient of $\Delta T = 9\,$K. b) MR measurement of the Pt stripe as a function of the applied external magnetic field for parallel and antiparallel in-plane orientation, using a probing current of $100\,\mu$A. The data are part of Ref. [p4].

Up to now we have only discussed samples with a thickness of more than $100\,$nm. As an example for thinner films, we will briefly present the behavior observed in a $20\,$nm thick YIG film grown on a GGG(001) substrate, shown in Fig. 4.7a). Compared to the previous samples, this one shows a more isotropic behavior, as the saturation field S_S for both probing directions match. We cannot observe a difference between the two coercive fields, which suggests the absence of a uniaxial anisotropy in this sample. An additional measurement along $45\,^\circ$ is needed to entirely exclude an in-plane uniaxial anisotropy. The zero field value S_R yields $0.77\,\mu\mathrm{V} \pm 0.06\,\mu\mathrm{V}$ for SSE, while the $90\,^\circ$ measurement gives a SSE amplitude in saturation of $1.08\,\mu\mathrm{V} \pm 0.02\,\mu\mathrm{V}$. If we calculate the easy axis by making use of the sinusoidal behavior for the SSE, we obtain an angle of $\Theta = 45\,^\circ \pm 3\,^\circ$. Like the other sample, this YIG film has been grown on a GGG (001) substrate, where a cubic magnetic anisotropy along the $\langle 110 \rangle$ directions is expected for this sample. It has to be emphasized that despite the film being a factor of 15 thinner compared to the sample shown in Fig. 4.6a), we are able to detect a signal of up to $1\,\mu\mathrm{V}$ in amplitude. In Sec. 4.2 it will be shown that the SSE obeys a characteristic thickness dependence leading to a decrease of signal with the thickness of the investigated ferromagnet. This disadvantage can be overcome by optimizing the interface quality between the ferromagnet under investigation and the probing layer, which optimizes the spin mixing conductance can therefore increase the signal strength (see Sec. 4.2). In contrast to the $300\,\mathrm{nm}$ sample in Fig. 4.6a) the interface of the $20\,\mathrm{nm}$ sample was treated by Ar-ion etching prior to the deposition of the Pt detection layer in order to improve the quality. This strong influence of the interface quality on the signal strength will also be subject of the sample comparison in Sec. 4.2.

Beside the SSE signal, also the novel MR effect [77] of the detection layer can be used to probe the magnetization within the sample. Fig. 4.7b) shows the MR measurements for the $20\,\mathrm{nm}$ sample. The origin of this novel MR is still subject of current research and is discussed in detail in Sec. 2.3.3. For the further discussion it suffices to known that, independent of the origin, both common theories [77, 79, 175] predict a correlation between the measured MR and the sample magnetization, which should allow to probe the sample magnetization by the MR. Our measurements can confirm this correlation as the MR shows a mirrored signal shape, if one compares the perpendicular measurement with the parallel one. The magnetic field dependence of the MR signal resembles the one from the SSE and shows the same saturation field values, highlighting that the same interpretation can be used to extract the anisotropy information from this probing method. It is interesting to note that the resistivity increases with the magnetic field for the perpendicular orientation and lowers for the parallel orientation. This behavior is identical to the behavior expected from a normal AMR [176]. In order to distinguish a normal MR from the novel MR effect, one would also need to measure the out-of-plane angular dependence. Independent of its origin, we can confirm that the MR of the detection layer as well as the SSE can be used to probe the magnetic anisotropy of the ferromagnetic layer free from contributions of the used substrate. Thus both methods present novel methods for magnetometry and provide a new toolkit for the investigation of thin film samples where conventional magnetometry is difficult.

4.1.6 Determination of the absolute spin Seebeck efficiency

Up to now the temperature difference (ΔT) between the copper blocks was used as a measure for the thermal gradient across the sample. As ΔT strongly depends on the design of the SSE setup, the derived SSC is different for each setup. Furthermore, for a qualitative comparison with predictions from theory it is essential to know the actual temperature difference and thus the gradient across to the Pt/YIG stack. Up to now, the only estimation of the actual temperature gradient has been given by finite element simulations [12] or by changing the description of the SSC from voltage per degree of temperature difference to voltage per heat flux [177]. The first approach relies on thermal conductivity data for bulk material, although studying only nm thin films. Since thin films are known to have a higher defect concentration, the actual value might strongly deviate. Furthermore, the first method can only provide an estimation of the temperature on the backside of the sample and thus only provide assumptions of thermal resistance of the interfaces, which are taken into account for model description of the effect [12]. The second approach [177] uses a $4\,\mu$m thick YIG film and assumes a bulk like thermal conductivity as well. Additionally the experiment is not able to detect any temperature directly on any of the sample surfaces, causing an error as the thermal resistance of the setup interfaces are not negligible.

Our approach to this problem is the simultaneous measurement of the temperature of the Pt stripe on the surface of the YIG, used for the detection of the SSE, and the temperature on the backside of the GGG substrate. Using a double side polished substrate GGG, we can additionally deposit and structure a second Pt stripe on the backside. To connect this stripe, we use an Al_2O_3 substrate with four $\sim 100\,$nm thick Au pads on the surface and indium foil as illustrated in Fig. 4.8.

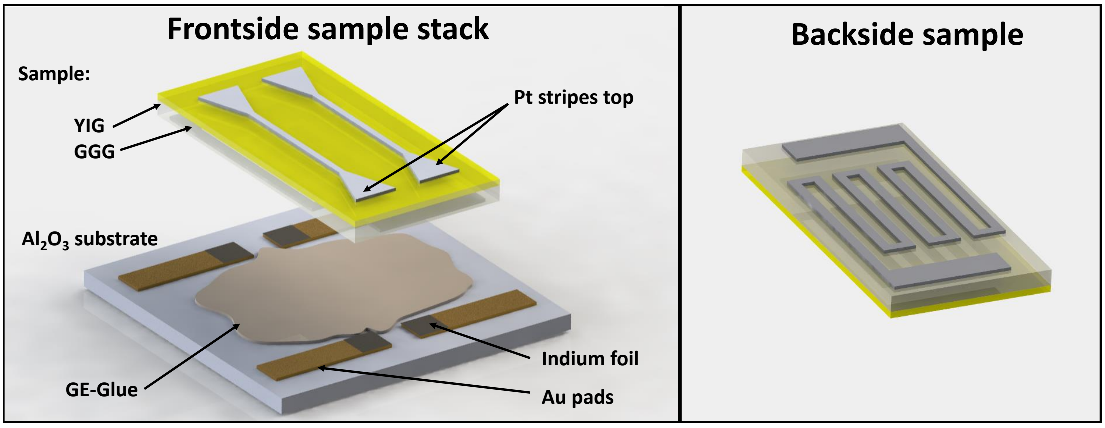

Fig. 4.8: The left image shows an illustration of the sample stack, used for the determination of the temperature difference of the sample. The right image shows the backside of the GGG substrate with the Pt thermometer.

The thermal contact in the mid part of the sample is established by thermally conductive but electrically insulating GE glue. Since the position of the Pt contacts highly affects the signal height of the SSE, the Pt-contact Pads have been coated with a $50\,$nm thick Au layer, which short circuits every SSE signal generated within the pad. This provides an identical geometry for the SSE contacts, independent of the contact position on the Au pads, caused by the ISHE (see Sec. 2.3.2).

First we take at look on the SSC derived from the temperature difference (ΔT) of the setup, as presented in the previous sections. Fig. 4.9a) shows the SSC obtained for both heating directions in the room temperature setup. The graph contains as well the linear fit of eq. 4.2, which yields the SSC and intercept presented in Tab. 4.1. The results reveal SSCs of around $0.09\,\mu\mathrm{V/K}$, which are identical for both heat flow directions within the error. The SSC values are smaller compared to other measurements performed in the same setup (see Sec. 4.1.3 and 4.2.2), although the sample has a similar layering (Pt $5.5\,\mathrm{nm}$ / YIG $65\,\mathrm{nm}$ / GGG (111)). In contrast to the previous shown samples, this stack of three substrates bears the problem of a more complicated heat flow, especially since the GGG backside to Al_2O_3 interface is separated by a larger gap, due to the indium foil contacts. Thus we expect that the smaller signals result from the higher thermal interface resistance. For heating from below, we obtain a larger zero ΔT_0 offset, which further confirms our assumption of a higher interface resistance below the sample. Furthermore, one has to consider that despite the similar SSC, both measurement directions yield a different absolute value for the SSE for the same temperature difference, as can be seen in Fig. 4.9a). This indicates a temperature offset within the system and an asymmetric heat flow. Since the SSC is similar for both heat flow directions, the actual temperature difference per target temperature step of $2\,\mathrm{K}$ must be comparable.

Temperature difference	Heat flow	SSC (μV/K)	ΔT_0 (μV)
Setup	above	0.088(1)	-0.012(1)
Setup	below	0.089(1)	-0.051(1)
Sample	above	0.98(3)	-0.02(1)
Sample	below	0.87(2)	0.02(1)

Tab. 4.1: Linear fitting values for the SSE as a function of temperature difference of the setup and sample.

To obtain the real ΔT applied to the sample, the Pt resistances are measured for each temperature step. Calibrated with a temperature sweep measurement without magnetic field and thermal gradient, one can calculate the corresponding ΔT of the sample for respective applied ΔT of the setup. The derived values are shown in Fig. 4.9b). From the evaluation we obtain a factor of ten smaller ΔT across the sample compared to ΔT of the setup. For heating from above we obtain a negligible offset for no applied temperature gradient, while a linear fit yields an offset $\Delta T_0 = -0.08\,\mathrm{K}$ for heating from below. This negative temperature difference explains the smaller absolute SSE signals, as the setup intrinsically has a temperature difference for this heating configuration. This offset is possibly caused by the thermal coupling to the environment due to the Au and indium pads below the sample. By comparing the difference between both heating direction for ΔT across the sample as a function of ΔT across the setup, it can be seen that the difference decreases for higher ΔT across the setup. This behavior points to an asymmetry in the heat flow of the setup, which can arise from higher heat conductivity of the metal contacts below the sample. For $\Delta T = 10\,\mathrm{K}$ of the setup, the heating from below measurements yield a higher ΔT for the sample than for heating from above, which matches to the observation of the difference between the SSE signals for both directions. Taking this offset in the temperature difference into account, one can understand the behavior we derived for the SSE as a function of the ΔT over the sample, shown in Fig. 4.9c).

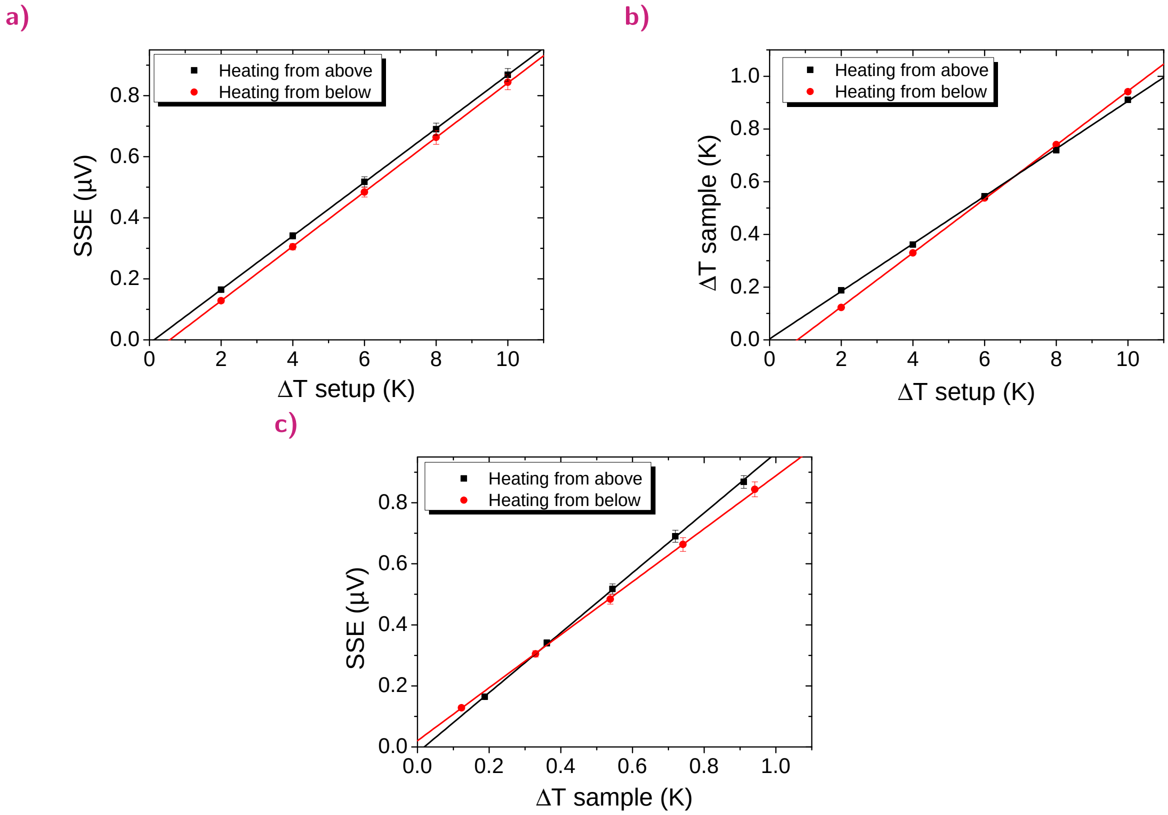

Fig. 4.9: a) SSE signal as a function of ΔT measured for the setup. b) Calculated ΔT over the sample as a function of ΔT of the setup. c) SSE signal as a function of calculated ΔT of the sample.

For heating from above the linear fit yields a SSC of 0.98 µV/K, highlighting that the actual SSE efficiency is a factor of ten higher than the SSC derived from ΔT of the setup. The exact values are given in Tab. 4.1. The discussed asymmetry for the heat flow and the negative offset for ΔT for heating from below lead to a lower SSC of 0.87 µV/K for the other direction of the temperature gradient. Still both values for the SSC show an increase by one order of magnitude compared to the SSC derived from the setup. Thus point out the importance of determination of the actual temperature difference used for the calculation of the absolute SSE coefficient, the SSC. These results not only present the first measurements of the temperature difference over the sample in the longitudinal configuration, they also emphasize that for a comparison of absolute SSE signals between different setups, a knowledge of the actual ΔT over the sample is essential. The sample shown is the first standardized sample, that is sent to different research groups around the world within the "Round Robin" project.[1] The next step for a more accurate determination of the SSC, is the calculation of the actual ΔT applied over the YIG layer. For this, not only a measured value for the thermal conductivity of the thin YIG layer is necessary but knowledge about the interface resistances. Additionally,

---

[1] This is part of the European Metrology project "SpinCal".

our measurements revealed an asymmetry within the heat flow of the used setup, due to metal contacting of the backside, requiring to take environmental temperature into account for an accurate calculation. A finite element simulation of the sample layers would provide a solution for this problem but is beyond the scope of this thesis. A rough estimation of the YIG temperature gradient can be given using the definition for the heat flow rate [27] of $\dot{Q} = \frac{A\lambda\Delta T}{l}$, where A denotes the area, l the thickness and λ the thermal conductivity of the material. For our approximation we assume an equal heat flow through the YIG and GGG layer by $\dot{Q}_{GGG} = \dot{Q}_{YIG}$. Using a GGG thickness $l = 500\,\mu\text{m}$, a YIG thickness $l = 65\,\text{nm}$, thermal conductivities [p9] of $\lambda = 8\,\text{W/mK}$ and $\lambda = 9\,\text{W/mK}$ for GGG and YIG respectively, for $\Delta T = 1\,\text{K}$ over the sample, we derive ΔT of $0.12\,\text{mK}$ across the YIG layer. This leads to an increase of the SSC by a factor of 8500, leading to a SSC of $\sim 8\,\text{mV/K}$. Despite the high error of this estimation, it shows the order of magnitude, which should be expected for the absolute value of the SSC.

The best comparison of this value, should be given by bulk measurements of the SSE, where the smallest error of the temperature difference is expected. Compared to the SSC measured in bulk samples, our value overestimates the SSC by more than three orders of magnitude, since literature sources only detect signals of several µV [11, 97]. Hence, a fundamental characteristic of the SSE must lead to a limitation of the signals. In the next chapter we will show that this discrepancy between expected signal strength for bulk and thin film can be explained by a pure magnonic feature of the effect, which determines its characteristic length scale.

4.2 Origin of the spin Seebeck effect

All previous shown dependences of the SSE can either be explained by a magnonic model from the bulk [13, 54, 66, 104] or only small interface layers [12, 101]. Taking the proximity magnetization of the Pt layer into account, a Nernst effect arising from it would present a further explanation to the observed dependences and signals [14, 15]. In parallel to our own experiments, two type of attempts were pursued to provide answers to the question of the origin of the effect. The first type of experiment was already described in the historical introduction of the SSE (see Sec. 2.4.2). In this type the focus is to distinguish between a Nernst origin of the effect and a magnonic, by either changing the ISHE layer to material less likely to be magnetized by the YIG, such as Au [112] or by a comparison measurement geometries in which only Nernst effect contribution are expected with the LSSE geometry where a Nernst and SSE signal is expect. Both experimental approaches could indirectly show that only a part of the signal should be caused by the Nernst effect. Our results in contrast to this, do directly show that only a negligible part of the signal can be attributed to the Nernst effect.

The second approach aims to determine whether the SSE originates from the bulk or the interface by performing time resolved experiments [178–180] of the SSE. The time resolution should allow to determine a finite rise time of the signals, which in combination with simulations of the time evolution of the thermal gradient within the system, should allow one to determine the probing depth of the SSE. Thus an instant rise time can only be explained by a pure interface effect. The experiments performed up to now obtain contradicting results, since the results from only nm thick films are not able to detect any cut off frequency [178], while experiments on μm thick films find a characteristic rise time hinting to a bulk origin of the effect [179, 180]. Both experimental approaches rely on a detailed knowledge about the response characteristic of the used electronic circuit, as a capacitive coupling can be misinterpreted as an intrinsic feature. Furthermore the simulation of the probing depth relies on known parameters such as the thermal conductivity of the system and propagation speed of magnons, which allow for a wide range of interpretation of the data.

As we will show in the following, our approach of investigating the thickness dependence of the SSE bears the advantage of a clear data interpretation, as any dependence on the thickness of the ferromagnetic material hints towards a bulk origin of the effect. In order to verify these results we additionally present a comprehensive study of the magnetic material parameters and the interface MR, which allows us to exclude signal variations by either the sample quality or the interface itself. This strengthens our results of thickness dependence of the effect, which we can attributed to the bulk origin of the SSE. For the further interpretation of the observed behavior we use the atomic magnetic simulation model, of our collaboration of the University of Konstanz, introduced in Sec. 2.4.3, which allows us to explain the thickness dependence by the finite magnon propagation length of thermally excited magnons.

The sentences and data of the following sections are taken from Ref. [p5].

4.2.1 Material characterization and measurement methods

All $Y_3Fe_5O_{12}$ samples with a thickness below 1 µm were grown by pulsed laser deposition (PLD) on $Gd_3Ga_5O_{12}$ (001) substrates (film thicknesses 20 nm - 275 nm). The PLD samples were characterized by x-ray diffraction and x-ray reflectivity, revealing an epitaxial growth of the films in the (001) orientation and surface roughness below 0.5 nm [p2]. The µm thick samples were cut from industrially (Matesy) produced 3 inch wafers, grown by liquid phase epitaxy on GGG (111) substrates, ranging from 1.5 µm to 50 µm in thickness.
Pt, used for the detection by the ISHE, was deposited by DC-magnetron sputtering up to thickness of 10 nm and lithographically structured into stripes. A schematic depiction of the final sample structure is shown in the inset of Fig. 4.1b). The PLD samples are sorted into series, indicating an identical interface treatment and simultaneous Pt deposition, leading to an identical interface for all samples within a series.
Magnetometry shows constant magnetic properties for the films, except for the 20 nm films, shown in Fig. 4.10a).

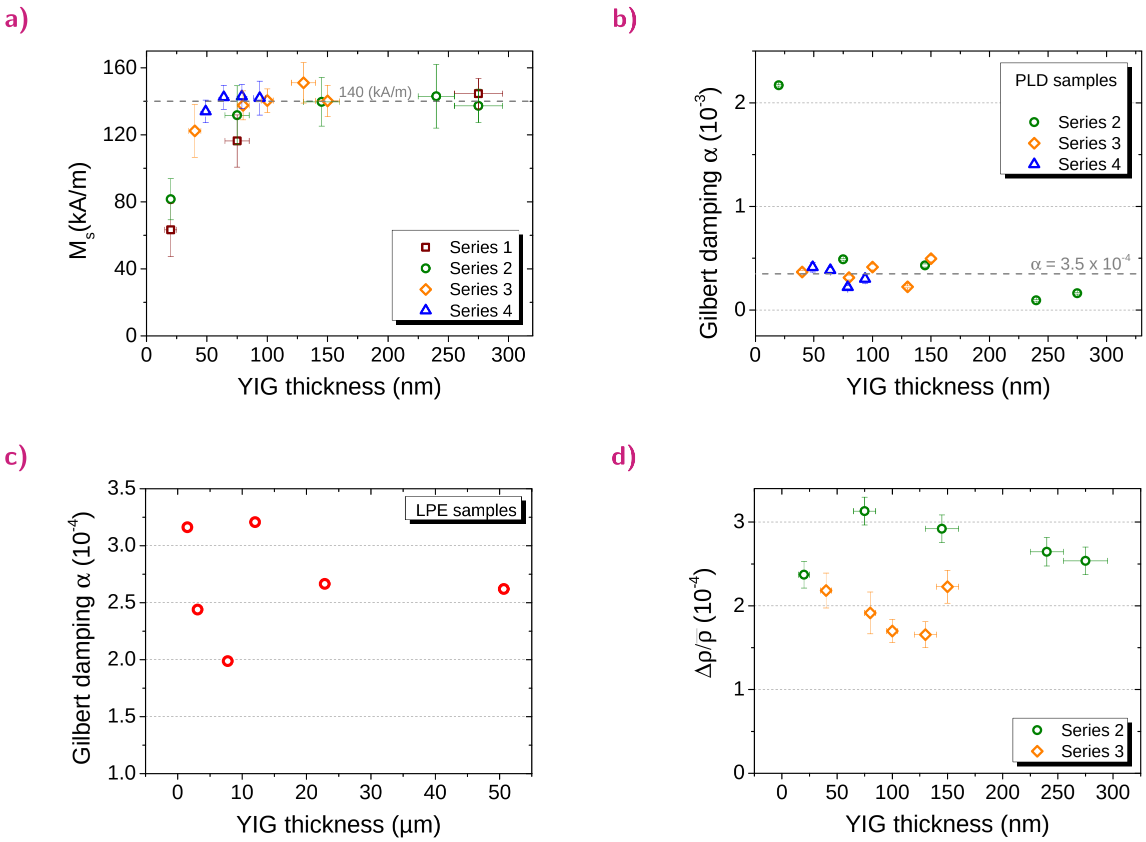

Fig. 4.10: Saturation magnetization a), Gilbert damping parameter α for PLD grown samples b) and LPE grown samples c) and MR ratio $\Delta\rho/\bar{\rho}$ d) as a function of the YIG film thickness for the samples grown by PLD.

To characterize the magnetodynamic properties of our samples, the Gilbert damping parameter α for the samples of series 2,3 and 4 was investigated by VNA-FMR measurements (see

Sec. 3.1.5). A similar behavior to M_s is observable for α. Only the $20\,\mathrm{nm}$ thin films shows a significant increase of damping parameter, while thicker films vary independent of the film thickness around a value of 3.5×10^{-4}, we obtain a mean value of $\alpha = 4.5 \times 10^{-4}$ for all samples, shown in Fig.4.10b). The value α of the LPE grown samples, shown in Fig. 4.10c), has been estimated from a δH at $3.1\,\mathrm{GHz}$ measurements, provided by the delivery company (Matesy), using eq. 2.19. Thus the α value contains contributions of an extrinsic part. The determined damping parameter shows no correlation with the film thickness and yields a mean value of $\alpha = 2.5 \times 10^{-4}$. To estimate the influence of the YIG/Pt interface coupling, we checked the magnetic field dependence of the Pt resistivity. The MR effect, which was observable in every sample, shows a dependence on the magnetization direction as well as an in-plane angular dependence that can be explained by the novel SMR effect (see Sec. 2.3.3). To determine the correlation with the YIG film thickness, we probe the MR for in-plane perpendicular $\rho_\perp$ and parallel $\rho_{||}$ magnetic field orientation with respect to the contacts on the Pt. From this data we calculate $\Delta\rho/\overline{\rho} = 2(\rho_{||} - \rho_\perp)/(\rho_\perp + \rho_{||})$, shown in Fig. 4.10d) for samples of series 2 and 3. Example measurements for the shape of the MR curves are shown in Fig. 4.7b). For both series $\Delta\rho/\overline{\rho}$ shows only a slight variation, independent of the YIG film thickness. Due to the identical interface conditions for samples of one series, we can deduce that the MR effect amplitude exhibits no significant dependence on the YIG-film thickness as expected for an interface-dominated effect. The changes of the absolute MR signal between the different series can be explained by the change of the Pt-thickness and a residual variation of the interface quality.

4.2.2 YIG thickness dependent measurements

The LSSE measurements are performed at RT (see Sec. 4.1.2 for details of the RT setup) and in a cryostat at $50\,\mathrm{K}$ (see Sec. 4.3.1 for details of the cryostat setup). We characterize the strength of SSE in our samples, using the SSC, which describes the SSE signal strength per degree of temperature difference applied on the system and provides a more robust value, than the absolute SSE signal (see Sec. 4.1.3).

First we will discuss our results obtained for the SSC in the PLD grown samples at room temperature, shown in Fig. 4.11a). Films below $\sim 90\,\mathrm{nm}$ show an increase of the signal amplitude with increasing thickness, which is in agreement with observations for polycrystalline Bi substituted YIG [8]. Looking at our epitaxial pure YIG films we find for larger thicknesses a decreasing slope, which leads to a saturation of the signal. The samples of series 3 generated signals a factor of two lower than the other series, attributed to the lack of interface etching prior to the Pt deposition, which leads to a less transparent interface for the magnons and, therefore, a smaller spin mixing conductance [181]. This observation underlines the importance of the interface conditions for the comparison of different samples, but the absolute trend of the thickness dependence is not affected.

In order to understand the origin of the signal, we compare the thickness dependence of the SSC with the thickness dependence of possible underlying mechanisms: Firstly, from the

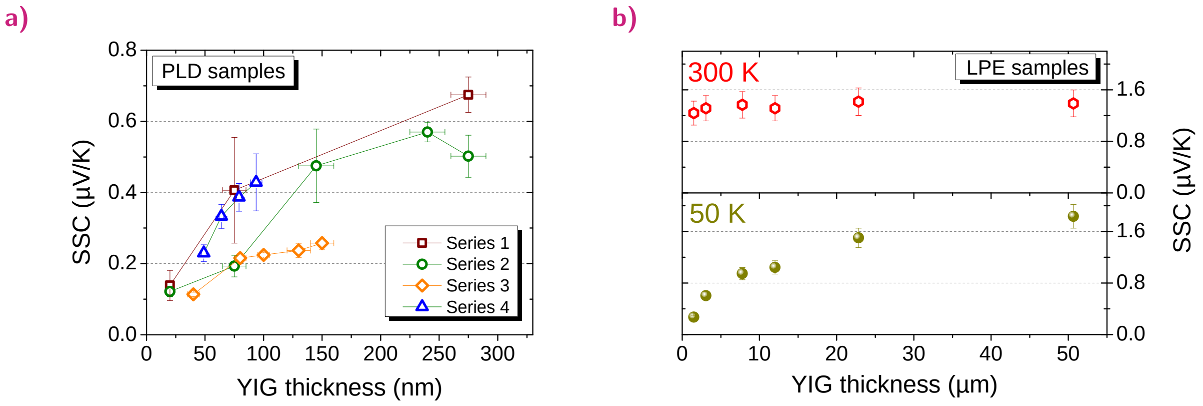

Fig. 4.11: Spin Seebeck coefficient as a function of YIG layer thickness for samples produced by PLD a) and LPE b). The series sorting for the PLD samples highlights an identical interface. Data points of each series are connected for clarity. The inset of a) shows a schematic depiction of the sample structure and the used measurement configuration for the SSE.

thickness dependence of the MR effect of the Pt, shown in Fig. 4.10d), one would expect a constant contribution to the measured signals independent of the YIG film thickness. This offset can be understood if the MR effect in combination with a thermal gradient leads to a Nernst effect, which might provide an additional constant contribution to the signals that we measure. As the MR is independent of the YIG film thickness, the resulting contributions to the signal will also be constant. The increase with increasing YIG film thickness, observed for the SSC, must therefore have a different origin. This is of major importance as it allows us to conclude that the source of the observed signals is not the currently discussed proximity effects at the interface [14] and that the clear thickness dependence points to an origin in the bulk of the YIG.

Secondly, we compare the thickness dependence of the magnetic material parameters of the film with the one observed for the SSC. From the M_s data shown in Fig. 4.10a) we see that only the 20 nm thick films shows a noticeable reduced M_s, which could have an influence on the SSC. Thicker films show only a negligible variation, which furthermore exhibits no correlation with the thickness dependence of the SSC, which shows a steep signal increase with increasing film thickness up to 100 nm. The same assumption is valid for the Gilbert damping of all films, as the measurements shown in Fig. 4.10b) for PLD and Fig. 4.10c) for LPE samples, find no correlation with the YIG film thickness. Thus both materials parameters show in the important thickness range between 50 nm to 300 nm only small and random variations, while the SSC is strongly and consistently increasing and leveling off. Thus we conclude that the observed thickness dependence of the SSC cannot be attributed to a thickness dependence of the magnetic properties of the films.

To show that the observed behavior is a generic property of the SSE and not limited to PLD-grown samples, we next investigate LPE grown YIG, which is generally accepted to have the highest quality and can be grown to larger thicknesses (we use up to 50 µm), shown in Fig. 4.11b). While the LPE samples used have a $\{111\}$ surface texture different compared to

$\{100\}$ of the PLD samples, we have also done measurements for both orientations for the same thicknesses, which have shown no noticeable difference for the SSE signals, allowing us to compare the behavior of both sets of samples. At room temperature the SSC is constant for thicknesses above $1.5\,\mu$m showing that the signal is saturated at those thicknesses. This saturation behavior matches with our expectation obtained from the PLD samples, which suggest the increasing signal with YIG thickness can only be observed for samples thinner than $1\,\mu$m. However at a lower temperature of $50\,$K, we find a thickness dependence qualitatively similar to the PLD samples. The lower graph in Fig. 4.11b) shows the signal increase with YIG thickness, with a levelling off above a thickness of $20\,\mu$m.

4.2.3 Finite thermal magnon propagation length

To understand this universal behavior of an increasing and saturating signal with increasing film thickness, we assume for the following theoretical calculations that the influence of the YIG thickness on the SSE might be due to a finite length scale for magnon propagation in the YIG material. In order to investigate this, we simulate the propagation of thermally excited magnons in a temperature gradient using an atomistic spin model, which is able to describe the full magnons frequency spectra[2]. Our generic model contains a ferromagnetic nearest-neighbor exchange interaction J and a uniaxial anisotropy with easy-axis along the z-direction and anisotropy constant $d_z = 0.1J$. We investigate a cubic system with $8 \times 8 \times 512$ spins, which are initialized parallel to the z-axis. The dynamics of the spin system is calculated by solving the stochastic Landau-Lifshitz-Gilbert equation numerically with the Heun-Method [116]. The phonons provide a heat-bath for the spin system assuming a linear temperature gradient over the length L in the z-direction as shown in Fig. 4.12a). This temperature profile remains constant during the simulation. Here, for simplicity, we assume that the temperature of the cold area, acting as the contact to the nonmagnetic material, is zero. After an initial relaxation, the local, reduced magnetization $m(z)$ is determined as an average over all spins $\mathbf{S}_i$ in the corresponding x-y-plane and, additionally, as an average over time.

Due to the temperature gradient, magnons propagate from the hotter towards the colder region leading to deviations of the local magnetization $m(z)$ from its local equilibrium value $m_0(z)$, which would follow from the local temperature $T_\mathrm{p}(z)$ of the phonon system. A temperature dependent calculation of the equilibrium magnetization $m_0(T)$ for a system with constant temperature allows us to define a magnon accumulation $\Delta m(z) = m(z) - m_0(T_\mathrm{p}(z))$ [54]. Fig. 4.12a) exemplifies this magnon accumulation Δm as a function of spatial coordinate z in a system with a damping constant of $\alpha = 0.01$ and a linear temperature gradient of $\nabla T = 10^{-5} J/(k_\mathrm{B}a)$ over two different lengths L, where a is the lattice constant of the cubic system. At the hotter end of the gradient magnons propagate towards

---

[2] All simulations were carried out by U. Ritzmann and the group of U. Nowak at the University of Konstanz.

the cooler region and this increases the local magnetization. On the other side, at the cold end of the gradient, magnons arriving from hotter parts of the system decrease the local magnetization. The resulting magnon accumulation is symmetric in space and changes its sign at the center of the temperature gradient.

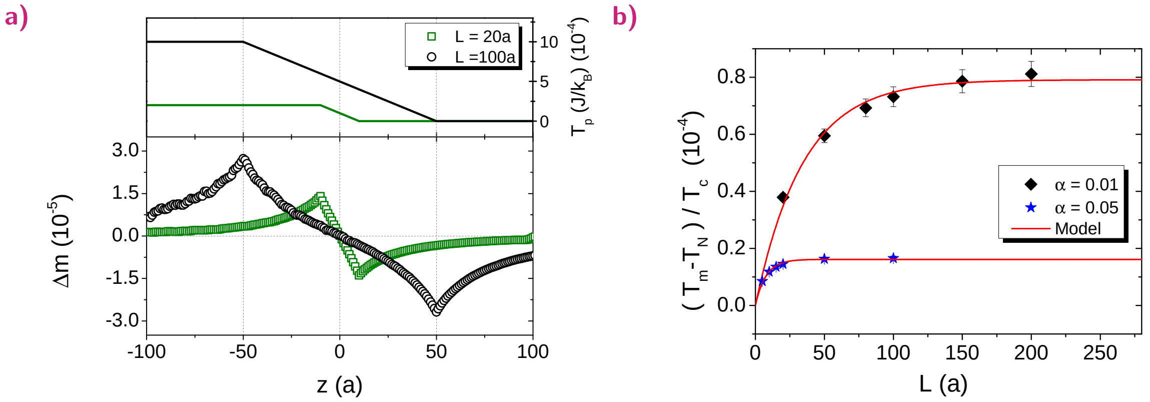

Fig. 4.12: a) Magnon accumulation Δm as a function of the spatial coordinate z in units of the cubic lattice constant a for a given phonon temperature T_p including a temperature gradient over two different lengths L. b) Numerical data of the temperature difference $T_\mathrm{m} - T_\mathrm{N}$ at the cold end of the temperature gradient in units of the Curie temperature T_c as a function of the length L of the temperature gradient for two different damping constants α. The solid lines corresponds to a fit using eq. 4.3.

The absolute value of the magnon accumulation at the cold end of the gradient increases with increasing length L. The temperature difference $T_\mathrm{m} - T_\mathrm{N}$ at the cold end of the gradient can be calculated from the local magnon accumulation. Following Xiao *et al.* [66] this temperature difference can be related to the magnonic spin current, which is propagating to the detector material and then measured in experiments. Fig. 4.12b) shows this temperature difference dependent on the length L of the temperature gradient for two different damping constants. For small length L the temperature difference increases with increasing thickness until a saturation value is reached. The characteristic length scale of the saturation depends on the damping constant. Previously we have shown that the propagation length of the magnons scales theoretically with $1/\alpha$ [54]. In a temperature gradient, where a broad distribution of frequencies contributes, the mean value of the propagation length scales similarly, to first order. The magnon spin current can be understood as the averaged sum of magnons, reaching the end of the gradient. As illustrated in Fig. 4.13a) only those magnons from distances smaller than their propagation length contribute to the resulting magnonic spin current at the cold end of the temperature gradient. Therefore a saturation of the magnonic spin current sets in if the length (sample thickness for our geometry) overcomes the mean propagation length of the magnons.

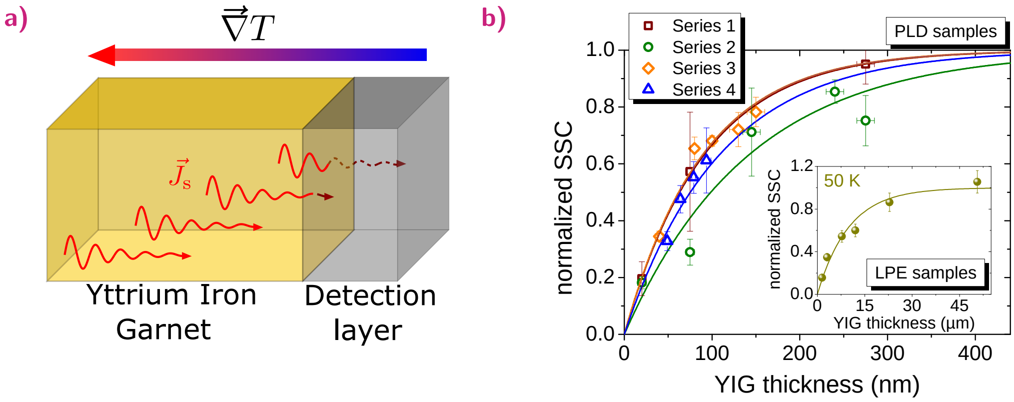

Fig. 4.13: a) Illustration of a finite magnon propagation length. The net magnon current carries angular momentum antiparallel to the thermal gradient. Only magnons excited at distances smaller than their propagation length contribute to the detected signal, leading to a saturation effect. b) Normalized SSC data and corresponding fit functions plotted as a function of the YIG thickness for PLD and for the LPE sample at $50\,\mathrm{K}$ in the inset. The SSC data have been normalized to the saturation value for an infinitely large system. The lines show the fit via eq. 4.3.

$$T_\mathrm{m} - T_\mathrm{N} \propto (1 - \exp(-L/\xi)), \tag{4.3}$$

where ξ describes the mean propagation length of the magnons. A fit of the numerical data is included in Fig. 4.12b) as solid lines and can describe the observed saturation behavior and the dependence on the damping constant. Due to the large computational effort of the performed simulation, it is not possible to simulate the YIG system. To compare the value for the mean propagation length with the experimental results, we extrapolate the numerical data towards lower damping and lower anisotropy. From measurements of the damping measurements, we obtain a mean damping constant of $\alpha = 2.5 \times 10^{-4}$ for the LPE films and $\alpha = 4.5 \times 10^{-4}$ for the PLD samples at $300\,\mathrm{K}$ [p2]. To take into account the temperature dependence of the damping parameter, we use in the $0\,\mathrm{K}$ simulations a damping parameter of $\alpha = 1 \times 10^{-4}$. We expect that the dominant anisotropy contribution is given by the shape anisotropy and using the value for the saturation magnetization we use an anisotropy constant of about $d_z = 10^{-4} J$, where J is the exchange constant. Using a $1/\alpha$-scaling of the mean propagation length and including the dependence on the frequency gap and therefore on the anisotropy reported by Ritzmann *et al.* [p6] we extrapolate a mean propagation length of about 10 µm from the numerical calculations.

We analyze our experimental data using eq. 4.3. Each series is evaluated separately as can be seen in Fig. 4.13b). We obtain a mean magnon propagation lengths between $90\,\mathrm{nm}$ and $140\,\mathrm{nm}$ for the PLD samples, while for the LPE samples at room temperature we can only give an upper limit for propagation length of $1\,\mu\mathrm{m}$, in agreement with the results of time dependent measurements [179, 180]. For $50\,\mathrm{K}$ the fit yields a value of $8\,\mu\mathrm{m}$, which is close to the value estimated from the simulations for $0\,\mathrm{K}$.

We would like to point out, that our result of a finite volume of the YIG contributing to the measured SSE signals allows us to link our thin film measurements to the published bulk results: Since only a few hundred nanometers of YIG close to the Pt contribute to the measured SSE signals at room temperature, it is not surprising that we obtain SSC signals for our thickest samples of the order of $1.5\,\mu\text{V/K}$, which is in line with measurements of bulk materials [97, 182], which use a similar definition of the temperature difference within their setup.

In conclusion, we have shown that the SSE features a characteristic increase and saturation of the signal with increasing YIG film thickness. As we observe changes in the spin Seebeck signal with changing thickness, even within a series of samples that have identical magnetic properties such as the saturation magnetization, we can rule out a dominating influence of magnetic properties or the MR effect in the Pt detection layers. Instead we present a model based on atomistic simulations that attributes this characteristic behavior to a finite propagation length of thermally excited magnons, which are created in the bulk of the ferromagnetic material. An increase and saturation of the SSC with increasing YIG film thickness has also been predicted by a theory of S. Hoffman *et al.* [103], who attribute a saturation of the SSE signal for large thicknesses also to the finite propagation length of thermally excited magnons. From the evaluation of our data at room temperature measured in samples grown by PLD, we obtain a mean propagation length of the order of $100\,\text{nm}$ for thermally excited magnons, which is in agreement with other studies predicting a finite propagation length of thermally excited magnons of the order of $100\,\text{nm}$ [99]. For LPE grown samples, we can observe a constant signal at room temperature in line with a propagation length below $1\,\mu\text{m}$. Measurements at $50\,\text{K}$ reveal that the magnon propagation length is coupled to the absolute system temperature as we find a length of $8\,\mu\text{m}$. This thermal magnon propagation length is in quantitative agreement with the results of our simulations, which estimate in the limit of low damping a propagation length of order 10 μm for low temperatures showing that our model can reproduce the observed results.

4.3 Temperature dependence of the spin Seebeck effect

Up to now we only discussed SSE measurements at room temperature and at $50\,\text{K}$. In the TSSE [96, 106] and LSSE [104, 107, 108] configuration, a maximum of the SSE signal as a function of temperature is found at low temperatures. The appearance of this peak is currently attributed to a phonon-magnon drag effect. In the theory of the thermal conductivity (see Sec. 2.1.3), we explained that the competition between different scattering mechanisms for phonons leads to the occurrence of a peak of the thermal conductivity for lower temperatures, shown in Fig. 2.3. Thermal conductivity measurements of the samples used for the TSSE measurements reveal that this peak is close to the peak of the SSE voltage [96, 106]. Thus a strong phonon-magnon interaction would enhance magnon propagation at this temperature, as the phonons drag the propagating magnons along their path causing an increase of the SSE signal. While this concept holds for low temperatures, a strong magnon phonon interaction would consequently cause a strong decrease of magnon propagation length for higher temperatures. Boona *et al.* [59] performed low temperature ($< 12\,\mathrm{K}$) measurements of the thermal conductivity of the magnetic and phononic lattice. Based on their results they concluded that magnons, responsible for the heat transport of the magnetic lattice, and corresponding phonons must have a similar propagation length at these temperatures. Furthermore they concluded that this strong coupling between magnons and phonons would limit the magnon propagation mean free path to a few nm at room temperature, in contrast to our findings presented in the last section. Additionally this model contradicts findings of the magnetic field suppression of the SSE [113], which are presented in the Sec. 4.4. This discrepancy is currently explained by so called sub-thermal magnons [59, 102, 183], which are considered to have lower interaction probability with phonons. If the SSE can be mainly attributed to sub-thermal magnons, then a decrease of the phononic mean free path should influence the magnon propagation length less, allowing a longer propagation at room temperature.

In the following section, we present our systematic study on the concept of a strong magnon phonon interaction by probing the SSE as a function of temperature and thickness of the YIG, which will be published in Ref. [p10]. In the beginning we introduce the two methods and setups that have been developed in this project to probe the SSE at variable temperatures in a cryostat. Having established the measurement principles, we show our results for temperature dependent measurements of the SSE in LPE grown YIG. Additional thermal conductivity κ measurements of the same samples, in detail described in Ref. [p9], reveal that the interpretation based on the magnon-phonon drag cannot provide a complete description of our combined results for SSE and κ. We present another concept based on the propagation of thermal magnons with weaker magnon-phonon interaction, that can explain the occurrence of the peak and thickness dependence of the SSE signals at low temperatures.

4.3.1 Measurement methods for low temperature investigations

The measurement of SSE in a cryostat bears several additional challenges compared to measurements at room temperature. The temperature range from $300\,\mathrm{K}$ to $4\,\mathrm{K}$ excludes the usage of Peltier elements, as their efficiency rapidly decreases below $150\,\mathrm{K}$. Thus one has to make use of the He flow in the variable temperature inset (VTI) of the cryostat. The He flow cools one side of the setup, while the other side is heated. For an efficient processes this side needs to be shielded from the environment. Two setups, which both make use of this principle, have been developed and used in this thesis. The first setup, shown in Fig. 4.14, is similar to the room temperature setup as it sandwiches the sample between two copper blocks. The surface area of the copper blocks has been maximized to increase the cooling efficiency. A cartridge heater and a Pt-100 element are mounted in each copper block to adjust the temperature and ΔT. This setup is developed for invertible SSE measurements from $10\,\mathrm{K}$ to $330\,\mathrm{K}$ and can be inserted into the VTI of a $3D$ vector magnet cryostat.

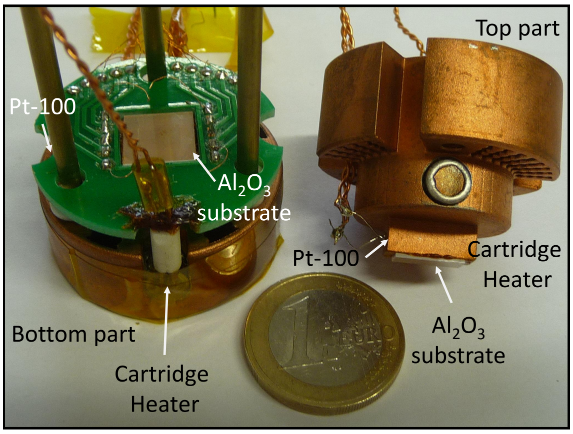

Fig. 4.14: Picture of the sample mounting for the $3D$ cryostat setup. The sample is glued on the Al_2O_3 substrate of the bottom part. The top part is guided by the three brass rods and pressed by springs onto the bottom part.

The second setup is a compact design for a smaller VTI. A picture of an assembled sample is shown in Fig. 4.15a) and Fig. 4.15b), while Fig. 4.15c) gives a schematic illustration components. The idea of this design is to mount the sample between a heater and a thermometer substrate to determine the temperature difference. The heater substrate is glued on top of the sample and consists of an $10\,\mathrm{mm} \times 5\,\mathrm{mm}$ Al_2O_3 single crystalline substrate, covered with a $10\,\mathrm{nm}$-$20\,\mathrm{nm}$ thick Pt film, structured into a meander pattern. Since Pt possesses a strong temperature dependent resistance the element can also be used as a thermometer at the same time. The heater area of the Al_2O_3 is covered by a piece of Teflon to reduce the thermal connection to the He environment. A second Al_2O_3 substrate with a size of $10\,\mathrm{mm} \times 10\,\mathrm{mm}$ is attached to the backside of the sample. Using a diagonal orientation for the Pt stripe on the surface of this substrate, it is possible to connect the stripe and use it as a thermometer. All three films are glued together with GE-VARNISH, which ensures a homogenous heat contact. The stack itself is glued and pressed by a screw mount onto a larger copper block, functioning as a heat sink.

Both setups enable us to perform two types of measurements. The first method consists of hysteresis measurements at a stable temperature, which is identical to the measurement principle at room temperature. For this the VTI is set to a specific temperature, while a heating current is applied to the heater substrate. After a steady state has been reached the magnetic field is swept and the SSE signal is measured (see Sec. 4.1.3). The $500\,\mu\mathrm{m}$ thick Al_2O_3 substrate isolates the Pt detection stripes from the heating meander. To prevent any influence of capacitive coupling, each data point for a fixed field is measured for negative and positive heating current. Beside the thermovoltage, the resistance of the Pt heater as well as the resistance of the second Pt stripe on top of the YIG and the resistance of the Pt stripe

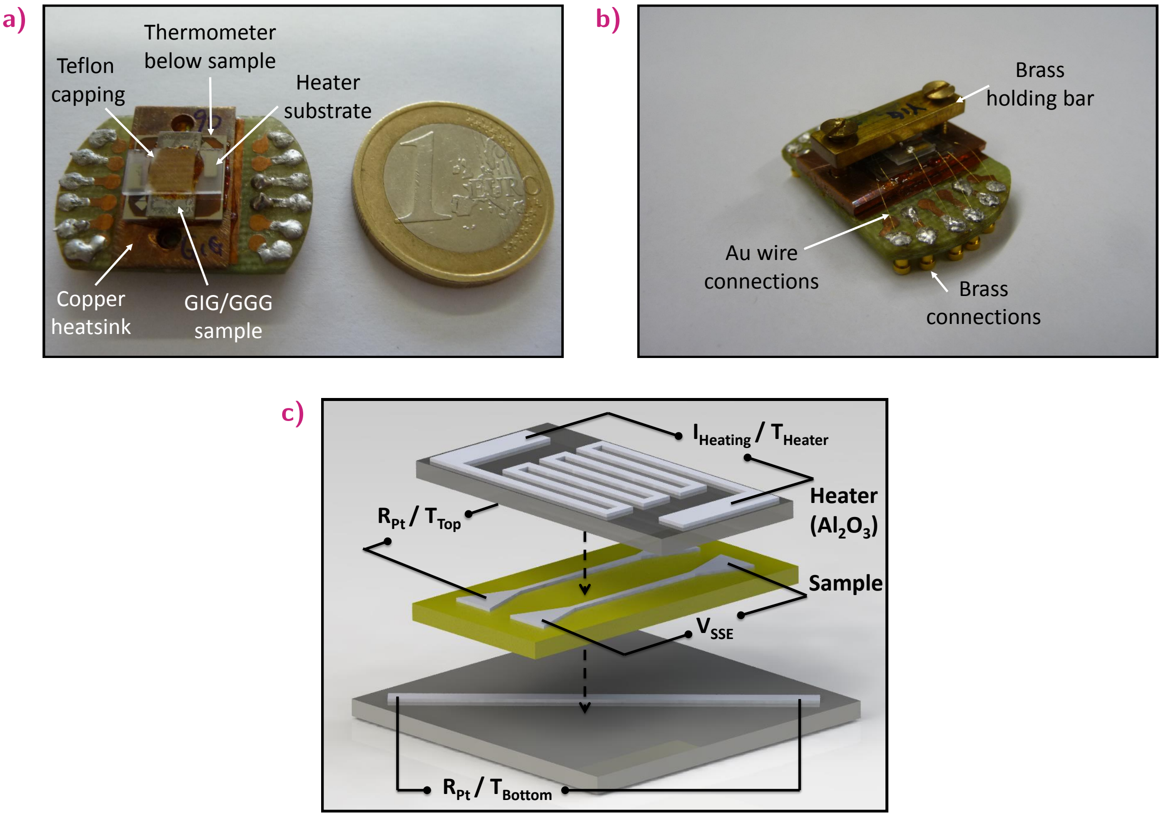

Fig. 4.15: a) Picture of the sample stack, allowing to measure the SSE in the 12T magnetic field cryostat. b) Picture of the connected sample, pressed by a brass holding bar. c) Illustration of the mounting principle of the sample stack shown in b).

below the sample are recorded. Using a temperature sweep for calibration, it is possible to determine the temperature difference applied to the sample and the temperature on top of the YIG from these three resistances. Fig. 4.16a) shows four example measurements for a $\sim 200\,\mathrm{nm}$ thick YIG sample. The advantage of this method is that the SSE can be clearly separated from other effects, such as conventional Seebeck voltages. These parasitic voltages occur due to the temperature difference along the connection path from sample to voltmeter and the used cable material, which consists either of Cu, Au or Constant, with Seebeck coefficients of several μV/K for both materials [21]. Additionally, other high magnetic field effects can influence the measurement, as the SSE voltage is sensitive to changes in the Pt stripe resistivity and can thus be influenced for instance by the Lorentz magnetoresistance [184]. Other setup parameters like the He environmental pressure play only a minor role, as the detection of the actual temperature difference over the sample allows one to scale the data. A disadvantage of this method is the time necessary to acquire data points for different temperatures. Each hysteresis measurement, shown in Fig. 4.16a), including the optimized temperature sweep takes up to $3\,\mathrm{h}$, however one obtains multiple ΔT data sets.

The second measurement method directly makes use of the temperature sweep of the whole system. For these measurements the temperature of the VTI is swept, while the magnetic field is set to a fixed value and a constant current is applied to the heater above the sample.

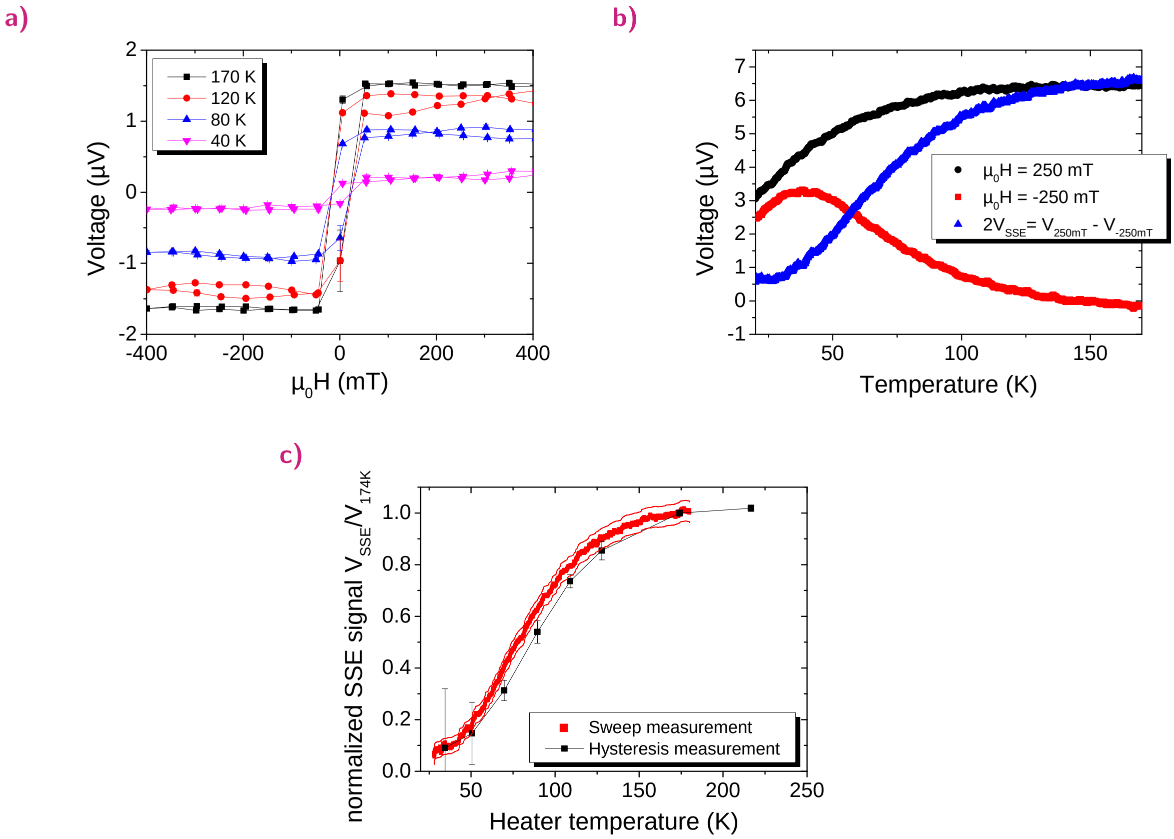

Fig. 4.16: a) SSE hysteresis measurements for four different temperatures. b) Temperature sweep measurements of the detected thermovoltage for 250 mT (black curve) and -250 mT (red curve). The blue curve corresponds to SSE voltage $2 \cdot V_{SSE} = V_{250\,\mathrm{mT}} - V_{-250\,\mathrm{mT}}$. c) Comparison of the SSE signals obtained by the hysteresis measurements (black curve) and sweep measurements (red curve). The red solid lines correspond error of the sweep measurement, which are not shown for the following measurements to provide a better overview. Both data have been normalized for the SSE signals at 174 K to allow a qualitative comparison.

The measurement has to be performed for both magnetic field directions, as only one branch of hysteresis is probed by each temperature scan. Fig. 4.16b) shows the temperature sweep measurements for the same sample. It is crucial that the magnetic field is high enough to saturate the SSE signal, but low enough to prevent influences of the magnetic field dependence of the SSE (see Sec. 4.4) and the magnetoresistive effects of the Pt stripe. The field values are obtained from hysteresis measurements at the highest and lowest temperature. In order to extract the SSE signal from the positive and negative magnetic field temperature sweep measurements, it is essential to use the same He pressure, sweep rate and heating current. Otherwise both measurements contain different background signals caused by parasitic thermovoltages of the setup. Since these voltages do not solely depend on the applied temperature difference but also on the pressure and other conditions, different measurement conditions make it impossible to separate the SSE signals.

In case these requirements are fulfilled for both measurements, one needs to use the simultaneously recorded resistance to calibrate both measurements to the actual temperature of the system. Afterwards the two signals can be subtracted from each other, yielding the SSE voltage shown as blue curve in Fig. 4.16b). The obtained voltage signal corresponds to the difference ΔV (see eq. 4.1) of the hysteresis measurements. The advantage of this probing method is the continuous measurement of the SSE as a function of temperature, which provides a better overview of the signal trend.

A qualitative comparison of the methods is shown in Fig. 4.16c). The data have been normalized for the SSE voltage measured at $174\,\mathrm{K}$, as different heating powers have been used. A quantitative comparison of both methods is discussed in Sec. 5.1.1 and presented in Fig. 5.3 for a GIG sample. Independently from the applied power, both methods show the same temperature trend for the SSE signals for lower temperature, revealing that both methods provide the same results. Starting at around $180\,\mathrm{K}$, the SSE signals measured by both methods decrease rapidly upon cooling until $\sim 50\,\mathrm{K}$ to about 8% of the signal at $180\,\mathrm{K}$. Below this temperature the signal decreases more slowly.

A general decrease of the SSE signal with lower temperatures could be caused by other sources than an intrinsic dependence of the effect, as the thermal conductivity and capacitance of the setup are decreasing. Since many different components are used in the setup, it is expected that the thermal resistance at the interfaces between the components changes with temperature. The thermal flow determines the actual signal height, thus the decrease of the SSE voltage might originate from the setup itself. In order to provide more meaningful results, it is necessary to use the SSE coefficient (SSC, see eq. 4.2), which takes this change of the temperature gradient as a function of temperature into account and is therefore used for the presentation of the following results. Additionally it should be pointed out that the signals show no peak in the investigated temperature range, in contrast to the results reported for bulk YIG samples [107]. To understand this discrepancy we investigate the SSC for a wider range of YIG film thicknesses.

4.3.2 Combination of thickness and temperature dependence of the spin Seebeck effect

Tests of the concept of the magnon-phonon drag

For our systematic study of the thickness and temperature dependence of the SSE, we use μm thick LPE grown samples, cut out of industrially produced wafers (Matesy), as presented in Sec. 4.2.1. The YIG wafers' thicknesses range from $150\,\mathrm{nm}$ to $50\,\mu\mathrm{m}$. Additional measurements have been performed using a $1\,\mathrm{mm}$ thick single crystalline YIG sample. On all samples, $6\,\mathrm{nm}$ Pt has been sputtered and structured into two Pt stripes (see Sec. 4.1.1). For the measurement of the SSE as a function of temperature we use the temperature sweep method. The advantage of this method is that we obtain an almost continuous set of data points compared to the hysteresis measurements, which allows us to clearly determine the temperature of the expected peak. Fig. 4.17 shows the SSC as a function of temperature for

10 LPE YIG samples with different thicknesses and the bulk sample. The used temperature is calculated from the resistance of the Pt stripe on the YIG surface. For the calculation of the SSC, the temperature difference between Pt on the YIG surface and Pt on top of Al_2O_3 substrate below the YIG film has been used (see Fig. 4.15c)).

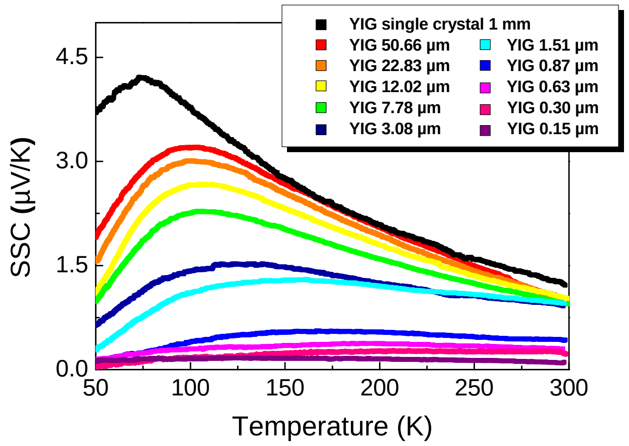

Fig. 4.17: SSC as a function of temperature of the Pt stripe on the YIG surface.

From the measurements one can see the occurrence of a clear peak of the SSE in samples thicker than $0.87\,\mu$m, while thinner samples show a signal decrease for lower temperatures. The observed temperature dependence of the SSC for the $150\,$nm and $300\,$nm thick LPE grown samples is the same as determined for SSE signals of the $200\,$nm PLD grown sample shown in Fig. 4.16c). Therefore the signal decrease for lower temperatures cannot be dominated by variations of the setup parameters but must originate from the SSE. An explanation for the intrinsic origin of the signal decrease as a function of temperature can be given by the decreasing amount of thermally excited magnons, since less energy is provided by the thermal excitation at lower temperatures. To determine the amount of thermally excited magnons, one additionally needs to take into account their dispersion relation, which is topic of Sec. 4.4.

However, the appearance of a peak for the SSC at lower temperatures cannot be solely explained by the amount of thermally excited magnons. The peak is more pronounced for thicker YIG films, showing a clear maximum for the bulk sample, while the LPE grown films show a broader width of the peak and a linear signal increase upon cooling down from room temperature. The peak temperature shifts to lower values, as the film thickness increases. For our bulk sample we determine a maximum at $T_{\text{peak}}^{SSE} = 74\,\text{K}\pm 5\,\text{K}$, which is $25\,$K higher than the temperature of $T_{\text{peak}}^{SSE} = 50\,\text{K}$ reported by Uchida *et al.* [107] for a $1\,$mm bulk sample. A better agreement of $T_{\text{peak}}^{SSE} = 130\,\text{K}\pm 10\,\text{K}$ of our $7.78\,\mu$m thick LPE film is found with the value of $T_{\text{peak}}^{SSE} = 130\,\text{K}\pm 20\,\text{K}$ reported by Rezende *et al.* [104] for a $8\,\mu$m thick sample. Tests of the dependence of the peak position on the applied temperature gradient, reveal no shift of the peak within the resolution of our measurements. The peak height scales linearly with ΔT as known for the SSE signals, which hints to an intrinsic relation to the SSE.

To determine the origin of this peak we test the concepts of different models. We first investigate the mechanism of the magnon-phonon drag. In order to test this correlation, we determined κ for several LPE samples, using a novel method to evaluate the thermal conductivity of this complex system. More information about the data evaluation and the used 3ω measurement method[3] is given in Ref. [p9]. Here we focus on the obtained temperature for the maximum of κ_{max}, shown in Fig. 4.18. For an easier comparison we also include T^{SSE}_{peak} to the Figure.

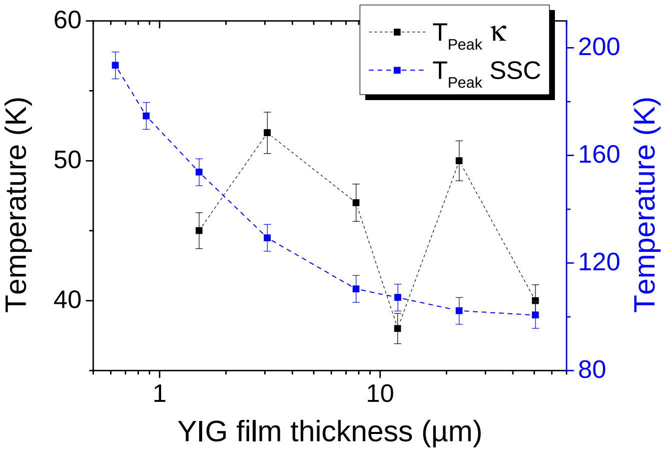

Fig. 4.18: Maximum temperature of κ_{max} and T^{SSE}_{peak} of the SSC in LPE grown YIG samples as a function of the film thickness. The data of the thermal conductivity have been taken from Ref. [p9]. The data have been linearly connected as guide to the eye.

The data of the thermal conductivity measurements reveal no monotonous dependence on the film thickness but only show an arbitrary variation. If no crystal defects limit the phonon propagation, the peak position of κ_{max} only depends on the film thickness, as the boundary scattering is determined by the sample size. A decrease of the film thickness reduces the maximum of the phonon's mean free path and therefore shifts the peak of κ_{max} to higher temperatures (see Sec. 2.1.3). The observed thickness independence must therefore originate from other defect scattering sources than the boundary limit. A possible origin might be Pb impurities, which result from the LPE growth process (see Sec. 3.2.1).

Furthermore our findings for κ do not agree with to the concept of a strong magnon-phonon coupling, which expects a similar temperature shift for κ_{max} with increasing thickness as observed for T^{SSE}_{peak} of the SSE. Additionally the found temperature difference between both maxima is raises questions about influence of the magnon-phonon drag on the SSE peak. For the thickest LPE film of 50 µm, we determine a peak temperature of $T^{\kappa}_{\text{peak}} = 40\,\text{K} \pm 1\,\text{K}$, which is $60\,\text{K}$ lower than the corresponding SSC maximum of $T^{SSE}_{\text{peak}} = 100\,\text{K} \pm 5\,\text{K}$. A similar discrepancy is found for our 1 mm thick bulk sample, showing a maximum at $T^{SSE}_{\text{peak}} = 74\,\text{K} \pm 5\,\text{K}$, which is $50\,\text{K}$ higher value than the reported literature value of $T^{\kappa}_{\text{peak}} = 25\,\text{K}$ [59]. Since T^{κ}_{peak}

---

[3] The thermal conductivity measurements and data evaluation has been done by C. Euler.

reveals no obvious thickness dependence, the temperature difference between the peaks for κ and T_{peak}^{SSE} increases for the 1.51 µm film up to ~ 110 K. This temperature difference is in contradiction to findings only determined for the TSSE [96, 106, 108]. By comparing our results of the LSSE geometry with the TSSE, one has to consider that the substrate cannot be neglected in the TSSE configuration as for the LSSE, which leads to a different experimental situation for both geometries. This contrast between TSSE and LSSE for the magnon-phonon drag has also been pointed out by Siegel *et al.* [108]. In their experiments using a 50 nm thick Bi:YIG film, they were only able to observe a peak in the TSSE but not the LSSE configuration. They explain this difference by assuming that in the TSSE configuration the phonons of substrate and film couple to another, due to the parallel heat transport. In contrast to this, in the LSSE configuration the phonons of substrate cannot cause a drag of the phonons in the film and therefore of the magnons. Since no additional thermal conductivity measurements were provided [108], the absence of the peak for the LSSE was attributed to the thickness of the sample, which is assumed to be too thin to allow the occurrence of the drag effect. Our results represent to our knowledge the first combined thermal conductivity and SSE measurements in the longitudinal configuration. This allows us to show that the explanation of Siegel *et al.* needs to be expanded as our measurements, shown in Ref. [p9], yield a pronounced peak for κ even for the 200 nm thick YIG sample grown by PLD. The presence of a peak for κ shows that a drag effect could take place, but cannot be detected in our SSE measurements in the same sample, as shown in Fig. 4.16c).
In conclusion our combined thickness and temperature dependent thermal conductivity and SSE measurements find no agreement with the prediction of the phonon-magnon drag model neither for temperature nor the thickness dependence of both parameters. Therefore our results do not agree with the interpretation of a dominating magnon-phonon drag that leads to the peak of the SSE as a function of temperature.

Temperature dependence of the magnon propagation length

Next we focus on a solely magnonic picture of the SSE, which considers only a phononic excitation of the magnons. Using our model of thermally excited magnons (see Sec. 4.2), we can extract the magnon propagation length from our temperature dependent SSC data. Fig. 4.19a) shows exemplary, the fit of eq. 4.3 for three temperatures, while their magnon propagation length as a function of temperature is plotted in Fig. 4.19b). Additionally to the LPE samples used in the measurements in Sec. 4.2, we include thinner LPE grown films to allow a better extrapolation of the propagation length at higher temperatures. Since the films have an up to a factor of four higher Gilbert damping, the error of our derived magnon propagation length is larger. The magnon propagation length shows an increase with lower temperatures, as expected from our results discussed in Sec. 4.2. Additional to our previous findings we obtain a more complete picture, which indicates that the magnon propagation length is proportional to $1/T$, as indicated by the fit in Fig. 4.19b). Following our theoretical model, the propagation length ξ is expected to be proportional to $1/\alpha$. FMR measurements have shown that α follows in highly pure YIG an almost linear decrease as a function of temperature [185–188]. Considering $\xi \propto 1/\alpha(T)$, this dependence quantitatively fits to our observation of an increasing magnon propagation length with decreasing temperature. We can now use this concept of the thermal magnon propagation length to explain the appearance of a peak for SSE solely by a competition between the magnon propagation length and the amount of thermally excited magnons, which is decreasing with temperature.

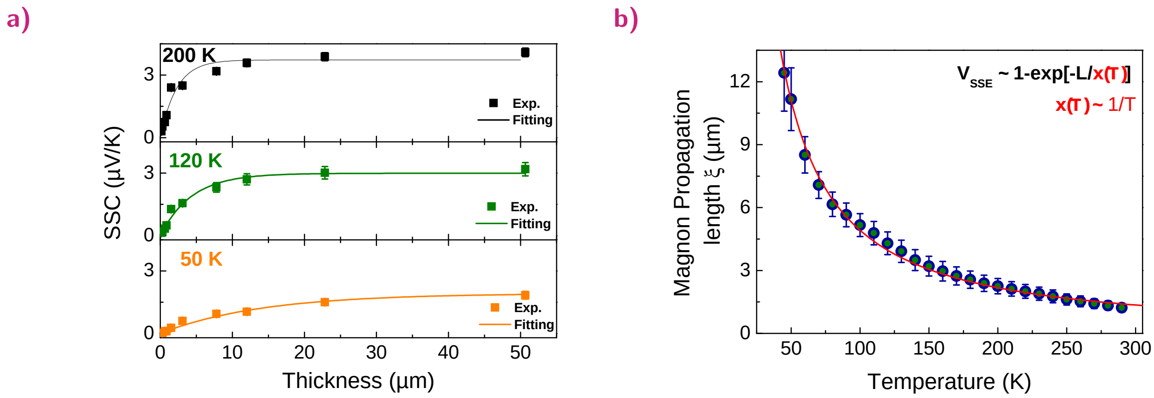

Fig. 4.19: a) SSC as a function of film thickness for three different temperatures. The solid line corresponds to a fit of eq. 4.3. The determined thermal magnon propagation length ξ for more temperatures is shown in b). The solid line shows the fit of $y = a/T^b$ ($a = 1099(109)\,\mu\mathrm{m\,K}$, $b = 1.17(2)$).

Therefore this phenomenological concept is analogue to the one of phonons (see Fig. 2.3). The thickness dependence of T_{peak}^{SSE} can therefore be explained by the propagation length of the thermal magnons, which increases with decreasing temperature and reaches a maximum determined by the boundary scattering. For even lower temperatures the magnon propagation length stays constant. In parallel, the amount of thermally excited magnons decreases for lower temperatures. Their number can be calculated by $N = \int D(E) f(E,T)_{BE} dE$, where $D(E)$ marks the magnonic density of states and $f(E,T)_{BE}$ the Bose-Einstein distribution. Since YIG is a ferrimagnet with an interaction between two magnetic sub-lattices, the material might exhibit a temperature dependent magnonic density of states. For this reason the best approximation for the number of thermally excited magnons is given by the experimentally accessible heat capacity c_m of the magnetic lattice, which as well depends on the number of thermal magnons. For low temperatures thermal conductivity measurements find $c_m \propto T^{3/2}$ [59], yielding a rapid decrease of the amount of thermal magnons. This decrease of thermal magnons leads to a signal decrease, which competes with the signal increase caused by the increasing number of magnons, which reach the detection layer due to a longer propagation length ξ. Since ξ is limited at a certain temperature, a peak for the SSE signal is expected to occur as a function temperature. This phenomenological concept explains well the shift of the peak position to higher temperatures for thinner films, as the boundary scattering limits ξ at higher temperatures.

Additionally one can understand the absence and reduction of the peak in thinner films. At room temperature the magnon propagation length of our fit yields a mean propagation length of $\xi \sim 1.2\,\mu\text{m}$, which represents the mean value of the broad thermally excited magnon spectrum. In the next section we show that the propagation length is also frequency dependent, which is important for this concept as we find that thermal magnons with a high frequency have a shorter ξ than low frequency magnons. As now the temperature decreases, the magnon propagation length for all magnons increases until ξ equals the thickness of the film. For films around $1\,\mu\text{m}$ thickness and thinner, some parts of the thermal magnon spectrum have a mean free path longer than the sample thickness already at room temperature. Thus only a smaller fraction of the magnon spectrum can increase and then be limited at lower temperatures by the boundary scattering, leading to a less pronounced peak closer to room temperature in thinner films. As a result the peak is shifted to higher temperatures and the broader distribution of thermally excited magnons at these temperatures, due to the Bose-Einstein distribution, broadens as well the peak width for the SSE, as can be seen in Fig 4.17. For thicker films, like the bulk sample, the magnon propagation length never reaches the actual sample size. Instead it is expected that the magnon propagation length is at very low temperatures and thick films limited by defect scattering within the materials, which represents the extrinsic contribution ΔH_0 to the Gilbert damping. The scattering at defects and crystal boundaries dominates over the intrinsic contribution in polycrystalline material, which explains the results of Uchida *et al.* [107] who observed no peak in polycrystalline bulk films. Thus our phenomenological model, based on weak interaction between thermal magnons contributing to the SSE and phonons, can give an explanation for the observed temperature and thickness dependence of the SSE.

Two additional points have to be mentioned. Firstly it has to be pointed out that our model is based on the observed $1/T$ dependence for α measured by FMR experiments. The origin of the $1/T$ dependence of α is attributed to the intrinsic relaxation rate of the Fe^{3+} sublattices [187], which takes magnon-phonon and magnon-magnon scattering into account. Since FMR experiments are performed at a stable temperature an influence of a phonon drag effect cannot be detected. Furthermore already a small percentage of rare earth impurities can lead to a divergence of α in the temperature range of $30 - 100\,\text{K}$ [187], which gives another explanation for the appearance of the peak.

Secondly the found $1/T$ is similar to the propagation length dependence of phonons [18,59]. In case of a strong interaction the thermal magnon length propagation would therefore just follow the phononic one. Our model finds that the magnon important for the SSE differ from the thermal magnons probed in thermal conductivity measurements [59], since we determine a peak in κ and the SSE at different temperatures and an orders of magnitude longer mean free path than expected for magnons transferring the heat [59]. Additionally the peak of the magnetic thermal conductivity, equivalent to the one of phonons, is usually found in the temperature range from $10\,\text{K}$ to $50\,\text{K}$ [59] [p9]. This difference in the peak temperature gives a further hint for a difference between the magnons contributing to the thermal conductivity and the magnons important for the SSE [102].

Independent of the explanation, the occurrence of a peak in the SSE signals as a function of temperature indicates, that the SSE is a transport phenomenon [104] from the bulk of the ferromagnet, as an interface based origin can give no explanation for the observed peak and the additionally derived thickness dependence.

Influence of the interface on the SSE temperature dependence

As the last point for the temperature dependence of the SSE, we study the influence of the interface and detection material, since the SSE is always measured in combination with a certain detection layer. In addition to the standard Pt layer we investigate two different scenarios using always a 50 µm thick YIG samples cut from the same wafer. The first test sample uses 6 nm Palladium (Pd) as a detection layer, which allows to determine the peak position for a different spin Hall angle. Our second test sample we separate the YIG and Pt layer by a 2 nm thick Cu layer. This layer allows us to exclude possible proximity magnetization effects in the Pt. Fig. 4.20 shows our results of the temperature dependent SSC measurements for all three probed interface configurations. The measurements show a clear difference for the signal amplitude and peak position, for the different used detection materials. The signal decrease with the additional Cu layer can be explained by the layer itself, since the Cu layer shortcuts the spin accumulation in the Pt. Pd is known to have a lower spin Hall angle [189] than Pt, which explains the lower signals. To allow the comparison of the different detection layers one needs to divide the SSC data by the temperature dependent resistance of the detection stripe, since otherwise contributions unrelated to the intrinsic origin are not excluded. Fig. 4.20 shows the SSC current corrected for the resistance, revealing only small shifts towards lower temperatures. The peak position of the YIG/Pt is shifted by more than 5 K to a

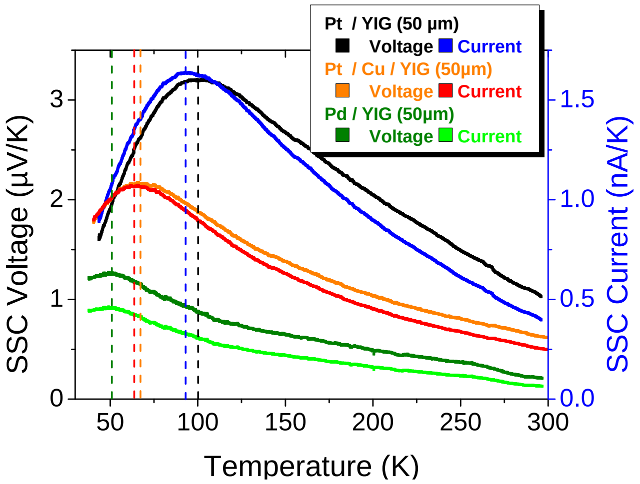

Fig. 4.20: SSC voltage (darker color) and current (brighter color) as a function of temperature. Black and blue represents the YIG / Pt, orange and red YIG / Cu / Pt and light and dark green the YIG / Pd sample.

lower value. It should be mentioned that the shift due to the resistance of the detection layer does not affect our results on the magnon propagation length of the last section, since all used samples have a Pt layer. This leads to an identical shift for all samples, which does not alter the determined magnon propagation length.

The resistance corrected data yield SSE peak temperatures of $T^{SSE}_{\text{peak}} = 94\,\text{K} \pm 5\,\text{K}$ and $T^{SSE}_{\text{peak}} = 65\,\text{K} \pm 5\,\text{K}$ for YIG/Pt and YIG/Cu/Pt respectively. For YIG/Pd the measurements show an even lower peak temperature of $T^{SSE}_{\text{peak}} = 51\,\text{K} \pm 5\,\text{K}$. Our purely magnonic model, cannot explain this discrepancy, since the intrinsic properties determining the magnon propagation length are identical for the samples and therefore the peak temperature should not be affected by the interface or detection material.

The correction of the resistance revealed that a temperature dependent parameter can alter the temperature of the peak. As only the detection layer has been changed, we exclude any influence by the YIG. Therefore the only parameters, which could cause these differences are the spin mixing conductance $g^{\uparrow\downarrow}$ and the spin hall angle θ_{SHE}. Based on the theoretical model, the spin mixing conductance should describe an temperature independent scattering parameter of the interface. Experimental results on this topic are limited and always correlated to influences of the spin Hall angle. Recent results of Meyer *et al.* [190] find no significant temperature dependence of $g^{\uparrow\downarrow}$ or θ^{Pt}_{SHE} in YIG/Pt in agreement with results of Marmion *et al.* [191]. The temperature independence of θ^{Pt}_{SHE} has also been confirmed by spin diffusion experiments [192], allowing us to exclude further temperature influences in our YIG /Pt samples. No experimental reports on YIG/Pd but only on Py/Pd [193] are available. The results show a clear temperature dependence of θ^{Pd}_{SHE} with a linear increase of θ^{Pd}_{SHE} by a factor of two as the temperature decreases from room temperature to $120\,\text{K}$. A correction of our SSC data, based on eq. 2.24, for the sample YIG / Pd yields a SSE peak temperature of $T^{SSE}_{\text{peak}} = 55\,\text{K} \pm 5\,\text{K}$, which is still lower than the one with the Pt.

Based on our current knowledge, we cannot explain the observed discrepancy of the SSE peak temperature even when taking the above mentioned additional temperature dependent parameters into account. A solely bulk based explanation expects the same peak temperatures for all three samples. This assumption is valid for our magnonic concept, as well as for the magnon-phonon drag. The interface dependence of the peak position can explain the difference between our results and the LSSE results reported by Uchida *et al.* [107], and highlight that the close peak position for YIG/Pd to the peak of T^{κ}_{peak} is no indication for a correlation. In case of an influence of the detection layer on the ferromagnet, an explanation can be given by the additional damping parameter. This additional damping would be smaller for Cu/Pt and Pd than for Pt, yielding a longer propagation. Still this model should only be valid for the macrosspin concept (see Sec. 2.3.1), which is only valid for FMR experiments. In Sec. 5, we present our results on the SSE in GIG, showing a more complex temperature dependence compared to the SSE in YIG. In this material as well we observe a strong influence of the detection layer on the investigated effect. Since YIG has been treated as ferromagnet so far, a possible discrepancy of this behavior might originate from the ferromagnetic picture, since it is actually a ferrimagnet. Further temperature dependent and thickness dependent studies of a true ferromagnetic material and different detection layers are needed to provide a more comprehensive picture of the origin of this low temperature behavior of the SSE.

In conclusion, our temperature and thickness dependent SSE measurements find a characteristic temperature dependence, which can only result from a transport dominated effect, confirming the bulk origin. Our combined results of the SSE and thermal conductivity raise questions about the strength of magnon-phonon interaction, and about the origin of the observed peaking of the SSE signals at low temperatures which is in literature attributed to the magnon-phonon drag. Our model of the finite magnon propagation length derives a $1/T$ dependence for the mean magnon propagation length, which we can quantitatively explain by the temperature dependence of the Gilbert damping parameter. Furthermore a phenomenological expansion of the model allows for an understanding of the observed temperature and thickness dependence of the SSE peak. By changing the detection layer and interface, we find a strong change of the SSE peak position, which is in contrast to results expected from the magnon-phonon drag model, as well as from our solely magnonic picture, revealing the limitations of our simple model. To explain the results one would either need to take into account a significant temperature dependence of the ISHE or the spin mixing conductance, which has not been determined so far. Further research of the ISHE and SSE is necessary to understand the found complex dependence of our signals. In the following we present another characteristic dependence of the SSE, which confirms the magnonic origin of the effect but indicates that the effect shows an even more complex behavior for high magnetic fields.

4.4 High magnetic field suppression of the spin Seebeck effect

The discussion of the thickness and temperature dependence of the SSE revealed that a thermally excited magnonic spin current from the bulk of the ferromagnet can explain the observed dependences, while interface related theories are not capable deriving both behaviors. From the discussion of the theory of the magnons (see Sec. 2.2.4), a further signal feature can be predicted for high magnetic fields, which should lead to signal suppression in case of a magnonic origin of the SSE. To understand this behavior we have to include the magnetic field and magnetic anisotropy, which expands the in eq. 2.21 presented dispersion relation for exchange magnons to

$$\hbar\omega(k) = 4J|S|(1-\cos(ka)) + g\mu_B\mu_0 H + 2d_z, \tag{4.4}$$

where the second term presents energy shift by the external magnetic field and the third term the energy change by an magnetic anisotropy (here uniaxial). Both terms cause to a frequency gap at $k = 0$ for the thermally excited magnons, which allows us to shift the dispersion relation to higher frequencies. While its difficult to selectively tailor the anisotropy, the magnetic field enables us to actively suppress the thermal magnon excitation. Thus behavior has been observed for thermal conductivity measurements of the magnetic lattice at temperatures $< 30\,\mathrm{K}$ (see Sec. 2.2.4). In contrast to thermal conductivity measurements, the SSE is only sensitive to contribution of the magnetic lattice and should therefore be more sensitive to changes of the thermal magnon flow within the system. Still the results reported by Kikkawa *et al.* [113] are surprising as they find a magnetic field suppression of the SSE at room temperature. An extrapolation, based on the knowledge of the thermal conductivity measurements, predicts that a suppression should not be observable at room temperature [59], since the amount of suppressed magnons should negligible. Kikkawa *et al.* [113] focus in their investigation of the suppression only on the Pt thickness dependence. Since they are not able to determine any influence on the suppression, they conclude that the behavior can be attributed to material itself and not the interface.

Our in the following shown study takes up their results and presents a more systematic investigation of the field suppression combined with a explanation based on the numerical simulations of the atomistic LLG equation (see Sec. 2.4.3 and 4.2), performed by U. Ritzmann of the group of Prof. U. Nowak of the University of Konstanz.

The following sections presents work in progress of the joined publication [p6].

4.4.1 Magnetic field suppression at room temperature

The SSE measurements shown so far were limited to magnetic fields of up to $30\,\mathrm{mT}$, for which we did not observe any signal suppression by the magnetic field, as shown in Fig. 4.3. The determined signal behavior revealed only a dependence on the sample magnetization, leading to a saturation at magnetic fields high enough to completely align the magnetization (see Sec. 4.1.5). To observe a noticeable influence of the field suppression at room temperature, we found that it is necessary to use magnetic fields higher than $0.2\,\mathrm{T}$. An example of a high field measurement up to $9\,\mathrm{T}$ of a $50\,\mu\mathrm{m}$ thick YIG sample is shown in Fig. 4.21a). All measurements have been performed in the cryostat setup described in Sec. 4.3.1. The signals show a non-linear decrease with increasing magnet field strength down to $70\,\%$ of the low field signal. The inset of Fig. 4.21a), shows the low field behavior, indicating that the signal dependence does not result from a misalignment of the sample. A misalignment leads to signal decrease for small fields up to $\sim 180\,\mathrm{mT}$, which corresponds to the saturation field for YIG ($M_s = 140\,\mathrm{kA/m}$), but has no effect on the signal for higher fields.

We investigate a second sample of YIG/Cu/Pt with an additional copper layer to determine the influence of MR of the Pt layer and interface on the field suppression. The $2\,\mathrm{nm}$ thick copper layer allows to exclude any proximity magnetization in the Pt layer. The measurements, shown in Fig. 4.21b), are normalized to the low field value, since the $2\,\mathrm{nm}$ thick Cu layer reduces the signal amplitude by $38\,\%$. The sample shows the same field dependence as the first sample, indicating that the origin of the observed field suppression must originate from the ferromagnetic material.

For better comparison, the inset of Fig. 4.21b) shows only the positive magnetic field region. Both signals agree within the experimental measurement error, substantiating our assumption. The observed behavior agrees with the theory of the SMR (see Sec. 2.3.3) and our results of the thickness dependence of the SSE (see Sec. 4.2), which expect no further contribution to the SSE signal for fields higher than the saturation field. Since we can rule out the interface as the source of the observed behavior, we probe the dependence of the field suppression on the YIG film thickness. Fig. 4.22a) shows the normalized high field SSE hysteresis measurements for 8 different thicknesses ranging from 300 nm to $50\,\mu$m. The data have been normalized to the maximum voltage for a better comparison, since the thickness dependence of SSE (see Sec. 4.2) and variations of the interface quality lead to different signal heights unrelated to the field suppression. Our measurements find a systematic thickness dependence of the high field suppression of the SSE signals. For thicker films we observe a higher suppression than for thinner films, leading to no visible suppression for the 300 nm thick film, as shown in Fig. 4.22b). In all samples the field suppression shows a non-linear behavior, indicating a leveling off at much higher fields than accessible with our experimental setups.

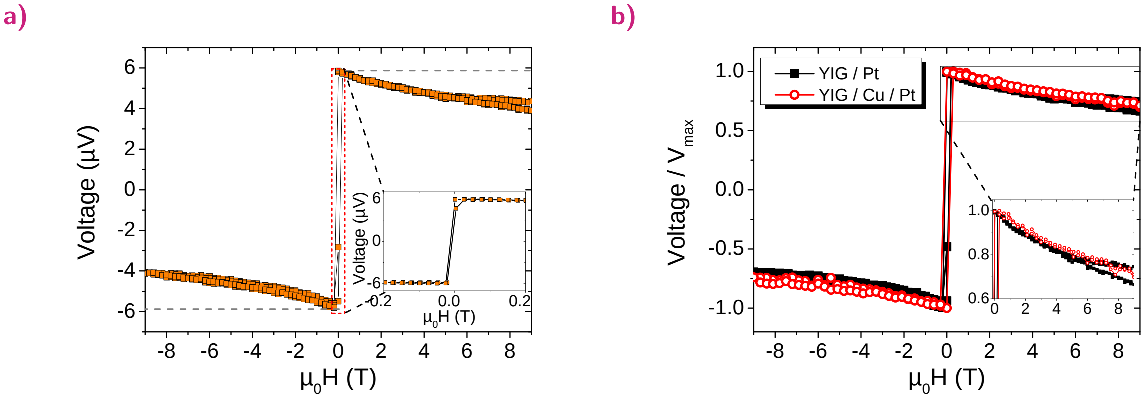

Fig. 4.21: a) SSE hysteresis measurement of a $50\,\mu$m thick LPE grown YIG film, using Pt as the detection layer. The grey line indicates the initial voltage signal directly after the switching of the magnetization. The region indicated by the red rectangle marks the so far discussed low magnetic field region, also shown in the inset. b) Comparison between SSE hysteresis measurements for YIG/Pt and YIG/Cu/Pt, normalizing the signals to the maximum signal determined at low magnetic fields. The inset shows a close up of the positive field region. The difference between the two branches for the YIG/Pt signals results from a temperature drift. The data have been linearly connected as guide to the eye.

Using the numerical simulation model introduced in Sec. 2.4.3 and 4.2, we can give a qualitative explanation of the observed behavior. Besides the exchange interaction, we additionally consider the magnetic field dependence. Identical to the thickness dependence simulations, the magnon accumulation Δm at the end of the temperature gradient is determined for different lengths L of the temperature gradient, corresponding to variations of the sample thickness in the experiments. The temperature gradient is kept identical, independent of its length, which yields for the simulated system a propagation length of $\xi = 72\,a$, where a is the lattice constant of the cubic system (see See. 4.2).

Fig. 4.23a) shows the influence of an additional external magnetic field on the magnon accumulation. For increasing field strength the total amount of magnon accumulation detected at the end of the temperature gradient decreases. Furthermore we derive from the fit a decrease of the mean magnon propagation length with increasing field strength. This shorter mean propagation length leads to a smaller signal amplitude for higher fields, since less magnons reach the detection layer. To provide a better comparison with our experimental probing configuration we plot the magnon accumulation as a function of the magnetic field, as shown in Fig. 4.23b). To eliminate the influence of the non field dependent propagation length

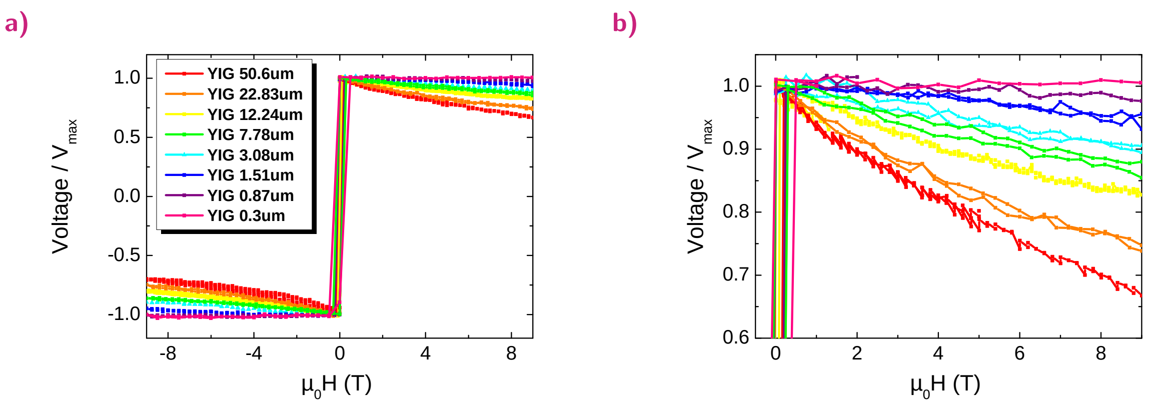

Fig. 4.22: a) SSE hysteresis measurements for LPE grown YIG for film thickness of $300\,\mathrm{nm}$ to $50\,\mu\mathrm{m}$. b) Close up of the positive field region using the same color code for the thickness of the films. The data have been linearly connected as guide to the eye.

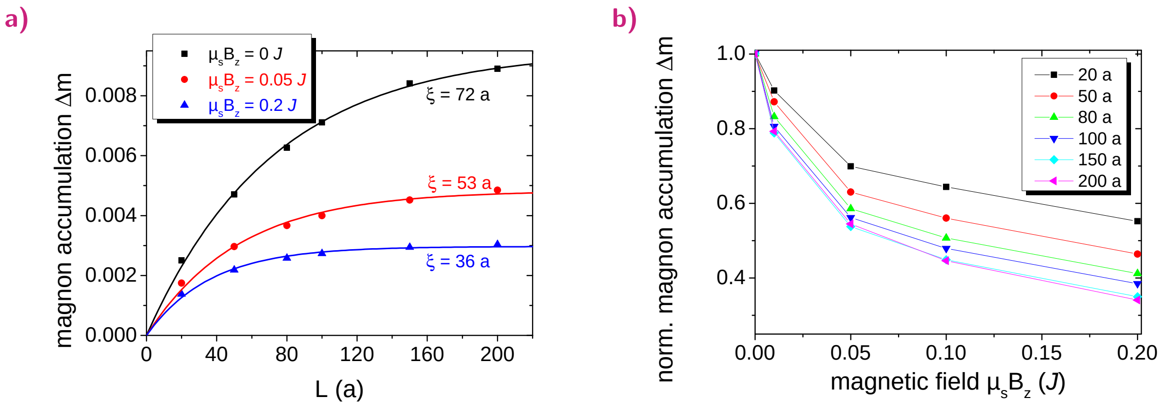

Fig. 4.23: a) Magnon accumulation Δm as a function of the length L of the temperature gradient. The black points correspond to the simulation without applied field. For the red and blue simulations magnetic field of $0.05\,J$ and $0.2\,J$, in units of the exchange constant J, has been used. The solid lines correspond to fits of eq. 4.3. b) Magnon accumulation Δm normalized for the zero field value as a function of the applied field. Each color represents a different length L of the temperature gradient. The data have been linearly connected as guide to the eye and have been taken from Ref [p6].

(see Sec. 4.2.3), which causes the shift of Δm for zero field, we normalize the data to the zero field value. The accumulation shows a decrease with the magnetic field similar to the one observed in the experiments, shown in Fig. 4.22b). Since the magnetic field alters the magnon propagation, the accumulation depends on the length L of temperature gradient as seen in the experiments. To provide a more qualitative comparison, we determine the functional dependence of the field suppression. As can be seen in Fig. 4.24, the simulated, as well as the experimentally observed field suppression can be described by an exponential decay. The simulations show a more pronounced saturation than experimentally observed for the SSE signals.

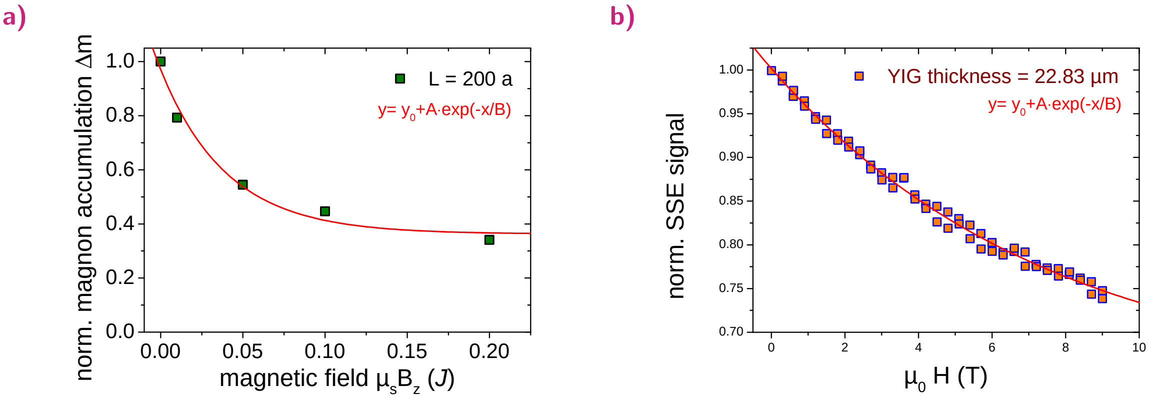

Fig. 4.24: Normalized simulated magnon accumulation a) and experimentally determined SSE signal b) as a function of external magnetic field. The solid line corresponds to a fit of $y = y_0 + A \cdot exp(-x/B)$, which yields $y_0 = 0.363(4)\ \Delta m, A = 0.61(6)\ \Delta m, B = 0.04(1)\ a$ and $y_0 = 0.64(2), A = 0.36(1), B = 7.5(5)$ T for the simulation and the experimental data, respectively.

This difference results from the fact that $\mu_s B_z = 0.2\,J$ roughly corresponds to $200\,$T, which is beyond our experimental capabilities. To compare the thickness dependence of the experiments with the one obtained from the simulation, one needs to plot the normalized accumulation and SSE signal for a fixed field as a function of the film thickness, as shown in Fig. 4.25. Qualitatively the simulated and measured data show the same behavior as a function of the thickness following an exponential decay with the film thickness. The functional agreement for the field and thickness dependence indicates that the intrinsic origin of the suppression can be explained by our magnonic simulations, although the relation between the functional parameters and intrinsic mechanisms causing the exponential decay is currently unclear.

To obtain a deeper understanding, we change to an analytical description of the propagation length. Using the solution of the linearized LLG, one is able to show [54] [p6] that the magnon propagation length can be related to the frequency gap of the dispersion relation in eq. 4.4.

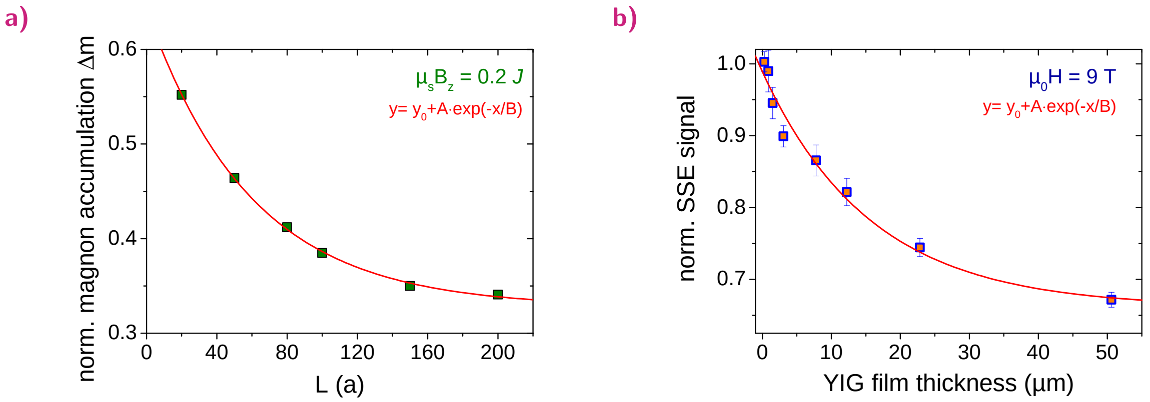

Fig. 4.25: a) Normalized magnon accumulation Δm and as a function of the length L of the temperature gradient for $0.2\,J$. b) normalized SSE signal as a function of the YIG film thickness for $\mu_0 H = 9\,\mathrm{T}$. The solid line corresponds to a fit of $y = y_0 + A \cdot exp(-x/B)$, which yields $y_0 = 0.328(4)\ \Delta m, A = 0.314(5)\ \Delta m, B = 60(3)$ L and $y_0 = 0.66(2), A = 0.33(2), B = 16(3)$ µm for the simulation and the experimental data, respectively.

The analytical model yields a propagation length of

$$\xi_{\omega_q} = \frac{\sqrt{J^2 - (\frac{1}{2}(\hbar\omega_q - \hbar\omega_{min}) - J)^2}}{\alpha\hbar\omega_q}, \tag{4.5}$$

for a magnon of a certain frequency ω_q, where $\omega_{min} = \mu_s B_z + 2d_z$ marks the frequency gap caused by the magnetic field and uniaxial anisotropy. Since the dependence on ω_{min} and ω_q is not directly obvious from eq. 4.5, it is plotted as a function of ω_q and ω_{min} in Fig. 4.26.

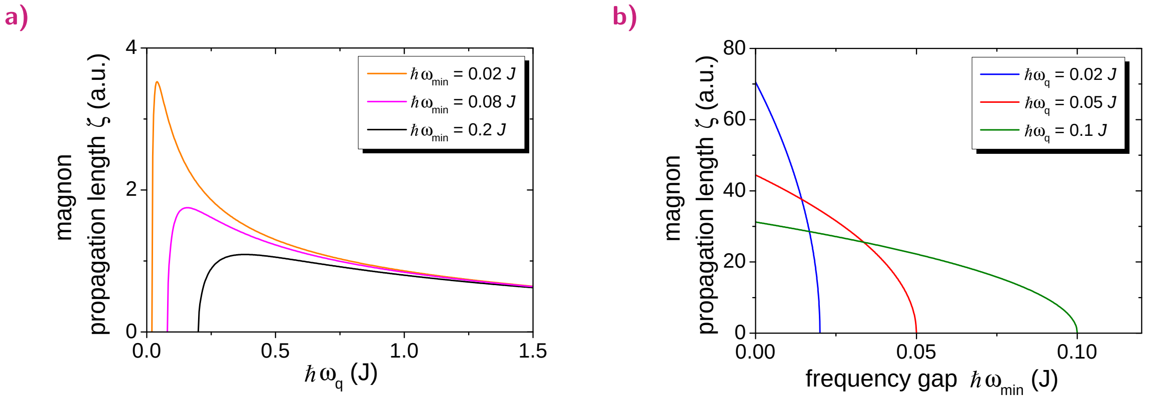

Fig. 4.26: Calculated magnon propagation length ξ as a function of the magnon frequency ω_q a) and as function of frequency gap ω_{min} b) using eq. 4.5, in units of the exchange constant J. All graphs have been calculated for a fixed Gilbert damping value of $\alpha = 0.001$.

For ξ as a function of the magnonic frequency it can be seen that the ξ is very small for low frequency magnons and steeply increases with frequency and shows a peak, shown in Fig. 4.26a). The increase and peak shift towards higher energies as ω_{min} increases, which corresponds to a higher applied magnetic fields or magnetic anisotropy. In contrast to this the propagation length for magnons with a higher frequency is less affected by ω_{min}, as all curves converge at high values. For a fixed magnon frequency, one can see in Fig. 4.26b), that the magnon propagation length ξ decreases as the frequency gap ω_{min} or respectively the magnetic field increases. Furthermore the plot reveals that magnons with a low frequency propagate further, but are more affected and therefore earlier suppressed the field gap than magnons with a higher frequency. This information is important for a deeper understanding, as the shown simulations only contain information about the mean magnon propagation length, which averages over all contributing magnons. Ref. [p6] contains a more complex analysis of the contributing magnon spectrum based on a Fourier analysis of the magnetic excitations in the simulations, which yields a similar result to the analytical description.

Based on the knowledge of frequency dependence of the field suppression, one can understand the signal suppression for higher magnetic fields. The higher magnetic fields not only reduce the amount of thermally excited magnons by a gap in the spectrum but also reduces the length of magnonic propagation, the more the lower the frequency of the magnon. The propagation length of high frequency magnons is less affected by the magnetic field than the one of low frequency magnons, leading to a faster signal reduction for low magnetic fields and levelling for higher fields. In contrast to a shifted cut-off frequency, which just reduces the total amount of magnons, this explanation holds for all temperatures and can therefore explain our observation of a field suppression at room temperature. Additionally this concept can explain the weaker field suppression in thinner samples, as the propagation length even for low frequency magnons is closer to the sample thickness. Thus for higher fields, the amount of magnons which are hindered from reaching the Pt interface is lower in thin film samples than in samples thicker than the mean propagation length. The high percentage of field suppression of $40\,\%$ indicates that magnons which dominate the SSE signal are different from magnons transferring the heat in the system. As mentioned in the beginning, less then $2\,\%$ [59, 194] of these magnons are expected to be suppressible at these high temperatures assuming that the magnon gap opening dominates the SSE. Like the low temperature measurements this indicates that the measured magnons [102] are different from the thermal conductivity magnons and can be qualitatively described by the model developed by the group of Prof. U. Nowak.

To obtain a more complete picture of the influence of the magnetic field suppression and its correlation with the frequency gap, we present in the following our results on the combined temperature and high magnetic field strength measurements.

4.4.2 Temperature dependence of the magnetic field suppression

For our investigation of the temperature dependence of the magnetic field suppression we use an LPE grown YIG $50\,\mu$m/Cu $2\,$nm/Pt $6\,$nm sample. We perform SSE hysteresis measurements at different temperature up to a magnetic field of $9\,$T. Fig. 4.27a) shows the complete field dependence for different temperatures, while Fig. 4.27b) depicts only the positive field region for better overview.

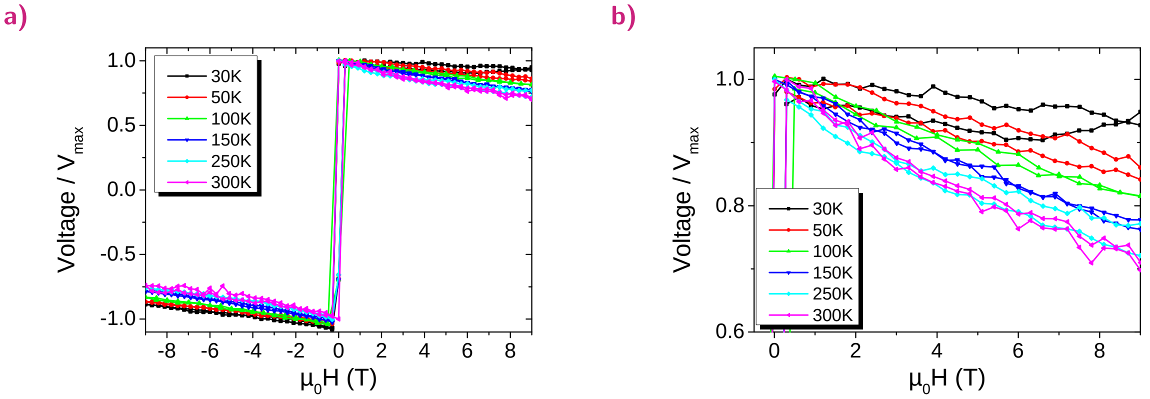

Fig. 4.27: a) SSE hysteresis measurements for an LPE grown YIG film coated with a Cu/Pt detection layer. The hysteresis loops are normalized to the low field signal. b) Close up of the positive field region. The data have been linearly connected as guide to the eye.

Our experimental results reveal a weaker SSE signal suppression for lower temperatures than for higher temperatures. This finding is in contrast to the concept of the frequency gap, which expects the inverse behavior if this effect was dominating, since more magnons can be suppressed by the magnetic field, the lower the temperature [59]. It furthermore underlines the difference between the magnons responsible for the heat transport and the ones of the SSE. To emphasize our results we plot the normalized SSE signal at $9\,\mathrm{T}$ as a function of temperature in Fig. 4.28a).

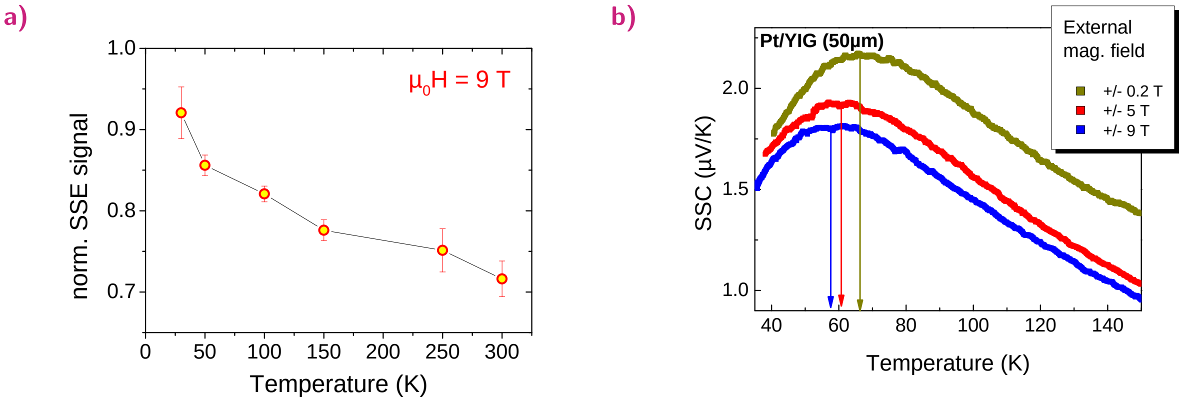

Fig. 4.28: a) SSE signal normalized to the zero magnetic field value as a function of temperature for an applied magnetic field of $9\,\mathrm{T}$. b) Temperature sweep SSE measurements for different applied magnetic fields.

The data clearly indicate that the magnetic field suppression is reduced for lower temperatures. From our concept this can be understood as a result of the increasing propagation length $\xi(T) \propto 1/T$ with decreasing temperatures (see Sec. 4.3.2). On the other hand the high magnetic field counteracts this trend by reducing the magnonic propagation length.

Therefore the ratio between the suppressed and the initial length for propagation changes as a function of temperature, which results in a similar signal trend for thicker samples at low temperatures and thinner samples at higher temperatures. Thus we determine an equally high field suppression at $30\,\mathrm{K}$ in our $50\,\mu\mathrm{m}$ sample and in our $3\,\mu\mathrm{m}$ sample at room temperature. This interpretation is in agreement with the thermal conductivity measurements, which expect no noticeable reduction of the total magnonic spectrum at both temperatures [59].

Another indication for the validity of our concept can be obtained from the temperature sweep measurements at fixed high magnetic fields, shown in Fig. 4.28b). The SSE peak shifts to lower temperatures the higher the applied magnetic field. This observation cannot be explained by a pure magnon-phonon drag model, which expects no shift. However, the concept of suppression and increase of the propagation length can explain the measured behavior. At room temperature the propagation length is reduced by the magnetic field, explaining the lower signal for higher fields. Therefore the propagation length can increase upon cooling until it is limited by the intrinsic boundary scattering mechanism. Since the propagation length increases with $1/T$ independent of the applied field, the peak temperature is determined by the initial propagation length and therefore shifts the peak to lower temperatures for higher fields.

In conclusion we have shown that the magnetic field dependence of the SSE can be understood by our model of the thermal magnon propagation length. The model finds an influence of the magnetic field on the propagation length, showing a reduction for higher magnetic fields. We can furthermore link our model to the frequency gap in the magnonic dispersion relation, which by itself can neither explain the found behavior at room temperature nor the temperature or thickness dependence. In contrast to this, the propagation length model can qualitatively explain our results from the thickness and magnetic field strength dependent measurements and phenomenologically describe the combined magnetic field strength and temperature dependence. This highlights the advantages of our model compared to other concepts like the magnon-phonon drag, which are unable to explain all of the observed effects.

Further high field measurements at even lower temperatures could strengthen our model, since at temperatures of $10\,\mathrm{K}$ and lower the thermal conductivity is dramatically reduced by the frequency cut off, presumably causing a sharper reduction of the SSE signals. Such measurement would give an insight to the correlation between magnons responsible for the thermal conductivity and the ones for the SSE. Additional combined high field and low temperature measurements with different detection materials will provide a better understanding of the detection mechanism itself, since the high field suppression allows one to select the contributing parts of the magnonic frequency spectrum. This might explain the found shift of the peak position caused by the detection material.

4.5 Conclusion of the SSE in YIG

The work presented in this chapter aims at enhancing the understanding of the SSE. Based on the magnonic concept of the SSE, we explained the basic dependences of the SSE like the linear increase with applied temperature difference and that the magnonic spin current follows the orientation of the magnetization of the sample. Exemplarily we showed that this allows one to probe the magnetic anisotropy of the ferromagnetic, which presents a novel application of the SSE. A first concept for the determination of the absolute SSE efficiency was presented, which is of major importance for future applications. After these basic introductions, we used thickness dependent measurements at room temperature to show that the SSE can be explained by thermal magnons excited in the ferromagnetic layer, which confirms the magnonic model used so far. The results of our combined temperature and thickness dependent SSE and thermal conductivity measurements yield a disagreement in the peaking of both effects. Using a phenomenological extension of our magnonic concept we are able to explain the observed behavior, which highlights its advantages compared to current concepts like the magnon-phonon drag. Further measurements with different detection materials find a significant influence pointing out limitations of the simple magnonic model. Our systematic and comprehensive study revealed that, as expected from a magnonic origin, the magnetic field has a non-negligible influence on the magnetization dynamics of the ferromagnet. The magnonic model derives a qualitative agreement with the magnetic field suppression over the complete investigated temperature range. Furthermore the low temperature and the high magnetic field strength measurements yield that the magnons contributing to the SSE must differ from the magnons responsible for the thermal conductivity of the magnetic lattice. Our work presents an important contribution to the understanding of the origin and complex dependences of the SSE as we undoubtedly show that the effect can be understood by the concept of magnonic spin currents emitted by the bulk of the ferromagnet.

In the following and last chapter of this thesis, we present results of SSE measurements in a ferrimagnetic material, which again highlight that not only our magnonic concept holds, but also that the true ferrimagnetic nature of the material has to be considered in order to provide a sufficient explanation of the SSE in more complex materials.

5

Spin Seebeck effect in Gadolinium Iron Garnet

Most experimental investigations of the SSE in insulators have been performed in ferromagnets, such as $CoFe_2O_4$[1], or ferrimagnets that show a temperature dependence similar to a ferromagnet like YIG or substituted garnets, such as Bi:YIG [108]. Despite the ferrimagnetic order of YIG, the theoretical description of the SSE in insulators commonly relies on ferromagnetic models. These models derive a direct correlation between the SSE and the net magnetization of the material. The presented low temperature experiments for YIG could show that the SSE does not follow the temperature dependence of the magnetization but rather can be described by magnons emitted by the magnetic lattice. Recent high temperature experiments measuring the SSE up to T_{Curie} of YIG [174], revealed a similar discrepancy between the magnetization of the material and the SSE amplitude. Both types of experiments pointed out that a description by a solely ferromagnetic model is not sufficient to explain all observed dependences of the SSE.

In the following we will present temperature dependent SSE measurements in the insulating ferrimagnetic garnet Gadolinium Iron Garnet ($Gd_3Fe_5O_{12}$, GIG). GIG exhibits a ferrimagnetic temperature dependence of the magnetization, showing a magnetic compensation point (T_{comp}) for the bulk material at around $280\,\mathrm{K}$. A detailed introduction to the origin of the magnetic properties and the growth of thin film GIG is given in Sec. 3.2.3. Our measurements reveal a correlation between the SSE and the magnetic compensation point, as well as an additional second signal feature hinting to a more complex behavior of the SSE than explainable by a simple magnetization model.

In the beginning of this chapter we first give an overview of the complete temperature dependence for the SSE measured in thin GIG films, which shows two sign changes as a function of temperature. Our study of the first sign change at higher temperatures reveals that its temperature is close to T_{comp}. This correlation is investigated for different T_{comp} and interface materials showing good agreement between the temperatures of both features. Afterwards the dependence on the detection material and the interface for the second sign change is presented, revealing another mechanism as the origin. At the end of this chapter we introduce two theoretical models, which are both able to explain our experimentally observed signal features by a competition between the magnetic sub-lattices of the material. The results presented in this chapter are part of the joined publication [p7] by the Walther-Meißner-Institute, the Tohoku University and of the University of Mainz and partially belong to work in progress for publication [p8].

---

[1] private communication

5.1 Probing the spin Seebeck effect in a compensated ferrimagnet

As a first example we present our initial results of the temperature dependent measurements of the SSE in GIG, which triggered our further investigation of the correlation between the SSE and the magnetic sub-lattices of GIG. For our measurements we use a 100 nm thick GIG film grown by PLD on a GGG (001) substrate, using an oxygen pressure of 2×10^{-2}mbar at $650°$C. The deposition conditions for this sample deviate from the later presented samples, as beam optics, pressure sensors and substrate heating processes of the PLD chamber had been further developed after this first sample. The Pt detection layer of 8 nm was not patterned leading to small signal artifacts due to misalignment of the voltage contacts with respect to the applied magnetic field. For our measurements we use the $3D$ low temperature setup introduced in Sec. 4.3.1. Identical to the SSE measurements in YIG, we record SSE hysteresis loops at different temperatures, to extract the SSE signal as the voltage difference of the saturated signal. The measurements yield the typical hysteresis shape for the thermoelectric signal, which follows the magnetization of the sample. Fig. 5.1a) shows three of these SSE hysteresis measurements for 285 K, 165 K and 45 K.

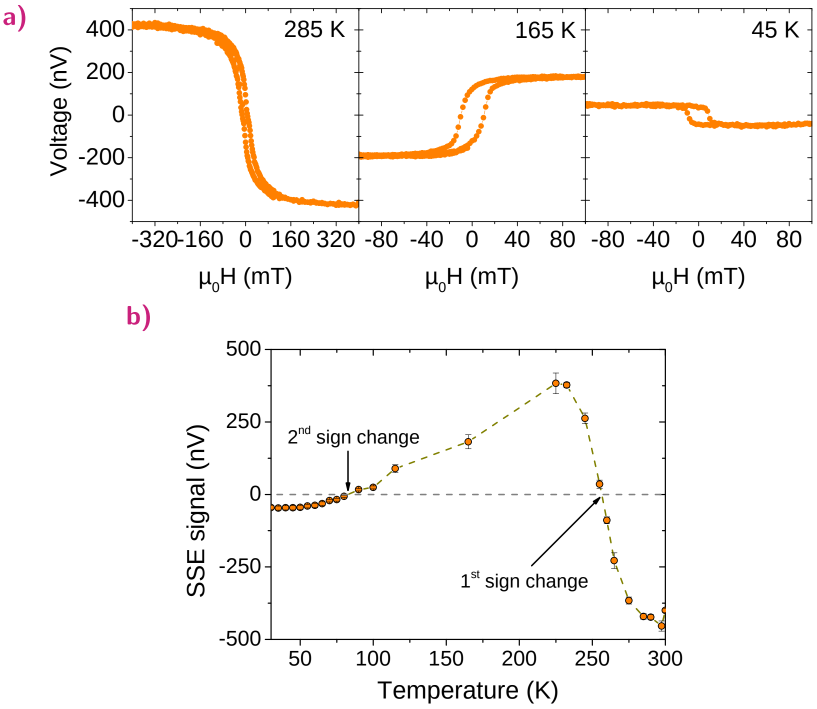

Fig. 5.1: a) SSE hysteresis measurements for three different temperatures. b) SSE signal as a function of temperature. The shown temperature dependence is part of Ref. [p7].

The hysteresis measurement for 285 K and 45 K show a similar field dependence but an order of magnitude smaller signal amplitude for the lower temperature. For a sample temperature of 165 K, the measured SSE signal exhibits a mirrored behavior compared to the other two, which results in an inversion of the SSE signal. By repeating the measurements shown in Fig. 5.1a) for further temperatures, we obtain a more detailed picture of the temperature dependence of the SSE, shown in Fig 5.1b). The entire temperature dependence of the SSE signals, reveals two sign changes as a function of temperature. The first sign change appears at a temperature of around 257 K, causing an inversion of the signal compared to room temperature. For lower temperatures of around 82 K we observe a second sign change, restoring the SSE signal sign to the one observed at room temperature. To determine the correlation to the sample magnetization, we probe the magnetization by SQUID magnetometry, which reveal a temperature of about 285 K ± 5 K for the magnetic compensation point. Compared to the first sign change of the SSE this means a temperature difference of 25 K. Based on net magnetization, one expects an agreement in temperature between T_{comp} and the first sign change. Since our initial sample design and temperature measurement have not been optimized to provide a high temperature accuracy, we cannot exclude that a systematic error. To exclude our measurement method as the origin of this temperature discrepancy and to obtain a more detailed picture of the temperature dependent behavior of the SSE, we improved the measurement method by changing from the hysteresis to the temperature sweep measurement method, using a more compact sample stack geometry (see Sec. 4.3.1). The almost continuous measurement provides a more coherent picture of the SSE signal as a function of the temperature and by this allows us probe the temperature width of the sign transitions.

The second sample used for the comparison measurements is a 100 nm thick GIG sample grown by PLD in on GGG (001) substrate at the optimized growth conditions discussed in Sec. 3.2.3. To minimize the influence of the geometry, we structured the 5.5 nm thick Pt layer into two stripes, which enables us to simultaneously probe the SSE and the surface temperature of the GIG. To verify our data and to exclude systematic errors we perform additional SSE hysteresis measurements at selected temperatures. Fig. 5.2a) shows four SSE hysteresis measurements at different temperatures.

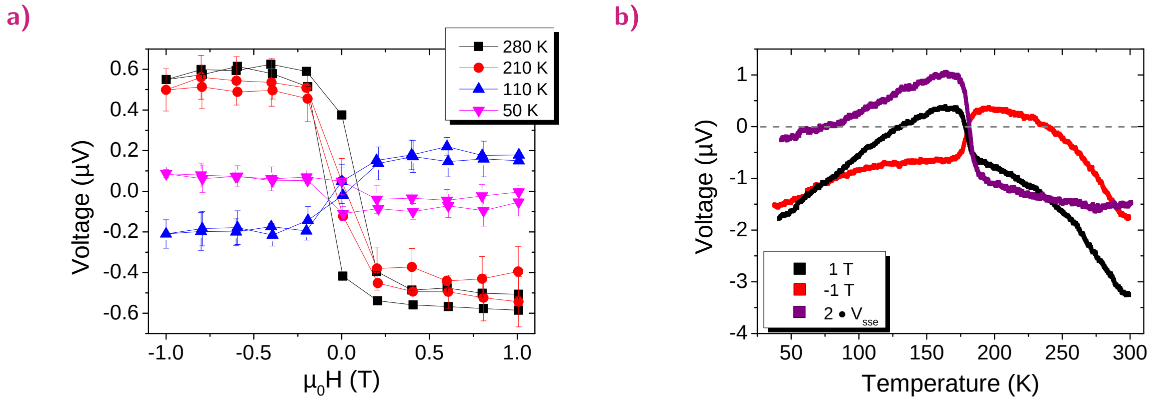

Fig. 5.2: a) SSE hysteresis measurements at four different temperatures. b) The red and black curve correspond to the raw signals of the temperature sweep measurements for 1 T and −1 T. The purple curve marks the signal difference $V_{1\,\mathrm{T}} - V_{-1\,\mathrm{T}}$.

The corresponding sweep measurements are shown in Fig. 5.2b). A magnetic field strength of 1 T has been used for the positive and negative magnetic field for the sweep measurements to guarantee a saturation of the SSE signals. From the SSE hysteresis loops in Fig. 5.2a) we can see that the field is sufficient to saturate the magnetization of the GIG film. We use the temperature determined from the Pt stripe on top of the GIG and below the substrate, to normalize the SSE signal of both measurements methods to the applied temperature difference, shown in Fig. 5.3. The data show an agreement of signal amplitude, sign and transition temperature within the measurement errors, highlighting the validity of our sweep measurement.

In order to allow a better comparison between the SSE signals and the net magnetization of the sample, the SQUID magnetometry data are shown in the top of Fig. 5.3.

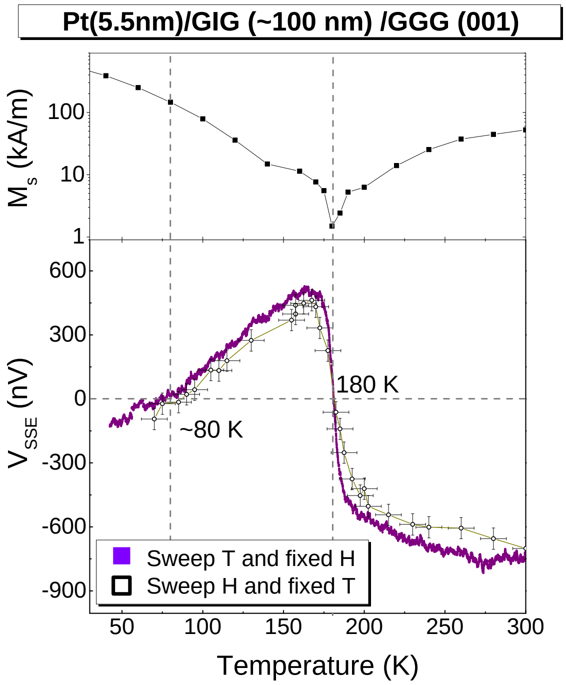

Fig. 5.3: Combined SSE signals of the results from the hysteresis measurements and sweep mode measurements as a function of temperature. The top graph shows the magnetic moment as a function of temperature determined by SQUID magnetometry.

Starting at 300 K, both measurement methods yield a SSE signal strength of around 600 nV, which decreases as the temperature decreases. Close to $T_{comp} = 180\,\mathrm{K} \pm 5\,\mathrm{K}$ the signal rapidly goes to zero and undergoes the first sign change, as in our first sample. We determine the same temperature of $180\,\mathrm{K} \pm 5\,\mathrm{K}$, for the sign change and magnetic compensation. This good agreement in temperature, determined with our more detailed analysis, highlights that our first results might be influenced by a systematic temperature offset. This offset can result from inhomogeneities in the GIG film and voltage contact misalignment, which both are caused by the unstructured Pt layer. Another reason for the offset could be the omitted correction of temperature using the Pt detection stripe on top of the film.

After this first sharp sign change of the SSE signal, the amplitude decreases further until it again goes to zero at $\sim 80\,\mathrm{K}$. This temperature marks a second transition as the signal amplitude rises again for lower temperature but shows the same sign as for temperature above the first sign change. From the temperature dependence of the total magnetization, one would expect only a signal decrease below T_{comp}, identical to the temperature dependence observed for YIG (see Sec. 4.3.1). The measured second sign change at $80\,\mathrm{K}$ thus presents a novel feature, which clearly deviates from the expectation of a ferromagnetic model, which only considers the total magnetization.

In order to verify that the found signal features results for the SSE and not from other parasitic effects within our setup, we test two fundamental dependences of the SSE. Since these dependences do not change the signal shape of the SSE, the two tests should not influence the two sign changes.

As a first control of the origin of these two sign changes, one needs to investigate the dependence on the applied temperature difference. Since the compensation point marks an intrinsic material parameter, its temperature will not be affected by the applied temperature gradient. On the other hand parasitic thermoelectric effects will increase with increasing temperature difference, causing a shift of the temperatures of the two observed sign changes.

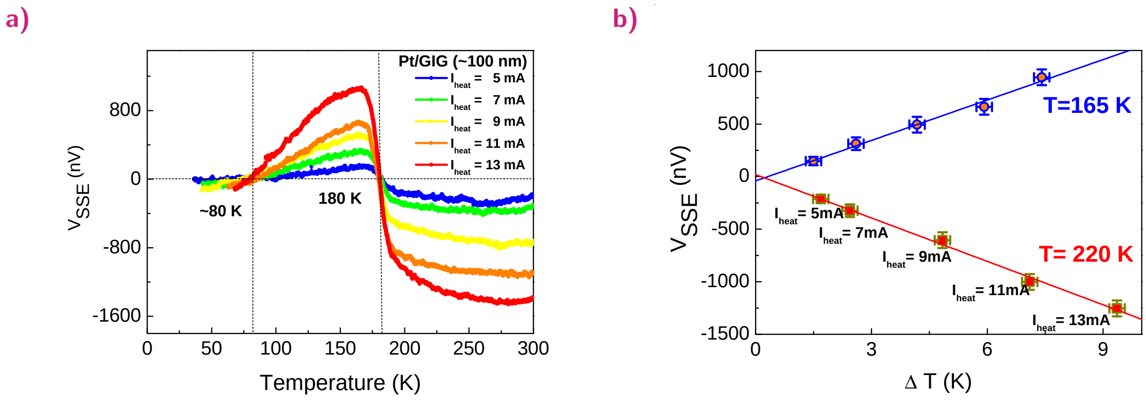

Fig. 5.4: a) SSE sweep measurements for different applied heating currents. The resulting temperature difference over the sample is proportional to I^2. b) SSE signal amplitude as a function of the applied temperature difference for $T = 250\,\mathrm{K}$ (red) and $T = 165\,\mathrm{K}$ (blue). The solid line correspond to linear fits of the data.

The measurements shown in Fig. 5.4a) find no influence of the applied temperature difference on either the first or the second sign change, allowing us to conclude that both sign changes must originate from the SSE of the GIG film. A second verification of the thermal spin current origin of the signals, is provided by controlling the signal's scaling with the applied temperature difference to the sample. From the previous measurements we expect a linear amplitude increase, where a deviation of this behavior hints to another influence on the measured signals. Using the resistance of the Pt stripe on the substrate below and the Pt stripe on top of the sample, we calculate the temperature difference applied to the sample for the different heating currents (see Sec. 4.3.1). Fig. 5.4b) shows the SSE signal strength as a function of the derived temperature difference above ($T = 250\,\mathrm{K}$) and below ($T = 165\,\mathrm{K}$)

the magnetic compensation point and first sign change. For both temperatures, we find the expected linear dependence of the signal amplitude on the applied temperature difference, which is a characteristic feature of the SSE (see Sec. 4.1.3). Thus both tests allow us to exclude other signal sources than the SSE as an origin for the observed two sign changes.

5.1.1 Measurement of the compensation point

The agreement between the temperature of the magnetic compensation point and the first sign change of the SSE hints to a direct correlation. In order to verify this dependence, the possibility to tailor T_{comp} with the thickness of the GIG film provides an ideal tool to probe this conjecture (see Sec. 3.2.3). The combined results of SQUID magnetometry and SSE measurements of four GIG films with different thicknesses, deposited at different oxygen pressures, are shown in Fig. 5.5. The films, shown in Fig. 5.5a), belong to batch 1, which has been produced at an oxygen pressure of 5×10^{-2} mbar, while the doubled pressure of 1×10^{-1} mbar has been used for batch 2, shown in Fig. 5.5b). As discussed in Sec. 3.2.3, the higher oxygen pressure during the deposition increases T_{comp} by 100 K for the samples thinner than 100 nm. From our x-ray and SQUID analysis we could only exclude oxygen vacancies as the origin of the shift, while other sources like an off-stoichiometry need to be investigated.

Despite its unknown origin, the difference for T_{comp} allows us to highlight that the temperature of the first sign change of the SSE essentially agrees with the temperature of the compensation point. This behavior seems to be independent from the deposition condition or from the film thickness. For films shown in Fig. 5.5a) the first sign change shows a sharp transition for both the thin and thick films. For the 41 nm thick film the first sign change is 10 K higher than T_{comp}, while for the 155 nm sample we observe the first sign change 10 K lower than T_{comp}. The observed temperature difference between T_{comp} and the first sign change is within the combined errors of the SQUID and our SSE measurement. For the films grown at an oxygen pressure of 1×10^{-1} mbar, shown in Fig. 5.5b), we as well find an agreement of T_{comp} and the first sign change within the accuracy of both methods. The 28 nm film of this batch shows a much broader first transition than the similar thick 41 nm film, which was deposited at half the oxygen pressure. Despite the thinner film thickness but similar Pt thickness the 28 nm GIG film shows an in general higher signal than the 41 nm with a maximum voltage of $\sim 0.7\,\mu$V compared to $\sim 0.4\,\mu$V. Similarly the 130 nm thick film of batch 2 has twice the SSE signal amplitude at 300 K of the 155 nm thick samples of batch 2. Taking the higher T_{comp} and the higher magnetic moment for temperatures below 100 K, seen in the upper part of both graphs of Fig. 5.5, into account, we attribute this behavior to a difference in stoichiometry between both batches. Since T_{comp} results from the ratio of the Gd to Fe concentration, a higher T_{comp} might be caused by a higher concentration of Gd within samples of batch 2.

Further SSE and SQUID measurements for more samples are summarized in Fig. 5.6a). All investigated samples show an agreement between the temperature of the first sign change

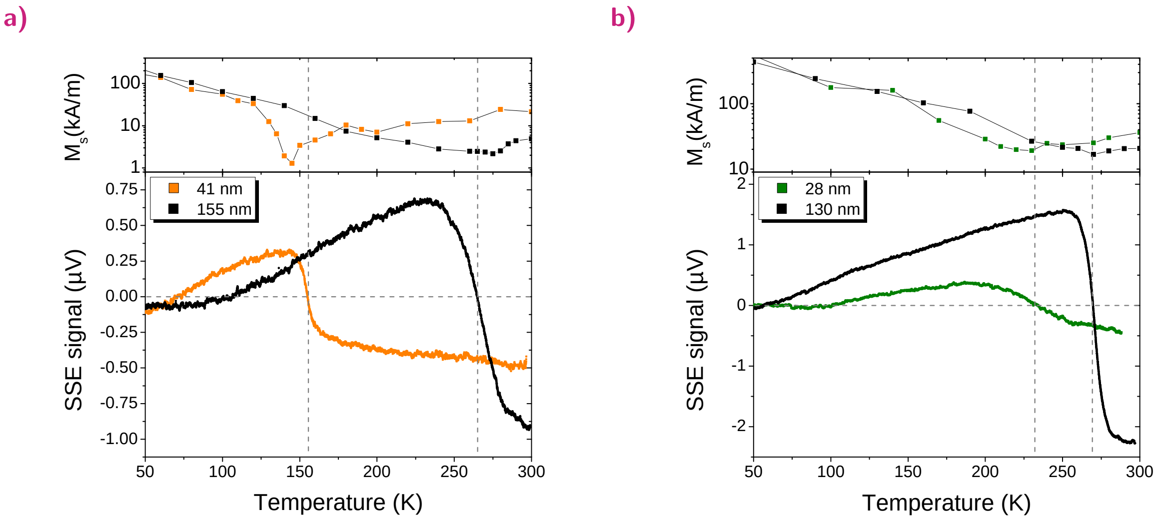

Fig. 5.5: The upper graph shows the magnetic moment, while the lower graph contains the corresponding SSE signals as a function of temperature. Films shown in a) have been deposited at 5×10^{-2} mbar, films in b) at 1×10^{-1} mbar. The vertical line indicates the temperature of the first sign change.

and T_{comp} within the tolerance of $10\,\mathrm{K}$ of both measurement methods. A hint that this temperature difference only results from our experimental accuracy, is given by the fact that the difference shows no systematic trend for a higher or lower value. However we cannot exclude a systematic shift within our errorbars.

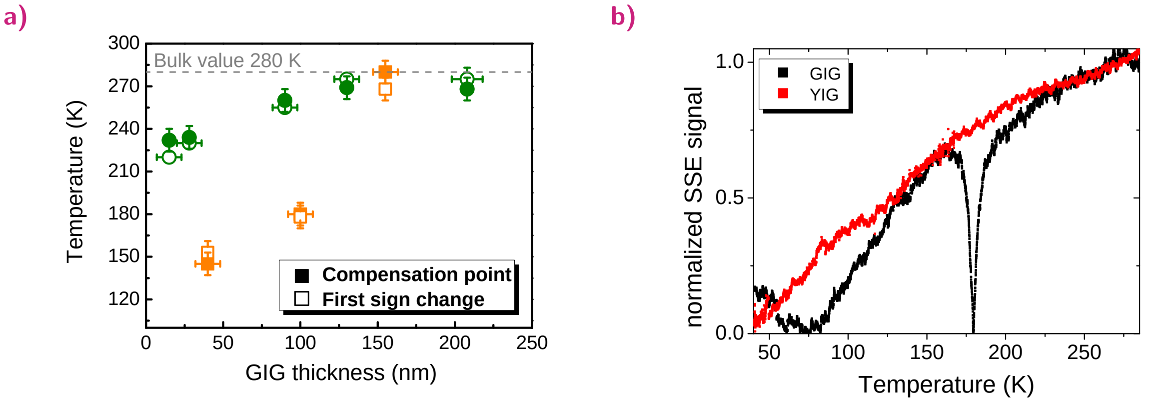

Fig. 5.6: a) Magnetic compensation point temperature and temperature of the first sign change as a function of the GIG film thickness for two series of GIG samples. Samples colored in green have deposited at an oxygen pressure of 1×10^{-1} mbar, samples in orange at 5×10^{-2} mbar. b) Absolute value of the SSE signal in YIG and GIG as a function of the temperature. The both signals have been normalized for value measured at $270\,\mathrm{K}$ to allow a better comparison.

Our results highlight, as the previous measurements, the correlation between the magnetic compensation point and the first sign change, independent of the temperature compensation point.

To explain the correlation between the SSE and the compensation point, we can again make use of the magnonic picture of the SSE based on a theory of Ohnuma *et al.* [195]. GIG consists in contrast to YIG of three coupled magnetic sub-lattices. The Fe ions on the a and d site are antiferromagnetically coupled, while the Gd on the c site is antiferromagnetically coupled to the a site Fe and ferromagnetically to the d site, as illustrated in Fig. 3.21. The model of Ohnuma simplifies this situation to a two sub-lattices model, by combining the Fe on the a and d site to one joined sub-lattice, which competes with the Gd on the d site. As in the real lattice, the different temperature dependences of the magnetic moments for the Fe and Gd, lead to the occurrence of T_{comp}. Additionally the interaction between the sub-lattice leads to the appearance of two magnon modes, which can be excited thermally. These two modes possess opposite sign, resulting from the sub-lattices. Since the ISHE does not allow for distinguishing between both modes, only the sum of both modes is detected.

In this first model, this sum of spin currents is temperature independent and switches its sign at the temperature of the magnetic compensation point. The switching should only be observable in a finite magnetic field, since only this field causes a reorientation of the magnetic lattice at which the Fe and Gd lattice exchange roles.

In Sec. 4.1.5 we explained in detail, that the signal of the SSE is coupled to the orientation of the emitting ferromagnet. Since the orientation of the magnetic lattice switches at T_{comp}, also the sign of the SSE reverses.

Furthermore the model predicts an abrupt switching, with the same signal amplitude above and below the compensation temperature. To compare this with our experimental results, we have to neglect the temperature dependence of the magnonic spin current, which is considered of the model of Ohnuma. Therefore we plot in Fig. 5.6b) the normalized absolute value of the SSE signal as a function of the temperature for a $100\,\mathrm{nm}$ thick GIG film in comparison with a $300\,\mathrm{nm}$ thick YIG film. From the comparison one can see that GIG shows for temperatures above and close to the first sign change a similar temperature dependence as YIG. Since the GIG signal approaches before and after the first sign change the signal of YIG, we can conclude that it possesses the same amplitude, as predicted by the model.

In contrast to the theoretical prediction, we do not observe an abrupt sign change for the first sign transition but a gradual symmetric change with a finite temperature range for all our samples. The same broadening of the transition is also detected for samples of our collaboration with the WMI. As can be seen in the measurements in Fig. 5.5, the width of the transition does not dependent on the temperature of the compensation point nor on the momentum increase of the magnetization close to the compensation point. A possible explanation of this finite width of the transition is given by variations of the interface quality with the detection stripe, leading to a smearing of the transition. In the next section our measurements will show that this assumption does not hold, since the first sign change remains unaltered by changes of the interface quality between detection layer and GIG and other detection materials.

A second theory based on calculations of spin wave power spectra of GIG and is discussed in more detail at the discussion at the sign change. For the discussion of the first sign change, it is only important to know that this model explains the occurrence of the first sign change as well as the first theory by a switching of the orientation of the magnetic sub-lattices at the compensation point. Although this model only considers the magnetic film properties combined with a thermal excitation of magnonic modes of the film, the second model cannot explain the smearing of the first sign change.

Up to know we have only discussed the lattice magnetization itself. Beside the magnetic compensation point, ferrimagnets additionally possess an angular moment compensation point. At this point the angular moment ($M_{Fe/Gd}/\gamma_{Fe/Gd}$) of the sub-lattices chancel each other, leading to vanishing net angular momentum of the material. At this temperature the Gilbert damping parameter exhibits a peak [196–198]. Taking the detection method of the ISHE into account, one might understand that the smearing is somehow related to the angular moment compensation point of the material. The detection method by the ISHE does not allow one to distinguish between the different orientations or magnon modes. The detected voltage thus only depicts an integral of the converted spin currents as a voltage. At the angular moment compensation point, the momentum of magnons of the different modes chancel another, which could as well lead to zero signal. This assumption is in contrast to expectations of the model of Ohnuma *et al.* [195], which expects a vanishing SSE signal only at the magnetic compensation point. While for GdFeCo the magnetic and angular momentum compensation point are known to have different temperatures [197], there are no experimental reports for GIG. Therefore observed temperature difference between T_{comp} and the angular momentum compensation point might results of its actual correlation to the angular momentum compensation point. A detailed investigation of the angular moment compensation point for GIG is missing up to now, and presents an elaborate study beyond the scope of this thesis. Based on our derived results the assumption of an identical temperature for angular and magnetic compensation points seems valid presents an explanation. Thus further studies for materials with a known difference between angular and magnetic compensation point might allow to further enhance the understanding of the SSE in ferrimagnetic materials.

5.1.2 Second sign change at low temperatures below the compensation point

The second sign change occurring below 130 K appears to have no direction correlation with the temperature of magnetic compensation point. Films, shown in Fig. 5.5a), show a shift of the second sign change in line with a shift of the first sign change to higher temperatures, while the opposite behavior is observed for the films presented in Fig. 5.5b). Additionally the second sign change appears to have a more gradual transition over a wider temperature range, than the first sign change, as can be seen in Fig. 5.6b). At temperatures below T_{comp} the magnetometry measurements of the total sample magnetization give no hint for a possible correlation, since only a constant increase of the moment with decreasing temperature can be detected, see Fig. 5.5.

So far we have only discussed the magnetic compensation point, which can be derived from classical magnetometry measurements. Neutron scattering experiments on bulk GIG samples, found a magnetic phase transition below 100 K [199]. This phase transition is the ferromagnetic self-ordering of the Gd sub-lattice. At room temperature, the exchange coupling strength of the Gd sub-lattice itself can be neglected and considered to be paramagnetic "exchange-enhanced" coupled [172]. The coupling strength between the Gd lattice sides increases with decreasing temperatures, leading to a change from paramagnetic to ferromagnetic ordering at the so called Gd ordering temperature [199]. X-ray magnetic circular dichroism measurements of the Gd -L_3 edge, performed by our collaborators from the WMI, reveal an increase of the magnetic contrast with decreasing temperature. The observed temperature dependence of the Gd -L_3 edge agrees with the stronger signal decrease for the GIG signals starting at 150 K to lower temperatures, compared to the one of YIG, as can be seen in Fig. 5.6b). This concept of a temperature dependent contribution from an effective rare earth sub-lattice coupling, matches with the assumption of two competing magnetic sub-lattices. In this scenario the Fe sub-lattices dominates the emitted spin wave spectra above the Gd ordering temperature. At lower temperatures the Gd influence of the magnon spectra becomes gradually more important. The Gd sub-lattice is antiparallel aligned to the dominating Fe sub-lattice. Therefore the Gd influence will favor the emission of magnons with an opposite sign to Fe sub-lattices, leading to a graduate decrease in net signal as observed. Since detected ISHE-signals represent a sum of the whole magnonic accumulation at the interface, it is impossible to identify individual contributions of different modes. However as the Gd and Fe have different spin mixing conductance $g^{\uparrow\downarrow}$, an influence of the interface of the second transition might be possible as it determines the coupling strength between emitter and detector.

To probe such a dependence, one can test the consequences of a change in the interface quality or the detection material on the second sign change. First we will discuss the influence of a change in the interface quality. To exclude an influence of the sample quality variations, the measurements are performed on the identical GIG sample, that has been cleaved into two pieces prior the deposition of the detection layer, thus the GIG film is identical. One part of the sample has been treated by an oxygen plasma etching prior the Pt deposition, while this step has been omitted for the other half. Since the plasma etching step is only performed for 20 s, a resulting change on the bulk properties of the material can be excluded. To ensure an identical Pt layer, the same deposition condition have been used for both pieces of the sample.

From the measurements shown in Fig. 5.7a), one can see a weaker signal strength for the etched sample compared to the untreated sample, which confirms that the etching must have altered the interface. We observe no influence on the first sign change within the resolution of our setup, which strengthens our previous finding of a correlation between the magnetic compensation point and this sign change, as the bulk properties are not affected by the etching. In contrast to this, one can observe a difference of ~ 30 K for the second sign change between both samples, which hints to a dependence of the interface. For a second test of the interface influence, one can alter the detection material. Similar to the previous measurements, the sample has been cleaved into two pieces prior to the deposition of the detector material. One half of the sample is coated by Pt, while we use Pd as a detector layer for the second half. The SSE measurements of both parts are shown in Fig. 5.7b).

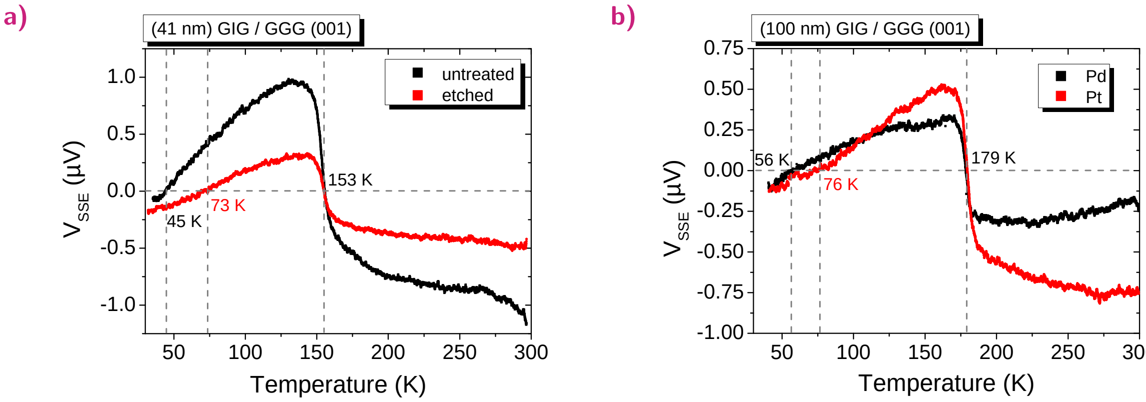

Fig. 5.7: SSE measurements as a function of the temperature for different interface treatments a) and different detection layers b). The black curve in plot a) corresponds to the untreated part, while the red curve shows the results of the etched interface of the same sample. Pd has been used as a detection layer for the data shown as a black curve in b), while Pt has been used for the detection of the red curve.

The first sign change reveals no dependence on the detection material, which confirms its correlation to the compensation point. For the second sign change we find a temperature difference of $\sim 20\,\mathrm{K}$ between the two detection layers. Furthermore for high temperatures, the sample with the Pd detection layer shows a weaker signal strength than the one with Pt. The lower signals are due to the smaller spin Hall angle of Pd [189] compared to Pt, while the low temperature behavior is the result of a more complex interplay as we will explain in the following.

In order to understand the origin of the two sign changes observed for the SSE in GIG, we explain now more in detail the previously briefly introduced two theories.

The original two sub-lattices model of Ohnuma *et al.* [195], only an equal spin pumping efficiency of the two competing magnonic sub-lattices was considered and a temperature independent net spin current, revealing no second sign change. In an extension of this linear response model, presented in Ref. [p7] and Fig. 5.8, it is shown that a difference in the spin pumping efficiency between the two sub-lattices leads to the occurrence of a second sign change. In detail the model starts again with the assumption of two antiferromagneticly coupled sub-lattices, consisting of the combined Fe sub-lattices and Gd lattice. Using this approach, two main modes can be identified, which are of relevance for the thermally excited magnons. I_s^α represents the magnons emitted by a soft-mode, whose major contribution is given by the Gd lattice. The spin current labeled by I_s^β results mode separated by an energy gap from the first mode. The gap Δ_β originates of the exchange coupling between the two sub-lattices, which leads to a temperature dependent contribution of this mode. The major contribution to this mode is given from the Fe sub-lattices. Fig. 5.8 illustrates the temperature dependence of both emitted spin currents and the detected sum.

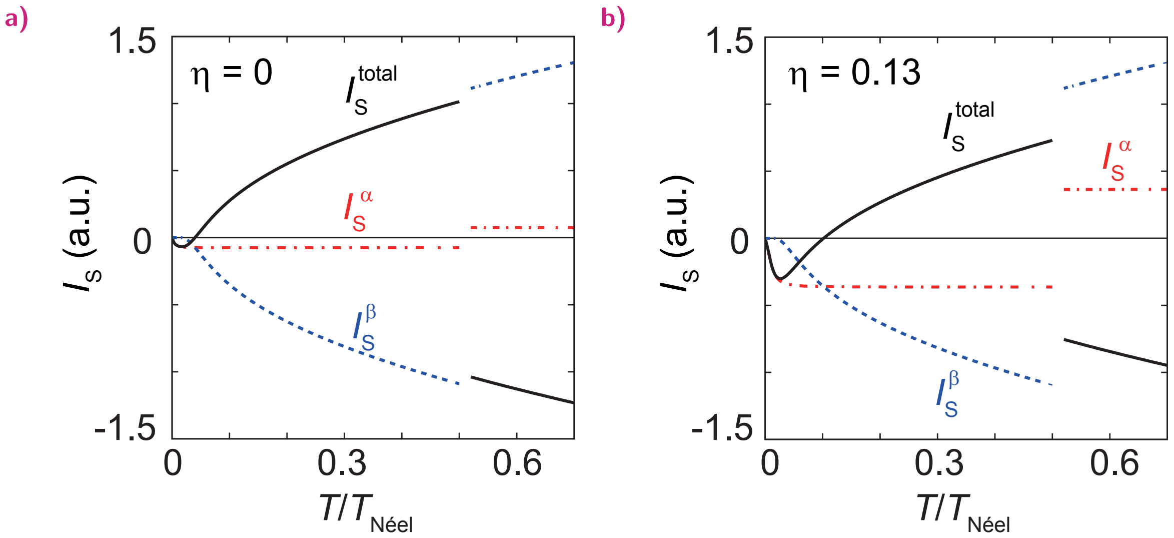

Fig. 5.8: Spin currents I_s^α, I_s^β and the sum I_s^{total} as a function of temperature for $\eta = 0.13$ a) and $\eta = 0.01$ b), based on the calculations by Ohnuma *et al.*, taken from [p7].

To understand the behavior shown, one has to consider that I_s^α and I_s^β possess the opposite sign due to the antiparallel alignment of the Fe and Gd sub-lattices. The higher contribution of I_s^β is explained by an higher interface exchange constant J_{Iex} for magnons emitted by I_s^β, which is equal to a higher spin mixing conductance for the Fe lattice. As the temperature decreases, Δ_β leads to a decrease of the magnonic population of I_s^β and thus less emitted magnons. For the shown situation of $J_{Iex}^\alpha << J_{Iex}^\beta$ the second sign change occurs at lower temperatures than the first sign change, showing a gradual transition. As discussed in the section of the first sign change, the occurrence of it is attributed to the reorientation of the sub-lattices at the compensation point.

Thus the theoretically obtained temperature dependence of the net spin current qualitatively agrees with our experimental observation of a more gradual second sign change and steady signal decrease with temperature. Furthermore the model derives two parameters, which allow us to understand the temperature shift of the two sign changes. The first parameter is the gap Δ_β, defined by the exchange coupling between Fe and Gd. Since this coupling strength depends on the Fe to Gd ratio of the material, a change in stoichiometry alters the temperature of the compensation point. As pointed out in our material analysis, further knowledge about our thin film composition is necessary to correlate this parameter with the observed shifts of the first and second sign change between the different batches. The second parameter is the relative interface exchange coupling strength $\eta = J_{Iex}^\alpha / J_{Iex}^\beta$ between the two modes. η is an important parameter as it allows us to understand the observed behavior in our experimental tests of the different interface treatments and detection materials, shown in Fig. 5.7. A change of η roughly corresponds in our experimental situation to an altering of the ratio between the different spin mixing conductance $g_{Gd}^{\uparrow\downarrow}/g_{Fe}^{\uparrow\downarrow}$. We assume that in the interface treatment experiment we modified $g_{Gd}^{\uparrow\downarrow}/g_{Fe}^{\uparrow\downarrow}$ by the etching. The etching is an element dependent process and thus leads to a difference in the interface stoichiometry compared to the untreated sample part. Hence the etching step alters the ratio $g_{Gd}^{\uparrow\downarrow}/g_{Fe}^{\uparrow\downarrow}$

at the interface between GIG and Pt, which explains the observed shift of the second sign change. A similar situation applies for the experiments with different detection materials. The $g^{\uparrow\downarrow}$ marks an element specific parameter (see Sec. 2.3.1), which is different for element combinations, which occur at the interface, leading to four unique combinations. The Fe-Pt interface spin mixing conductance $g^{\uparrow\downarrow}_{Fe-Pt}$ differs from $g^{\uparrow\downarrow}_{Fe-Pd}$, which both differ from the corresponding Gd $g^{\uparrow\downarrow}_{Gd-Pt}$ and $g^{\uparrow\downarrow}_{Gd-Pd}$, respectively. This can lead to a difference in the ratios $g^{\uparrow\downarrow}_{Gd-Pt}/g^{\uparrow\downarrow}_{Fe-Pt}$ and $g^{\uparrow\downarrow}_{Gd-Pd}/g^{\uparrow\downarrow}_{Fe-Pd}$, which could then be responsible for the shift of the second sign change.

The theory can therefore give an explanation for our experiential observation of temperature shift for the second sign change by altering the interface, either by its treatment or the detection layer. According to the theoretical model one would expect a lower temperature for the second sign change for a smaller contribution of spin currents emitted by I_s^{α}, as shown in Fig. 5.8b). Since we cannot verify the different $g^{\uparrow\downarrow}$ of our samples, we only can identify that this situation corresponds to the experimental investigation of the untreated interface and the usage of Pd as detection material.

As a second theoretical approach, we present a theoretical model developed by Barker *et al.* [p7], which only considers the GIG sub-lattices and does not take into account the interface. The model is based of numerical calculations of the GIG spin wave power spectra, using the atomistic spin model of the LLG equation. In order to differentiate between the influence of the spin-lattice coupling and the magnon-magnon coupling, the model assumes a temperature independent Gilbert damping and exchange constant. Based on this, the model derives three main modes within the spin wave spectra, illustrated for $k = 0$ in Fig. 5.9a) for low temperatures.

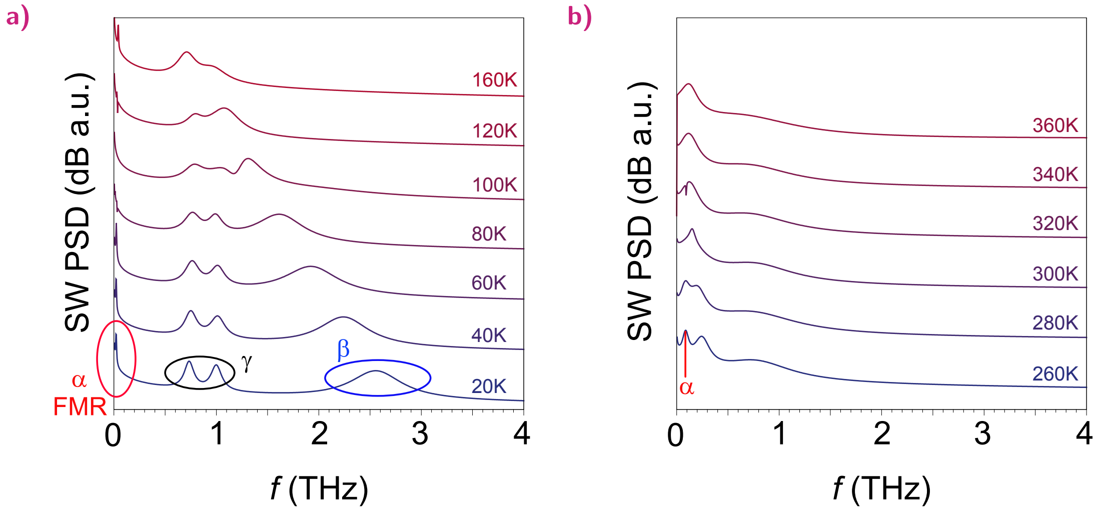

Fig. 5.9: Spin wave power spectra at $k = 0$ for different temperatures based on simulations by Barker *et al.*, taken from [p7]. The spectra shown in a) ranges from 20 K to 160 K and contains a labeling of the important modes, while the high temperature spectra is shown in b).

The first mode, the α-mode, which can be identified as the FMR-Goldstone mode of the whole ferrimagnetic lattice, is considered to lead to the "normal" sign spin current, compared with YIG. The second mode, a gapped optical β-mode, is attributed to the Gd momentum influenced by the exchange field of the two Fe sub-lattices. The gap between the second and third mode, is caused by the Fe-Gd exchange coupling and will be important for temperature dependent discussion of the mode spectra. The third mode, a parabolic shaped γ band, is attributed to the ordered Gd sub-lattice at low temperatures. To understand the temperature dependence of this picture one has to take into account that only magnons within a certain energy range can be thermally be excited. The thermal excitation responds to approximately $1\,\mathrm{THz}$ per $50\,\mathrm{K}$, highlighting that at very low temperatures only the FMR mode can be excited. As the temperature increases higher modes can be populated within the spectrum. Additionally the weakening Gd moment causes a red shifting of the γ mode and increases its amplitude. At the temperature of the second sign change the magnons of the α, β and γ mode compensate one another, while for even higher temperatures, the combined β and γ dominate of the FMR α mode. Again it is assumed that magnons of α and γ mode possess opposite polarization, while the contribution of the β mode can be neglected. At temperatures close to the magnetic compensation point, the strong temperature dependence of the Gd moment leads to a decrease of the γ and β mode amplitude as can be seen in Fig. 5.9b). At T_{comp} the γ and α branches exchanges roles, causing the reorientation of magnetization and of the sign change of spin current. The model itself does not take into account any influence of the interface as it only describes the mode spectra within the GIG. Thus the model does not explain the interface dependence which we observed. Compared to the model of Ohnuma et al., the model derives similar results, as the α mode of Barker corresponds to the I_s^{α} mode of the first model, and the γ and its temperature dependence, matches with Δ_{β} and I_s^{β}.

5.2 Conclusion of SSE in GIG

In conclusion we were able for the first time to probe the SSE in a magnetic material, which shows the characteristic magnetization behavior of a ferrimagnet. We observed two consecutive sign changes of the SSE as a function of temperature. The first sign change is found to be close to the magnetic compensation point of the material, while the second sign change occurs at temperatures below 100 K. To determine the origin of both sign changes we performed SSE measurements for systematic variations of the compensation point temperature and interface qualities as well as for different detection materials. The measurements revealed an interface and detection material independence for the first sign change, which agrees with the interpretation of a correlation with the magnetic compensation point, while the second sign change can be strongly influenced. Two different theoretical approaches, developed by our collaboration in Tohoku, demonstrate that these sign changes originate from the complex interaction of the magnetic sub-lattices and the interface exchange coupling to the detection material. Thus the SSE does not simply follow the net magnetization of the material but can be attributed to magnonic spin currents, which mimic the complex temperature dependent interplay of the sub-lattices.

Conclusion

6

In this thesis, we have investigated the origin of the spin Seebeck effect in magnetic insulators. We presented a comprehensive study of the dependences of the effect and employed a model, developed in collaboration with the University of Konstanz, based on thermally excited magnons to explain our observations.

In detail we first studied the growth of different types of magnetic garnets in order to gain control about the magnetic material parameter. In collaboration with the group of Prof. Ross at MIT, we have shown that we are capable of growing high quality YIG thin films by PLD, which allowed us to study the SSE as a function of the YIG film thickness. In combination with YIG films grown by LPE, and a systematic study of the magnetic material parameters, we have shown that the SSE features a universal dependence on the thickness of the ferromagnetic material that cannot be explained by interface effects. For increasing thickness of the ferromagnet the SSE signals show a saturation, which shifts for lower temperatures to higher thicknesses. A model of thermally excited magnons, developed by the group of Prof. U. Nowak in Konstanz, yields a quantitative agreement with our experimental results. Therefore we attributed the found behavior to a finite magnon propagation length for thermally excited magnons. Our results unambiguously show that the SSE originates from magnonic spin currents emitted by the bulk of the ferromagnetic material.

A more detailed investigation of the temperature and thickness dependence of the SSE revealed a peaking of the SSE signals as a function of temperature. The measured peak shifts with increasing film thickness to lower temperatures. Additional thermal conductivity measurements found no corresponding behavior for the phonon peak, which indicates that the SSE peak position is not dominated by magnon-phonon drag only. The solely magnonic model however yields a quantitative agreement between expected behavior of the thermal magnon propagation length and our data. Using a phenomenological expansion of the model, we could explain the observed behavior as a competition between the amount and the mean free path of thermal magnons. Independent of the applied model, the behavior can only be described by a transport phenomenon and additionally suggests that the majority of magnons responsible for the SSE must differ from the magnons transferring the heat in the magnetic lattice. Further measurements using different detection materials found a dependence of the SSE signals on the detection layer. These results are not explainable purely by magnon-phonon drag or purely by the magnonic model, indicating that a further expansion of the theoretical description SSE is necessary to understand this behavior by taking into account the temperature dependence of the spin transport across the interface.

By probing the high magnetic field strength dependence of the SSE, we observed a suppression of the signals even at room temperature, independent of the interface. The suppression decreases with decreasing film thickness as well as for lower temperatures. Based on the theoretical model of U. Ritzmann, we were able to qualitatively explain this behavior by a magnetic field dependence of the thermal magnon propagation length.

Our improvements in the deposition of garnet by PLD enabled us to study the SSE in GIG, a compensated ferrimagnet, in collaboration with the Walther-Meißner-Institute and the Tohoku University. The experiments find two consecutive sign changes of the SSE as a function of temperature, one close to the magnetic compensation point and one at lower temperatures. Exploiting the thickness dependence of the magnetic compensation point, we could confirm a correlation between the first sign change and the magnetic compensation point, while measurements with different interface qualities and detection materials yielded a dependence of the second sign change. Two theoretical models developed by Ohnuma *et al.* and Barker *et al.* explain the first sign change by the switching of the magnetization at the compensation point, while the second sign change results from a complex interplay of the magnonic modes in combination with the interface exchange coupling strength.

In summary, the experimental results and observations reported in this thesis not only reveal the origin of the SSE as a bulk effect, but also show that the detected thermal magnons are the result of a complicated interaction between the thermal phononic excitation and the magnetic sub-lattices. Furthermore our findings point out that a comprehensive theoretical description of the effect also needs to take the detection layer into account to be able to explain all observed features of the SSE.

6.1 Outlook and open questions

Our pioneering work revealing the magnonic origin of the SSE and therefore its spin current nature allows to think of novel spintronic applications and devices such as nanoscale magnetic engines [200]. Theoretical predictions propose an all magnonic thermal domain wall motion [13], which drags the domain wall from the cold to the hot end of the material due to the STT caused by the thermal magnons [201]. With the confirmation of the presence of thermal magnon currents, our work inspires further research on this topic. Furthermore our work on the growth and optimization of epitaxial Ce:YIG presents a starting point for the research on the direct imagining of the thermal domain wall motion in garnets by using Kerr microscopy. While the pure thermal motion might be too inefficient, one might also think of thermal assisted motion. In this concept the actual device is either in contact with the thermal spin current source or is itself exposed to a thermal gradient, which leads a contribution of the thermal magnons to the current induced domain wall motion. As our results have shown, the efficiency of this contribution strongly depends on the interface quality and type of material, motivating future experimental and theoretical work to improve the understanding of the interplay between the ISHE and the SSE. Additionally our understanding of the effect confirms already found observations [202], which can only be explained by thermal spin currents but has lacked of further evidence. Future work is necessary to determine the impact of phonon magnon interaction, since the detected thermal magnons can only be excited by phonons. As our results suggest a weaker coupling than originally predicted, future work should aim to investigate the SSE at even lower temperatures in order to probe the effect at temperatures where phonons and magnons can be decoupled.

7

List of own and involved publications

[p1] **Thickness and power dependence of the spin-pumping effects in Y_3 Fe_5 O_{12} / Pt heterostructures measured by the inverse spin Hall effect**, M.B. Jungfleisch, A.V. Chumak, A. Kehlberger, V. Lauer, D.H. Kim, M. C. Onbasli, C.A. Ross, M. Kläui and B. Hillebrands, *Physical Review B*, **91**, 134407 (2015)

[p2] **Pulsed laser deposition of epitaxial yttrium iron garnet films with low Gilbert damping and bulk-like magnetization**, M.C. Onbasli, A. Kehlberger, D.H. Kim, G. Jakob, M. Kläui, A.V. Chumak, B. Hillebrands and C.A. Ross, *Applied Physics Letters Materials* **2**, 106102 (2014)

[p3] **Enhanced magnetooptic Kerr effect and magnetic properties of epitaxial CeYIG thin films**, A. Kehlberger, K. Richter, G. Jakob, M.C. Onbasli, D.H. Kim, T. Goto, C.A. Ross, G. Götz, G. Reiss, T. Kuschel, and M. Kläui, *Physical Review Applied*, **4**, 014008 (2015)

[p4] **Investigation of the magnetic properties of insulating thin films using the longitudinal spin Seebeck effect**, A. Kehlberger, G. Jakob, M.C. Onbasli, D.H. Kim, C.A. Ross and M. Kläui, *Journal of Applied Physics* **115**, 17C731 (2014)

[p5] **Length scale of the spin Seebeck effect**, A. Kehlberger, U. Ritzmann, D. Hinzke, E.J. Guo, G. Jakob, M.C. Onbasli, D.H. Kim, C.A. Ross, B. Jungfleisch, B. Hillebrands, U. Nowak and M. Kläui, *Physical Review Letters*,**115**, 096602 (2015)

[p6] **Magnetic field control of the spin Seebeck effect**, U. Ritzmann, D. Hinzke, A. Kehlberger, E.J. Guo, M. Kläui and U. Nowak, *Physical Review B*, **92**, 174411 (2015)

[p7] **Spin Seebeck effect: a powerful probe of magnon properties in compensated ferromagnets**, S. Gepärgs, A. Kehlberger, F.D. Coletta, Z. Qiu, E.J. Guo, T. Schulz, C. Mix, S. Meyer, A. Kamra, M. Althammer, G. Jakob, G. Huebl, Y. Ohnuma, H. Adachi, S. Maekawa, J.

Barker, G.E.W. Bauer, R. Gross, E. Saitoh, S.T.B. Goennenwein and M. Kläui, *submitted to Nature Communications* (2015)

[p8] **Observation of spin Seebeck effect in authentic ferrimagnetic thin films** E.J. Guo, A. Kehlberger, G. Jakob and M. Kläui, *in preparation* (2015)

[p9] **Thermal conductance of thin film YIG determined using Bayesian statistics**, C. Euler, P.Holuj, T. Langner, A. Kehlberger, V. I. Vasyuchka, M.Kläui and G. Jakob, *Physical Review B*, **92**, 094406 (2015)

[p10] **Origin of the thickness-dependent low-temperature enhancement of spin Seebeck effect in YIG films**, E.J. Guo, A. Kehlberger, J. Cramer, G. Jakob and M. Kläui, *submitted to Physical Review X* (2015)

[p11] **Electric field modification of magnetotransport in Ni thin films on (011) PMN-PT piezosubstrates**, A. Tkach, A. Kehlberger, F. Büttner, G. Jakob, S. Eisebitt and M. Kläui *Applied Physics Letters* **106**, 062404 (2015)

[p12] **Electronic properties of Co_2FeSi investigated by x-ray magnetic linear dichroism** M. Emmel, A. Alfonsov, D. Legut, A. Kehlberger, E. Vilanova, I.P. Krug, D.M. Gottlob, M. Belesi, B. Büchner, M. Kläui, P.M. Oppeneer, S. Wurmehl, H.J. Elmers and G. Jakob, *Journal of Magnetism and Magnetic Materials* **368**, 364–373 (2014)

Bibliography

[1] T. J. Seebeck, “Magnetische Polarisation der Metalle und Erze durch Temperatur-Differenz,” *Abh. K. Akad. Wiss., Berlin*, 265, 1823.

[2] L. E. Bell, “Cooling, Heating, Generating Power, and Recovering Waste Heat with Thermoelectric Systems,” *Science*, **321**, 1457, 2008.

[3] J. Sootsman, D. Chung, and M. Kanatzidis, “New and Old Concepts in Thermoelectric Materials,” *Angew. Che. Int. Ed.*, **48**, 8616, 2009.

[4] J. C. A. Peltier, “Nouvelles experiences sur la carolicité des courants electrique,” *Ann. Chem. Phys.*, **56**, 1834.

[5] L. Onsager, “Reciprocal Relations in Irreversible Processes. I.” *Phys. Rev.*, **37**, 405, 1931.

[6] Y. Kajiwara, K. Harii, S. Takahashi, J. Ohe, K. Uchida, M. Mizuguchi, H. Umezawa, H. Kawai, K. Ando, K. Takanashi, S. Maekawa, and E. Saitoh, “Transmission of electrical signals by spin-wave interconversion in a magnetic insulator,” *Nature*, **464**, 262, 2010.

[7] K. Uchida, S. Takahashi, K. Harii, J. Ieda, W. Koshibae, K. Ando, S. Maekawa, and E. Saitoh, “Observation of the spin Seebeck effect,” *Nature*, **455**, 778, 2008.

[8] A. Kirihara, K. Uchida, Y. Kajiwara, M. Ishida, Y. Nakamura, T. Manako, E. Saitoh, and S. Yorozu, “Spin-current-driven thermoelectric coating,” *Nature Mater.*, **11**, 686, 2012.

[9] K. Uchida, T. Nonaka, T. Yoshino, T. Kikkawa, D. Kikuchi, and E. Saitoh, “Enhancement of Spin-Seebeck Voltage by Spin-Hall Thermopile,” *Appl. Phys. Express*, **5**, 093001, 2012.

[10] A. B. Cahaya, O. A. Tretiakov, and G. E. W. Bauer, “Spin Seebeck power generators,” *Appl. Phys. Lett.*, **104**, 042402, 2014.

[11] K. Uchida, M. Ishida, T. Kikkawa, A. Kirihara, T. Murakami, and E. Saitoh, “Longitudinal spin Seebeck effect: from fundamentals to applications,” *J. Phys.: Condens. Matter*, **26**, 343202, 2014.

[12] M. Schreier, A. Kamra, M. Weiler, J. Xiao, G. E. W. Bauer, R. Gross, and S. T. B. Goennenwein, “Magnon, phonon, and electron temperature profiles and the spin Seebeck effect in magnetic insulator/normal metal hybrid structures,” *Phys. Rev. B*, **88**, 094410, 2013.

[13] D. Hinzke and U. Nowak, “Domain Wall Motion by the Magnonic Spin Seebeck Effect,” *Phys. Rev. Lett.*, **107**, 027205, 2011.

[14] S. Y. Huang, X. Fan, D. Qu, Y. P. Chen, W. G. Wang, J. Wu, T. Y. Chen, J. Q. Xiao, and C. L. Chien, “Transport Magnetic Proximity Effects in Platinum,” *Phys. Rev. Lett.*, **109**, 107204, 2012.

[15] G. Y. Guo, Q. Niu, and N. Nagaosa, “Anomalous Nernst and Hall effects in magnetized platinum and palladium,” *Phys. Rev. B*, **89**, 214406, 2014.

[16] N. W. Ashcroft and D. Mermin, *Festkörperphysik*, 2nd ed. Oldenbourg Wissenschaftsverlag, 2005.

[17] C. Kittel, *Introduction to Solid State Physics*, 8th ed. John Wiley & Sons, 2004.

[18] M. T. Tritt, *Thermal Conductivity Theory, Properties and Applications*. Kluwer Academic / Plenum Publishers, 2004.

[19] G. E. W. Bauer, E. Saitoh, and B. J. van Wees, “Spin caloritronics,” *Nature Mater.*, **11**, 391, 2012.

[20] J. P. Moore and R. S. Graves, “Absolute Seebeck coefficient of platinum from 80 to 340 K and the thermal and electrical conductivities of lead from 80 to 400 K,” *J. Appl. Phys.*, **44**, 1174, 1973.

[21] A. Guan, H. Wang, H. Jin, W. Chu, Y. Guo, and G. Lu, “An experimental apparatus for simultaneously measuring Seebeck coefficient and electrical resistivity from 100 K to 600 K,” *Rev. Sci. Instrum.*, **84**, 043903, 2013.

[22] W. Thomson, “On an absolute thermometric scale,” *Philos. Mag.*, **33**, 1848.

[23] L. Onsager, “Reciprocal Relations in Irreversible Processes. II.” *Phys. Rev.*, **38**, 2265, 1931.

[24] H. B. Callen, “The Application of Onsager’s Reciprocal Relations to Thermoelectric, Thermomagnetic, and Galvanomagnetic Effects,” *Phys. Rev.*, **73**, 1349, 1948.

[25] J. Flipse, F. L. Bakker, A. Slachter, F. K. Dejene, and B. J. van Wees, “Direct observation of the spin-dependent Peltier effect,” *Nature Nanotech.*, **7**, 166, 2012.

[26] F. K. Dejene, J. Flipse, and B. J. van Wees, “Verification of the Thomson-Onsager reciprocity relation for spin caloritronics,” *Phys. Rev. B*, **90**, 180402, 2014.

[27] H. Goldsmid, *Introduction to Thermoelectricity*. Springer New York, 2010.

[28] N. Nagaosa, J. Sinova, S. Onoda, A. H. MacDonald, and N. P. Ong, “Anomalous Hall effect,” *Rev. Mod. Phys.*, **82**, 1539, 2010.

[29] T. Miyasato, N. Abe, T. Fujii, A. Asamitsu, S. Onoda, Y. Onose, N. Nagaosa, and Y. Tokura, “Crossover Behavior of the Anomalous Hall Effect and Anomalous Nernst Effect in Itinerant Ferromagnets,” *Phys. Rev. Lett.*, **99**, 086602, 2007.

[30] A. D. Avery, M. R. Pufall, and B. L. Zink, “Determining the planar Nernst effect from magnetic-field-dependent thermopower and resistance in nickel and permalloy thin films,” *Phys. Rev. B*, **86**, 184408, 2012.

[31] A. D. Avery, M. R. Pufall, and B. L. Zink, “Observation of the Planar Nernst Effect in Permalloy and Nickel Thin Films with In-Plane Thermal Gradients,” *Phys. Rev. Lett.*, **109**, 196602, 2012.

[32] S. L. Yin, Q. Mao, Q. Y. Meng, D. Li, and H. W. Zhao, “Hybrid anomalous and planar Nernst effect in permalloy thin films,” *Phys. Rev. B*, **88**, 064410, 2013.

[33] O. Jaoul, I. Campbell, and A. Fert, “Spontaneous resistivity anisotropy in Ni alloys,” *J. Magn. Magn. Mater.*, **5**, 23, 1977.

[34] H. Haken and W. H. Christoph, *Atom- und Quantenphysik: Einführung in die experimentellen und theoretischen Grundlagen*. Springer-Lehrbuch, 2004.

[35] M. Farle, “Ferromagnetic resonance of ultrathin metallic layers,” *Rep. Prog. Phys.*, **61**, 755, 1998.

[36] S. Blundell, *Magnetism in Condensed Matter*. Oxford University Press, U.S.A., 2001.

[37] G. F. Dionne, *Magnetic Oxides*. Springer Science+Business Media, 2009.

[38] S. A. Manuilov, S. I. Khartsev, and A. M. Grishin, “Pulsed laser deposited $Y_3Fe_5O_{12}$ films: Nature of magnetic anisotropy I,” *J. Appl. Phys.*, **106**, 123917, 2009.

[39] S. A. Manuilov and A. M. Grishin, “Pulsed laser deposited $Y_3Fe_5O_{12}$ films: Nature of magnetic anisotropy II,” *J. Appl. Phys.*, **108**, 013902, 2010.

[40] L. Vosika, P. Novák, and A. čejchan, “Correction to the single ion anisotropy model,” *Czech. J. Phys. B*, **33**, 221, 1983.

[41] W. P. Wolf, “Effect of Crystalline Electric Fields on Ferromagnetic Anisotropy,” *Phys. Rev.*, **108**, 1152, 1957.

[42] R. Pearson, “Magnetocrystalline Anisotropy of Rare-Earth Iron Garnets,” in *Proceedings of the Seventh Conference on Magnetism and Magnetic Materials*, J. Osborn, Ed. Springer US, 1962, 1236. Online: http://dx.doi.org/10.1007/978-1-4899-6391-8_87

[43] L. Baselgia, M. Warden, F. Waldner, S. L. Hutton, J. E. Drumheller, Y. Q. He, P. E. Wigen, and M. Maryško, “Derivation of the resonance frequency from the free energy of ferromagnets,” *Phys. Rev. B*, **38**, 2237, 1988.

[44] I. Neudecker, G. Woltersdorf, B. Heinrich, T. Okuno, G. Gubbiotti, and C. Back, “Comparison of frequency, field, and time domain ferromagnetic resonance methods,” *J. Magn. Magn. Mater.*, **307**, 148, 2006.

[45] T. Gilbert, “A phenomenological theory of damping in ferromagnetic materials,” *IEEE Trans. Magn.*, **40**, 3443, 2004.

[46] C. E. Patton, “Magnetic excitations in solids,” *Phys. Rep.*, **103**, 251, 1984.

[47] H. Suhl, “Theory of the magnetic damping constant,” *IEEE Trans. Magn.*, **34**, 1834, 1998.

[48] G. Counil, J.-V. Kim, T. Devolder, C. Chappert, K. Shigeto, and Y. Otani, “Spin wave contributions to the high-frequency magnetic response of thin films obtained with inductive methods,” *J. Appl. Phys.*, **95**, 5646, 2004.

[49] F. Vescial, T. J. Hutchings, E. D. Jacobs, and W. L. Zingery, “Ferromagnetic Resonance Measurements in Ni–Fe Films from 2–100 Mc/sec,” *J. Appl. Phys.*, **36**, 1054, 1965.

[50] D. Stancil, *Theory of Magnetostatic Waves*. Springer Verlag, 1993.

[51] F. Bloch, “Zur Theorie des Ferromagnetismus,” *Zeitschrift für Physik*, **61**, 206, 1930.

[52] J. R. Eshbach and R. W. Damon, “Surface Magnetostatic Modes and Surface Spin Waves,” *Phys. Rev.*, **118**, 1208, 1960.

[53] A. A. Serga, A. V. Chumak, and B. Hillebrands, “YIG magnonics,” *J. Phys. D: Appl. Phys.*, **43**, 264002, 2010.

[54] U. Ritzmann, D. Hinzke, and U. Nowak, “Propagation of thermally induced magnonic spin currents,” *Phys. Rev. B*, **89**, 024409, 2014.

[55] B. Y. Pan, T. Y. Guan, X. C. Hong, S. Y. Zhou, X. Qiu, H. Zhang, and S. Y. Li, “Specific heat and thermal conductivity of ferromagnetic magnons in Yttrium Iron Garnet,” *Europhys. Lett.*, **103**, 37005, 2013.

[56] J. E. Rives, G. S. Dixon, and D. Walton, “Effect of Magnons on Thermal Transport in Insulators,” *J. Appl. Phys.*, **40**, 1555, 1969.

[57] D. J. Sanders and D. Walton, “Effect of magnon-phonon thermal relaxation on heat transport by magnons,” *Phys. Rev. B*, **15**, 1489, 1977.

[58] D. Walton, J. E. Rives, and Q. Khalid, “Thermal Transport By Coupled Magnons and Phonons in Yttrium Iron Garnet at Low Temperatures,” *Phys. Rev. B*, **8**, 1210, 1973.

[59] S. R. Boona and J. P. Heremans, “Magnon thermal mean free path in yttrium iron garnet,” *Phys. Rev. B*, **90**, 064421, 2014.

[60] G. E. W. Bauer and Y. Tserkovnyak, “Spin-magnon transmutation,” *Physics*, **4**, 2011.

[61] A. Brataas, Y. Tserkovnyak, G. Bauer, and P. Kelly, *Spin pumping and spin transfer*, S. Maekawa, S. O. Valenzuela, E. Saitoh, and T. Kimura, Eds. Oxford University Press, 2012, arXiv:1108.0385.

[62] E. B. Myers, D. C. Ralph, J. A. Katine, R. N. Louie, and R. A. Buhrman, “Current-Induced Switching of Domains in Magnetic Multilayer Devices,” *Science*, **285**, 867, 1999.

[63] Y. Tserkovnyak, A. Brataas, and G. E. W. Bauer, “Enhanced Gilbert Damping in Thin Ferromagnetic Films,” *Phys. Rev. Lett.*, **88**, 117601, 2002.

[64] K. Ando, S. Takahashi, J. Ieda, Y. Kajiwara, H. Nakayama, T. Yoshino, K. Harii, Y. Fujikawa, M. Matsuo, S. Maekawa, and E. Saitoh, “Inverse spin-Hall effect induced by spin pumping in metallic system,” *J. Appl. Phys.*, **109**, 103913, 2011.

[65] H. Nakayama, K. Ando, K. Harii, T. Yoshino, R. Takahashi, Y. Kajiwara, K. Uchida, Y. Fujikawa, and E. Saitoh, "Geometry dependence on inverse spin Hall effect induced by spin pumping in $Ni_{81}Fe_{19}$/Pt films," *Phys. Rev. B*, **85**, 144408, 2012.

[66] J. Xiao, G. E. W. Bauer, K. Uchida, E. Saitoh, and S. Maekawa, "Theory of magnon-driven spin Seebeck effect," *Phys. Rev. B*, **81**, 214418, 2010.

[67] Y. K. Kato, R. C. Myers, A. C. Gossard, and D. D. Awschalom, "Observation of the Spin Hall Effect in Semiconductors," *Science*, **306**, 1910, 2004.

[68] T. Kimura, Y. Otani, T. Sato, S. Takahashi, and S. Maekawa, "Room-Temperature Reversible Spin Hall Effect," *Phys. Rev. Lett.*, **98**, 156601, 2007.

[69] J. Sinova, S. O. Valenzuela, J. Wunderlich, C. H. Back, and T. Jungwirth, "Spin Hall effect," *Rev. Mod. Phys.*, in press, 2014.

[70] S. Maekawa, S. O. Valenzuela, E. Saitoh, and T. Kimura, *Spin Current*. Oxford University Press, 2012.

[71] L. Wang, H. H. Du, C. Y. Pu, R. Adur, C. Hammel, P. and Y. Yang, F. "Scaling of Spin Hall Angle in 3d, 4d, and 5d Metals from $Y_3Fe_5O_{12}$/Metal Spin Pumping," *Phys. Rev. Lett.*, **112**, 197201, 2014.

[72] T. Tanaka, H. Kontani, M. Naito, T. Naito, D. S. Hirashima, K. Yamada, and J. Inoue, "Intrinsic spin Hall effect and orbital Hall effect in $4d$ and $5d$ transition metals," *Phys. Rev. B*, **77**, 165117, 2008.

[73] J.-C. Rojas-Sánchez, N. Reyren, P. Laczkowski, W. Savero, J.-P. Attané, C. Deranlot, M. Jamet, J.-M. George, L. Vila, and H. Jaffrès, "Spin Pumping and Inverse Spin Hall Effect in Platinum: The Essential Role of Spin-Memory Loss at Metallic Interfaces," *Phys. Rev. Lett.*, **112**, 106602, 2014.

[74] V. Castel, N. Vlietstra, J. Ben Youssef, and B. J. van Wees, "Platinum thickness dependence of the inverse spin-Hall voltage from spin pumping in a hybrid yttrium iron garnet/platinum system," *Appl. Phys. Lett.*, **101**, 132414, 2012.

[75] V. Vlaminck, J. E. Pearson, S. D. Bader, and A. Hoffmann, "Dependence of spin-pumping spin Hall effect measurements on layer thicknesses and stacking order," *Phys. Rev. B*, **88**, 064414, 2013.

[76] T. Yang, M. Kohda, T. Seki, K. Takanashi, and J. Nitta, "Platinum layer thickness dependence of spin-Hall induced effective magnetic field in Pt/Co/Pt structures," *Jpn. J. Appl. Phys.*, **53**, 04EM06, 2014.

[77] H. Nakayama, M. Althammer, Y.-T. Chen, K. Uchida, Y. Kajiwara, D. Kikuchi, T. Ohtani, S. Geprägs, M. Opel, S. Takahashi, R. Gross, G. E. W. Bauer, S. T. B. Goennenwein, and E. Saitoh, “Spin Hall Magnetoresistance Induced by a Nonequilibrium Proximity Effect,” *Phys. Rev. Lett.*, **110**, 206601, 2013.

[78] W. J. Antel, M. M. Schwickert, T. Lin, W. L. O’Brien, and G. R. Harp, “Induced ferromagnetism and anisotropy of Pt layers in Fe/Pt(001) multilayers,” *Phys. Rev. B*, **60**, 12933, 1999.

[79] Y. M. Lu, Y. Choi, C. M. Ortega, X. M. Cheng, J. W. Cai, S. Y. Huang, L. Sun, and C. L. Chien, “Pt Magnetic Polarization on $\mathbf{Y}_3\mathrm{Fe}_5\mathbf{O}_{12}$ and Magnetotransport Characteristics,” *Phys. Rev. Lett.*, **110**, 147207, 2013.

[80] S. Geprägs, S. Meyer, S. Altmannshofer, M. Opel, F. Wilhelm, A. Rogalev, R. Gross, and S. T. B. Goennenwein, “Investigation of induced Pt magnetic polarization in Pt/Y3Fe5O12 bilayers,” *Appl. Phys. Lett.*, **101**, 262407, 2012.

[81] N. Vlietstra, J. Shan, V. Castel, B. J. van Wees, and J. Ben Youssef, “Spin-Hall magnetoresistance in platinum on yttrium iron garnet: Dependence on platinum thickness and in-plane/out-of-plane magnetization,” *Phys. Rev. B*, **87**, 184421, 2013.

[82] M. Althammer, S. Meyer, H. Nakayama, M. Schreier, S. Altmannshofer, M. Weiler, H. Huebl, S. Geprägs, M. Opel, R. Gross, D. Meier, C. Klewe, T. Kuschel, J.-M. Schmalhorst, G. Reiss, L. Shen, A. Gupta, Y.-T. Chen, G. E. W. Bauer, E. Saitoh, and S. T. B. Goennenwein, “Quantitative study of the spin Hall magnetoresistance in ferromagnetic insulator/normal metal hybrids,” *Phys. Rev. B*, **87**, 224401, 2013.

[83] T. Chiba, W. Bauer, Gerrit E. and S. Takahashi, “Current-Induced Spin-Torque Resonance of Magnetic Insulators,” *Phys. Rev. Applied*, **2**, 034003, 2014.

[84] A. Slachter, F. L. Bakker, J.-P. Adam, and B. van Wees, “Thermally driven spin injection from a ferromagnet into a non-magnetic metal,” *Nature Phys.*, **6**, 879, 2010.

[85] M. Walter, J. Walowski, V. Zbarsky, M. Münzenberg, M. Schäfers, D. Ebke, G. Reiss, A. Thomas, P. Peretzki, M. Seibt, J. S. Moodera, M. Czerner, M. Bachmann, and C. Heiliger, “Seebeck effect in magnetic tunnel junctions,” *Nature Mater.*, **10**, 742, 2011.

[86] A. Sugihara, M. Kodzuka, K. Yakushiji, H. Kubota, S. Yuasa, A. Yamamoto, K. Ando, K. Takanashi, T. Ohkubo, K. Hono, and A. Fukushima, “Giant Peltier Effect in a Submicron-Sized Cu–Ni/Au Junction with Nanometer-Scale Phase Separation,” *Appl. Phys. Express*, **3**, 065204, 2010.

[87] J. Flipse, F. Dejene, D. Wagenaar, G. Bauer, J. B. Youssef, and B. van Wees, "Observation of the Spin Peltier Effect for Magnetic Insulators," *Phys. Rev. Lett.*, **113**, 027601, 2014.

[88] K. Uchida, J. Xiao, H. Adachi, J. Ohe, S. Takahashi, J. Ieda, T. Ota, Y. Kajiwara, H. Umezawa, H. Kawai, G. E. W. Bauer, S. Maekawa, and E. Saitoh, "Spin Seebeck insulator," *Nature Mater.*, **9**, 894, 2010.

[89] N. Liebing, S. Serrano-Guisan, K. Rott, G. Reiss, J. Langer, B. Ocker, and H. W. Schumacher, "Tunneling Magnetothermopower in Magnetic Tunnel Junction Nanopillars," *Phys. Rev. Lett.*, **107**, 177201, 2011.

[90] J. Bass and W. P. Pratt, "Spin-diffusion lengths in metals and alloys, and spin-flipping at metal/metal interfaces: an experimentalist's critical review," *J. Phys.: Condens. Matter*, **19**, 183201, 2007.

[91] S. Y. Huang, W. G. Wang, S. F. Lee, J. Kwo, and C. L. Chien, "Intrinsic Spin-Dependent Thermal Transport," *Phys. Rev. Lett.*, **107**, 216604, 2011.

[92] M. Schmid, S. Srichandan, D. Meier, T. Kuschel, J.-M. Schmalhorst, M. Vogel, G. Reiss, C. Strunk, and C. H. Back, "Transverse Spin Seebeck Effect versus Anomalous and Planar Nernst Effects in Permalloy Thin Films," *Phys. Rev. Lett.*, **111**, 187201, 2013.

[93] S. Bosu, Y. Sakuraba, K. Uchida, K. Saito, W. Kobayashi, E. Saitoh, and K. Takanashi, "Thermal artifact on the spin Seebeck effect in metallic thin films deposited on MgO substrates," *J. Appl. Phys.*, **111**, 07B106, 2012.

[94] S. Bosu, Y. Sakuraba, K. Uchida, K. Saito, T. Ota, E. Saitoh, and K. Takanashi, "Spin Seebeck effect in thin films of the Heusler compound Co_2MnSi," *Phys. Rev. B*, **83**, 224401, 2011.

[95] C. M. Jaworski, J. Yang, S. Mack, D. D. Awschalom, J. P. Heremans, and R. C. Myers, "Observation of the spin-Seebeck effect in a ferromagnetic semiconductor." *Nature Mater.*, **9**, 898, 2010.

[96] C. M. Jaworski, J. Yang, S. Mack, D. D. Awschalom, R. C. Myers, and J. P. Heremans, "Spin-Seebeck Effect: A Phonon Driven Spin Distribution," *Phys. Rev. Lett.*, **106**, 186601, 2011.

[97] K. Uchida, H. Adachi, T. Ota, H. Nakayama, S. Maekawa, and E. Saitoh, "Observation of longitudinal spin-Seebeck effect in magnetic insulators," *Appl. Phys. Lett.*, **97**, 172505, 2010.

[98] H. Adachi, J.-i. Ohe, S. Takahashi, and S. Maekawa, "Linear-response theory of spin Seebeck effect in ferromagnetic insulators," *Phys. Rev. B*, **83**, 094410, 2011.

[99] A. A. Kovalev and Y. Tserkovnyak, "Thermomagnonic spin transfer and Peltier effects in insulating magnets," *Europhys. Lett.*, **97**, 67002, 2012.

[100] K. Nakata, "Thermal spin pumping mediated by magnons in the semiclassical regime," *J. Stat. Mech.-Theory E*, **2012**, P05020, 2012.

[101] H. Adachi, K. Uchida, E. Saitoh, and S. Maekawa, "Theory of the spin Seebeck effect," *Rep. Prog. Phys.*, **76**, 036501, 2013.

[102] K. S. Tikhonov, J. Sinova, and A. M. Finkel'stein, "Spectral non-uniform temperature and non-local heat transfer in the spin Seebeck effect," *Nat. Commun.*, **4**, 1945, 2013.

[103] S. Hoffman, K. Sato, and Y. Tserkovnyak, "Landau-Lifshitz theory of the longitudinal spin Seebeck effect," *Phys. Rev. B*, **88**, 064408, 2013.

[104] S. M. Rezende, R. L. Rodríguez-Suárez, R. O. Cunha, A. R. Rodrigues, F. L. A. Machado, G. A. Fonseca Guerra, J. C. Lopez Ortiz, and A. Azevedo, "Magnon spin-current theory for the longitudinal spin-Seebeck effect," *Phys. Rev. B*, **89**, 014416, 2014.

[105] K. Uchida, H. Adachi, T. Ota, H. Toda, B. Hillebrands, S. Maekawa, and E. Saitoh, "Long-range spin Seebeck effect and acoustic spin pumping," *Nature Mater.*, **10**, 737, 2011.

[106] H. Adachi, K. Uchida, E. Saitoh, J.-i. Ohe, S. Takahashi, and S. Maekawa, "Gigantic enhancement of spin Seebeck effect by phonon drag," *Appl. Phys. Lett.*, **97**, 252506, 2010.

[107] K. Uchida, T. Ota, H. Adachi, J. Xiao, T. Nonaka, Y. Kajiwara, G. E. W. Bauer, S. Maekawa, and E. Saitoh, "Thermal spin pumping and magnon-phonon-mediated spin-Seebeck effect," *J. Appl. Phys.*, **111**, 103903, 2012.

[108] G. Siegel, M. C. Prestgard, S. Teng, and A. Tiwari, "Robust longitudinal spin-Seebeck effect in Bi-YIG thin films," *Sci. Rep.*, **4**, 4429, 2014.

[109] M. Agrawal, V. I. Vasyuchka, A. A. Serga, A. D. Karenowska, G. A. Melkov, and B. Hillebrands, "Direct Measurement of Magnon Temperature: New Insight into Magnon-Phonon Coupling in Magnetic Insulators," *Phys. Rev. Lett.*, **111**, 107204, 2013.

[110] D. Meier, D. Reinhardt, M. van Straaten, C. Klewe, M. Althammer, M. Schreier, S. T. B. Goennenwein, A. Gupta, M. Schmid, C. H. Back, J.-M. Schmalhorst, T. Kuschel, and G. Reiss, "Longitudinal spin Seebeck effect contribution in transverse spin Seebeck effect experiments in Pt/YIG and Pt/NFO," *Nat. Commun.*, **6**, 8211, 2015.

[111] M. Weiler, M. Althammer, F. Czeschka, H. Huebl, M. Wagner, M. Opel, I.-M. Imort, G. Reiss, A. Thomas, R. Gross, and S. Goennenwein, "Local Charge and Spin Currents in Magnetothermal Landscapes," *Phys. Rev. Lett.*, **108**, 106602, 2012.

[112] D. Qu, S. Y. Huang, J. Hu, R. Wu, and C. L. Chien, "Intrinsic Spin Seebeck Effect in Au/YIG," *Phys. Rev. Lett.*, **110**, 067206, 2013.

[113] T. Kikkawa, K. Uchida, S. Daimon, Y. Shiomi, H. Adachi, Z. Qiu, D. Hou, X.-F. Jin, S. Maekawa, and E. Saitoh, "Separation of longitudinal spin Seebeck effect from anomalous Nernst effect: Determination of origin of transverse thermoelectric voltage in metal/insulator junctions," *Phys. Rev. B*, **88**, 214403, 2013.

[114] U. Ritzmann, "Computer Simulationen zum spinkalorischen Transport," Master's thesis, Universität Konstanz, 2011.

[115] D. Hinzke and U. Nowak, "Domain Wall Motion by the Magnonic Spin Seebeck Effect," *Phys. Rev. Lett.*, **107**, 027205, 2011.

[116] H. Kronmüller and S. Parkin, *Handbook of Magnetism and Advanced Magnetic Materials*. John Wiley & Sons, 2007.

[117] R. Eason, *Pulsed Laser Deposition of Thin Films: Applications-Led Growth of Functional Materials*. WILEY-INTERSCIENCE, 2007.

[118] Neocera. Neocera Pulsed Laser Deposition, Homepage (2015-03-14). Online: http://www.neocera.com/PDF/PLD%20Brochure.pdf

[119] C. Mix, "Laserablation von oxidischen Multilagenstrukturen zur Untersuchung von heteroepitaktischen Grenzflächenzuständen," Dissertationsschrift, Johannes-Gutenberg Universität Mainz, 2014.

[120] S. Fähler and H. U. Krebs, "Calculations and experiments of material removal and kinetic energy during pulsed laser ablation of metals," *Appl. Surf. Sci.*, **96-98**, 1996.

[121] H. M. Christen and G. Eres, "Recent advances in pulsed-laser deposition of complex oxides," *J. Phys.: Condens. Matter*, **20**, 264005, 2008.

[122] J. Venables, *Introduction to Surface and Thin Film Processes*. Cambridge University Press, 2000.

[123] K. Seshan, *Handbook of Thin Film Deposition, Process and Technologies (Second Edition)*. William Andrew, 2002.

[124] M. Birkholz, *Thin Film Analysis by X-Ray Scattering*. WILEY-VCH, 2005.

[125] H. Sawada, "Electron Density Study of Garnets: Z3Ga5O12;Z = Nd, Sm, Gd, Tb," *J. Solid State Chem.*, **132**, 300, 1997.

[126] L. G. Parratt, "Surface Studies of Solids by Total Reflection of X-Rays," *Phys. Rev.*, **95**, 359, 1954.

[127] D. Robbes, "Highly sensitive magnetometers—a review," *Sens. Actuators, A*, **129**, 86, 2006.

[128] R. Kleiner, D. Koelle, F. Ludwig, and J. Clarke, "Superconducting quantum interference devices: State of the art and applications," *Proc. IEEE*, **92**, 1534, 2004.

[129] R. L. Fagaly, "Superconducting quantum interference device instruments and applications," *Rev. Sci. Instrum.*, **77**, 101101, 2006.

[130] M. McElfresh and S. Li. Effects of Magnetic Field Uniformity on the Measurement of Superconducting Samples, (2015-03-28). Online: http://www.qdusa.com/sitedocs/appNotes/mpms/effects.pdf

[131] M. A. Gilleo and S. Geller, "Magnetic and Crystallographic Properties of Substituted Yttrium-Iron Garnet, $3\mathrm{Y_2O_3} \cdot x\mathrm{M_2O_3} \cdot (5-x)\mathrm{Fe_2O_3}$," *Phys. Rev.*, **110**, 73, 1958.

[132] S. S. Kalarickal, P. Krivosik, M. Wu, C. E. Patton, M. L. Schneider, P. Kabos, T. J. Silva, and J. P. Nibarger, "Ferromagnetic resonance linewidth in metallic thin films: Comparison of measurement methods," *J. Appl. Phys.*, **99**, 093909, 2006.

[133] C. Bilzer, T. Devolder, P. Crozat, C. Chappert, S. Cardoso, and P. P. Freitas, "Vector network analyzer ferromagnetic resonance of thin films on coplanar waveguides: Comparison of different evaluation methods," *J. Appl. Phys.*, **101**, 074505, 2007.

[134] C. E. Patton, "Linewidth and Relaxation Processes for the Main Resonance in the Spin-Wave Spectra of Ni-Fe Alloy Films," *J. Appl. Phys.*, **39**, 3060, 1968.

[135] C. E. Patton, *Magnetic Oxides*. Wiley, 1975.

[136] F. Jenkins and H. White, *Fundamentals of Optics*. McGraw-Hill Science/Engineering/Math, 2001.

[137] S. Polisetty, J. Scheffler, S. Sahoo, Y. Wang, T. Mukherjee, X. He, and C. Binek, "Optimization of magneto-optical Kerr setup: Analyzing experimental assemblies using Jones matrix formalism," *Rev. Sci. Instrum.*, **79**, 055107, 2008.

[138] T. Kuschel, H. Bardenhagen, H. Wilkens, R. Schubert, J. Hamrle, J. Pištora, and J. Wollschläger, "Vectorial magnetometry using magnetooptic Kerr effect including first- and second-order contributions for thin ferromagnetic films," *J. Phys. D: Appl. Phys.*, **44**, 265003, 2011.

[139] S. Trudel, G. Wolf, H. Schultheiss, J. Hamrle, and B. Hillebrands, "Probing quadratic magneto-optical Kerr effects with a tandem dual-beam system," *Rev. Sci. Instrum.*, **81**, 026105, 2010.

[140] F. Bertaut and F. Forrat, "Structure of ferrimagnetic rare-earth ferrites," *C.R. Acad. Sci., Paris*, **242**, 382, 1956.

[141] S. Geller and M. A. Gilleo, "Structure and ferrimagnetism of yttrium and rare-earth–iron garnets," *Acta Crystallogr.*, **10**, 239, 1957.

[142] P. Wigen, R. McMichael, and C. Jayaprakash, "Route to chaos in the magnetic garnets," *J. Magn. Magn. Mater.*, **84**, 237, 1990.

[143] E. Giess, J. Kuptsis, and E. White, "Liquid phase epitaxial growth of magnetic garnet films by isothermal dipping in a horizontal plane with axial rotation," *J. Cryst. Growth*, **16**, 36, 1972.

[144] S. Blank and J. Nielsen, "The growth of magnetic garnets by liquid phase epitaxy," *J. Cryst. Growth*, **17**, 302, 1972.

[145] J. Robertson, "Liquid phase epitaxy of garnets," *J. Cryst. Growth*, **45**, 233, 1978.

[146] O. d'Allivy Kelly, A. Anane, R. Bernard, J. Ben Youssef, C. Hahn, A. H. Molpeceres, C. Carrétéro, E. Jacquet, C. Deranlot, P. Bortolotti, R. Lebourgeois, J.-C. Mage, G. de Loubens, O. Klein, V. Cros, and A. Fert, "Inverse spin Hall effect in nanometer-thick yttrium iron garnet/Pt system," *Appl. Phys. Lett.*, **103**, 082408, 2013.

[147] R. C. Linares, R. B. McGraw, and J. B. Schroeder, "Growth and Properties of Yttrium Iron Garnet Single-Crystal Films," *J. Appl. Phys.*, **36**, 2884, 1965.

[148] F. Euler and J. A. Bruce, “Oxygen coordinates of compounds with garnet structure,” *Acta Crystallogr.*, **19**, 971, 1965.

[149] J. M. D. Coey, *Magnetism and Magnetic Materials*. Cambridge University Press, 2010.

[150] P. Larsen and R. Metselaar, “Defects and the electronic properties of $Y_3Fe_5O_{12}$,” *J. Solid State Chem.*, **12**, 253, 1975.

[151] K. I. Cherepanov V and L. V, “The saga of YIG: spectra, thermodynamics, interaction and relaxation of magnons in a complex magnet,” *Rep. Rev. Sec. Phys. Lett.*, **229**, 1993.

[152] R. C. O’Handley, *Modern Magnetic Materials: Principles and Applications*. John Wiley and Sons, 2000.

[153] H. Wang, C. Du, P. C. Hammel, and F. Yang, “Strain-tunable magnetocrystalline anisotropy in epitaxial $Y_3\mathrm{Fe}_5\mathrm{O}_{12}$ thin films,” *Phys. Rev. B*, **89**, 134404, 2014.

[154] C. Burrowes, B. Heinrich, B. Kardasz, E. A. Montoya, E. Girt, Y. Sun, Y.-Y. Song, and M. Wu, “Enhanced spin pumping at yttrium iron garnet/Au interfaces,” *Appl. Phys. Lett.*, **100**, 092403, 2012.

[155] Y. Sun, H. Chang, M. Kabatek, Y.-Y. Song, Z. Wang, M. Jantz, W. Schneider, M. Wu, E. Montoya, B. Kardasz, B. Heinrich, S. G. E. te Velthuis, H. Schultheiss, and A. Hoffmann, “Damping in Yttrium Iron Garnet Nanoscale Films Capped by Platinum,” *Phys. Rev. Lett.*, **111**, 106601, 2013.

[156] C. Hahn, G. de Loubens, O. Klein, M. Viret, V. V. Naletov, and J. Ben Youssef, “Comparative measurements of inverse spin Hall effects and magnetoresistance in YIG/Pt and YIG/Ta,” *Phys. Rev. B*, **87**, 174417, 2013.

[157] P. Pirro, T. Brächer, A. V. Chumak, B. Lägel, C. Dubs, O. Surzhenko, P. Görnert, B. Leven, and B. Hillebrands, “Spin-wave excitation and propagation in microstructured waveguides of yttrium iron garnet/Pt bilayers,” *Appl. Phys. Lett.*, **104**, 012402, 2014.

[158] M. Huang and S.-Y. Zhang, “Growth and characterization of cerium-substituted yttrium iron garnet single crystals for magneto-optical applications,” *Appl. Phys. A*, **74**, 177–, 2002.

[159] T.-C. Mao and J.-C. Chen, “Influence of the addition of CeO2 on the microstructure and the magnetic properties of yttrium iron garnet ceramic,” *J. Magn. Magn. Mater.*, **302**, 74, 2006.

[160] T.-C. Mao, J.-C. Chen, and C.-C. Hu, “Effect of the pulling rate on the quality of cerium-substituted YIG single-crystal fibers by LHPG,” *J. Cryst. Growth*, **296**, 110, 2006.

[161] T. Goto, M. C. Onbaşli, and C. A. Ross, “Magneto-optical properties of cerium substituted yttrium iron garnet films with reduced thermal budget for monolithic photonic integrated circuits,” *Opt. Express*, **20**, 28507, 2012.

[162] T. Goto, Y. Eto, K. Kobayashi, Y. Haga, M. Inoue, and C. A. Ross, “Vacuum annealed cerium-substituted yttrium iron garnet films on non-garnet substrates for integrated optical circuits,” *J. Appl. Phys.*, **113**, 17A939, 2013.

[163] W. Jiang, P. Upadhyaya, Y. Fan, J. Zhao, M. Wang, L.-T. Chang, M. Lang, K. L. Wong, M. Lewis, Y.-T. Lin, J. Tang, S. Cherepov, X. Zhou, Y. Tserkovnyak, R. N. Schwartz, and K. L. Wang, “Direct Imaging of Thermally Driven Domain Wall Motion in Magnetic Insulators,” *Phys. Rev. Lett.*, **110**, 177202, 2013.

[164] S. M. Shahrokhvand, A. S. H. Rozatian, M. Mozaffari, S. M. Hamidi, and M. M. Tehranchi, “Preparation and investigation of Ce:YIG thin films with a high magneto-optical figure of merit,” *J. Phys. D: Appl. Phys.*, **45**, 235001, 2012.

[165] H. Xu and H. Yang, “Magnetic properties of YIG doped with cerium and gadolinium ions,” *J. Mater. Sci.: Mater. Electron*, **19**, 589, 2008.

[166] T. Sekijima, H. Kishimoto, T. Fujii, K. Wakino, and M. Okada, “Magnetic, Optical and Microwave Properties of Rare-Earth-Substituted Fibrous Yttrium Iron Garnet Single Crystals Grown by Floating Zone Method,” *Jpn. J. Appl. Phys.*, **38**, 5874, 1999.

[167] M. Deeter, A. Rose, and G. Day, “Fast, sensitive magnetic-field sensors based on the Faraday effect in YIG,” *J. Lightw. Technol.*, **8**, 1838, 1990.

[168] S. Higuchi, K. Ueda, F. Yahiro, Y. Nakata, H. Uetsuhara, T. Okada, and M. Maeda, “Fabrications of cerium-substituted YIG thin films for magnetic field sensor by pulsed-laser deposition,” *IEEE Trans. Magn*, **37**, 2451, 2001.

[169] R. Pauthenet, “Spontaneous Magnetization of Some Garnet Ferrites and the Aluminum Substituted Garnet Ferrites,” *J. Appl. Phys.*, **29**, 253, 1958.

[170] D. Rodić, Z. Tomkowicz, L. Novaković, A. Szytula, and M. Napijalo, “The initial magnetic susceptibilities of Gd3Fe5O12 and Tb3Fe5O12 in the compensation point region,” *Solid State Commun.*, **73**, 243, 1990.

[171] S. Geller, H. J. Williams, and R. C. Sherwood, “Magnetic and Crystallographic Study of Neodymium-Substituted Yttrium and Gadolinium Iron Garnets,” *Phys. Rev.*, **123**, 1692, 1961.

[172] K. P. Belov, “Ferrimagnets with a ’weak’ magnetic sublattice,” *Physics-Uspekhi*, **39**, 623, 1996.

[173] M. Schreier, N. Roschewsky, E. Dobler, S. Meyer, H. Huebl, R. Gross, and S. T. B. Goennenwein, “Current heating induced spin Seebeck effect,” *Appl. Phys. Lett.*, **103**, 242404, 2013.

[174] K. Uchida, T. Kikkawa, A. Miura, J. Shiomi, and E. Saitoh, “Quantitative Temperature Dependence of Longitudinal Spin Seebeck Effect at High Temperatures,” *Phys. Rev. X*, **4**, 041023, 2014.

[175] Y. M. Lu, J. W. Cai, S. Y. Huang, D. Qu, B. F. Miao, and C. L. Chien, “Hybrid magnetoresistance in the proximity of a ferromagnet,” *Phys. Rev. B*, **87**, 220409, 2013.

[176] T. McGuire and R. Potter, “Anisotropic magnetoresistance in ferromagnetic 3d alloys,” *IEEE Trans. Magn.*, **11**, 1018, 1975.

[177] A. Sola, M. Kuepferling, V. Basso, M. Pasquale, T. Kikkawa, K. Uchida, and E. Saitoh, “Evaluation of thermal gradients in longitudinal spin Seebeck effect measurements,” *private communication*, 2015.

[178] N. Roschewsky, M. Schreier, A. Kamra, F. Schade, K. Ganzhorn, S. Meyer, H. Huebl, S. Geprägs, R. Gross, and S. T. B. Goennenwein, “Time resolved spin Seebeck effect experiments,” *Appl. Phys. Lett.*, **104**, 202410, 2014.

[179] M. Agrawal, V. I. Vasyuchka, A. A. Serga, A. Kirihara, P. Pirro, T. Langner, M. B. Jungfleisch, A. V. Chumak, E. T. Papaioannou, and B. Hillebrands, “Role of bulk-magnon transport in the temporal evolution of the longitudinal spin-Seebeck effect,” *Phys. Rev. B*, **89**, 224414, 2014.

[180] M. Agrawal, A. A. Serga, V. Lauer, E. T. Papaioannou, B. Hillebrands, and V. I. Vasyuchka, “Microwave-induced spin currents in ferromagnetic-insulator|normal-metal bilayer system,” *Appl. Phys. Lett.*, **105**, 092404, 2014.

[181] M. B. Jungfleisch, V. Lauer, R. Neb, A. V. Chumak, and B. Hillebrands, “Improvement of the yttrium iron garnet/platinum interface for spin pumping-based applications,” *Appl. Phys. Lett.*, **103**, 022411, 2013.

[182] K. Uchida, T. Nonaka, T. Kikkawa, Y. Kajiwara, and E. Saitoh, “Longitudinal spin Seebeck effect in various garnet ferrites,” *Phys. Rev. B*, **87**, 104412, 2013.

[183] J. S. Plant, “‘Pseudo-acoustic’ magnon dispersion in yttrium iron garnet,” *J. Phys. C.*, **16**, 7037, 1983.

[184] I. Knittel and U. Hartmann, “Lorentz magnetoresistance of thin films in the presence of surface scattering and domain structures,” *J. Magn. Magn. Mater.*, **294**, 16, 2005.

[185] E. G. Spencer and R. C. LeCraw, “Spin-Lattice Relaxation in Yttrium Iron Garnet,” *Phys. Rev. Lett.*, **4**, 130, 1960.

[186] E. G. Spencer, R. C. LeCraw, and R. C. Linares, “Low-Temperature Ferromagnetic Relaxation in Yttrium Iron Garnet,” *Phys. Rev.*, **123**, 1937, 1961.

[187] G. F. Dionne and G. L. Fitch, “Temperature dependence of spin-lattice relaxation in rare-earth iron garnets,” *J. Appl. Phys.*, **87**, 4963, 2000.

[188] M. Haidar, M. Ranjbar, M. Balinsky, R. K. Dumas, S. Khartsev, and J. Åkerman, “Thickness- and temperature-dependent magnetodynamic properties of yttrium iron garnet thin films,” *J. Appl. Phys.*, **117**, 2015.

[189] K. Ando and E. Saitoh, “Inverse spin-Hall effect in palladium at room temperature,” *J. Appl. Phys.*, **108**, 113925, 2010.

[190] S. Meyer, M. Althammer, S. Geprägs, M. Opel, R. Gross, and S. T. B. Goennenwein, “Temperature dependent spin transport properties of platinum inferred from spin Hall magnetoresistance measurements,” *Appl. Phys. Lett.*, **104**, 242411, 2014.

[191] S. R. Marmion, M. Ali, M. McLaren, D. A. Williams, and B. J. Hickey, “Temperature dependence of spin Hall magnetoresistance in thin YIG/Pt films,” *Phys. Rev. B*, **89**, 220404, 2014.

[192] L. Vila, T. Kimura, and Y. Otani, “Evolution of the Spin Hall Effect in Pt Nanowires: Size and Temperature Effects,” *Phys. Rev. Lett.*, **99**, 226604, 2007.

[193] Z. Tang, Y. Kitamura, E. Shikoh, Y. Ando, T. Shinjo, and M. Shiraishi, “Temperature Dependence of Spin Hall Angle of Palladium,” *Appl. Phys. Express*, **6**, 083001, 2013.

[194] S. M. Rezende and J. C. López Ortiz, “Thermal properties of magnons in yttrium iron garnet at elevated magnetic fields,” *Phys. Rev. B*, **91**, 104416, 2015.

[195] Y. Ohnuma, H. Adachi, E. Saitoh, and S. Maekawa, “Spin Seebeck effect in antiferromagnets and compensated ferrimagnets,” *Phys. Rev. B*, **87**, 014423, 2013.

[196] R. K. Wangsness, “Sublattice Effects in Magnetic Resonance,” *Phys. Rev.*, **91**, 1085, 1953.

[197] C. D. Stanciu, A. V. Kimel, F. Hansteen, A. Tsukamoto, A. Itoh, A. Kirilyuk, and T. Rasing, “Ultrafast spin dynamics across compensation points in ferrimagnetic GdFeCo: The role of angular momentum compensation,” *Phys. Rev. B*, **73**, 220402, 2006.

[198] M. Binder, A. Weber, O. Mosendz, G. Woltersdorf, M. Izquierdo, I. Neudecker, J. R. Dahn, T. D. Hatchard, J.-U. Thiele, C. H. Back, and M. R. Scheinfein, “Magnetization dynamics of the ferrimagnet CoGd near the compensation of magnetization and angular momentum,” *Phys. Rev. B*, **74**, 134404, 2006.

[199] J. Goulon, A. Rogalev, F. Wilhelm, G. Goujon, A. Yaresko, C. Brouder, and J. B. Youssef, “Site-selective couplings in x-ray-detected magnetic resonance spectra of rare-earth-substituted yttrium iron garnets,” *New J. Phys.*, **14**, 063001, 2012.

[200] G. E. W. Bauer, S. Bretzel, A. Brataas, and Y. Tserkovnyak, “Nanoscale magnetic heat pumps and engines,” *Phys. Rev. B*, **81**, 024427, 2010.

[201] J. C. Slonczewski, “Initiation of spin-transfer torque by thermal transport from magnons,” *Phys. Rev. B*, **82**, 054403, 2010.

[202] M. Mochizuki, X. Z. Yu, S. Seki, N. Kanazawa, W. Koshibae, J. Zang, M. Mostovoy, Y. Tokura, and N. Nagaosa, “Thermally driven ratchet motion of a skyrmion micro-crystal and topological magnon Hall effect,” *Nature Mater.*, **13**, 241, 2008.

Acknowledgement

Removed due to data privacy

Curriculum vitae

Removed due to data privacy

Eidesstattliche Erklärung

Hiermit erkläre ich an Eides statt, dass ich meine Dissertation selbständig und ohne fremde Hilfe verfasst und keine anderen als die von mir angegebenen Quellen und Hilfsmittel zur Erstellung meiner Dissertation verwendet habe. Die Arbeit ist in vorliegender oder ähnlicher Form bei keiner anderen Prüfungsbehörde zur Erlangung eines Doktorgrades eingereicht worden.

Mainz, den

Andreas Kehlberger